EXPERIMENTAL INVESTIGATIONS IN ELEMENTARY PARTICLE PHYSICS

W.W.M. Allison

Christ Church, Oxford.

A Dissertation submitted to the University of Oxford for the Degree of Doctor of Philosophy.

May, 1967.

Alonso: This is as strange a maze as e'er men trod;
And there is in this business more than nature
Was ever conduct of: some oracle
Must rectify our knowledge.

Prospero: Sir, my liege,
Do not infest your mind with beating on
The strangeness of this business: at pick'd leisure
Which shall be shortly, single I'll resolve you, -
Which to you shall seem probable, - of every
These happen'd accidents; till when, be cheerful,
And think of each thing well.

Shakespeare,
The Tempest.

ABSTRACT

An account is given of some of the results of an experiment undertaken by a collaboration of five British and one German Hydrogen Bubble Chamber Groups. A beam of 6 GeV/c K^- mesons was injected into the British National Hydrogen Bubble Chamber at the proton synchrotron at CERN, Geneva. A total of 300,000 pictures or 1800 kms. of K^- track was scanned for interactions. The scanning, measuring and identification of two classes of interaction in the Oxford sample of film are described in detail. A scheme which uses a computer to do the book keeping of the scanned information is mentioned - this was developed by the author as a result of experience with this experiment. The treatment of losses, biasses and ambiguities is discussed at some length - a new method is used to correct for the loss of sigmas at small decay angles in the laboratory and a discussion of the meaning of the probability associated with a kinematic fit leads to ideas affecting the interpretation of ambiguous fits.

Special problems affecting the analysis of multibody final states are discussed and solutions put into practice. Careful treatment is given to final states which derive large

weights from losses. A discussion of the optimum way of selecting resonances and choosing histogram bin sizes is to be found in an appendix. From a brief discussion of the theory of Unitary Symmetry we are lead to consider the omega minus and its quantum numbers. An original investigation by the author into the isospin of the omega takes the form of a search for a neutral baryon of strangeness -3. The fact that the state is not found is of even greater interest for the quark model of Unitary Symmetry. The latter is described briefly and a search is made for other states forbidden by the model.

A survey is made of final states containing a hyperon and mesons. Evidence in favour of a new Y_1^* resonance at 1680 MeV decaying to ($\Lambda\pi$) supports the findings of M. Derrick et al. at 5.5 GeV/c. A strong forward peak of lambdas in the lambda four pion and lambda five pion final states appears to be associated with strong production of positively charged meson resonances decaying into three pions. These resonances appear at 1100, 1300 and 1640 MeV and are identified with A1, A2 and $\pi(1640)$. The A2 appears to decay to ($\rho\pi$) although the data suggests that the A1 does not. Similar features were seen in the lambda four pion state at 3.5 GeV. These findings are important since the A1 has only been seen before in final states confused by "Deck" diffractive effects.

The decay correlations of the reaction $K^-p \rightarrow \quad \rho^0$ are calculated from first principles and compared with experiment. This paves the way for the study of the double peripheral production mechanism. Detailed discussion of two final states ($K^-p \rightarrow \Sigma^0\pi^+\pi^-$ and $K^-p \rightarrow K^{*-}\pi^+n$) is used to set forth the general features of the model. It is shown that the matrix element for the former may be derived directly from that for the well known reaction $\pi^-p \rightarrow \Sigma^0 K^{*0}$ by crossing symmetry. Although the data are not definitive, they provide general support for the model.

ACKNOWLEDGEMENTS

I should like to thank; Professor D.H. Wilkinson, FRS, for making it possible to carry out the course of research leading to the present thesis; the Scientific Research Council for their support; the Royal Commissioners for the Exhibition of 1851 and the Dean, Canons and Students of Christ Church without whose generosity many points discussed in this thesis might have remained unexplored; my supervisor Dr J.H. Mulvey, for his never failing enthousiasm and encouragement; Mrs Patricia Aidley and her staff of patient scanners, especially Mrs Carla Hine for her book keeping, Mrs Jodell Smith for her enthousiastic help with the scanning programme and Miss Kay Landon who drew most of the diagrams; Andres Cruz Flor for his hard work and cooperation; lastly my typist Miss Judy Owen for this flattering transformation of my script.

LIST OF CONTENTS

INTRODUCTION

This experiment was a collaboration between the Hydrogen Bubble Chamber Groups of the Rutherford High Energy Laboratory, the Max Planck Institute (Munich) and the Universities of Birmingham, Glasgow, Oxford and London (Imperial College). The purpose of the experiment was to investigate the interaction of K^- mesons with protons at a laboratory momentum of 6 GeV/c - this includes both the theory of production dynamics and the discovery of new particle states and their properties. The experiment was carried out in the 1.5 metre British National Hydrogen Bubble Chamber in the East Hall at the CERN proton synchrotron during 1964/65. The total of 300,000 good pictures was divided equally amongst the six laboratories. Each laboratory analysed this film and contributed a data summary tape containing the details of all the events satisfactorily analysed. These summaries were merged and copies made available at various computing installations so that statistical aspects of the data could be analysed.

In chapter 1 the beam and chamber are described. Owing to the breakdown of Nimrod I was not connected with the experiment at this early stage. The processing of our part of the film was undertaken by several graduate students - Andres Cruz and I were responsible for the four prong + V^o and four prong with charged decay events. This part of the work is described in chapter 2. Chapter 3 deals with the theory of Unitary Symmetry, the prediction and discovery of the omega minus and an investigation of its properties. This turns into a search for a similar neutral particle which is not found. The poor momentum resolution of the chamber and the high momentum of the beam conspire to make the problems of losses, biasses and ambiguities of considerable importance. This is the subject of chapter 4 and of two of the seven appendices. Chapter 5 is concerned with a survey of the hyperon + mesons final states. Some aspects of these have already been discussed by D.H. Locke and are not repeated here. The decay correlations of the reaction $K^-p \rightarrow \Lambda \rho^o$ are calculated from first principles and compared with experiment in appendix F. This paves the way for the study of the double peripheral production mechanism in chapter 6. The details of the algebra are given in Appendix G.

CHAPTER 1

THE BEAM, CHAMBER AND PICTURES

1.1 The beam

In this experiment a beam of 6 GeV/c K^- mesons was injected into the 1.5 metre British National Hydrogen Bubble Chamber at CERN. The beam was taken from an internal target in the proton synchrotron. A plan is shown in Fig. 1.1. The first stage consisted of a vertical (C_2) and a horizontal (C_1) collimator to define the angular size of the beam. The beam was then passed through a horizontal bending magnet M_1 and refocussed in the horizontal plane on a slit C_3. The effect of this is to give a momentum-dispersed image of the target in the plane of the slit C_3. By adjusting the field of the bending magnet M_1 and the separation of the jaws of C_3 the momentum and momentum bite could be selected. After the momentum selection stage came the separation stage. A focus in the vertical plane at C_4 was refocussed on the mass slit, C_6, 100 metres down stream. In between were three electrostatic separator tanks each ten metres long. The effect of the electrostatic field was compensated for by

Fig 1·1. Schematic layout of the O2 beam.

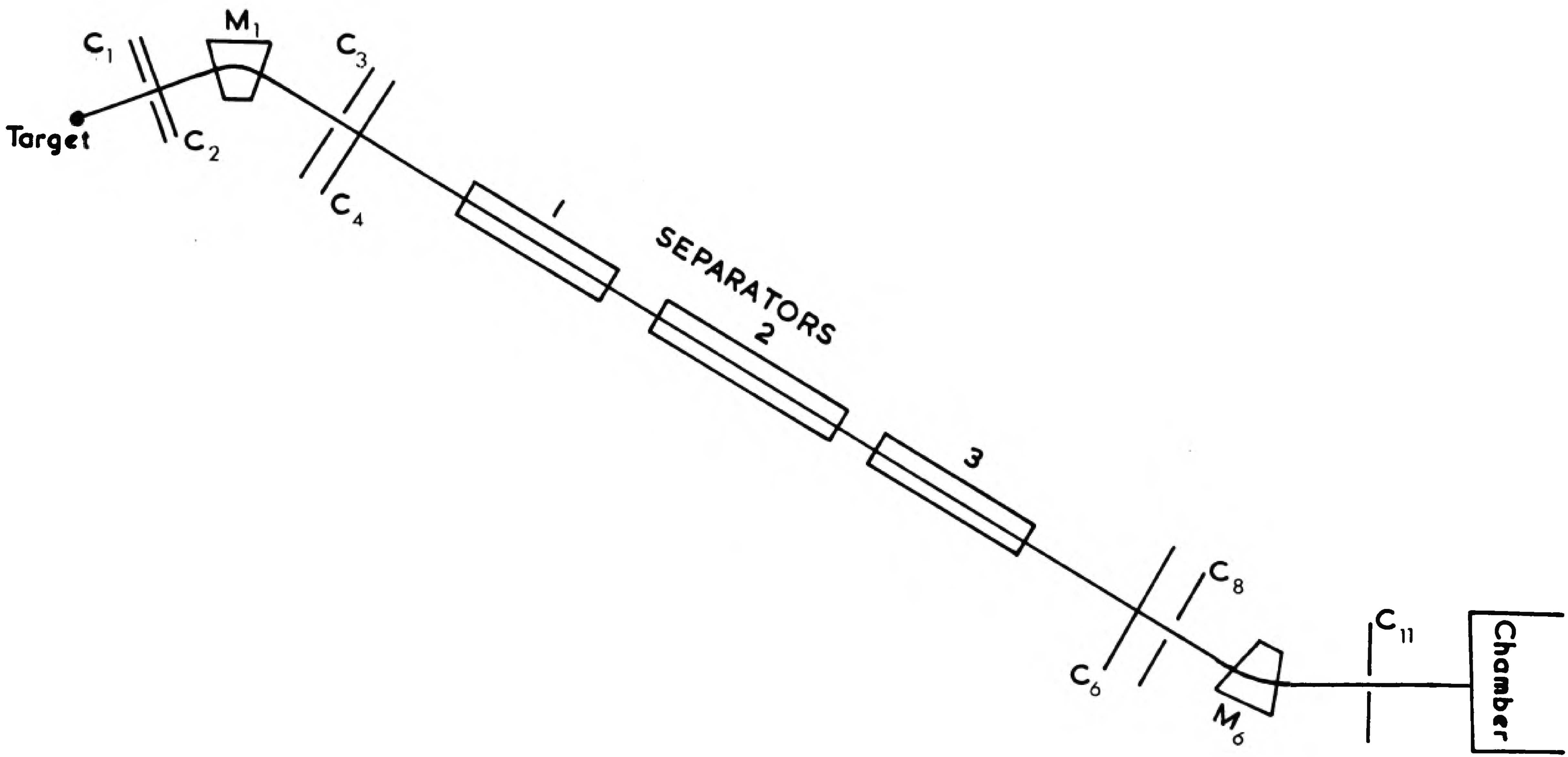

small bending magnets at the end of each tank. This compensation was arranged to image the kaons between the jaws of the mass slit C_6. Since the force on a particle in magnetic and electric fields is given by:

$$e(\underline{E} + \frac{1}{c}(\underline{v} \times \underline{H}))$$

this compensation is velocity dependent or (at fixed momentum as here) mass dependent. Therefore the unwanted π^- and $\bar{p}$ particles focussed at a different point, hit the jaws of the collimator and were removed. At this point the beam had travelled nearly 150 metres and the flux of muons and pions from the decay of pions and kaons was considerable. Those that decayed during the separation stage often succeeded in getting through the mass slit. They were distinguished by their low momentum. Therefore the separation stage was followed by another momentum defining geometry similar to the first. The beam now entered the chamber.

1.2 The chamber

The chamber is 150 cms long by 50 cms wide by 50 cms deep. Three cameras in a vertical plane view the chamber horizontally. Through the window on the opposite side of the chamber nine flash tubes in sets of three illuminate the volume of the chamber. The light from these is focussed on the plane of the camera lenses by three large condensing lenses. These foci are arranged symmetrically around each camera so that no light enters the camera except as a result of scattering e.g. on a bubble. The operation of the chamber is synchronised with the accelerator so that expansion takes place just before and illumination just after the particles pass through the chamber. Round the chamber vessel and its associated nitrogen and vacuum shields are the windings of the magnet and the vast iron yoke. The 12 Kgauss magnetic field is along the line of sight of the cameras.

A Cerenkov counter just in front of the chamber recorded the number of π's and μ's in the beam while a thin scintillation counter registered the total number of particles per picture. These counts were recorded on film for each frame and were used later to estimate the purity of the beam. The beam momentum and its spread were checked later by measuring τ decays and using the four constraint fit to determine the incident K^- momentum as well as possible. The results were consistent with the momentum parameters derived from the current in M1 and the geometry of the momentum definition stages of the beam.

Histogram of (Missing Mass)^2 of V^{0}s fitting K^0 decay.

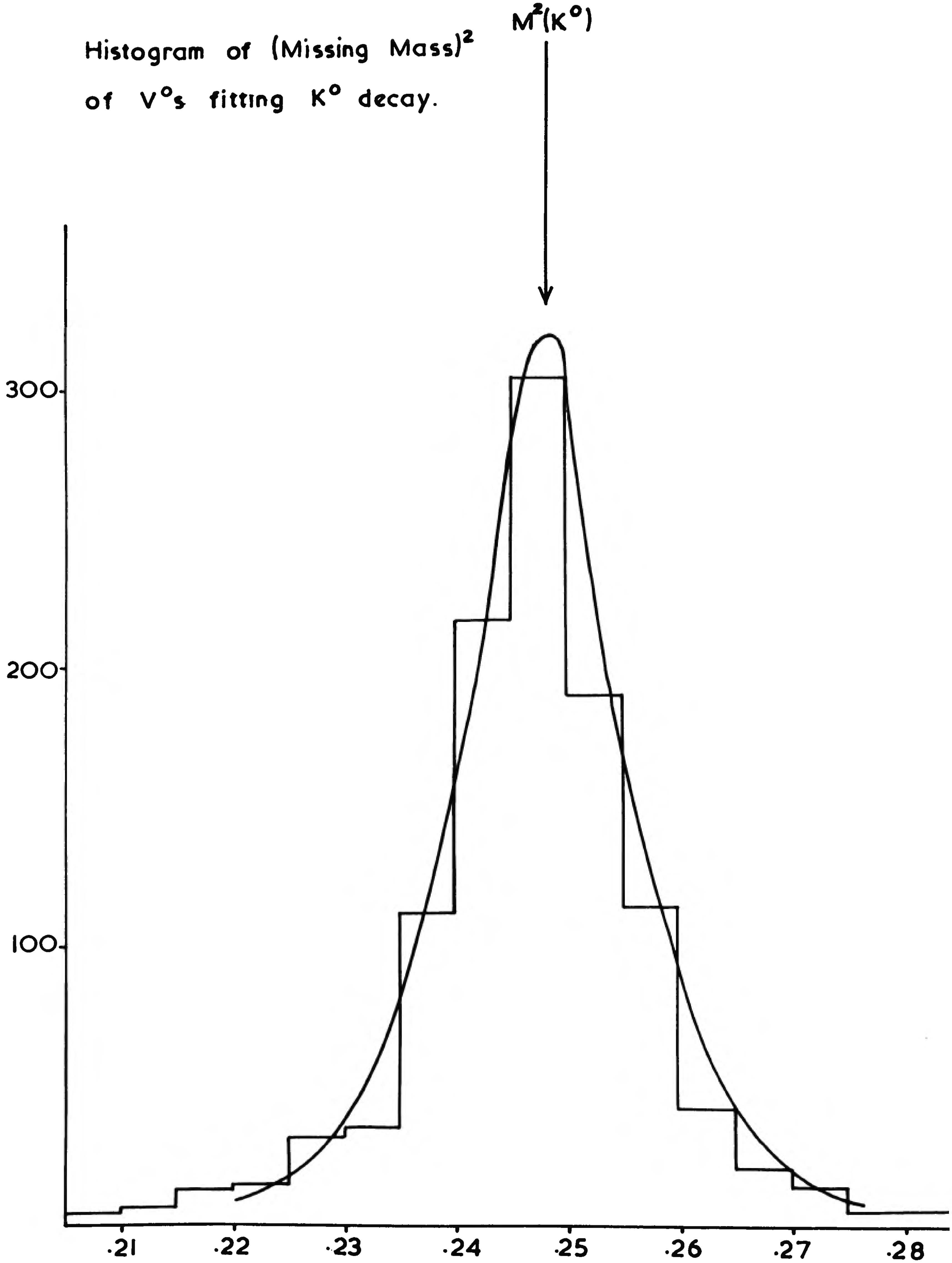

Fig 1.2.

The magnetic field was charted with a Hall effect probe and the geometrical constants of the chamber measured directly. The uncertainty in the geometrical constants and optical distortion effects were corrected by measuring all the fiducial marks on a large number of frames. By examining the fiducial reconstruction errors and the distance of the reconstruction from the plane of the window as a function of small changes in the constants the best values were found[1]. The absolute value of the magnetic field values was calculated by examining the missing mass and its dispersion for V^os identified as K^os. It may be shown that this is a sensitive function of the magnetic field[2]. Furthermore if the variations of the field are wrong the width of the peak would be greater than that expected from the observed errors. In Fig. 1.2 we show a histogram of this missing mass which is in excellent agreement with that expected. Only the z-component of the magnetic field was used - although the inhomogeneity of the latter implies the existence of transverse components these were shown to have a negligible effect.

1.3 The film exposures

The exposure took place in three separate runs (referred to as 'D', 'E' and 'F') and every sixth roll of film was sent to Oxford. The film quality was monitored in situ by developing a short strip at the end of each roll immediately.

Despite this the film quality was generally poor. The magnetic field was not high enough to give the required resolution. Furthermore the 1% momentum bite being 60 MeV/c turned out to be embarrassingly large when the problem of distinguishing Λ^0s from Σ^0s was tackled (see chapter 4). The purity of the beam however was quite good:

80% Ks

5% πs

15% μs

so that events in which a strange particle was observed could be safely taken as due to a K^-p interaction.

REFERENCES TO CHAPTER 1

(1) J. Allison D.Phil thesis (Oxford 1966).

(2) D.H. Locke D.Phil thesis (Oxford 1966).

CHAPTER 2

PROCESSING THE DATA ON THE OXFORD SAMPLE OF FILM

2.1 Scanning and Measuring

It was my responsibility to process the events of the type four prongs + V^0 and four prongs with a charged decay. (These are referred to as 401 and 410 events respectively.) Figs.2.1 and 2.2 show typical examples of these event types. Only events in which the primary interaction vertex lay within an inner box and the decay vertex lay within an outer box were accepted for analysis. These boxes are shown in Fig.2.3 in relation to the fiducial marks on view 2.

In the first instance the film was scanned twice by scanners. A physicist then examined the discrepancies between the two scans. From this information a first 'Master List' was drawn up. During these scans other topologies were also recorded and in particular τ decays of beam particles were counted. Two previous scans covering part of the film for rare events and τs had also been made. Each event on the first master list was measured on a film plane digitiser using Ferranti gratings and the Moire fringe technique.

→ beam direction

Fig 2·1. A 401 event.

→ beam direction

Fig 2.2. A 410 event.

Fig. 2·3. The scanning box.

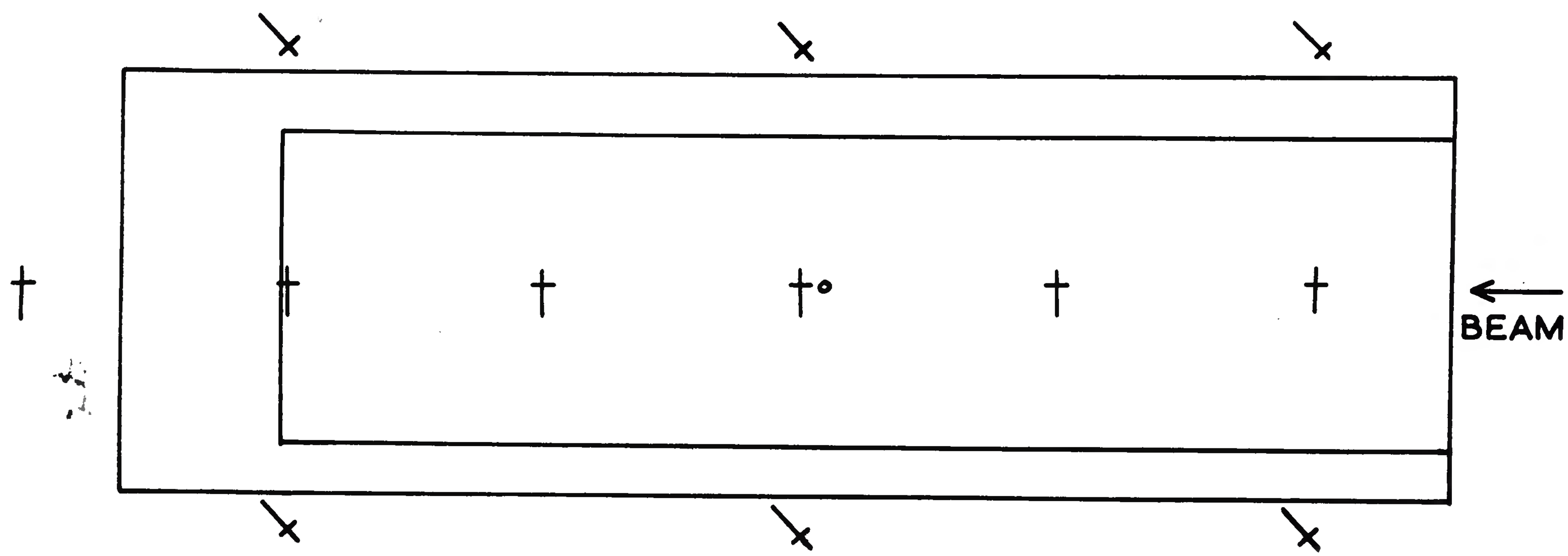

It was not until this point (due to the breakdown of Nimrod) that I became concerned with the 401 and 410 events. The scanning had not been very thorough and the measuring was proceeding slowly. Investigation showed several ways in which the measuring process could be accelerated. A senior scanner was appointed with special responsibility for this data and personal instruction improved both the quality and the quantity of the data processed. Under this regime a third scan of the film was made and discrepancies with the first master list examined either by Andres Cruz with whom I worked or by myself. Many new events emerged and the second master list was made. All events on the latter which were not on the first list were now measured. Despite this it was clear from my investigations that errors in manual transcription from one list to another, variable standards of scanning and the difficulties of retrieval of scanning information were seriously hampering the preparation and processing of the data. To set up a computer-based scan system to overcome these difficulties has taken an appreciable part of my time. Although it came too late to be of use in this experiment, it is in full production on other experiments and has been greeted enthusiastically by all concerned. It is described briefly in Appendix D and more thoroughly elsewhere(1).

The output of the digitising machines on five channel paper tape was checked and written to magnetic tape on the English Electric KDF9 at Oxford. Paper tapes with format errors were patched and recirculated. After transcription of this data onto IBM magnetic tape at the KDF9 at Culham it was taken to the IBM 7044 at Glasgow for geometrical reconstruction and kinematic fitting.

2.2 Geometrical Reconstruction

The process of three dimensional reconstruction from three stereoscopic views in the RHEL geometry programme is fully described elsewhere(2). Events for which only two views were measurable caused some trouble - the large number of tracks in our topologies meant that there was a high probability of a track passing close to the line joining the two cameras. When this happens it is impossible to calculate its depth in the chamber. Rolls in which one view was completely unmeasurable were removed from the sample. Of the remainder less than 5% suffered from a defective view. Just before geometry processing was started some important modifications were made to the programme by RHEL to correct certain shortcomings which had come to light as a result of detailed comparisons with the CERN THRESH programme. These concern the reconstruction of vertices which was formerly done by least squares point reconstruction of the vertex measurements i.e. vertices and tracks were reconstructed independently. In the new version after track reconstruction the vertex position was found by a least squares fit of the distance to the intersecting tracks as well as to the measured vertex points. Not all the data from the other laboratories was processed by the new programme - they claimed that the difference was small. The Munich data was processed through the Thresh Grind system.

All those events which failed geometrical reconstruction were remeasured; those that passed were processed by the RHEL kinematic fitting programme[3].

2.3 Identification of the 401 events by kinematic fitting and ionisation

Each 401 event was tried on the hypotheses listed in Table 2.1. After each hypothesis is given the fit sequence,

TABLE 2.1

Hypothesis	Name	Fit Sequence	Constraints	Cut off
$K^-p \rightarrow \Lambda^0\pi^+\pi^+\pi^-\pi^-$	401211	A	3, 4, 7	1% on Fit 2
$\Lambda^0\pi^+\pi^+\pi^-\pi^-\pi^0$	401221	A	3, 1, 4	5% on Fit 2
$\Sigma^0\pi^+\pi^+\pi^-\pi^-$	401311	B	3, 1, 1, 5	1% on Fit 3
$\bar{K}^0p\pi^+\pi^-\pi^-$	401011	A	3, 4, 7	1% on Fit 2
$\bar{K}^0p\pi^+\pi^-\pi^-\pi^0$	401021	A	3, 1, 4	5% on Fit 2
$\bar{K}^0n\pi^+\pi^+\pi^-\pi^-$	401031	A	3, 1, 4	5% on Fit 2
$K^-p \rightarrow pp\bar{p}\bar{K}^0\pi^-$	401013	A	3, 4, 7	1% on Fit 2
$nK^+K^-\bar{K}^0\pi^+\pi^-$	401023	A	3, 1, 4	5% on Fit 2
$pK^+K^-\bar{K}^0\pi^-$	401033	A	3, 4, 7	1% on Fit 2
$pK^+K^-\bar{K}^0\pi^-\pi^0$	401043	A	3, 1, 4	5% on Fit 2
$nK^0K^-K^-\pi^+\pi^+$	401053	A	3, 1, 4	5% on Fit 2
$pK^0K^-K^-\pi^+$	401063	A	3, 4, 7	1% on Fit 2
$pK^0K^-K^-\pi^+\pi^0$	401073	A	3, 1, 4	5% on Fit 2

TABLE 2.1 (cont'd)

Hypothesis	Name	Fit Sequence	Constraints	Cut off
$K^-p \rightarrow (\Lambda^0)K^0K^-\pi^+\pi^+\pi^-$	401083	A	3, 1, 4	5% on Fit 2
$(\Lambda^0)K^+\bar{K}^0\pi^+\pi^-\pi^-$	401093	A	3, 1, 4	5% on Fit 2
$\Lambda^0 p\bar{p}\pi^+\pi^-$	401213	A	3, 4, 7	1% on Fit 2
$\Lambda^0 K^+K^-\pi^+\pi^-$	401223	A	3, 4, 7	1% on Fit 2
$\Lambda^0 K^+K^-\pi^+\pi^-\pi^0$	401233	A	3, 1, 4	5% on Fit 2
$\Lambda^0(K^0)K^-\pi^+\pi^+\pi^-$	401243	A	3, 1, 4	5% on Fit 2
$\Lambda^0 K^+(\bar{K}^0)\pi^+\pi^-\pi^-$	401253	A	3, 1, 4	5% on Fit 2
$\Sigma^0 K^+K^-\pi^+\pi^-$	401313	B	3, 1, 1, 5	1% on Fit 3
$\Xi^0 K^+\pi^+\pi^-\pi^-$	401413	B	1, 1, 1, 3	5% on Fit 3
$(\Xi^0)K^0\pi^+\pi^+\pi^-\pi^-$	401423	A	3, 1, 4	5% on Fit 2
$(\Sigma^0)K^0K^-\pi^+\pi^+\pi^-$	401014	A	3, 1, 4	5% on Fit 2
$(\Sigma^0)K^+\bar{K}^0\pi^+\pi^-\pi^-$	401024	A	3, 1, 4	5% on Fit 2
$pK^+K^0(\bar{K}^0)\pi^-\pi^-$	401034	A	3, 1, 4	5% on Fit 2
$p(K^0)\bar{K}^0K^-\pi^+\pi^-$	401044	A	3, 1, 4	5% on Fit 2

FIT SEQUENCE A.

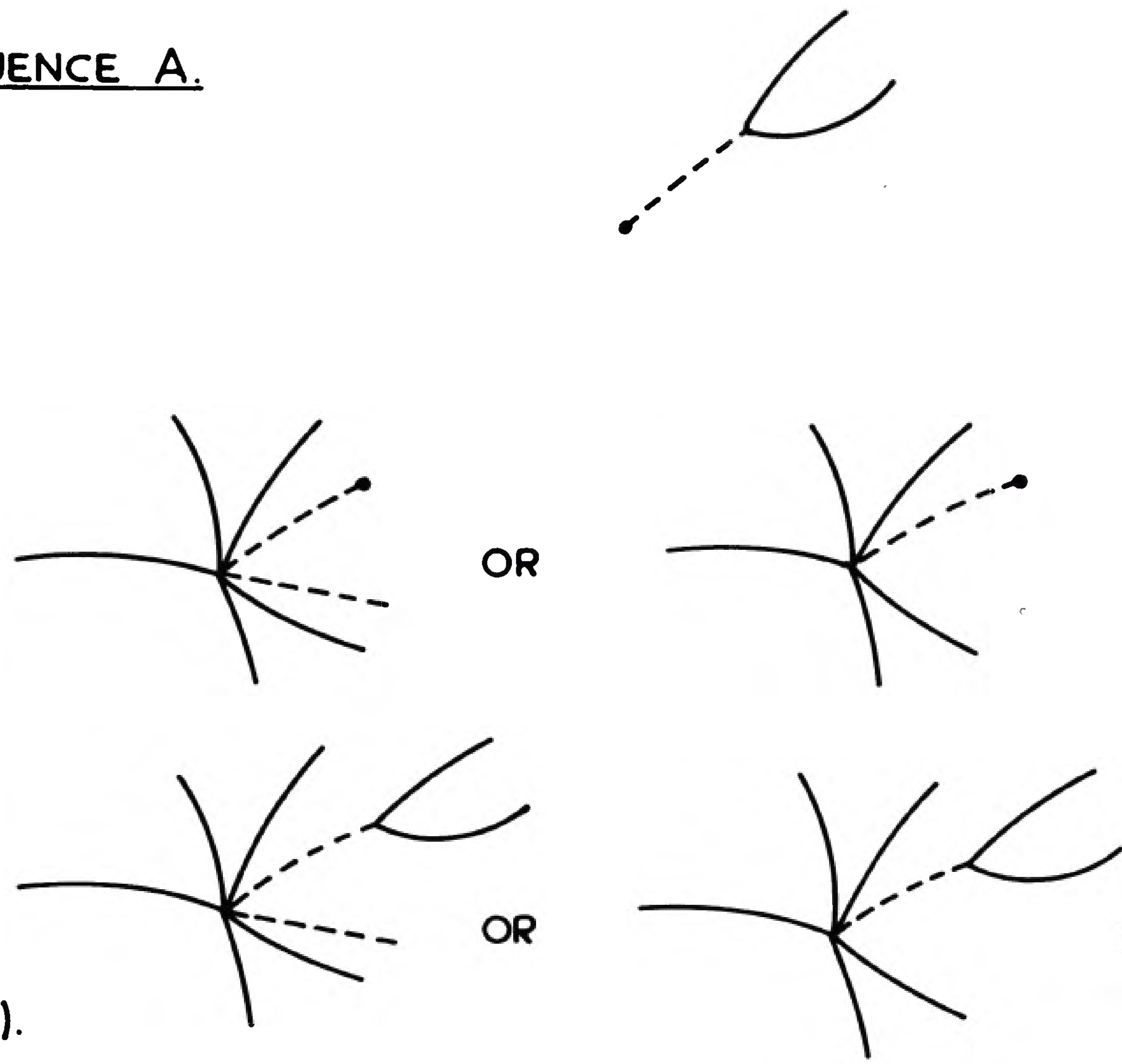

FIT 1.

FIT 2.

FIT 3.

Fig. 2·4 (a).

FIT SEQUENCE B.

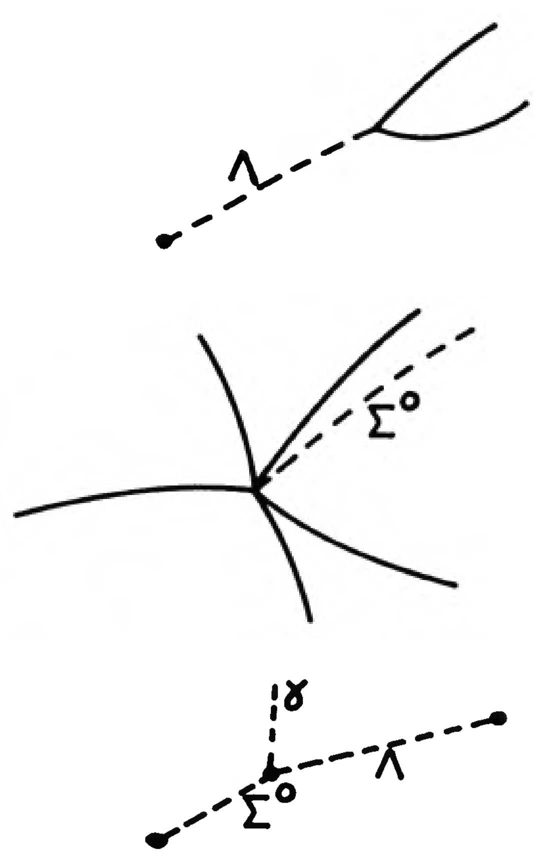

FIT 1.

FIT 2.

FIT 3.

Overall 3-vertex fit. FIT 4.

Fig. 2·4 (b).

the number of constraints in each fit of the fit sequence and the minimum probability that was accepted as a fit[4]. The fit sequence A involved a single vertex fit of the V^0 back to the production vertex, a single vertex fit at production using the momentum of the V^0 particle determined from fit 1 and finally an overall 2 vertex fit. Fit sequence B for Σ^0 hypotheses was as follows: a fit of the V^0 back to production as a Λ^0: a fit at production without the V^0 but with a free missing neutral track with Σ^0 mass: a fit at a neutral vertex i.e. conserving energy and momentum for the vertex $\Sigma^0 \to \Lambda^0 + \gamma$ where the Λ and Σ variables are those of fit 1 and 2. The last fit was an overall 3 vertex fit. The two fit sequences are shown in Fig.2.4. In the last column of Table 2.1 is the fit of the fit sequence on which the probability rejection criterion was applied. For fit sequence A the first fit in almost every case indicated an unambiguous Λ or K^0. Thus a low probability cut off was sufficient on the V^0 fit and all fits better than 1% were accepted. The cut off for fit 2 was taken as 5% for 1C fits and 1% for 4C fits. For Σ^0s the crucial fit is fit 3 - a 5% cut off was applied.

When each event had been tested against all the hypotheses it was re-examined on the scan table by Andres Cruz or me. The density of ionisation along a track being electromagnetic in origin depends only on the charge of the particle and the velocity of the charge through the hydrogen. The velocity of a relativistic particle is P/E whereas its curvature is related to P only. Therefore different hypotheses by assigning different masses to tracks predict different velocities and therefore different ionisations. A high momentum track has a velocity within a few percent of C independently of its mass and different mass assignments cannot be distinguished. Below 800 - 1300 MeV/c depending on the masses concerned, the ionisation predictions are sufficiently different to distinguish one hypothesis from another. Any fit requiring an ionisation incompatible with that observed was rejected.

The remaining ambiguities were further reduced by always accepting a fit to a common hypothesis (only one strange particle) rather than a fit to a rare one when these were ambiguous; also by accepting fits to $[\Lambda + \text{charged pions}]$ over fits to $[\Lambda + \text{charged pions} + x\ \text{zero}]$ when these were ambiguous. This procedure is justified by the discussion in

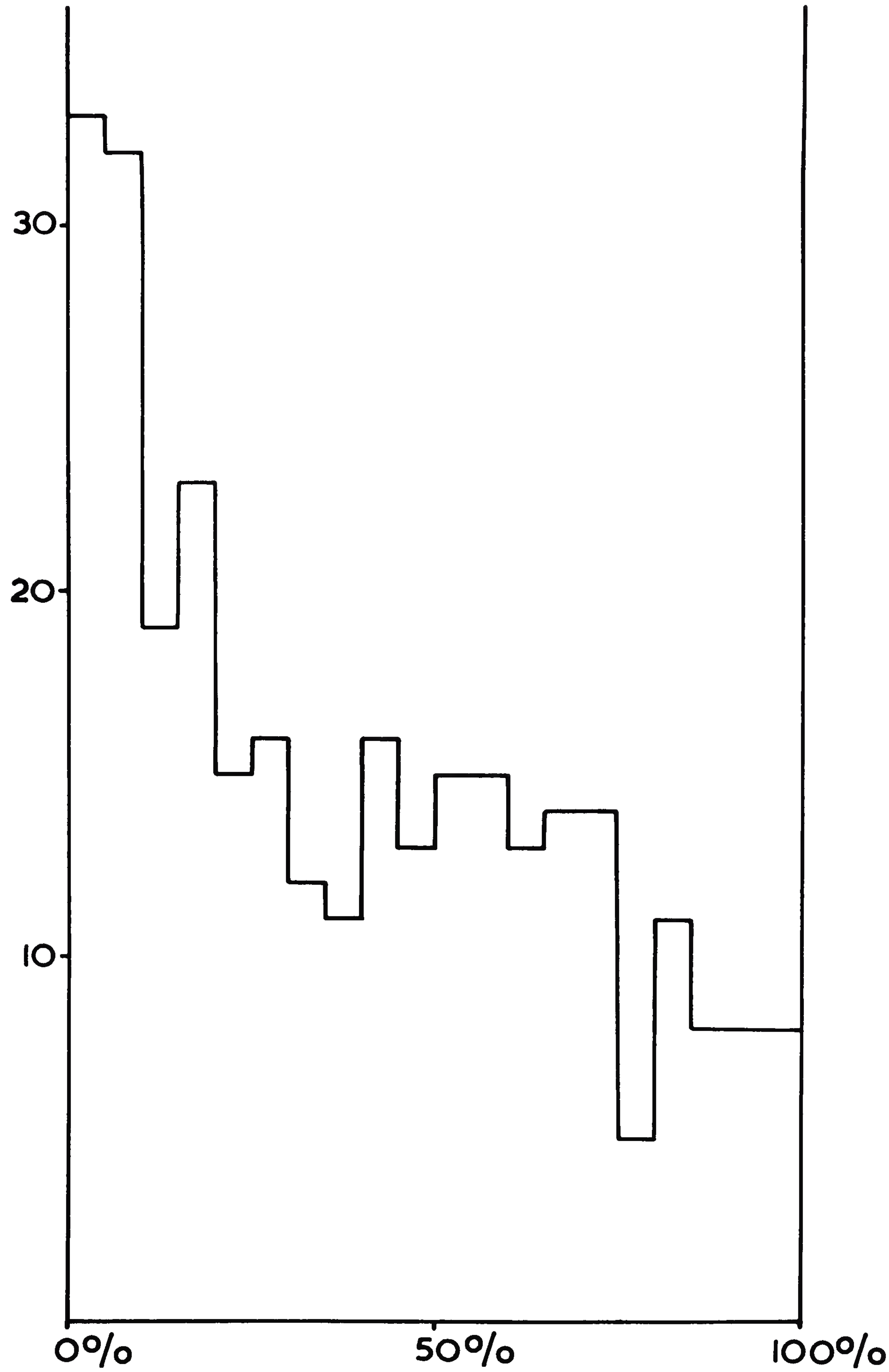

P_{χ^2} for events fitting $\Lambda\pi^+\pi^-\pi^+\pi^-$

Fig. 2.4 (c).

Appendix E and the experimental results of chapter 4. The remaining ambiguities were not resolved at this stage.

One of the shortcomings of bubble chamber film analysis is its theory of errors. The setting accuracy of the measuring machine, the theory of Coulomb multiple scattering and the goodness of the least squares fit in geometry may be used to derive the random element of the errors as the experiment proceeds. However, systematic effects remain unknown until a large body of data has been analysed. The ultimate test of whether the errors are correct lies in the probability distributions for fits to well constrained hypotheses. These should be flat. If the errors have been over-estimated they will peak at high probability or if under-estimated at low probability. Neither of these cases matters too much provided that in the one case the number of spurious fits due to the large errors is low and in the other the number of lost fits due to the small errors is low. Fig.2.4(c) shows the probability of the overall fit for events fitting the $\Lambda 4\pi$ final state from all laboratories. It is not entirely satisfactory; this is attributed to the fact that some laboratories did not compute their events with the best set of chamber constants[5] nor with the latest version of the geometry programme. They claimed that although the new constants improved the probability of a fit they did not increase the number of fits significantly.

2.4 Identification of the 410 events by kinematic fitting and ionisation

The 410s were fitted to the hypotheses of Table 2.2. These events were difficult to fit. As shown in chapter 3 Σs and Ξs turn through an exceedingly small angle before decaying so that any attempt to determine their momentum from curvature is more trouble than it is worth. This means that unless the production vertex is fitted first there is a zero constraint fit at decay. Consequently as shown in Fig.2.5 the fit sequence C follows the order: production, decay and overall. For the events with missing neutral at production (sequence D) the order was: decay, production and overall. In retrospect this was probably unwise; the production fit is of no significance and should have been omitted making the sequence: decay, overall. It was possible to recognise events with production vertices without missing neutrals by studying the missing momentum transverse to the straight track. Events with transverse momenta less than 100 MeV/c

TABLE 2.2

Hypothesis	Name	Fit Sequence	Constraints
$K^-p \rightarrow \Sigma^+_p\pi^+\pi^-\pi^-$	410911	C	3, 1, 4
$\Sigma^+_\pi\pi^+\pi^-\pi^-$	410921	C	3, 1, 4
$\Sigma^+_p\pi^+\pi^-\pi^-\pi^0$	410931	D	0, 1, 1
$\Sigma^+_\pi\pi^+\pi^-\pi^-\pi^0$	410941	D	0, 1, 1
$\Sigma^-_\pi\pi^+\pi^+\pi^-$	410611	C	3, 1, 4
$\Sigma^-_\pi\pi^+\pi^+\pi^-\pi^0$	410621	D	0, 1, 1
$K^-_\pi p\pi^+\pi^-$	410411	C	3, 1, 4
$K^-_\mu p\pi^+\pi^-$	410421	C	3, 1, 4
$K^-_\pi p\pi^+\pi^-\pi^0$	410431	D	0, 1, 1
$K^-_\mu p\pi^+\pi^-\pi^0$	410441	D	0, 1, 1
$K^-_\pi n\pi^+\pi^+\pi^-$	410451	D	0, 1, 1
$K^-_\mu n\pi^+\pi^+\pi^-$	410461	D	0, 1, 1
$\Xi^-_\pi K^+\pi^+\pi^-$	410713	C	3, 1, 4
$\Xi^-_\pi K^+\pi^+\pi^-\pi^0$	410723	D	0, 1, 1
$\Xi^-_\pi K^0\pi^+\pi^+\pi^-$	410733	D	0, 1, 1

FIT SEQUENCE C.

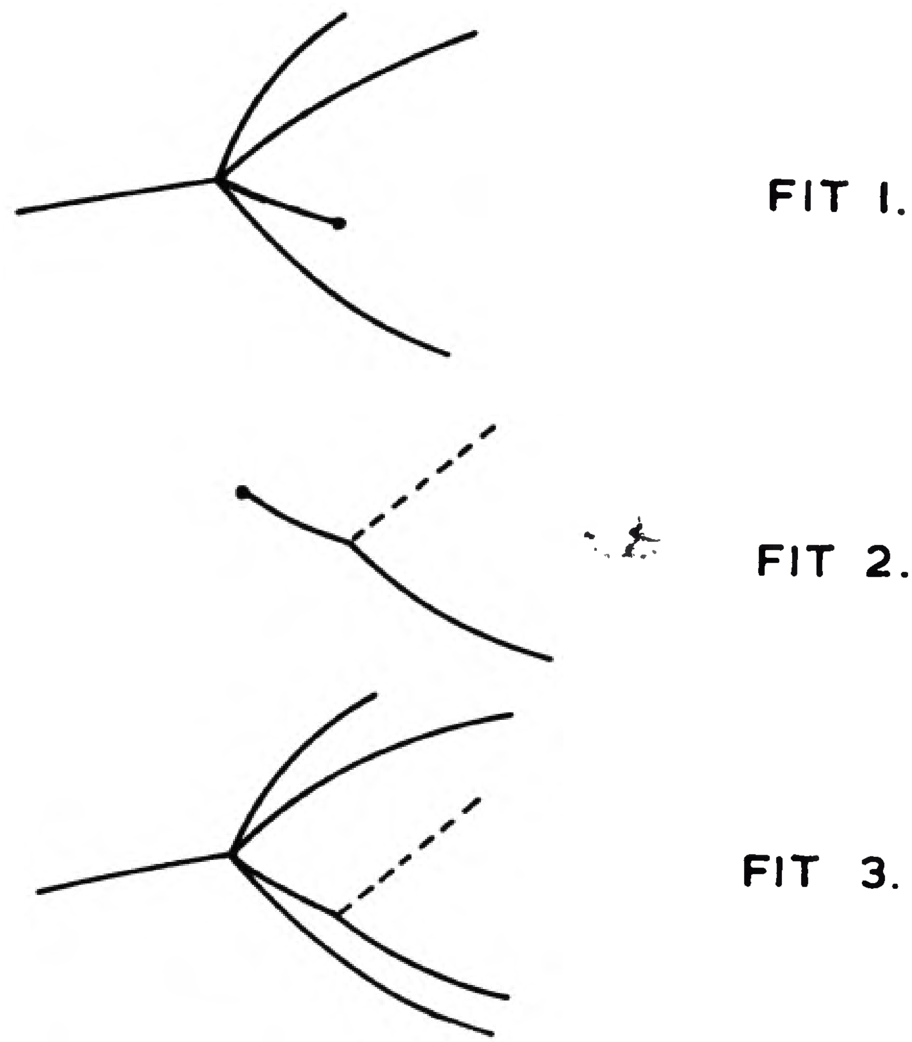

Fig. 2.5 (a).

FIT SEQUENCE D.

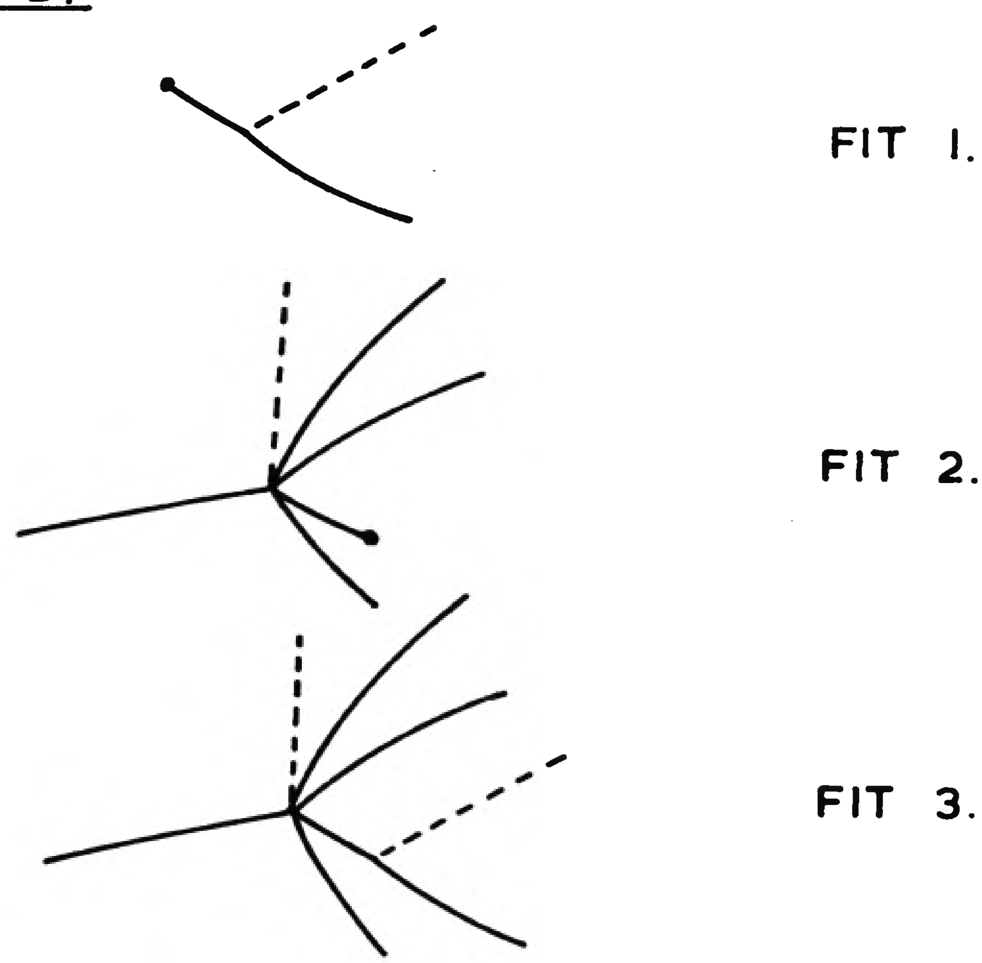

Fig. 2.5 (b).

which failed to fit a hypothesis were remeasured. Many of these then gave excellent fits to hypotheses without a neutral at production. The transverse momentum at the decay vertex was also a useful geometry quantity - low values suggesting a π-μ decay or scatter. In fact hypotheses with π_μ decays were run on a large sample of Oxford data and the ambiguity with Σ and Ξ fits shown to be small. Using these features as well as track ionisation, satisfactory fits were selected on the scanning table and dubious measurements repeated. A 5% cut off was used for all hypotheses. Events fitting Σ hypotheses were taken as such, other fits being rejected. The lifetime histogram for Σ events selected in this way showed no long life enhancement due to π/K decay contamination.

2.5 Estimation of cross sections

To calculate cross sections we need to know the number of protons/cc in the hydrogen, the total length of K^- track in the sample of film and the number of events in each channel corrected for losses.

The number of protons/cc of hydrogen = Nρ where N is

Avogadro's number and ρ is the density of liquid hydrogen.

$$N\rho = .0614 \times 6.02 \times 10^{23} = 3.70 \times 10^{22} \text{ protons/cc.}$$

The total K^- track length was calculated in two ways. First a count of beam tracks on every tenth frame of the film coupled with the Cerenkov data for that frame gave an estimate of the mean number of kaons per picture(6). A correction was made for the depletion of tracks between the Cerenkov counter and the centre of the fiducial volume. Multiplying by the number of frames and the length of the fiducial volume we get a total length of K^- track:

$$L_1 = 8.86\ (\pm .38) \times 80 \text{ cms} \times 50720 \text{ frames}$$
$$= (3.59 \pm 0.16) \times 10^7 \text{ cms.}$$

Secondly a count of τ decays of the K^- was made. In this decay a very characteristic 3 prong topology is observed in the chamber:

$$K^- \rightarrow \pi^+\pi^-\pi^-$$

There is a small contamination from the decays:

$$K^- \rightarrow \pi^-\pi^0$$
$$K^- \rightarrow \pi^0 e^- \nu_e$$
$$K^- \rightarrow \pi^-\pi^0\pi^0$$

in which one of the π^0 decays with a Dalitz pair:

$$\pi^0 \rightarrow e^+e^-\gamma$$

As discussed at the beginning of this chapter τ's were noted on every scan. However the Q value of the decay is very low and at a momentum of 6 GeV/c the opening angle of the decay is so small that it is very easy to miss. The first and third runs were scanned three times for taus and the second run five times. Using the analysis described in Appendix C the number of taus which were not seen was estimated.

Total taus seen 372

Total taus estimated, N_τ, 488 ± 40

Branching ratio to τ, f_τ .0595

Meanlife K^-, t, 12.29 ns

Beam momentum 6.02 ± .07 GeV/c

K^- path length L_2 = pct $N_\tau / m_k f_\tau$

$= (3.69 \pm .44) 10^7$ cms

This is in very satisfactory agreement with the previous estimate. We take the track count figure L_1 since it is more accurate.

Therefore a channel with n events represents a cross section of $n/L_1 N \rho$ cm^2

$= n \times 0.75$ (± .04) μbarns for the Oxford data.

In each channel the number of events was corrected by the following factors:

a) $\times\frac{100}{99}$ for the 1% probability cut on V^0 fits

b) $\times\frac{100}{95}$ for the 5% cut on 1C production fits of V events and for all 410 events (and $\frac{100}{99}$ for the 1% cut on 4C V events).

c) x scanning efficiency correction

d) $\times\frac{100}{66}$ for each Λ seen to correct for the $\Lambda \rightarrow n\,\pi^0$ decay mode

e) x mean wt as calculated in chapter 4 for short, long and small angle decays

f) x proportion of events not analyseable (20%) due to scatters, crossing tracks etc.

Σ^+ cross sections are calculated from the π^+ decay mode and multiplied by 2 to correct for the proton decay mode which is so difficult to analyse (see chapter 4).

	Mean wt
$\Sigma^+ 4\pi$	1.47
$\Sigma^+ 3\pi$	1.44
$\Sigma^- 4\pi$	1.30
$\Sigma^- 3\pi$	1.23

In Table 2.3 we show the total number of events fitted to the strange baryon hypotheses. Cross sections for $\overline{K}^0$ hypotheses will be discussed by Andres Cruz.

TABLE 2.3

Total cross sections from Oxford 401 and 410 data

Correction is made for unseen weak decay modes

Final State	Number	Correction Factor	Cross Section
$\Lambda 4\pi$	60	2.35	$107(\pm 20)\mu b$
$\Lambda 5\pi$	184	2.45	$345(\pm 30)\mu b$
$\Sigma^{0} 4\pi$	19	2.35	$34(\pm 8)\mu b$
$\Lambda p\bar{p} 2\pi$	0		$0(\pm 3)\mu b$
$\Lambda K^{+}K^{-} 2\pi$	3	2.35	$5(\pm 3)\mu b$
$\Lambda K^{+}K^{-} 3\pi$	14	2.45	$25(\pm 10)\mu b$
$\Lambda (K^{0}) K^{-} 3\pi$	17	3.72	$48(\pm 14)\mu b$
$\Lambda K^{+} (\bar{K}^{0}) 3\pi$	11	3.72	$31(\pm 12)\mu b$
$\Sigma^{0} K^{+}K^{-} 2\pi$	1	2.35	$2(\pm 3)\mu b$
$\Xi^{0} K^{+} 3\pi$	1	2.45	$2(\pm 3)\mu b$
$\Sigma^{+} 3\pi$	39	3.64	$107(\pm 20)\mu b$
$\Sigma^{+} 4\pi$	104	3.72	$290(\pm 40)\mu b$
$\Sigma^{-} 3\pi$	52	1.56	$61(\pm 8)\mu b$
$\Sigma^{-} 4\pi$	143	1.64	$176(\pm 15)\mu b$
$\Xi^{-} K^{+} 2\pi$	2		
$\Xi^{-} K^{+} 3\pi$	6		
$\Xi^{-} (K^{0}) 3\pi$	4		
Total 401	1375		(visible) $892\mu b$
Total 410	1092		(without correction) $819\mu b$

REFERENCES TO CHAPTER 2

(1) W. Allison: BABEL, A computer based scan system for high statistics bubble chamber experiments (unpublished) April 1966.

(2) J. Sparrow and J. Burren: RHEL Geometry Programme. See also Appendix E.

(3) A. Wilson: RHEL Kinematics Programme. E.C. Bedman: The 'JOKING' system. See also Appendix E.

(4) The meaning of a 'fit' and its probability is discussed in Appendix E.

(5) J. Allison: D.Phil thesis (Oxford 1966).

(6) R.L. Sekulin: D.Phil thesis (Oxford 1965).

C H A P T E R 3

UNITARY SYMMETRY

3.1 The mathematical theory of Unitary Symmetry

In February 1964 a group at Brookhaven discovered the omega minus[1]. Despite the fact that this was the first "long lived" strongly interacting elementary particle to be found for nearly ten years, its mass had been correctly predicted to an accuracy of two or three parts per thousand. I have described the theory which lead to this prediction in greater detail elsewhere[2]. The theory takes two forms: the mathematical theory and the quark model. The quark model is described in section 3.3.

The mathematical theory came first and has its origins in the hypothesis of charge independent nuclear forces. The algebra which describes the charge structure of nuclear energy levels and their transitions is the same as the more familiar angular momentum algebra arising from the hypothesis of magnetic substate independent interactions - i.e. angular momentum conservation. This algebra is known to mathematicians as SU(2), the group of unimodular (determinant = +1) unitary transformations of a two dimensional complex space. A multiplet of charge states related in this way is identified with a set of eigenstates for a representation of SU(2). Such a multiplet is characterised by a total "isotopic spin" and each state within the multiplet by its "third component of isotopic spin" - the terms arising from the analogy with angular momentum multiplets. The observation of such charge multiplets with almost identical masses in the spectrum of elementary particles lent considerable support to the hypothesis.

In the late fifties and early sixties the number of known multiplets increased rapidly. Two further principles were found:

a) The phenomenon of associated production leading to the conservation of a new quantum number called hypercharge (Y).

b) The charge formula: $Q = I_3 + Y/2$.

In an attempt to extend the I-spin group, particle states were plotted on an I_3 against Y plot. Since I-spin and its extensions are required to be Lorentz invariant, the generators of the group must commute with space time operators. In practice this means that all the states of a given I-spin multiplet or of a supermultiplet must have the same space-time quantum numbers (J^P). When the I_3 versus Y plots are examined for each value of J^P, the following features are seen amongst I-spin multiplets of well identified states:

1) In the case of $\frac{1}{2}^+$ a symmetrical pattern of 8 states is obtained,
2) In the case of 0^-, 1^-, 2^+ a similar pattern is obtained except that one extra state with $I = Y = 0$ is found,
3) In the case of $\frac{3}{2}^+$ a symmetrical triangle of 9 states with one corner missing is seen.

We are now in a position to ask a definite question: Are there any groups known to pure mathematics which:

a) have SU(2) as a subgroup (isospin),
b) contain two commuting independent linear operators whose eigenvalues we can identify with I_3 and Y (or some linear combination of them), [The linearity ensures that the eigenvalues will be additive in composite systems],
c) have an irreducible representation connecting eight eigenvectors which we can identify with the sets of eight states observed?

There are three groups satisfying conditions a) and b), but only one, SU(3), has the property c).

SU(3) is the group of unitary transformations of a three dimensional complex space. (The S means that we do not bother with the trivial transformations which multiply the whole space by $e^{i\phi}$.) The application of this group to physics depends on a hypothesis which we state as follows: the Hamiltonian of particle physics transforms as a linear combination of generators of the group SU(3). Very little progress was made with the stronger hypothesis of complete invariance under SU(3). The weaker hypothesis has lead to the theory of U-spin invariance of electromagnetic interactions and the Cabbibo theory of weak interactions as well as the Gell-Mann Okubo mass formula for strong interactions. Each particle state is represented by a tensor in this space. Since the space is 3-dimensional, the indices run from one to three. The $3/2^+$ states were identified with the ten symmetric tensors T^{ijk}. The mass spectrum fitted extremely well as shown in Fig 3.1. The completion of the multiplet required a new particle whose mass was given. This was the Ω^- and its discovery was the main purpose of this experiment. Several examples were indeed found and are described in

The decuplet of baryon states.

Mass operator $\sim M_0(1+\Sigma\delta^3_3)$

Mass (Mev)	The particles.			
1677	Ω^-			
1530	Ξ^{-*}	Ξ^{0*}		
1383	Y^{*-}	Y^{*0}	Y^{*+}	
1236	N^{*-}	N^{*0}	N^{*+}	N^{*++}

	The third rank symmetric tensors.			
$M_0(1+3\Sigma)$	T^{333}			
$M_0(1+2\Sigma)$	T^{331}	T^{332}		
$M_0(1+\Sigma)$	T^{311}	T^{123}	T^{322}	
M_0	T^{111}	T^{112}	T^{122}	T^{222}

$M_0=1236$ Mev $\qquad \Sigma M_0=147$ Mev

Fig 3.1.

detail elsewhere[3].

As the mathematical theory stands it appears as little better than a glorified rule of thumb - certainly the mumbo jumbo language of pure mathematics is very difficult to translate into a genuine physical picture. What is worse, the "symmetry breaking" terms linear in the group generators are so large that strong quadratic, cubic and other terms are expected. None is observed. This is not the first time that good results have been given by the first term of a divergent or weakly convergent perturbation expansion (e.g. unrenormalisable weak interactions).

In a sense the Ω^- prediction was obvious - could the pattern of the nine $^3/_2{}^+$ states be made symmetrical in any other way? One hardly needs the abstract concepts of group theory to complete a triangle with equal mass spacing!

In another sense the prediction is very profound. The other $J^P = {}^3/_2{}^+$ states are "resonances" decaying in 10^{-23} seconds by strong interaction - such a short time that their mass becomes poorly defined because of the Uncertainty Principle. Their existence can only be inferred from variations in angular distributions and enhancements in cross sections and invariant mass distributions. They are only one order of magnitude in lifetime from states which would be indistinguishable from background. These twilight states then predict the existence of a baryon state of strangeness -3 and mass 1675 MeV. The conservation of strangeness, baryon number and energy forbid the decay of such a state by strong interaction. Instead it must decay by weak interaction with a lifetime of the order of 10^{-10} secs. This corresponds to a few centimetres of track in the bubble chamber so that individual particles may be "seen". Thus the prediction described above as obvious spans thirteen orders of magnitude in time and uses symmetry to relate states with lifetimes in the same ratio as one second to a million years. We conclude from the discovery of the omega that resonant states are just as much real particles as those whose existence we infer directly from tracks in a bubble chamber.

3.2 Search for a neutral baryon of strangeness -3

The omega minus discovery has confirmed the existence of a strangeness -3 negative baryon of mass 1675 MeV. The other properties predicted for this particle are:

$$I = 0 \qquad J = \frac{3}{2} \qquad P = +$$

None of these properties is yet confirmed. We now describe an investigation of the I-spin of the omega.

If the I-spin of the omega was one or greater then the charge formula predicts the existence of "Ω^{--}" and "Ω°" charge states. The discovery of one of these states with the Ω mass would be highly embarrassing to the present state of physics. If the states are not found of course no conclusion may be drawn. States with these quantum numbers but different mass from the Ω are allowed on the mathematical SU(3) theory, but are forbidden on the quark model (except at very high mass). This is discussed in section 3.3.

No attempt is made here to find an Ω^{--} state. An Ω^{--} with mass less than 1810 MeV would decay weakly. The double negative track would appear as a "positive excess charge non-conservation" event in the chamber. The double negative track would "scatter" (with apparent excess negative charge) and one of the "scatter" tracks would be seen to decay (possibly with an associated V°). While such events would be very distinctive a complete rescan of the film would have been necessary to search for them.

The Oxford sample of film was analysed for evidence of the existence of a strangeness -3 neutral baryon with mass between 1450 and 1810 MeV. We refer to this state as "Ω^0" although its discovery would not necessarily imply that it was a member of the same I spin multiplet as the Ω^-.

Possible two body weak decay modes of such a state are:

1) $\Omega^0 \rightarrow \Sigma^0\gamma^0$ 1690 MeV threshold

2) $\Omega^0 \rightarrow \Sigma^+\pi^-$ 1690 MeV threshold

3) $\Omega^0 \rightarrow \Xi^0\pi^0$ 1450 MeV threshold

4) $\Omega^0 \rightarrow \Xi^-\pi^+$ 1450 MeV threshold

5) $\Omega^0 \rightarrow \Lambda^0\pi^0$ 1613 MeV threshold

Mode 3 has too many neutral decay vertices to be analyzable in a hydrogen bubble chamber experiment. Modes 1 and 5 appear in the two V zero topologies when the Λ^0 and Σ^0 decays are seen - however this only happens in 22% of the cases. Furthermore the threshold is higher than mode 4 and the topology on the scan table is not so distinctive. Modes 2 and 4 are much more peculiar and would give rise to the topologies shown in Fig 3.2. Furthermore the Λ decay in mode 4 should be seen $\frac{2}{3}$rds of the time. The only other decay chains that can give decaying V zeros are:

$$\Lambda \rightarrow p\pi^-; \qquad \pi^- \rightarrow \mu^- + \nu_\mu$$

$$K^0 \rightarrow \pi^+\pi^-; \qquad \pi^- \rightarrow \mu^- + \nu_\mu$$

$$K^0 \rightarrow \pi^+\pi^-; \qquad \pi^+ \rightarrow \mu^+ + \bar{\nu}_\mu$$

Weak decay modes of a $Q = 0$ $S = -3$ baryon "Ω^0".

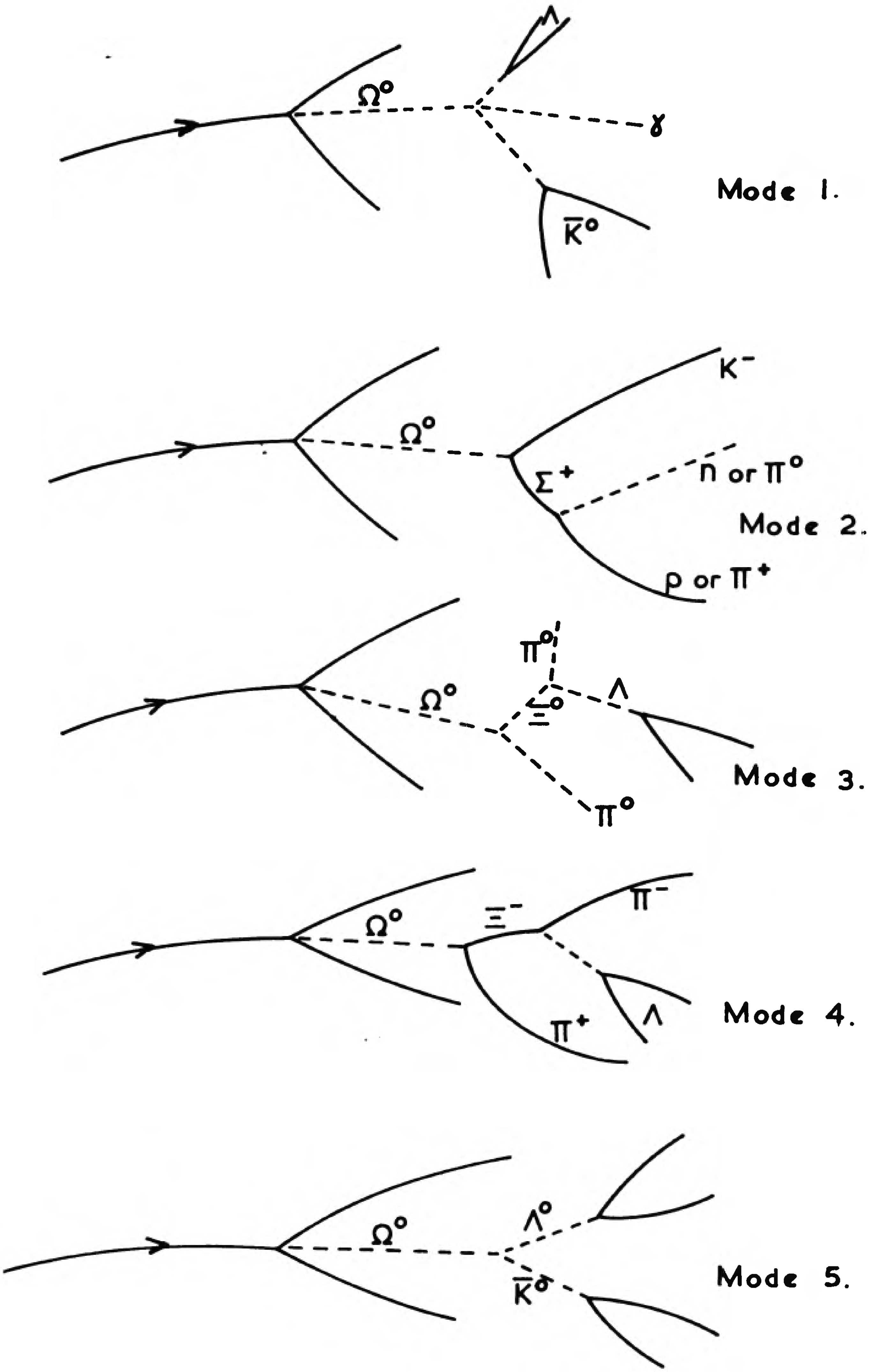

Fig 3·2.

To search for these decay modes all V^0 events were rescanned for evidence of decaying prongs. From 5800 V^0 events 25 events with positive decays and 82 events with negative decays were found. This sample of film represented 1.3($\pm$.2) events/μbarn. The number of events with a negative decay on a V zero and a second V^0 associated with the decay point was zero. A lifetime argument was used to reduce the number of candidates for mode 2 and mode 4 with unseen Λ still further.

Consider a particle mass m, momentum p, dip λ, proper life t moving in a magnetic field H.

$$\text{radius of helical trajectory} = \frac{10\, p \cos\lambda}{3H(\text{kilogauss})} \text{ cms}$$

$$\text{total path length} = \frac{t\, p\, c}{m}$$

$$\text{Therefore angle turned through} = \ell \cos\lambda / r$$

$$= \frac{t\, c}{m} \, \frac{3H}{10}$$

This is independent of p and λ. Inserting values for $\pi^{\pm}$, Σ^{+} and Ξ^{-}, we find that only 0.44% of πs decay within a 5 degree cut while only 0.22% of Ξs and 5.4×10^{-4}% of Σ^{+}s decay outside it. All events in which the decay track turned through more than 5° on the scan table were rejected. The angle turned through by the connecting track was calculated on the scan table from length and sagitta measurements. All tracks with a sagitta less than one millimetre were accepted as being less than 5 degrees regardless of length. This left 8 positive decay events and 25 negative decay events. From the total number of V^os we expect there to be about 8 positive and 25 negative π-μ decay events in which the π turns through less than 5 degrees. However many of these would have a decay angle which was too small to be seen. In addition to $\pi\mu$ decays the observed sample contained "decays" due to coulomb scattering of slow tracks and small angle scatters in which the recoil proton was too short to be observed.

Every event in the selected sample was measured twice and geometrical reconstruction carried out. All events for which the ionisation of a prong from production or of the non decaying prong of the V^o indicated the presence of a proton were eliminated. The remaining events were fitted to $\pi\mu$ decay hypotheses using the following fit sequence:

1. Zero constraint fit to the charged decay vertex;
2. Three constraint fit to the V^o vertex using the momentum of the connecting track derived from fit 1 and using the position of the production vertex to

to define the angles of the neutral track;

3. Three constraint overall fit to the two decay vertices together.

It was found in the 410 events (see chapter 2) that charged decays that fit $\pi^{\pm} \rightarrow \mu^{\pm} + \nu_{\mu}$ do not fit the decays

$$\Xi \rightarrow \pi^{-} + \Lambda^{0} \quad \text{or } \Sigma^{+} \rightarrow (\pi^{+} + n \text{ or } p + \pi^{0})$$

The masses of the Ξ and Σ are so different from that of the π that the ionisation predictions in the two cases tend to be very different any way. All events which fitted $\pi\mu$ decays with a probability greater than 1% and were consistent with ionisation were rejected.

Events with very small angle charged "decays" on heavily ionising tracks consistent with coulomb scattering and events which were subsequently found to have evidence of short recoil protons at "decay" were rejected. Only 6 candidates passed these criteria. None of these fitted modes 2 or 4 for Ω° mass in the range 1450 - 1810 MeV. The difficulty encountered in identifying these events is attributed to the small Q-value of the $\pi\mu$ decay and the resulting difficulty of finding physical starting values for poor measurements. Consequently we rely on the total lack of candidates for mode 4 with Λ seen. One such event would correspond to a cross section of one μbarn for the $\Xi^- \pi^+$ decay mode - we give this as an upper limit. This is to be compared with the cross section for Ω^- production. Two Ω^- were identified on this sample of film - it seems likely that the cross section is greater than 2 μbarns when correction has been made for small angle decays etc. A search for Ω^0 and Ω^{--} on a much larger scale is necessary before a significant answer can be given to the problem of the omega isospin.

3.3 The Quark model of Unitary Symmetry (4)

The quark model of Unitary Symmetry was originally proposed by Gell Mann and Zweig in an attempt to derive some physical picture from the unexpected success of the mathematical theory of Unitary Symmetry. In it the symmetry is interpreted as a symmetry under unitary transformation of three (complex) wave functions. Furthermore a tensor component T_{ijk} is interpreted as that product of these three wave functions which has the same transformation properties:

e.g. $$T_{ijk} \sim x_i \, x_j \, x_k$$

and $$T^{\ell}_{m} \sim x^{\ell} \, x_m$$

Now these products correspond physically to composites of the particles described by the wavefunctions according to the normal quantum-mechanical interpretation. So all we need are three particles x_1, x_2 and x_3 and a hypothesis suitably reworded in terms of their interactions; the rest of Unitary Symmetry then follows.

These three particles are named "quarks". In order that the known particles should have the correct quantum numbers, the following properties of quarks are necessary:

a) In addition to 3 quarks with baryon number $\frac{1}{3}$, there should be three antiquarks with baryon number $-\frac{1}{3}$.

b) They should have spin parity $\frac{1}{2}^{+}$ and fractional electric charges.

All known baryonic states are compatible with being composites of three quarks; all known meson states are compatible with being composites of one quark and one anti-quark. These features are not deducible from the mathematical theory but are very attractive on the quark model. Higher spin mesons and baryons are constructed by introducing orbital motion between the quarks and not by introducing quark-antiquark pairs.[5] This means that all mesons must be members of octets or singlets and all baryons members of decuplets, octets or singlets. Despite the evergrowing number of known particle states no exception is yet known to this rule. We consider detailed tests of it below.

There are several difficulties involved in the quark model:

1) Despite the fact that at least one quark must be absolutely stable (this follows from the conservation of charge), none has ever been observed, although some very sensitive experiments both on quark production and natural abundance have been performed.[6]

2) If they have not been observed because of their very high mass, then their binding energ~~ies~~y in particles is very high. As a result, any first order formula like the Gell Mann Okubo mass formula would be expected to break down very badly indeed - this is not the case.

3) In the case of the baryon states the lowest level (the $\frac{1}{2}^+$ baryon octet) does not have a symmetric space wave function if the quarks are assumed to obey fermi statistics.

In spite of these three problems the successes of the quark model are very numerous. In particular it forbids:

a) Hyperon states with strangeness minus three and non zero isospin.

b) Doubly charged meson states. In particular $I = \frac{3}{2}$ K^* mesons either produced on the mass shell or exchanged in a peripheral process.

c) $I = 2$ Y^* states.

We have already demonstrated the absence of evidence for states of type a) with mass below 1810 MeV. In chapter 5 we test the selection rules b) and c) against our data.

REFERENCES TO CHAPTER 3

(1) Barnes et al: Phys. Rev. Letters 12, 204 (1964).

(2) W.E.M. Allison and A.[illegible]. Brody: "Theory of Unitary Symmetry" (unpublished) 1964.

W.E.M. Allison: "Representations of Unitary Groups and their applications" (unpublished) 1964.

(3) J. Allison: D.Phil. thesis (Oxford) 1966.

D.C. Colley et al: Physics Letters 19, 152 (1965).

(4) M. Gell Mann: Physics Letters 8, 216 (1964).

(5) R.H. Dalitz: Proceedings of the Oxford Conference (1965).

P.G.O. Freund and B.W. Lee: Phys. Rev. Letters 13, 592 (1964).

(6) See for instance

O. Sinanoglu et al: Phys. Rev. Letters 14, 785 (1966).

[illegible].R. Bennett: Phys. Rev. Letters 14, 1196 (1966).

CHAPTER 4

LOSSES BIASSES AND AMBIGUITIES

4.1 Introduction

In the first part we consider the systematic losses in the sample of charged Σ events. In the second part we treat the problem of ambiguous fits to the Λ and Σ^0 channels.

The derivation of weights to correct for the various losses is necessarily approximate but the errors in these corrections are not significant compared with the statistical errors inherent in the data.

4.2 Charged sigma events

Charged sigma events are lost either because they are missed altogether at the scanning table, or because, having been seen, it is impossible to locate the vertices with sufficient accuracy for the correct reconstruction of the event to be made. These lost events are of two types: those with a small decay angle as seen on the film and those which decay within a short distance of the production vertex.

To analyse and correct for the loss of events with small decay angle we use two physical facts: firstly that the decay distribution in the sigma rest frame is isotropic if the sigma is unpolarised and secondly that the momentum spectrum of Σ^+ is the same whether it decays into π^+n or $\pi^0 p$. In fact the decay distribution is still isotropic for sigmas decaying to a charged π even if they are polarised since the asymmetry parameters α_{Σ^-} and $\alpha_{\Sigma^+_{\pi^+}}$ are essentially zero. To correct for losses of $\Sigma^+ \rightarrow p\pi^0$ we use the identity of the momentum spectra which makes no assumptions about the decay distribution.

Since the decay point has to be measurable on at least two views, the angle of the decay projected onto the plane of the front glass is chosen as a suitable parameter characteristic of the loss. The velocity of the nucleon in the sigma centre of mass is 0.2c whereas the velocity of the pion is 0.8c. This means that most of the decays of Σ^+ to $(p\pi^0)$ are at an angle which is too small to be observed whereas the majority of decays to $(n\pi^+)$ are seen.

The loss factor depends only on the decay mode and the component of the sigma momentum in the plane of the front glass since a Lorentz transformation perpendicular to the front glass does not change the projected decay angle. In

ALL Σ^- WITH LENGTH > 1 cm. PROJECTED ON FRONT GLASS,
CURVE FOR LOSS VARYING FROM 100% AT 0° TO 0% AT 8°
USING CORRECTED MOMENTUM SPECTRUM.

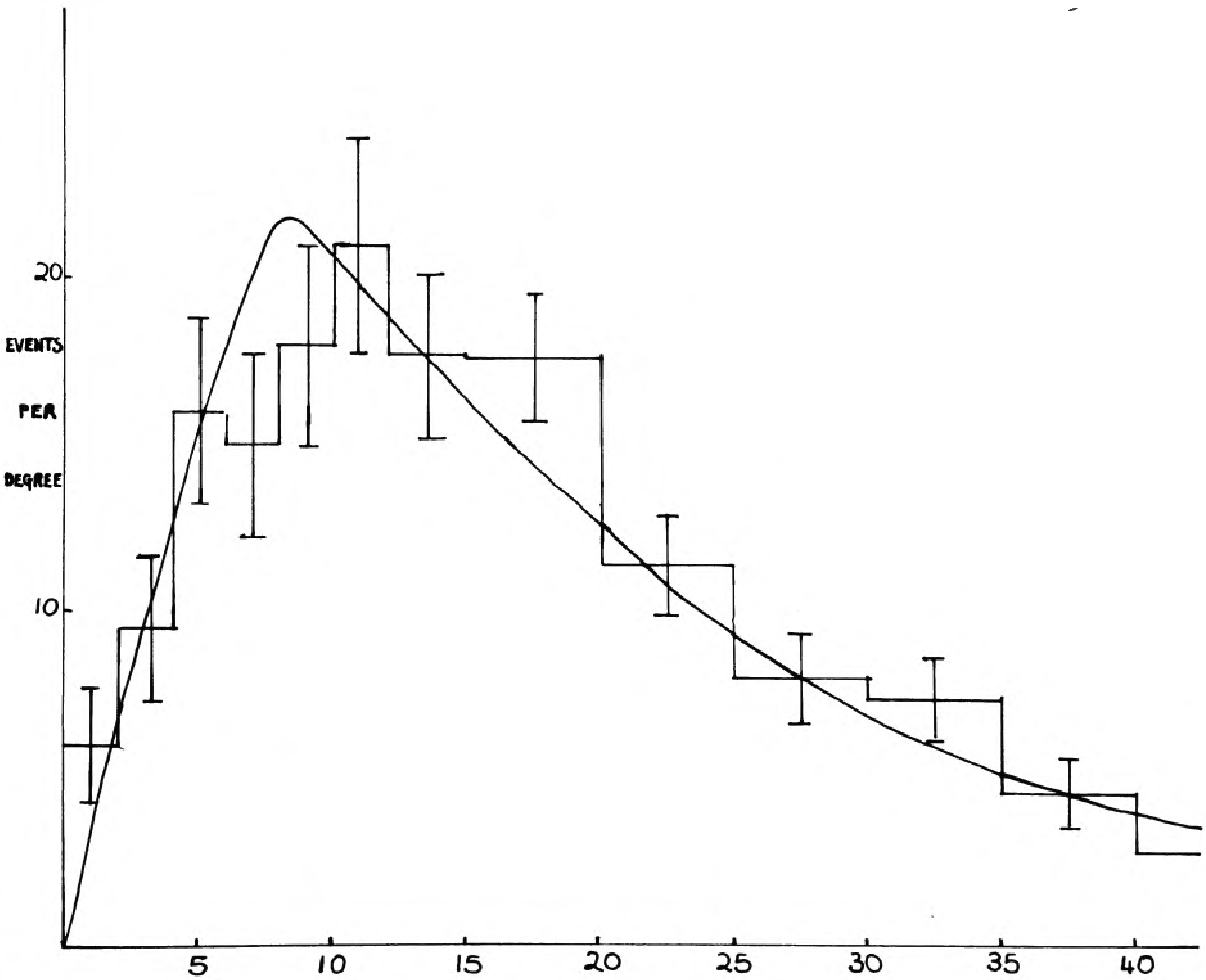

PROJECTED DECAY ANGLE ON FRONT GLASS.

Fig. 4.1

ALL Σ^{+}_{π} WITH LENGTH > 1 cm. ON FRONT GLASS

PLOTTED WITH CURVE FOR 0-8° LINEAR LOSS.

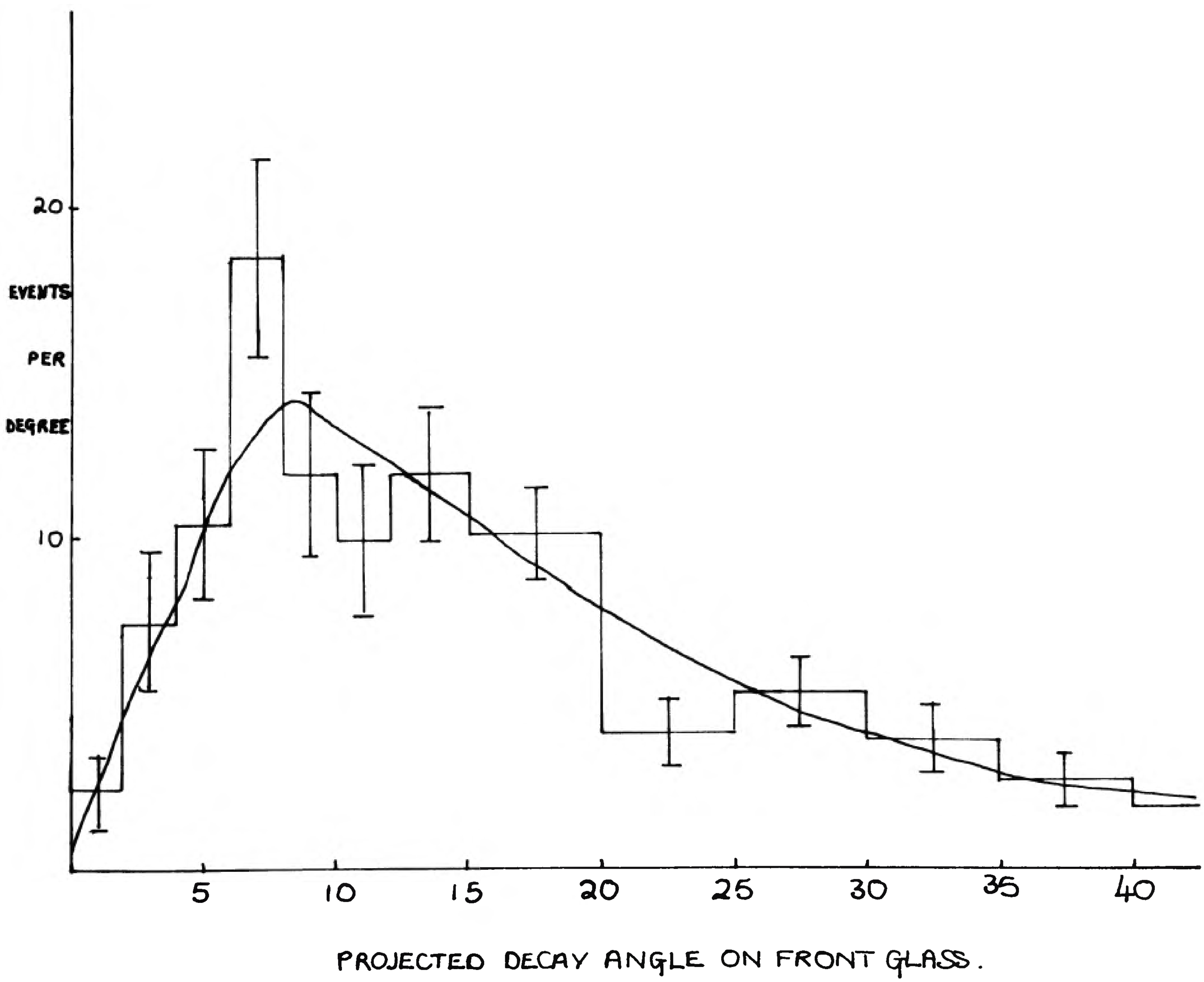

Fig. 4.2

Appendix A we show how to calculate the projected decay angle spectrum for fixed momentum component and decay mode. In Figs 4.1 and 4.2 are shown histograms of the observed projected decay angle for Σ_π^- and Σ_π^+ decays. Both show the loss at small angle. Even more striking are the relative numbers of $p\pi^0$ and $n\pi^+$ decays of Σ^+ observed:

$$\Sigma^+ \rightarrow p\pi^0 \qquad 156 \text{ events}$$

$$\Sigma^+ \rightarrow n\pi^+ \qquad 450 \text{ events}$$

whereas it is known that these two decay modes are equal. The efficiency of observation and fitting, ε, as a function of the projected decay angle, θ, is taken to be:

$$\varepsilon = 0 \text{ for } 0 < \theta < \theta_1$$

$$\varepsilon = (\theta - \theta_1)/(\theta_2 - \theta_1) \text{ for } \theta_1 < \theta < \theta_2$$

$$\varepsilon = 1 \text{ for } \theta_2 < \theta$$

Various values of θ_1 and θ_2 were tried and χ^2 fits obtained for the projected decay angle distributions of Σ_π^+ and Σ_π^-. It is clear from Figs 4.1 and 4.2 that a significant number of events are observed with very small projected decay angles. Correspondingly we have $\theta_1 = 0$. The χ^2 prob as a function of θ_2 is shown in Table 4.1.

θ_2	4	5	6	7	8	9	10	11	12
Prob %	1.3	6.1	8.9	15.9	10.2	6.1	2.1	0.4	0.07

TABLE 4.1

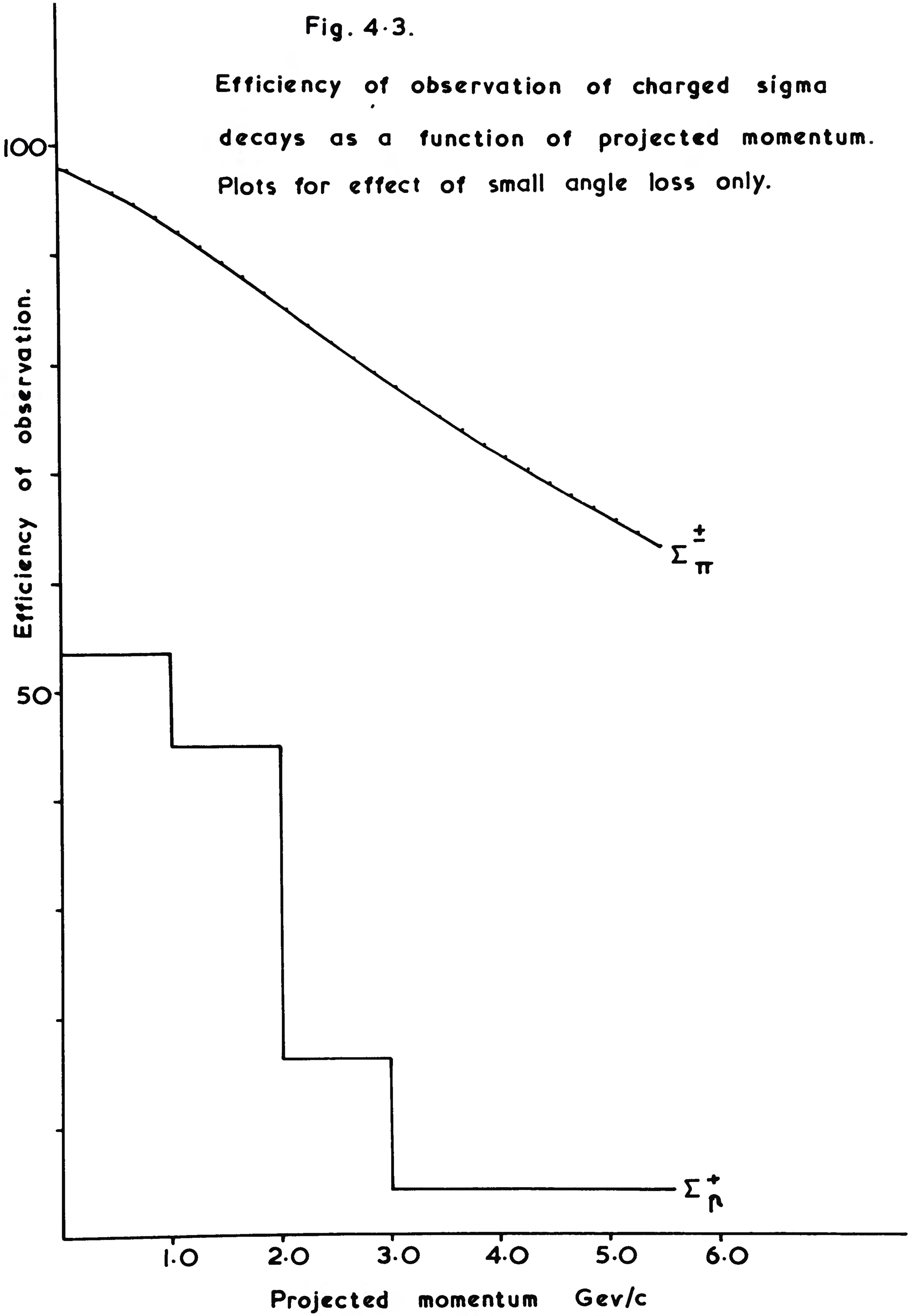

Fig. 4·3.

Efficiency of observation of charged sigma decays as a function of projected momentum. Plots for effect of small angle loss only.

Fig. 4·3.

Efficiency of observation of charged sigma decays as a function of projected momentum. Plots for effect of small angle loss only.

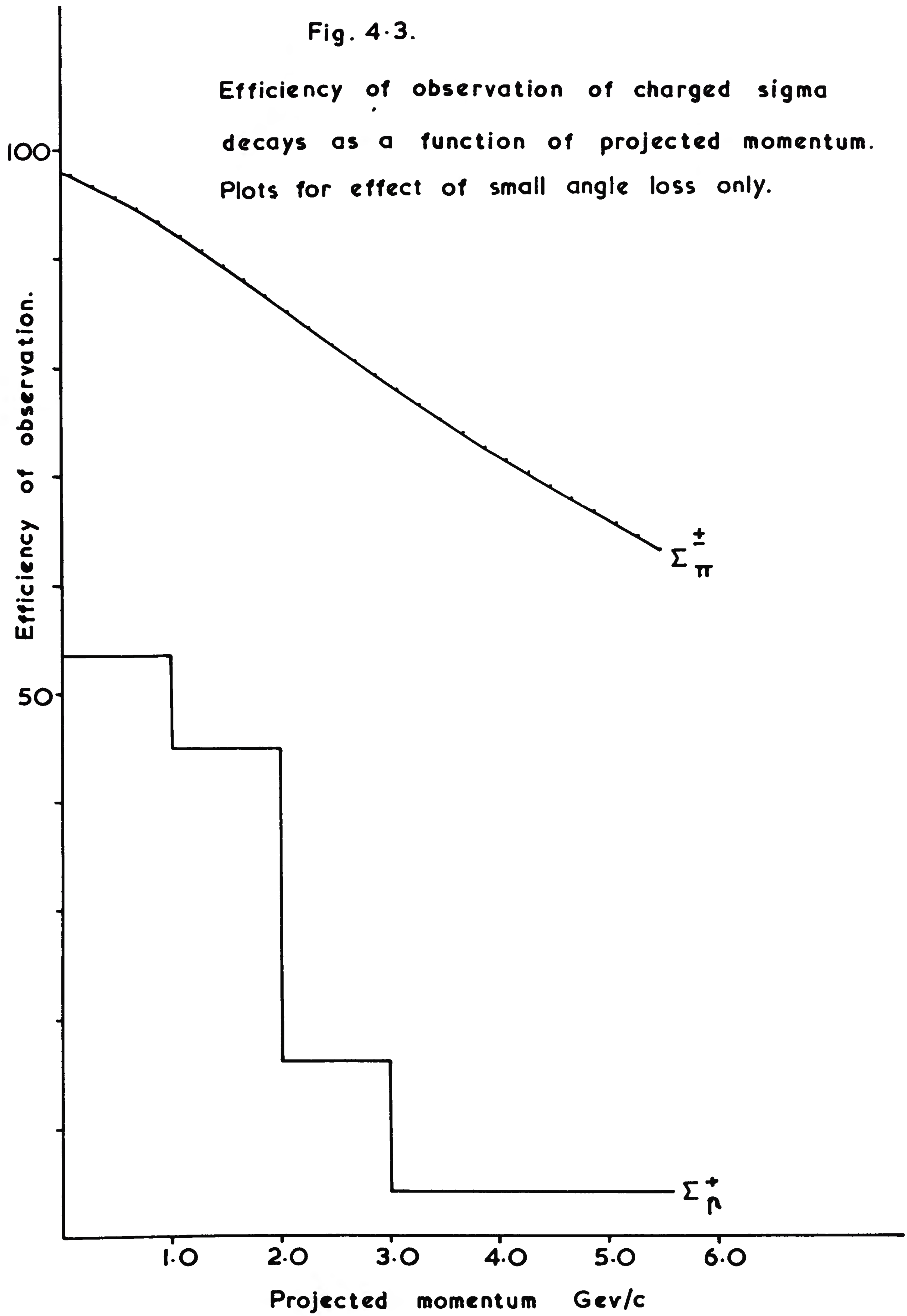

Figs 4.1 and 4.2 show the curves corresponding to $\theta_2 = 8^\circ$. The fit to both histograms is seen to be very reasonable. The fact that the fit is good for <u>both</u> indicates that this source of loss is independent of the length of the sigma track since the Σ^- lifetime is twice that of Σ^+. The events used in this analysis did not include those removed by the minimum length cut described below. However no weighting was used to compensate for those events decaying within this length since this does not affect the analysis.

A table of loss factors, $A(p_{11})$, as a function of $p_{\parallel}$, the projected momentum, was made and used to calculate a weight to correct for the angle losses

$$W_0(p_{11}) = \frac{1}{1 - A(p_{11})}$$

Fig.4.3 shows the efficiency of observation, (1-A), for decays derived in this way.

To treat Σ^+ to proton decay losses we compare the number of corrected Σ^+_π decays with the number of Σ^+_p decays observed within each range of momentum. The result is shown in Fig. 4.3. Only five Σ^+_p events are observed with projected momentum greater than 3.0 GeV/c.

Fig. 4·4a. Lab momentum distributions

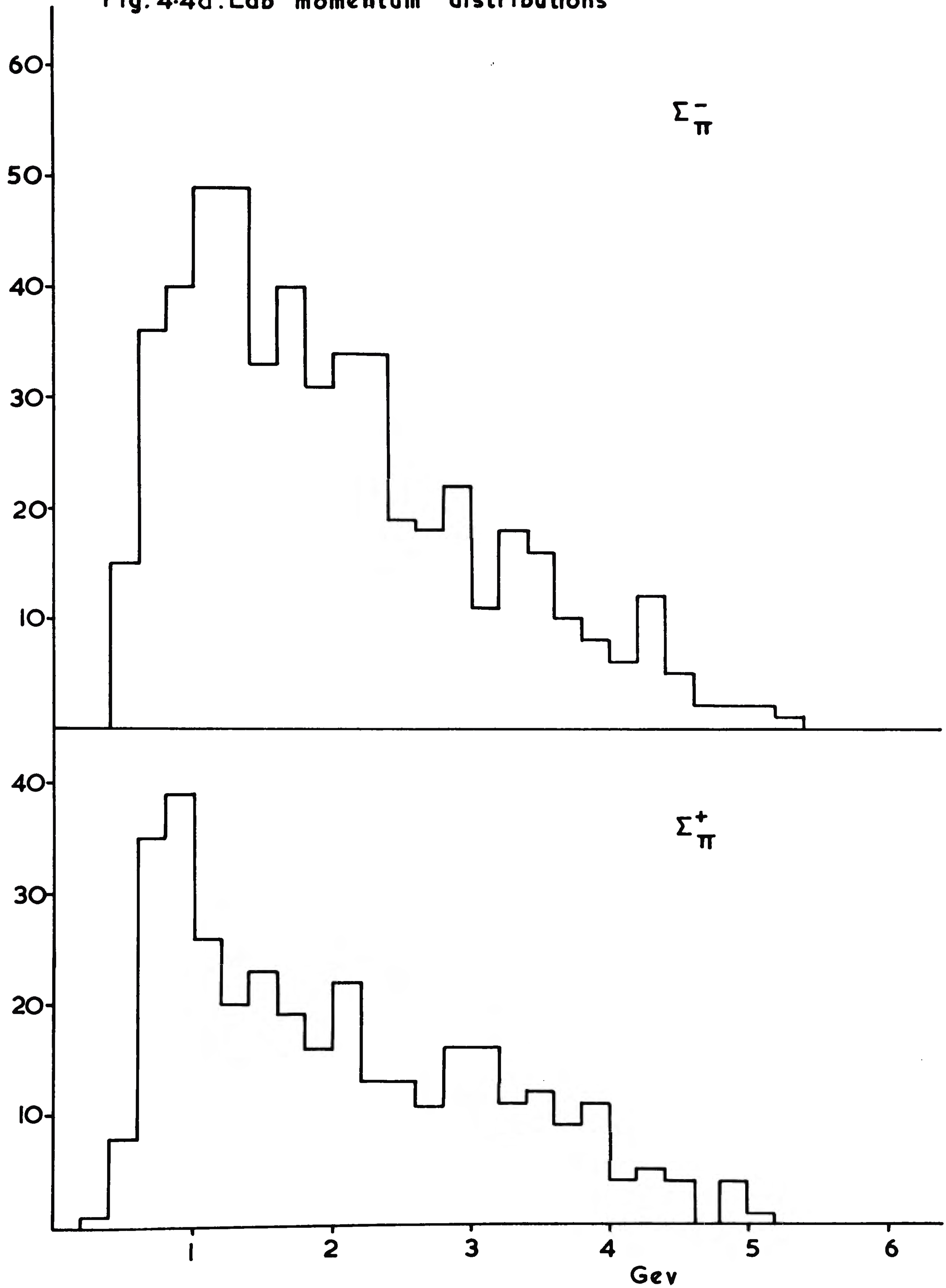

Fig. 4·4 b. Projected Length Distributions.

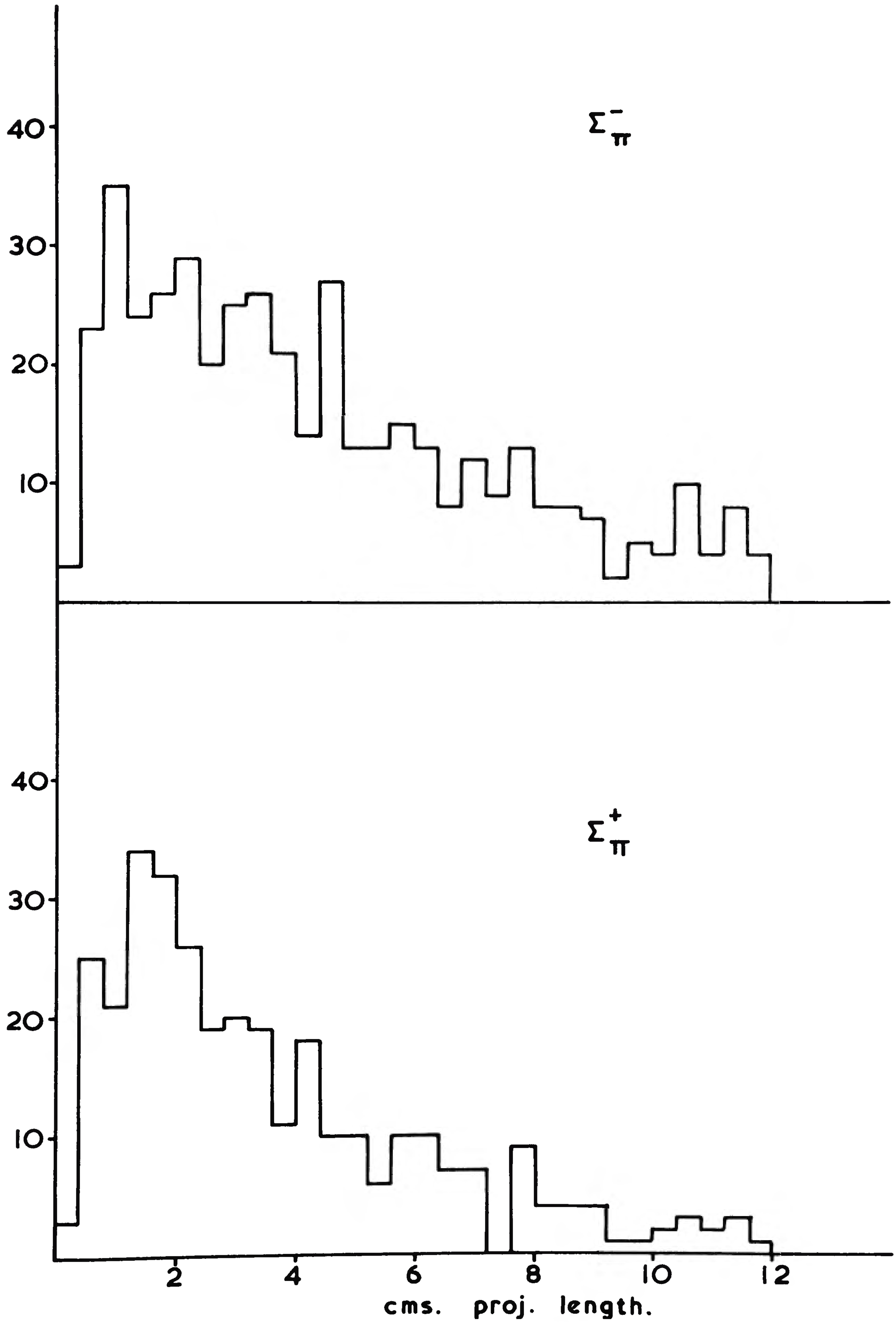

To analyse and correct for the loss of events at short decay lengths we use the exponential nature of decay at each momentum. In Fig.4.4 are shown the distributions of momentum and length projected on the front glass for Σ^+_π and Σ^-_π events. The lengths and momenta are such that very few Σ^- and essentially no Σ^+ tracks have a momentum determined from curvature. Furthermore the majority of events belong to the class with an unseen π^0 at production. They have therefore been assigned to a hypothesis and the unknown momentum determined on the basis of only one overall constraint for the variables at the two vertices (as well as having to satisfy ionisation criteria). They are thus contaminated both by events that have been fitted to the wrong hypothesis and also be events for which the unmeasured variables (including the sigma momentum) are very poorly defined and have large errors. The situation is particularly aggravated for events in which quantities derived from geometrical reconstruction are themselves badly determined. Those events which are seen with short decay lengths are of this type; the measured angles of the sigma track have large errors since the vertices are so close together; furthermore no ionisation assessment of the track is possible because the number of bubbles on it is not statistically significant. For these reasons having found the shortest projected length at which events are not being lost we apply a cut off and reject even those ones which are seen at a shorter projected length. If all events were observed the projected length distribution of sigmas of momentum p and dip λ would be:

$$N(l)\,dl \sim \exp\left(-\frac{l\,m}{p\,c\,\tau\cos\lambda}\right)dl$$

where τ is the sigma lifetime and $lm/pc\cos\lambda = t$, the proper time of a sigma of momentum p travelling a distance $l/\cos\lambda$ in space. Therefore a length plot of all events, each event being weighted with $(\exp + t/\tau)$ will be independent of length if no events are lost and if the moments have been correctly determined. Such plots are shown in Fig.4.5. The Σ^+_π events with $p < 1.2$ GeV have been excluded from this plot because of their large loss - those that are observed have large and relatively uncertain values of t/τ due to the high value of $\Delta p/p^2$. ($\Delta t = \dfrac{-lm\,\Delta p}{p^2 c\cos\lambda}$). The exponential nature of the weighting would then cause these low momentum events to dominate those of higher momentum whose proper time errors are small. (The fraction excluded from the plot is a third of the total.) The Σ^-_π events are not affected in this way

Fig 4.5a.

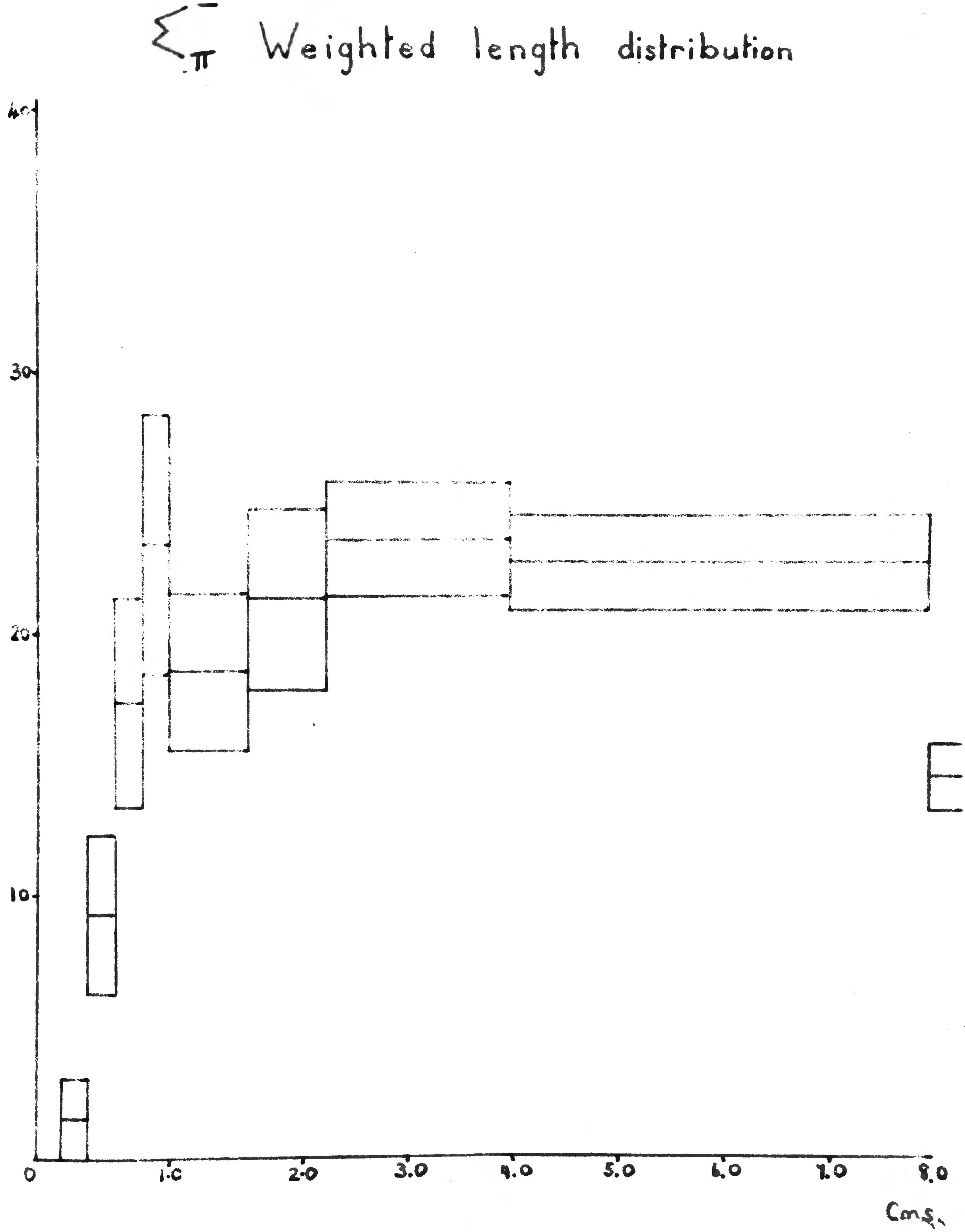
Σ_{π}^{-} Weighted length distribution
40
30
20
10
0
1.0
2.0
3.0
4.0
5.0
6.0
7.0
8.0
Cms.

Fig 4·5 b.

Σ_{π}^{+} Weighted length distribution

mom > 1.2 GeV

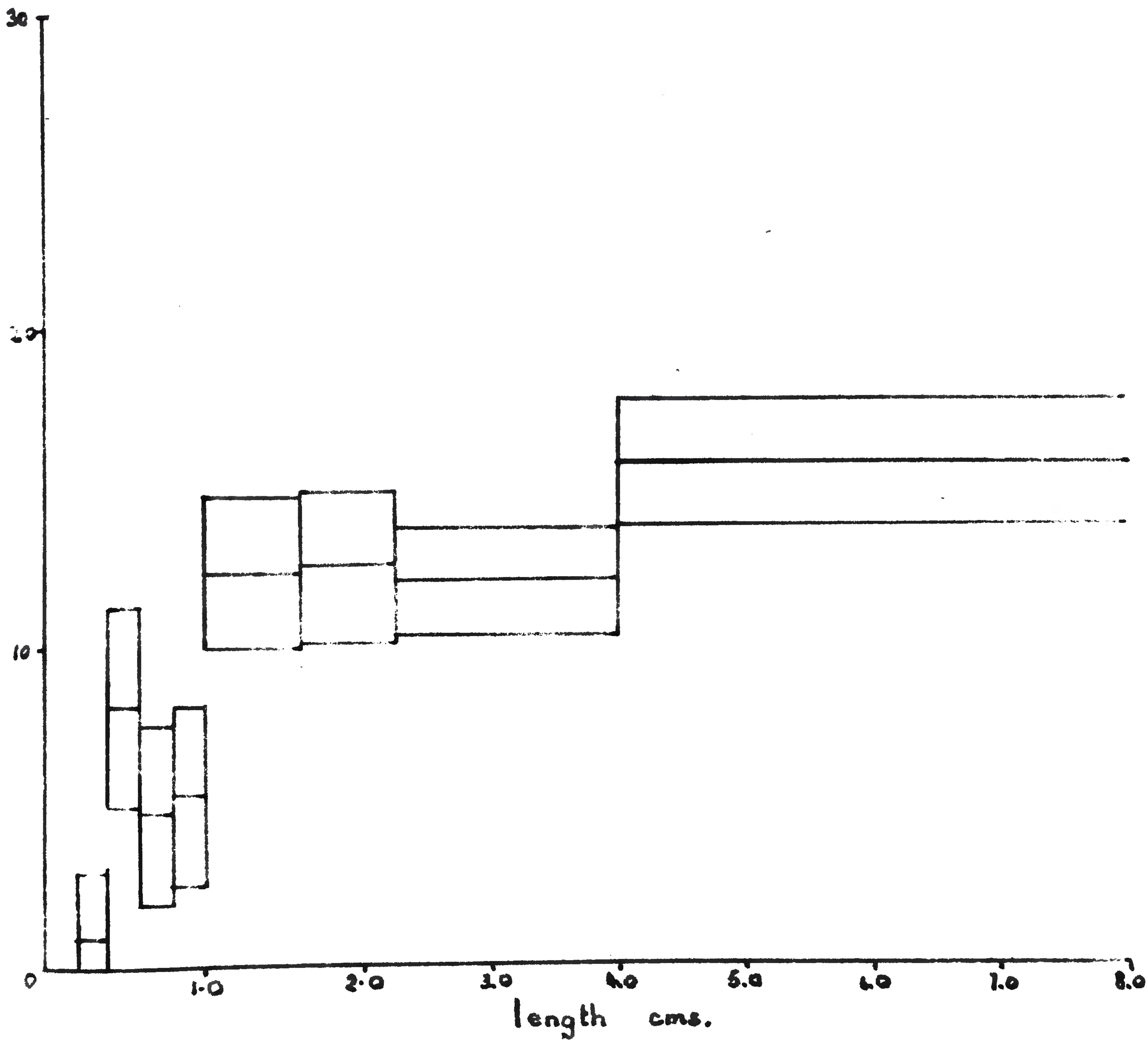

because those of low momentum travel twice as far as their positive counterparts so that their moments are determined better, they live twice as long so that the exponential factors are never so big and there are not so many of them anyway because of the absence of a strong production mechanism giving low moments in the lab. We conclude from the plots that there is no significant loss for lengths greater than one centimetre. (The low energy Σ^+_π events are studied further below.) We therefore reject all Σ events with projected lengths on the front glass of less than 1 cm.

To reduce possible contamination of the Σs from K and π decays we reject all Σs living longer than three lifetimes. In fact the lifetime curves are consistent with no such contamination. The actual numbers of events removed by the cuts is given in Table 4.2.

	No fitted	Less than 1 cm	3 lifetimes	Remaining
$\Sigma^+_\pi + 5\pi$	344	38	28	278
$\Sigma^+_\pi + 4\pi$	106	21	6	79
$\Sigma^-_\pi + 5\pi$	513	53	16	444
$\Sigma^-_\pi + 4\pi$	139	27	6	106

TABLE 4.2

Losses due to decays at small angles are not taken into account since they are independent of proper time at each momentum.

There appears to be a systematic discrepancy in that low momentum Σ^+_π from the hypothesis with missing π^0 have fewer short decays than can be accounted for by length loss considerations. See Fig.4.6. It seems likely that short Σ^+_π (1-2 cms) of low momentum are subject to losses in kinematic fitting. Alternatively this may be due to large systematic errors in the momentum itself. If the first explanation is true the number of low energy Σ^+_π is being underestimated by as much as 30 - 40%. If the second is true the number of low energy Σ^+_π is being slightly overestimated at the expense of those of higher momentum. No further attempt was made to correct this feature.

Each event which remained after the cuts was weighted with the reciprocal of the probability of acceptance

$$w_\ell = \left[\exp\left(- \frac{m}{\cos\lambda \; p c \tau}\right) - \exp\left(\max \left\{ \begin{matrix} -3 \\ -\frac{mL}{p c \tau} \end{matrix} \right\} \right) \right]^{-1}$$

where L is the distance from the production vertex to the limit of the outer box along the line of flight of the sigma. The behaviour of these weights is illustrated in Fig.4.7.

This length weight factor is multiplied by the factor to correct for small angle decays. The resulting weights are

Fig 4·6.

Slow Σ^+_π length distribution.

mom < 1·2 GeV/c

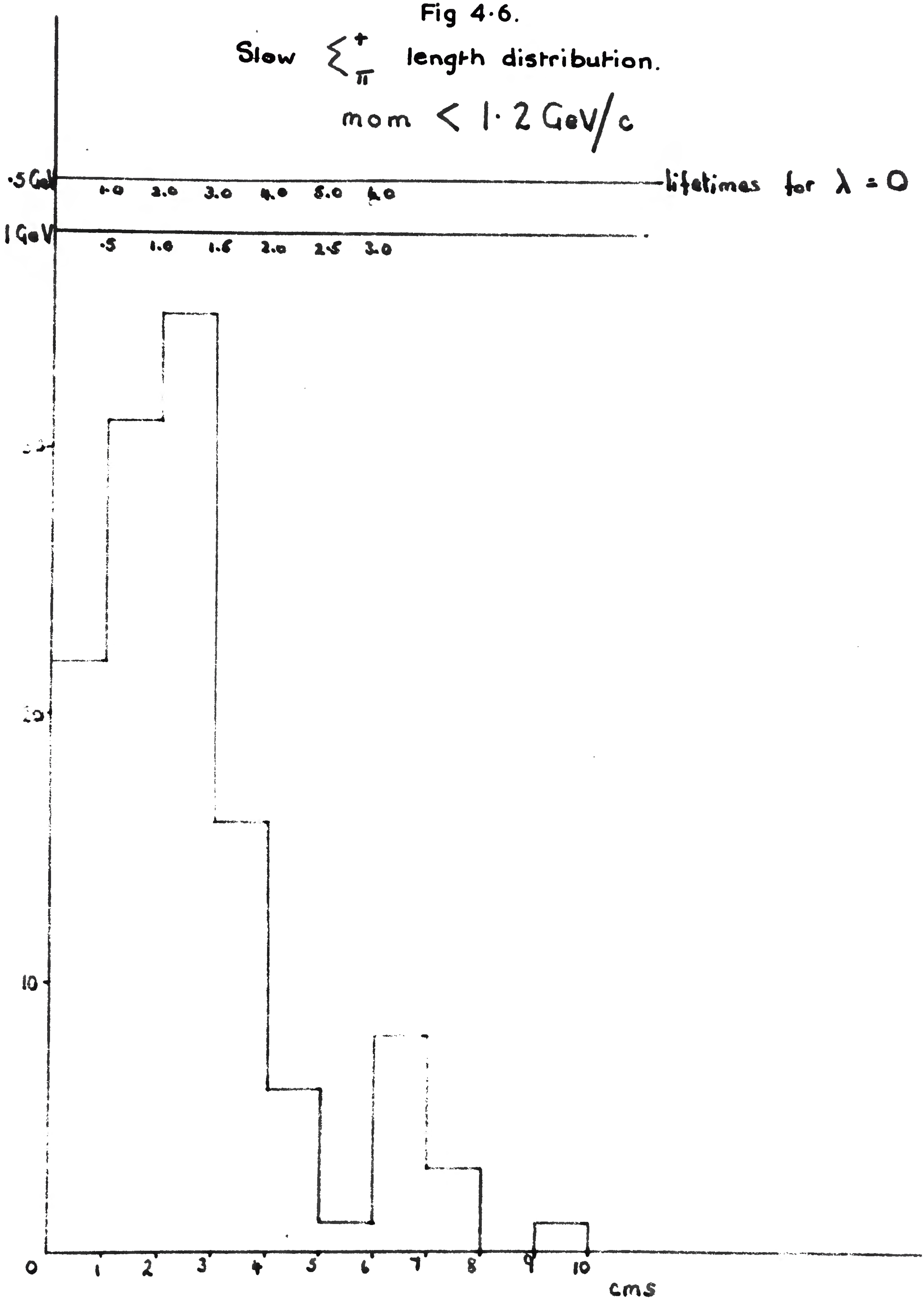

Fig. 4·7.

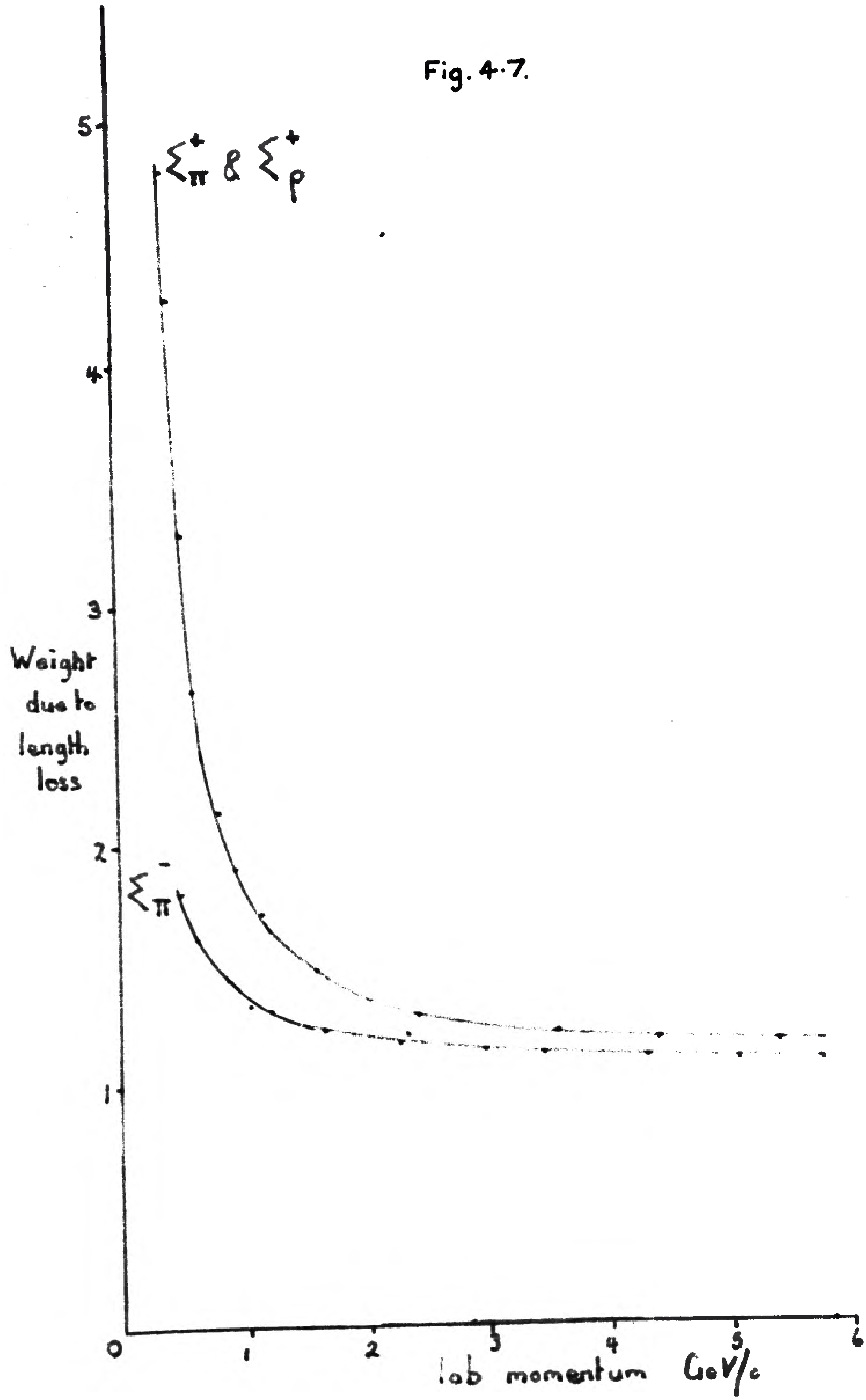

5
4
3
2
1
0
1
2
3
4
5
6
Σ_π^+ & Σ_p^+
Σ_π^-
Weight due to length loss
lab momentum GeV/c

Fig. 4.8.

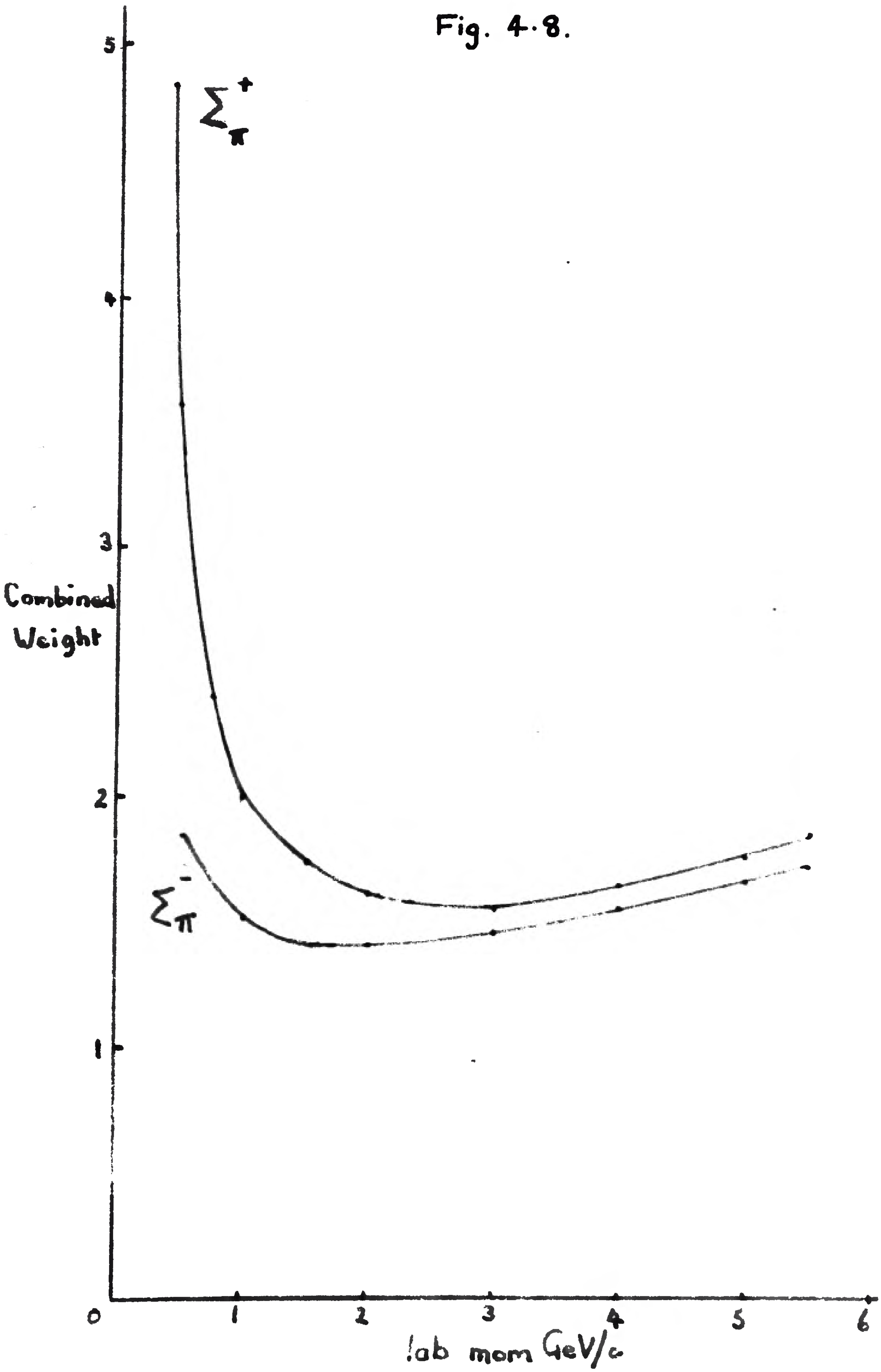

5
4
3
2
1
0
Combined Weight
Σ_π^+
Σ_π^-
1
2
3
4
5
6
lab mom GeV/c

used in all plots referred to as "weighted". Their general behaviour as a function of momentum is shown in Fig.4.8.

4.3 Neutral sigma and lambda events

A large proportion of events with a V^0 identified as a lambda zero gave fits both to Λ^0 and to Σ^0 at the production vertex, (see Chapter 2). These unresolved ambiguities were all written onto the data summary tape. The three hypotheses concerned are $\Lambda\pi^+\pi^-$, $\Sigma^0\pi^+\pi^-$ and $\Lambda^0\pi^+\pi^-\pi^0$ in the two prong +V topologies and the same with an extra $\pi^+\pi^-$ in the four prong +V events. Since the ambiguity and fitting process are the same for both topologies we choose the two prong +V events to analyse and apply our findings to the four prong +V - this choice avoids the irrelevant duplication of events by permutation of pions in the invariant mass plots examined below.

To resolve the ambiguity we use the fact that the branching ratio for $Y^{*+}(1385)$ decay is:

$\Sigma^0\pi^+ : \Sigma^+\pi^0 : \Lambda\pi^+ = 5:5:90$ (1)

Fig.4.9(a) shows the plots of $M(Y\pi^+)$ in the region of 1385 MeV. The lambda-sigma mass difference is 77 MeV so that when an event involving $Y^{*+}_{1385} \rightarrow \Lambda\pi^+$ is mistakenly fitted to a Σ^0

hypothesis an enhancement in the $(\Sigma^0\pi^+)$ effective mass is observed in the region of 1460 MeV. A Λ^0 event fitted to a Σ^0 hypothesis will appear to have a very low momentum γ in the laboratory. This means that the γ forward-backward ratio in the sigma centre of mass will be very small whereas it should be unity for true Σ^0 events.

Fig.4.9(a) shows that there are no $Y^{*+}_{1385} \to \Sigma^0\pi^+$ events in the unique Σ^0 plot in agreement with the assumed Y^* branching ratios. There are only four events in the 1460 region which is consistent with background. Therefore there is no substantial evidence of contamination of the unique Σ^0 fits by Λ^0 events.

In the case of unique $\Lambda\pi^+\pi^-$ fits 15% of $M(\Lambda\pi^+)$ are in the region of 1385 MeV. The ambiguous $\Lambda\pi^+\pi^-$ fits have 20% in this region and the corresponding peak at 1460 MeV is observed in the $(\Sigma^0\pi^+)$ mass when the events are interpreted as Σ^0 fits. Furthermore the γ forward-backward ratio in the Σ^0 centre of mass is 1.25 for unique Σ^0 fits and 0.5 for Σ^0 fits which are ambiguous with Λ^0. We conclude that there is good reason for accepting all such events as $\Lambda^0\pi^+\pi^-$ (2).

This leaves the ambiguities between $\Sigma^0\pi^+\pi^-$ and $\Lambda\pi^+\pi^-\pi^0$ to be resolved. There are three classes of events to be

FIG. 4.9(a) LOWER PART OF THE INVARIANT MASS SPECTRUM OF $(Y\pi^+)$

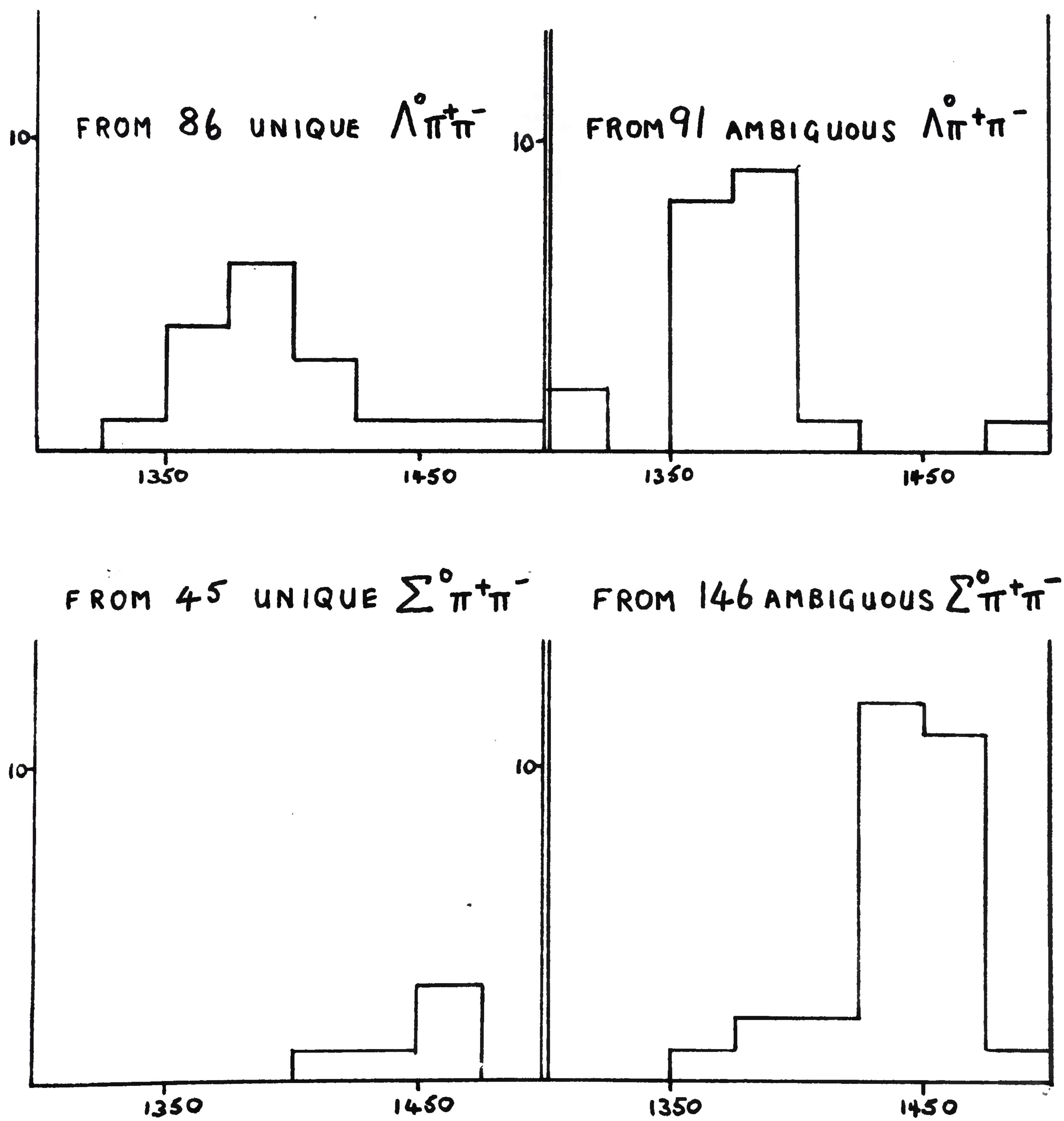

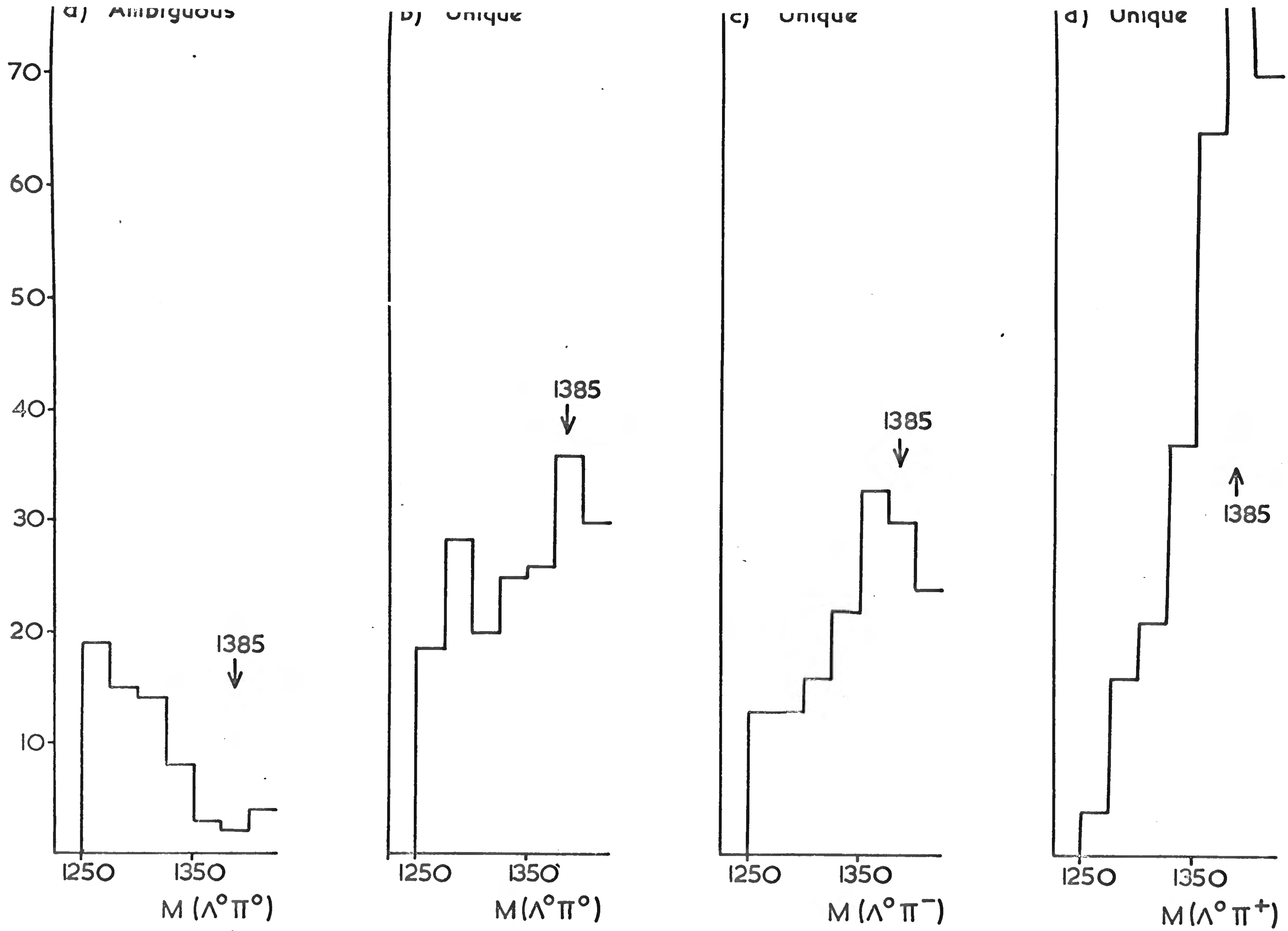

a) Ambiguous
b) Unique
c) Unique
d) Unique
70
60
50
40
30
20
10
1385
1250
1350
M ($\Lambda^\circ\pi^\circ$)
M ($\Lambda^\circ\pi^\circ$)
M ($\Lambda^\circ\pi^-$)
M ($\Lambda^\circ\pi^+$)

Fig. 4.9(b)

considered:

1) Unique $\Sigma^0\pi^+\pi^-$ events

2) Events ambiguous between $\Sigma^0\pi^+\pi^-$ and $\Lambda\pi^+\pi^-\pi^0$

3) Events fitting $\Lambda\pi^+\pi^-\pi^0$ uniquely.

Fig.4.9(b) shows that events of class 2 have $(\Lambda\pi^0)$ invariant masses below 1350 MeV. Also shown are the $(\Lambda\pi^0)$ $(\Lambda\pi^-)$ and $(\Lambda\pi^+)$ mass distributions for events of class 3. When compared with the $(\Lambda\pi^+)$ and $(\Lambda\pi^-)$ spectra, the $(\Lambda\pi^0)$ distribution shows an excess of some 30 events below 1350 MeV which are attributed to $\Sigma^0\pi^+\pi^-$ events that failed to fit the $\Sigma^0\pi^+\pi^-$ hypothesis. This suggests that events of class 2 are also $\Sigma^0\pi^+\pi^-$ events, and is consistent with the absence of $Y^*(1385)$ in any charge state in events of class 2 or of class 3 with $(\Lambda\pi^0)$ mass below 1350 MeV. We thus assign events of class 1 and 2 to the $\Sigma\pi\pi$ final state. Fig.4.10 shows the sigma zero forward-backward decay asymmetry as a function of sigma momentum in the chamber which is consistent with zero at all momenta. However the above discussion indicates that about 25% of the $\Sigma^0\pi^+\pi^-$ events have been fitted as unique $\Lambda\pi^+\pi^-\pi^0$. This loss could be serious and its effect is taken into account in chapter 6 where the $\Sigma\pi\pi$ final state is analysed.

The above analysis suggests the principle that of several ambiguous fits that which is most highly constrained should be

Fig. 4.10.

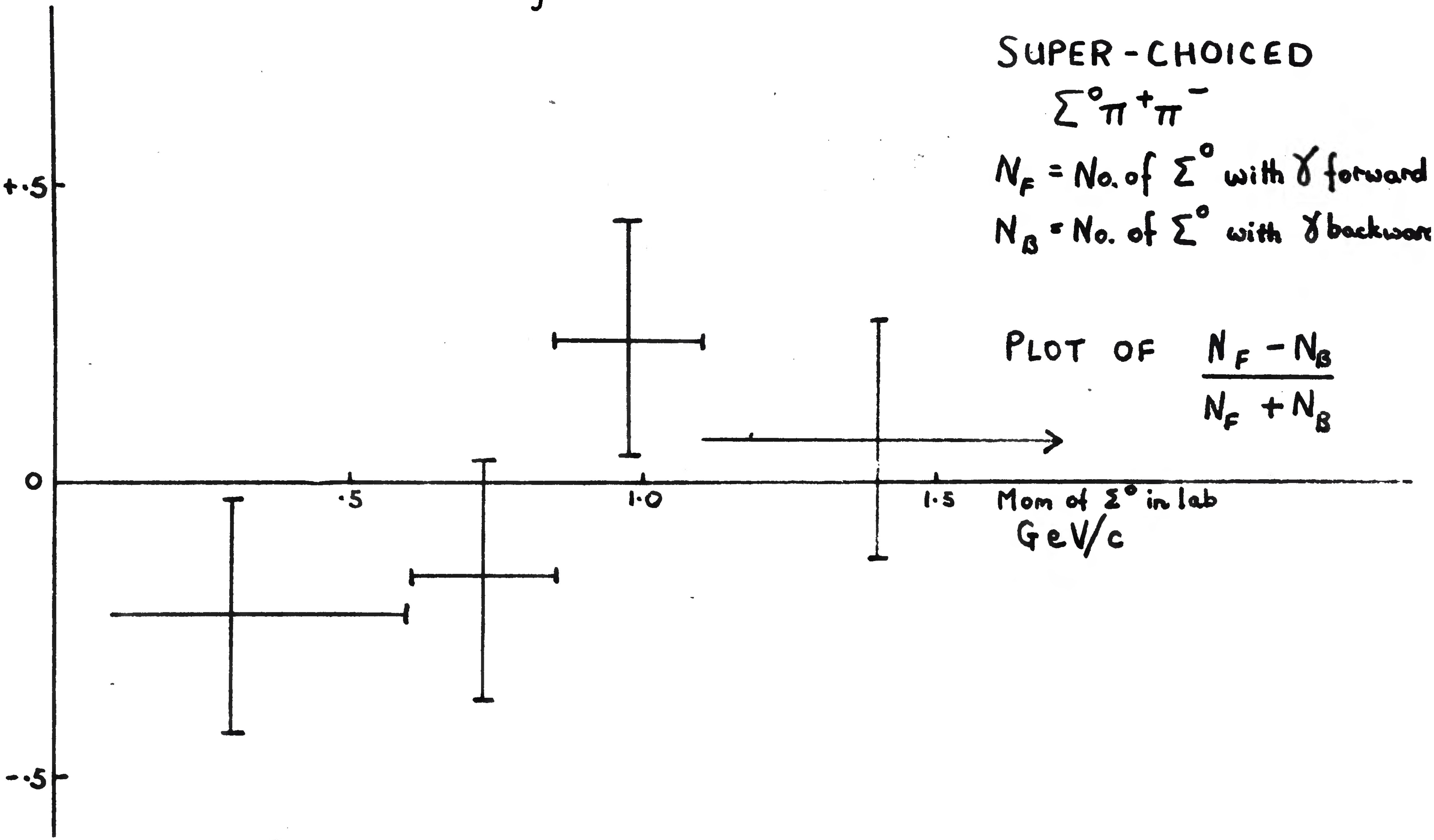
SUPER-CHOICED
$\Sigma^0\pi^+\pi^-$
N_F = No. of Σ^0 with γ forward
N_B = No. of Σ^0 with γ backward
PLOT OF $\frac{N_F - N_B}{N_F + N_B}$
+·5
0
-·5
·5
1·0
1·5
Mom of Σ^0 in lab
GeV/c

taken. This is in complete accord with the theoretical ideas developed in appendix E. This principle was applied both to the 201 and 401 events and a new data summary tape was written with the ambiguities resolved.

The contamination of the $\Lambda\pi^+\pi^-\pi^0$ and $\Lambda\pi^+\pi^-\pi^+\pi^-\pi^0$ channels by events with more than one π^0 is very hard to estimate - it is probably very high. The distribution of missing mass at production has a half width of .06 GeV^2. This is compatible with the mean error on this quantity and is to be compared with $m^2_{\pi^0}$ = .02 GeV^2. It is therefore virtually certain that all events with several π^0s having a combined invariant mass less than 300 MeV and most less than 500 MeV will be present in the sample. On the assumption that the two pi zero cross section is as big as that for a single pi zero the former limit involves only a 5% contamination and the latter only 20% assuming a phase space distribution for the invariant mass of $(\pi^0\pi^0)$. All hypotheses tend to be contaminated by events with two strange particles as is seen by the appearance of peaks in the invariant mass $(\pi^+\pi^-)$ at about 300 MeV which is really the process

$$\phi\ (1020) \rightarrow K^+K^-$$

This source of contamination is unlikely to exceed 10% in any channel.

To reduce the number of electron pairs misclassified as V zeros at the scanning table all Vs with zero opening angle on all three views were rejected. To estimate the number of Λs lost in this process we compare the observed opening angle distribution with the theoretical distribution calculated from the momentum distribution by a procedure similar to that described in appendix A. The results are shown in Fig 4.11. They ~~result is~~ are consistent with no loss. There is however the possibility of electron pairs being accepted and fitted as Λs. The good fit to the curve in Fig 4.11 shows that the number of line-of-flight (zero angle) decays of Λs is very close to that expected. Thus the contamination of Λs with electron pairs is small. The missing mass of Λ^0 Vees is shown in Fig 4.12. The peak is symmetrical and narrow showing that the fiducial volume was sufficiently small for V^0s within it to be accurately measured. Electron pairs of momentum greater than 280 MeV have missing mass as "lambdas" greater than the lambda mass.

Fig 4.13 shows the projected length distribution of Λ^0s. It is clear that for Λ^0 projected path lengths less than 2 mms there is a significant loss whereas there is no loss for longer lengths. The derivation of weights to compensate for this loss is exactly as discussed in the case of charged

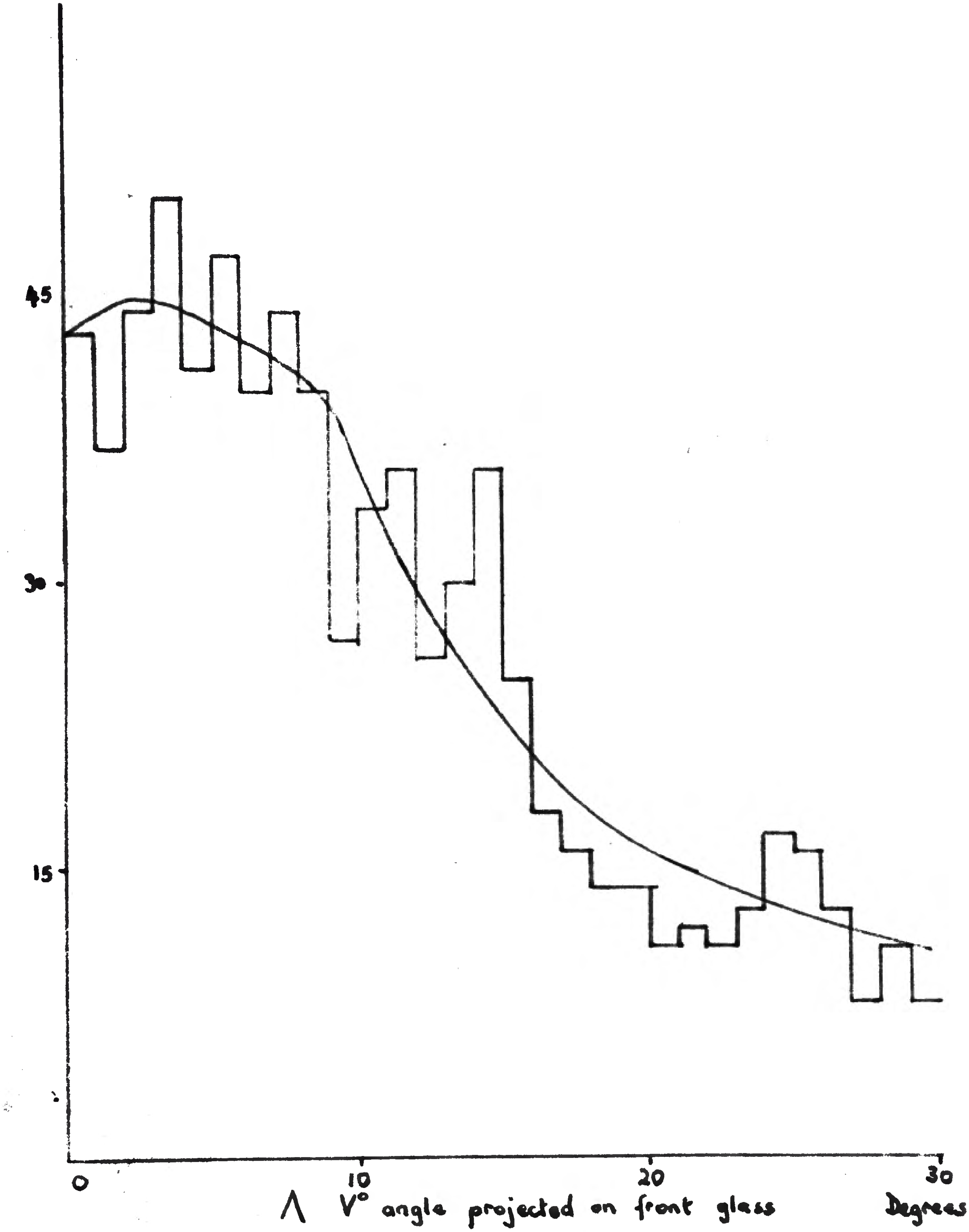

Fig. 4.11.

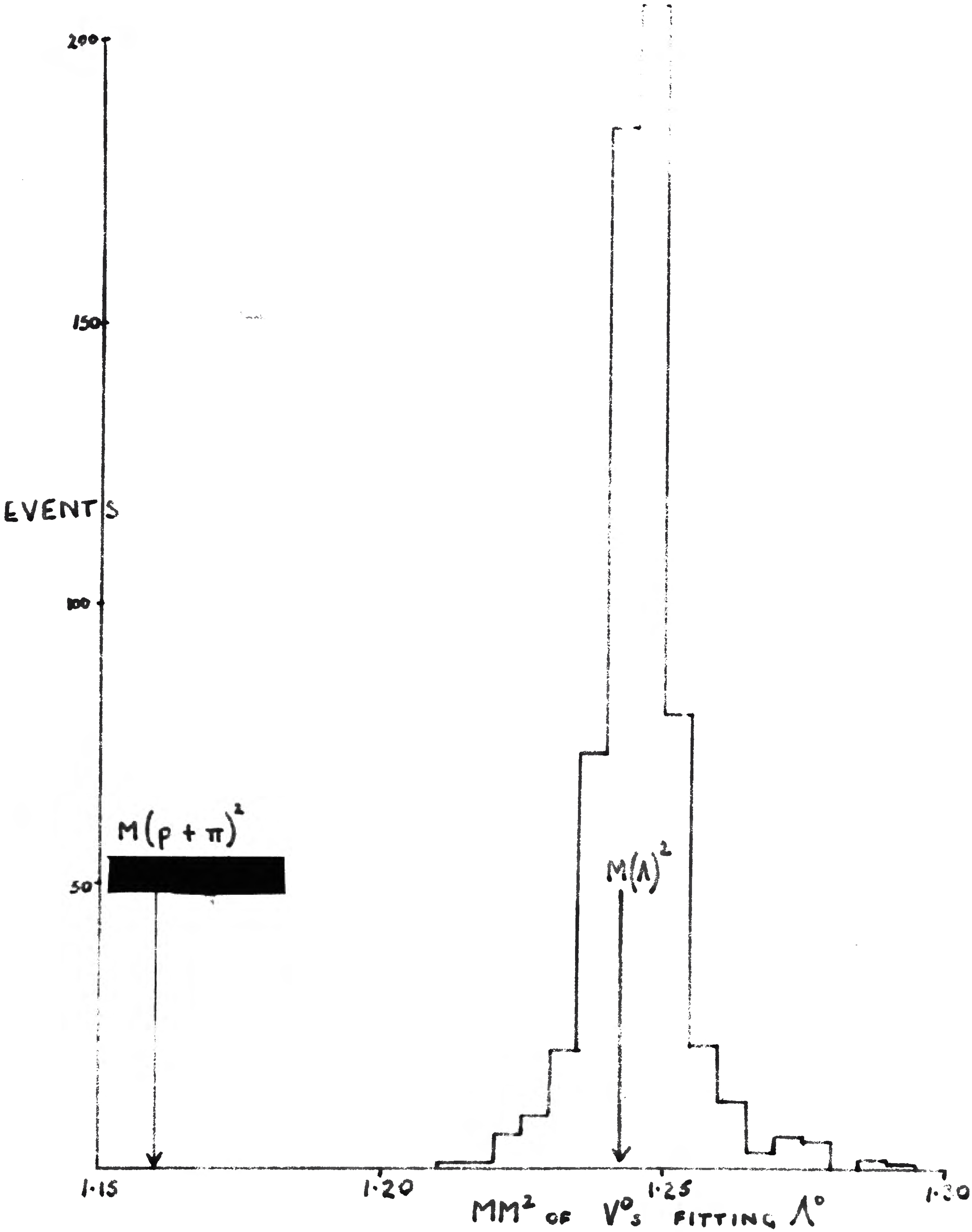
200
150
100
50
EVENTS
M(p + π)²
M(Λ)²
1·15
1·20
1·25
1·30
MM² OF V⁰s FITTING Λ⁰

Fig. 4.12.

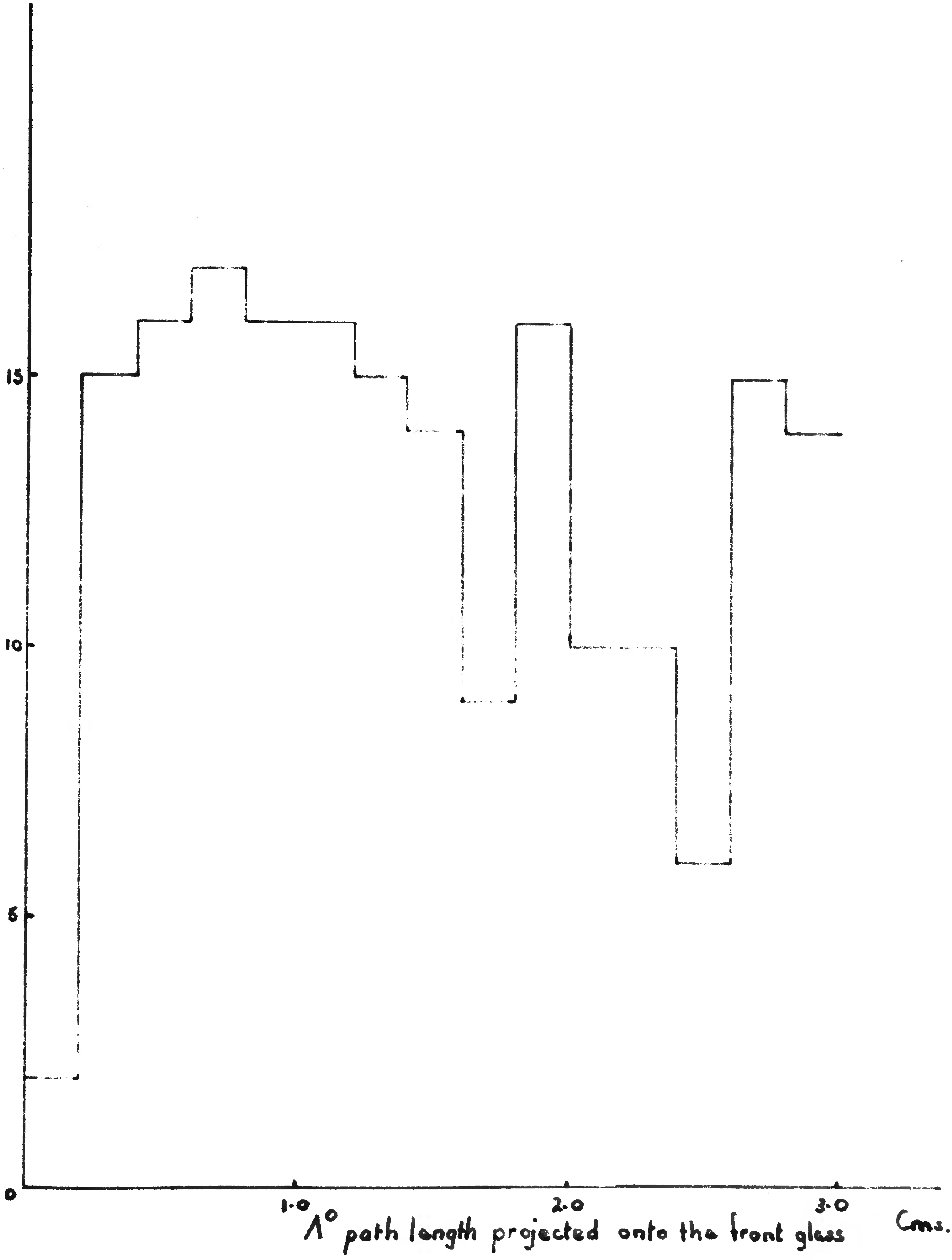
15
10
5
0
1·0
2·0
3·0
Cms.
Λ^0 path length projected onto the front glass

Fig. 4.13.

sigmas. A limit of four lifetimes was placed on the Λ and correction made for the size of the outer box:

$$w_\ell = \left[\exp\left(- \frac{0.2m}{\cos\lambda \, p c \tau}\right) - \exp\left(\max\left\{ \begin{array}{l} -4 \\ -\frac{mL}{p c \tau} \end{array} \right\}\right) \right]^{-1}$$

The mean weight was 1.16. Only 0.7% of events had weights above 2.5 while the highest weight was 3.9. This weighting was used for the Λ^o in Σ^o events also.

REFERENCES TO CHAPTER 4

(1) A.H. Rosenfeld et al: Rev. Mod. Phys. **39**, 1 (1967).

(2) Similar conclusions concerning the $\Lambda\pi\pi/\Sigma\pi\pi$ ambiguity have been reached by:

J. Mott et al: Phys. Rev. Letters **18**, 355 (1967) (using missing mass and taking techniques in 5.5 GeV/c K^-p)

W. Chinowsky et al: (private communication) (using the forward-backward symmetry in the centre of mass of 6 GeV/c p p collisions).

C H A P T E R 5

LAMBDA AND SIGMA FINAL STATES

5.1 Introduction

The analysis of this experiment is hampered by the low experimental resolution due to the low magnetic field compared with other experiments in the same momentum range. The Argonne-Northwestern K^-p experiment at 5.5 GeV/c was run in the 30" superconducting chamber with a 32.5 K gauss field compared with our modest 12 K gauss. For this reason we have not expended time and effort fitting parameters such as widths and masses of known resonances.

In section 5.2 we compare the hyperon centre of mass angle distributions with those of the nucleons and with the results of other experiments. In section 5.3 and 5.4 we discuss some topics in the lambda two and three pion final states. Section 5.5 and 5.7 survey the lambda four and five pion final states. Strong positive meson production is found to be associated with the forward lambdas. Section 5.8 and 5.9 discuss the sigma three and four pion final states. Interesting meson resonances are seen. The charged sigma

CENTRE OF MASS PRODUCTION ANGULAR DISTRIBUTIONS (cos θ^*)

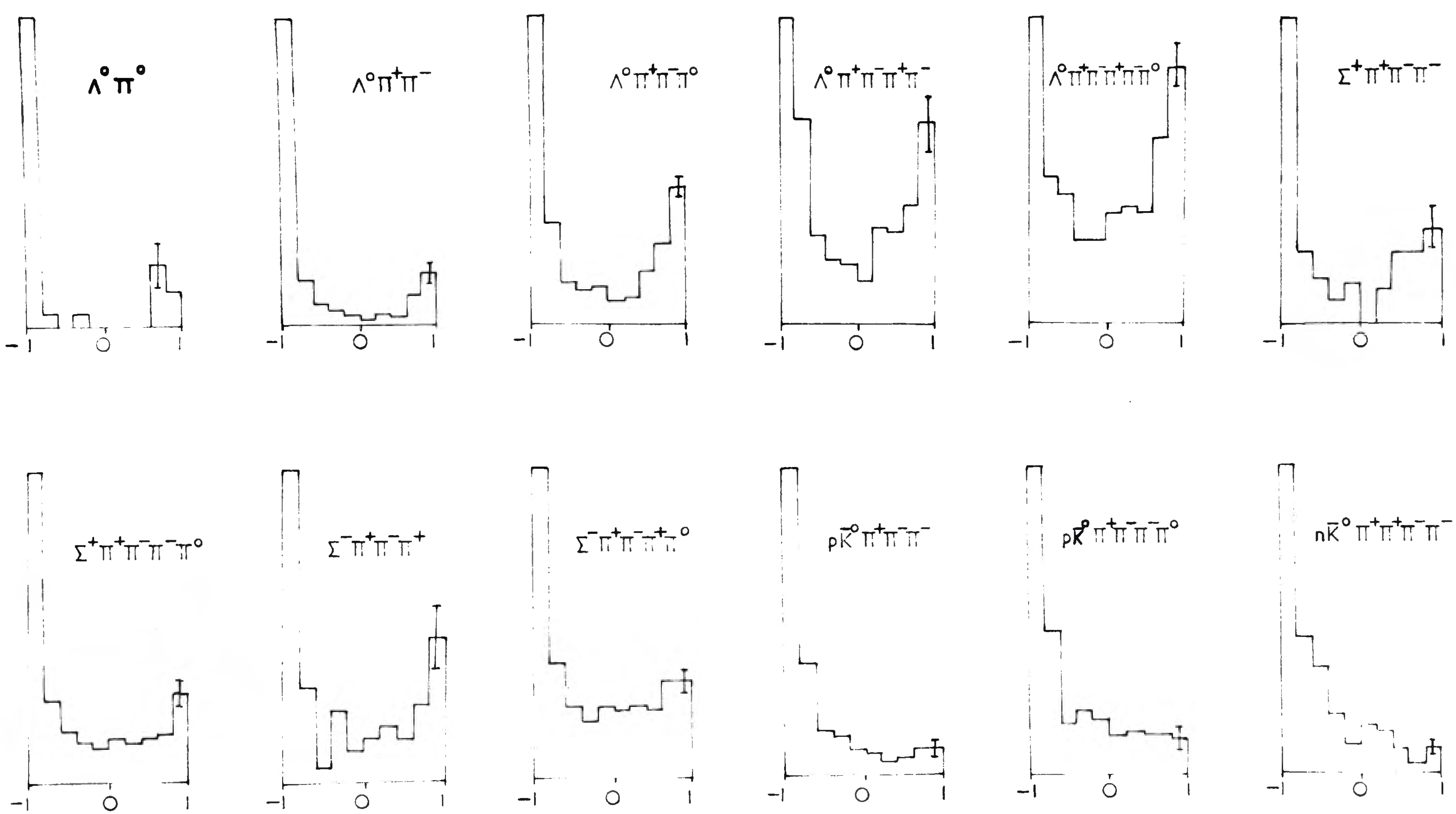

FIG. 5.1.

four pion final state is related to the neutral sigma four pion final state (briefly discussed in section 5.6) using a statistical model for the charge distribution. The model succeeds in explaining the low cross sections for $\Sigma^0 4\pi$ and $\Lambda^0 4\pi$ in the four prong $+ V^0$ topology.

5.2 Hyperon centre of mass angle distributions

Figure 5.1 shows the baryon centre of mass angle distributions. The plots are weighted as described in chapter 4 and are normalised to the contents of the backward bin. All the final states exhibit a pronounced backward peaking (the direction of the incident K^- is taken as 'forwards'); in addition hyperons have a substantial forward peak which is absent in the nucleon distributions. The peaks for forward Λ s are wider than those for backward Λ s and stronger than those for forward Σ s. The cross sections for forward and backward hyperons are given in table 5.1; we note that cross sections for Σ^+ channels are greater than those for Σ^- channels in every case.

The Λ final states show strong $Y^{*+}(1385)$ production; the (1385) production angles are shown in Fig 5.2. There is no forward peak of $Y^{*+}(1385)$ nor of any other strong Y^*

COS θ^* FOR $Y^{*+}(1385)$ IN $\Lambda n\pi$ FINAL STATES WITH BACKGROUND SUBTRACTED.

(plots are unweighted)

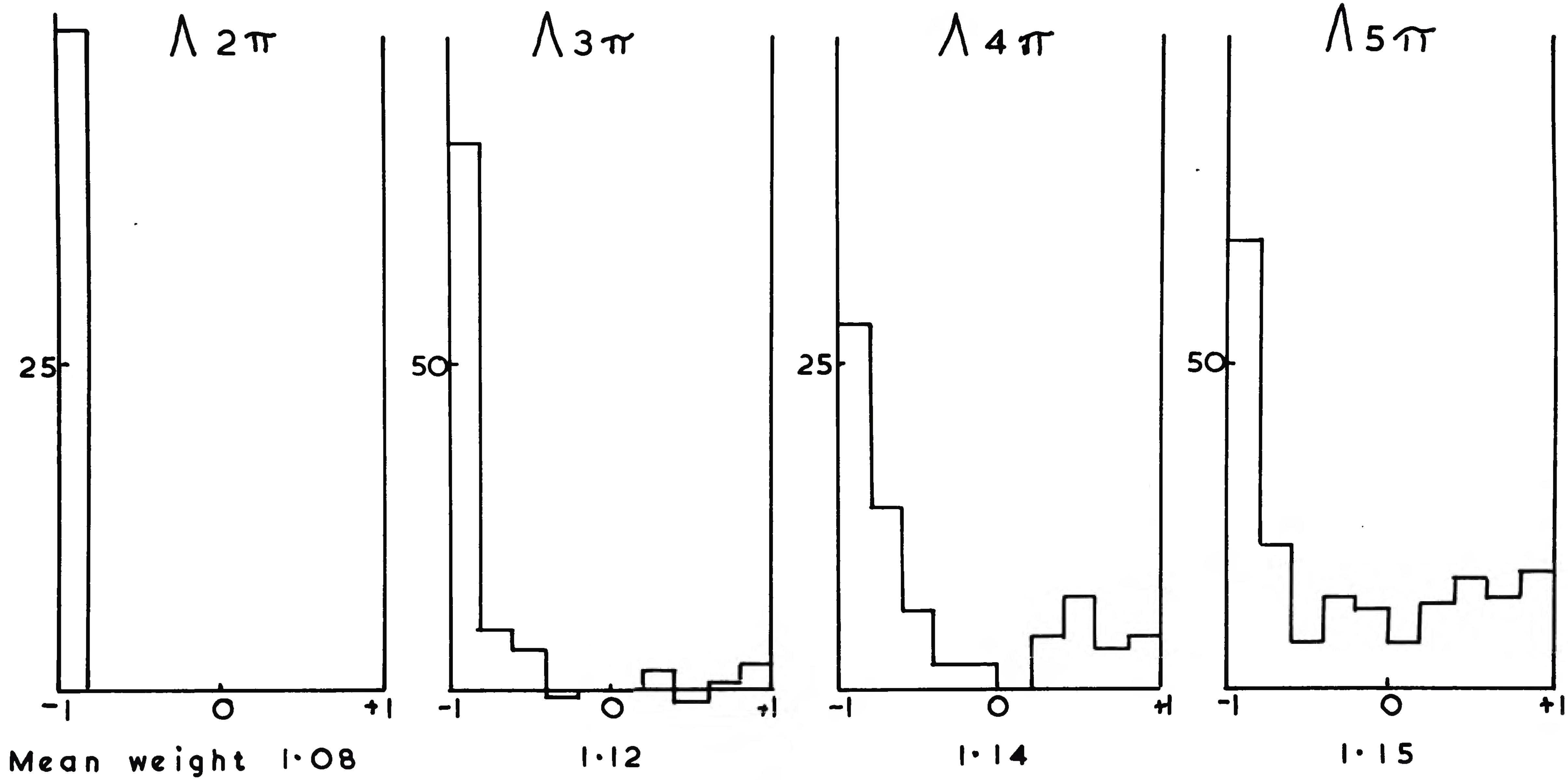

FIG. 5.2.

LONGITUDINAL COMPONENT OF Λ MOMENTUM

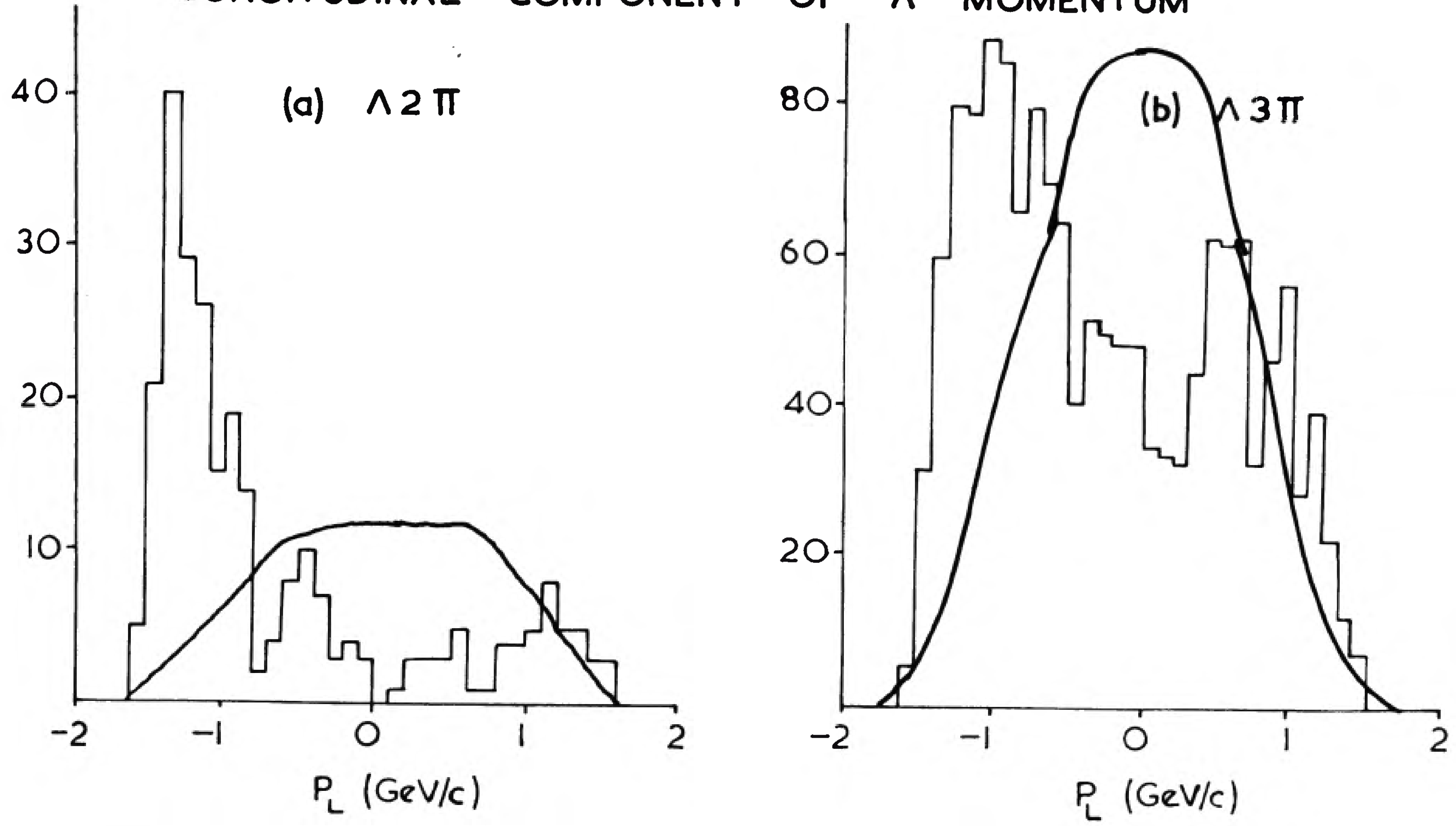

FIG.5.3.

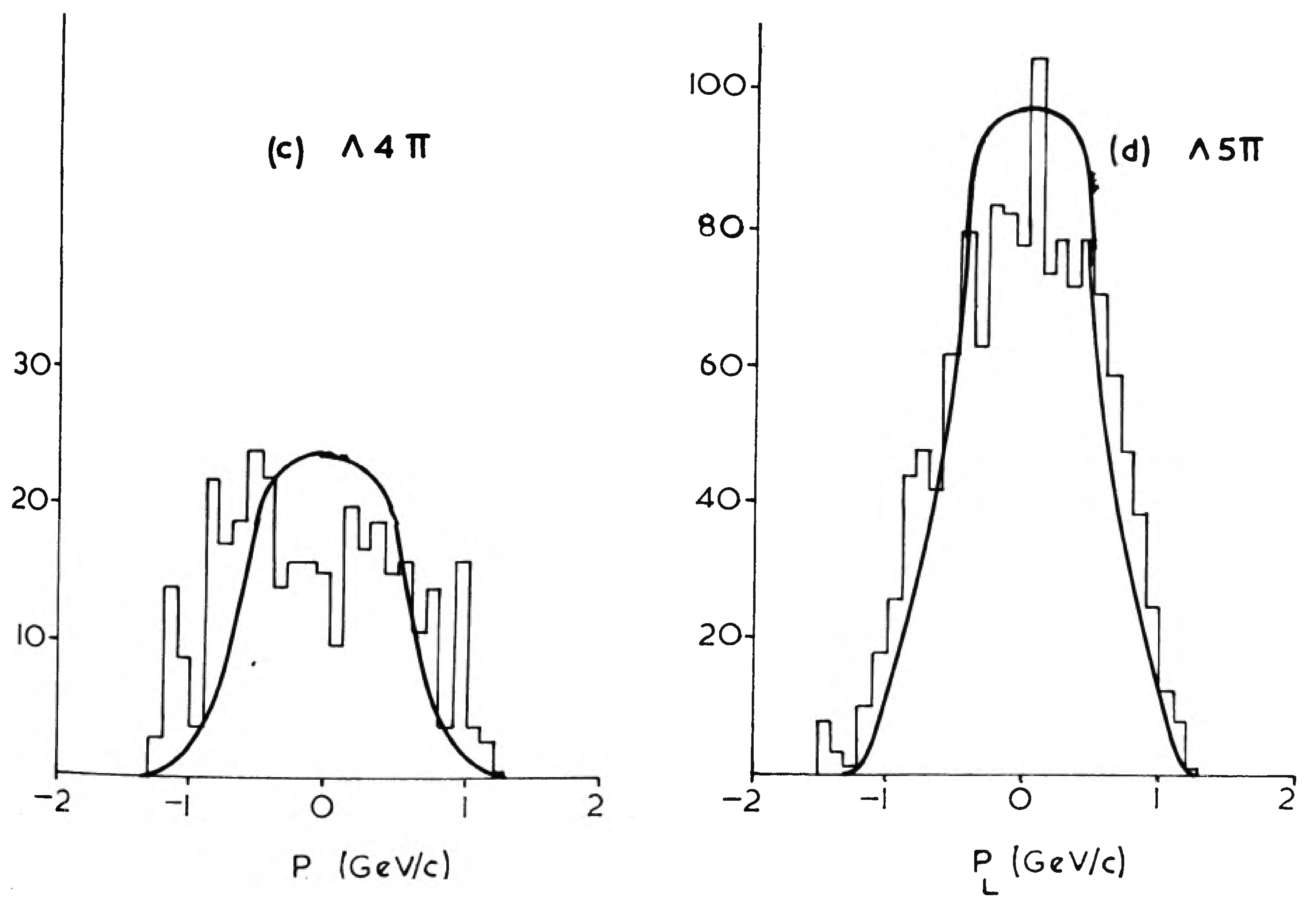

resonance. The low Q-value of the (1385) and the high mass of the Λ mean that the Y^* and corresponding lambda angular distributions are very similar. The contamination of mis-identified K^os amongst the forward Λ s is extremely small ($< 5\%$), as the kinematic fitting for these events involves two mass-dependent constraint equations. The ratio of the forward Λ peak to the backward Λ peak increases monotonically with the number of pions in the final state. These forward Λ s have high momentum in the overall centre of mass as can be seen from Fig 5.3. The curves on these plots are phase space curves. Even in the Λ 5π final state the Λ longitudinal momentum is significantly larger in both forward and backward directions than the phase space prediction.

The production of forward hyperons and not of forward nucleons is well known in two body K^-p baryon exchange reactions; forward nucleons would require the exchange of a strangeness +1 baryon. However no forward nucleon peaks comparable to the hyperon peaks of Fig 5.1 are seen in πp interactions(1) where there is no such selection rule. Forward Λ peaks similar to those shown here have been seen in 10 GeV/c K^-p interactions(2). In 10 GeV/c K^+p interactions

TABLE 5.1

Channel	Number of events in Fig 5.1	Cross sections (μbarns) Backward hemisphere baryon	Forward hemisphere baryon	$Y^{*+}(1385)$
$\Lambda\pi^0$	28	16±5	5±3	
$\Lambda\pi^+\pi^-$	220	52±11	13±3	15±5
$\Lambda\pi^+\pi^-\pi^0$	1100	260±39	150±21	31±6
$\Lambda\pi^+\pi^-\pi^+\pi^-$	301	58±8	49±7	23±6
$\Lambda\pi^+\pi^-\pi^+\pi^-\pi^0$	1123	169±22	176±23	60±9
$\Sigma^-\pi^+\pi^-\pi^+$	79	37±10	24±8	
$\Sigma^-\pi^+\pi^-\pi^+\pi^0$	493	109±15	68±10	
$\Sigma^+\pi^-\pi^+\pi^-$	89	68±15	39±8	
$\Sigma^+\pi^+\pi^-\pi^+\pi^0$	316	192±30	98±10	
$\bar{K}^0\pi^+\pi^-\pi^-p$	372	210±40		
$\bar{K}^0\pi^+\pi^-\pi^+\pi^-n$	305	160±25		
$\bar{K}^0\pi^+\pi^-\pi^-\pi^0p$	536	290±50		

forward nucleons could be produced by $\Lambda / \Sigma / Y^*$ exchange. Although a few such forward nucleons have been seen the cross section is small and the number of events is consistent with π^+'s being misidentified as protons[3]. The absence of forward peaks of $Y^*(1385)$ in our data ~~are~~ is equally puzzling. Two possible explanations are:

a) A highly inelastic resonance at 3.52 GeV. Its large visible partial cross section for decay to $\Lambda 3\pi$, $\Lambda 4\pi$ and $\Lambda 5\pi$ implies a cross section of some millibarns in spite of its small coupling to K^-p. This in turn implies a high spin - and why should it couple so strongly to $\Lambda 5\pi$? This explanation seems highly implausible.

b) Slight forward-backward peaking is expected from total angular momentum conservation on a statistical model for non central collisions. Why a statistical model should be relevant to Λ final states and irrelevant to Y^* or nucleon final states it is difficult to imagine - especially when the cross sections for the Λ channels are as high as those for the nucleon channels.

The sharp drop in the observed cross sections for well constrained channels suggests very strong contamination of the less well constrained hypotheses. To show that this is

TABLE 5.2

$\Lambda n\pi$ final states

Number of pions	Analysed cross section (μb)	Number of charge permutations	Number of these with less than $2\pi^0$	Correction factor	Estimated $n\pi$ cross section (μb)
1	21	1	1	1	21
2	65	3	2	1.5	97
3	410	7	6	1.2	480
4	107	19	6	3.2	342
5	345	51	30	1.7	585

not the case we refer first to chapter 4 where it is suggested that this contamination is of the order of 20%. Secondly we compare the analysed $\Lambda n\pi$ cross section with that expected for $\Lambda n\pi$ with more than one π^0. This is done by a very simple model of statistical charge distribution[4]. Although strong modification is expected from resonance production the results shown in table 5.2 indicate that the cross sections for $\Lambda n\pi$ do not fluctuate as a function of n as wildly as the figures of table 5.1 might suggest.

We conclude that the cross section for forward hyperon production in multibody final states is anomalously large.

5.3 <u>The lambda two pion final state</u>

Fig 5.1 shows the clear separation between the events with lambdas going forwards and backwards in the total centre of mass. Fig 5.4 is the Dalitz plot for events with lambdas in the backward hemisphere - the plot is dominated by the resonance channels $\Lambda\rho^0$, Λf^0 and $Y^{*+}(1385)\pi^-$. Fig 5.5 shows the momentum transfer and production angle distributions for these final states - they are all strongly peripheral.

<u>$K^-p \rightarrow \Lambda\rho^0$</u>. The decay distributions (Jackson angle, -, and Treiman Yang, ϕ) of the ρ^0 are shown in Fig 5.6. The

FIG 5.4

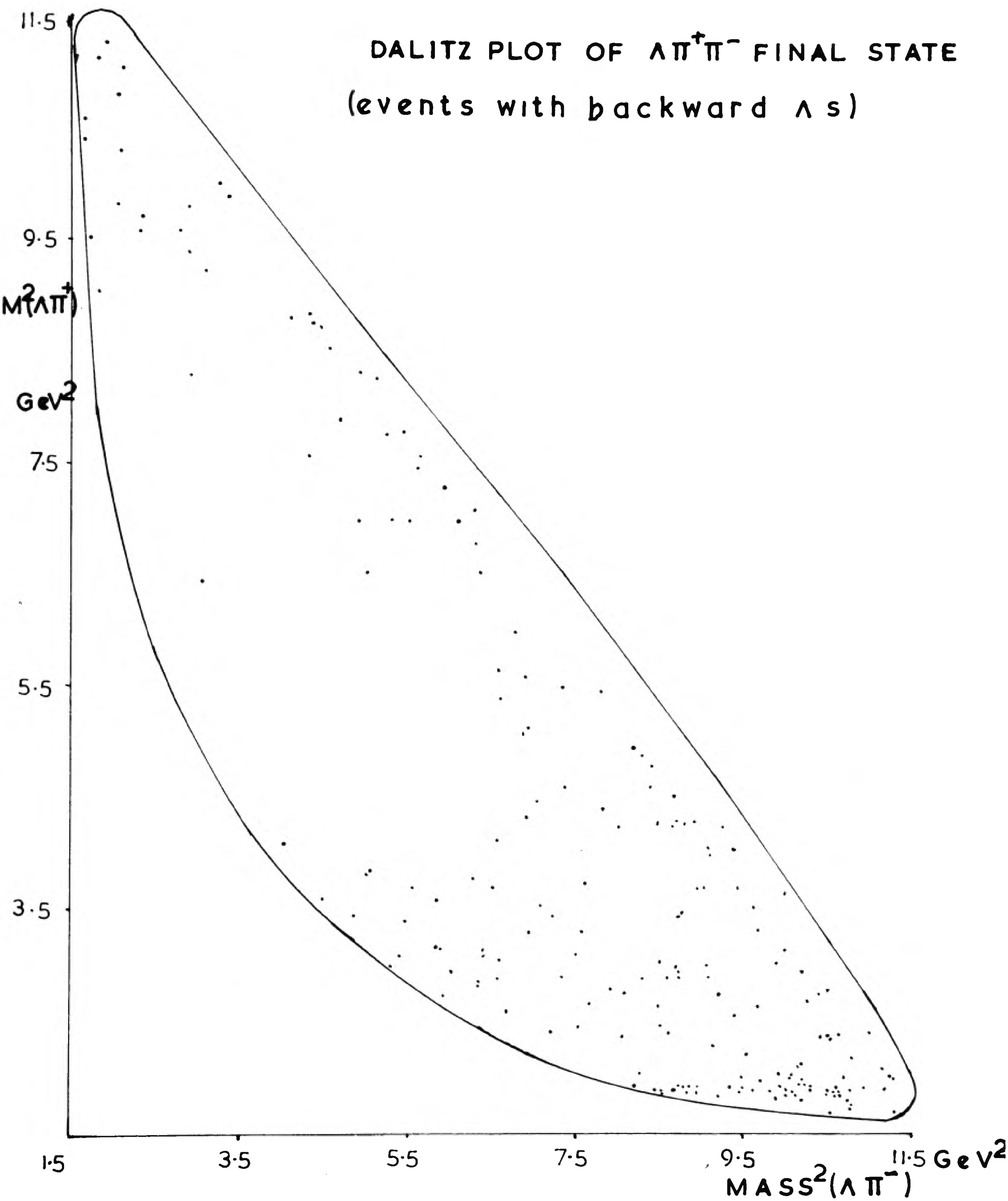
DALITZ PLOT OF $\Lambda\pi^+\pi^-$ FINAL STATE
(events with backward Λ s)
11·5
9·5
$M^2(\Lambda\pi^+)$
GeV^2
7·5
5·5
3·5
1·5
3·5
5·5
7·5
9·5
11·5 GeV^2
$MASS^2(\Lambda\pi^-)$

FIG 5.5

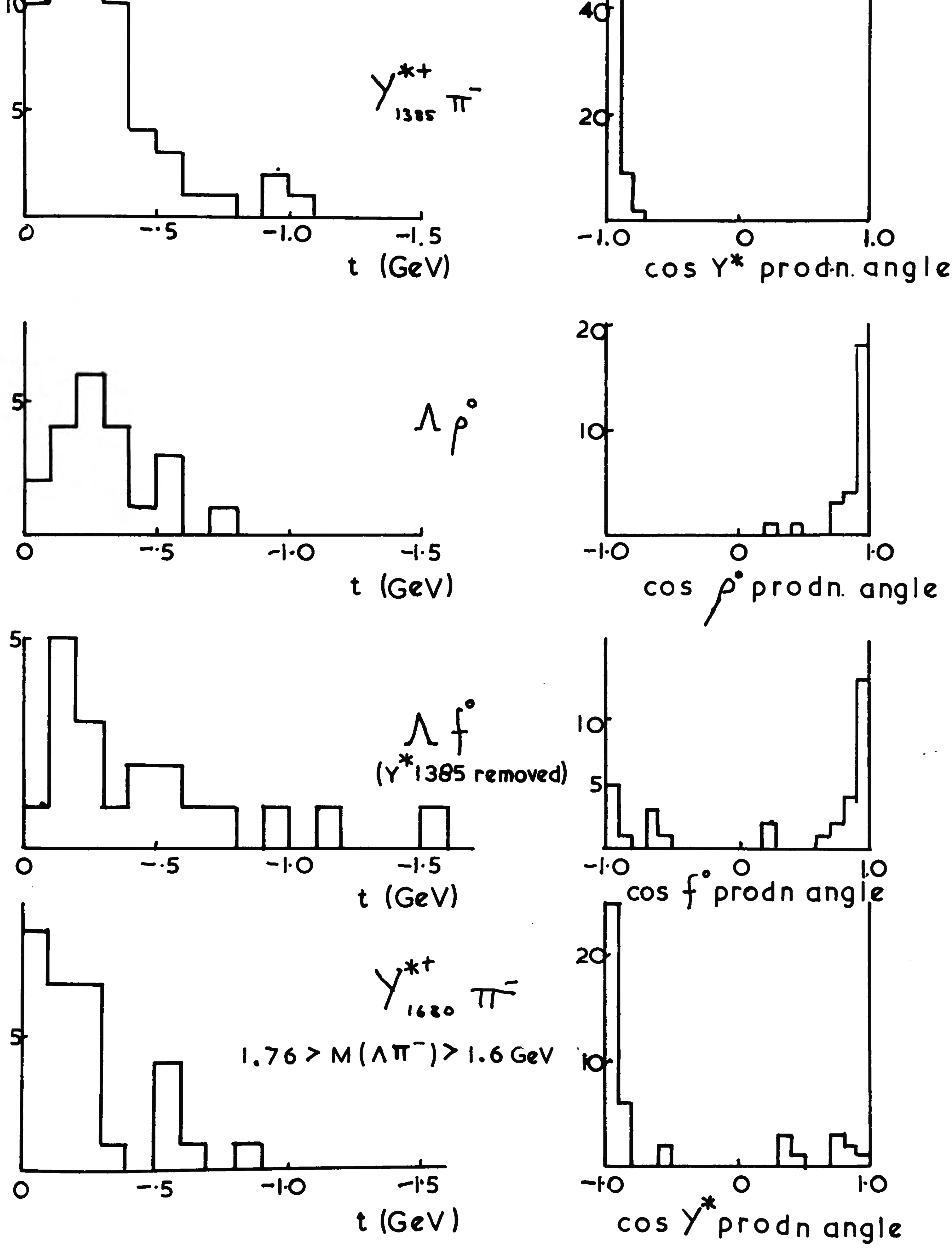
$Y^{*+}_{1385}\pi^-$
t (GeV)
cos Y* prodn. angle
$\Lambda\rho^0$
t (GeV)
cos ρ^0 prodn. angle
Λf^0
(Y*1385 removed)
t (GeV)
cos f^0 prodn angle
$Y^{*+}_{1680}\pi^-$
$1.76 > M(\Lambda\pi^-) > 1.6$ GeV
t (GeV)
cos Y* prodn angle

FIG.5.6.

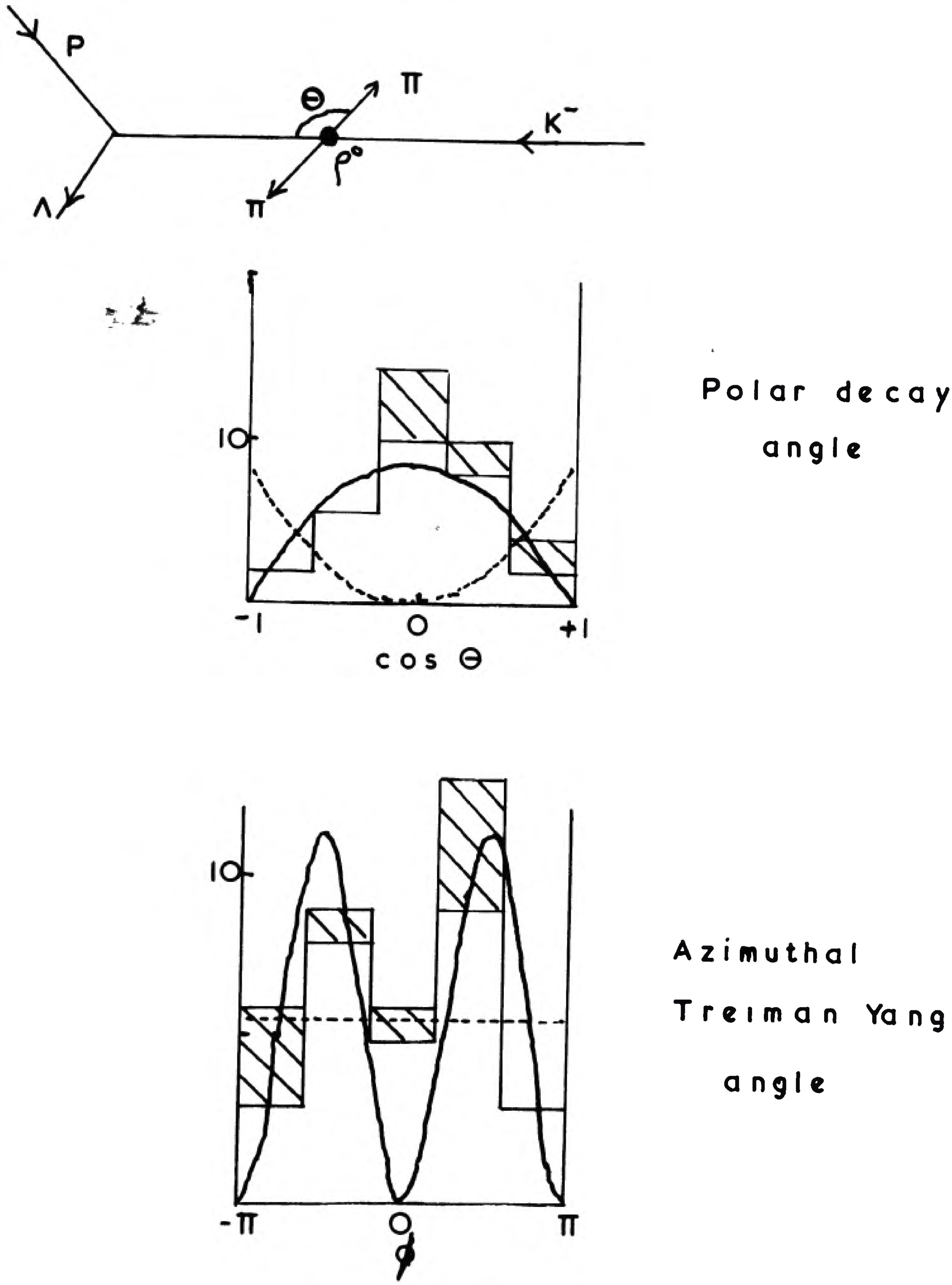

$K^- P \longrightarrow \Lambda^\circ \rho^\circ$

predictions for these are discussed in some detail in terms of the single particle exchange model in appendix F. The solid curves indicate the distributions expected for K^* exchange and the broken lines are for K exchange. The histograms suggest the dominance of K^* exchange while the more detailed analysis in appendix F (see Fig F.1) suggests that the K^* couples to the baryons with spin flip. This process is interesting in that it violates 'A parity' at the top vertex(5). So too does the reaction: $\pi^- p \to \Sigma^0 K^{*0}$ which goes predominantly by K^* exchange(6) and is discussed in appendix G. 'A parity' seems to be a rather poor quantum number.

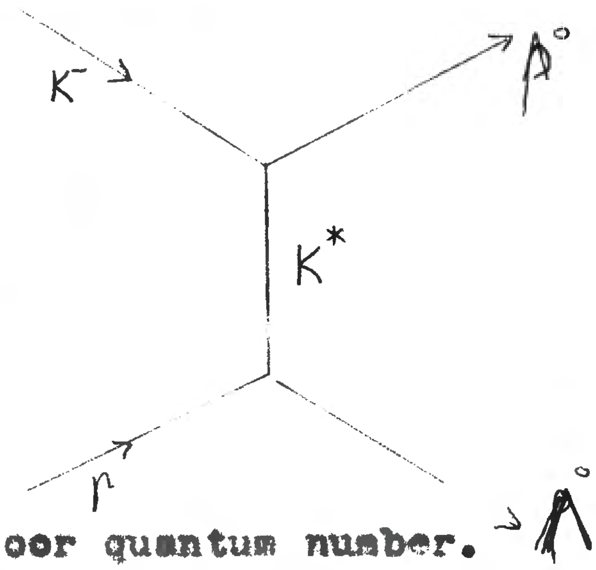

<u>$K^-p \to Y^{*+}(1385)\pi^-$.</u> This channel is quite strong whereas no $Y^{*-}(1385)\pi^+$ is seen. Indeed we can give an upper limit of .6μb for Y^{*-} production. Suppose there was an $I = \frac{3}{2}$ K meson being exchanged; then the $Y^{*-} : Y^{*+}$ cross sections should be 9 : 1 whereas the exchange of $I = \frac{1}{2}$ K mesons forbids Y^{*-} peripheral production. We conclude:

$$\frac{(I = \frac{3}{2}\text{ exchange})}{(I = \frac{1}{2}\text{ exchange})} \leq \frac{1}{20}$$

This is the result expected on the basis of the quark model described in section 3.3.

The spin density matrix of the Y^{*+} is also predicted by the quark model or rather by an extension of it applicable to collinear processes and known as W-spin symmetry[7]. These predictions came originally from a more ad hoc model[8]. First we note that K exchange is strictly forbidden by spin-parity conservation. Secondly a model involving K^* exchange has three independent types of coupling to choose between at the baryon vertex. These may be taken to be the three multipole amplitudes E2, L2 and M1. Stodolsky and Sakurai's original suggestion was that since the ρ meson couples so strongly to the photon may be the $(\rho N N^*)$ and $(\gamma N N^*)$ couplings were the same. The latter is known to be M1 and the $(\rho N N^*)$ and $(K^* N Y^*)$ couplings are related by unitary symmetry.

The quark model prediction does not depend on these extra assumptions. First of all we note N and Y^* are both L = 0 combinations of three quarks. Therefore an $(L = 0) \rightarrow (L = 0)$ transition is involved which is forbidden by E2. W spin symmetry assigns the vector and pseudoscalar K mesons into multiplets thus:

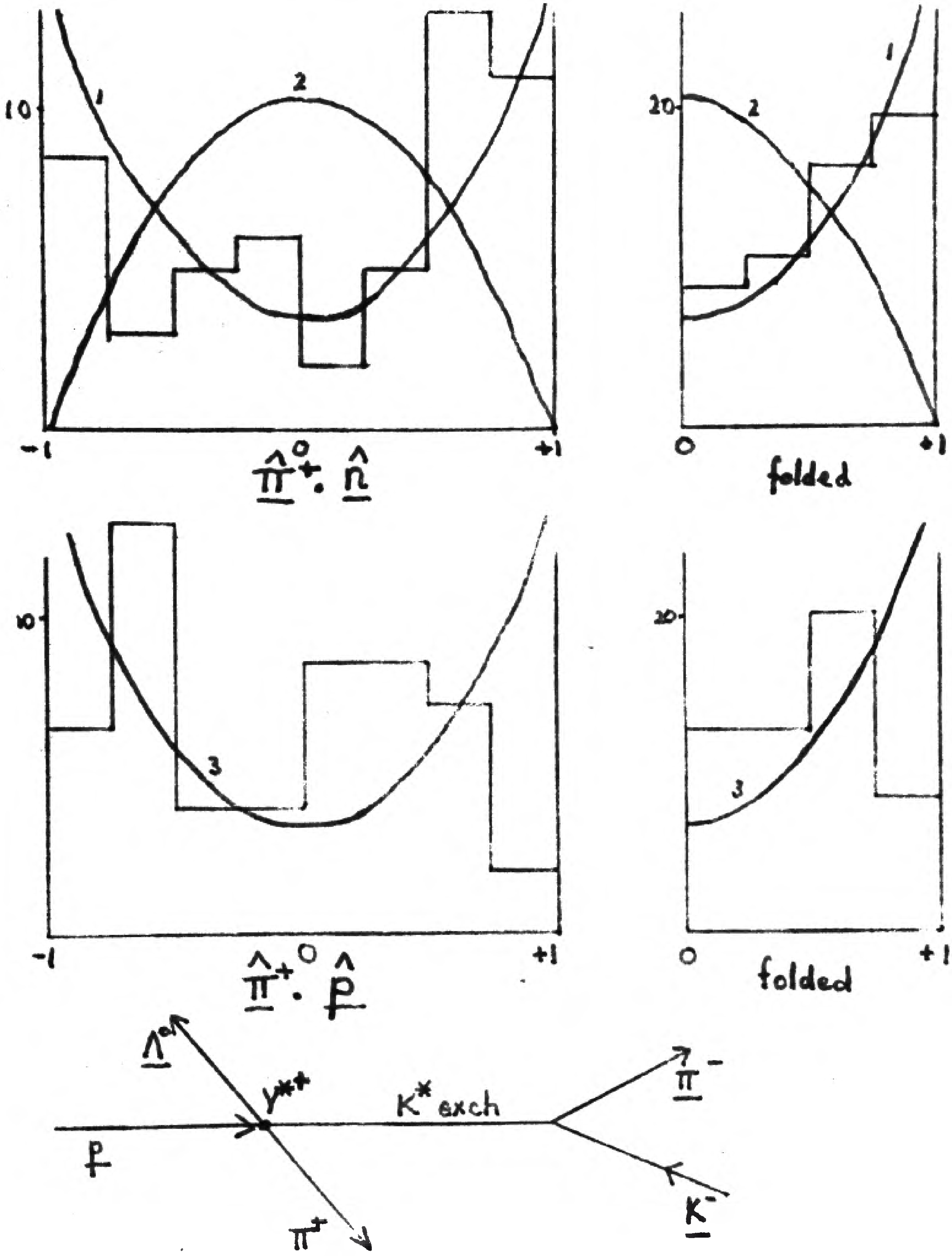

$$\underline{\hat{n}} = \underline{\hat{p}} \times \underline{\hat{K}}^{-}$$

1 Prediction of M1 coupling

2 Prediction of E2 coupling

3 Prediction of L2 coupling

FIG 5.7. DECAY DISTRIBUTIONS OF Y_1^{*+} 1385

	$W_z = -1$	$W_z = 0$	$W_z = 1$
$W = 1$	K^* $(\lambda = -1)$	K	K^* $(\lambda = 1)$
$W = 0$	-	K^* $(\lambda = 0)$	-

where λ is the K^* helicity. The W spin operators commute with the generators of Lorentz transformations in the Z-direction and therefore the symmetry is expected to hold good not only for non relativistic processes but also for collinear relativistic processes (by contrast with the normal spin SU(6) symmetry). Now the W spin of the proton is $\frac{1}{2}$ and of the $Y^*(1385)$ is $\frac{3}{2}$. Therefore coupling with the $W = 0$ state of the (K & K^*) mesons is forbidden. Thus the K^* is coupled as if it did not have a $\lambda = 0$ state - like a photon on the mass shell - this rules out longitudinal multipole transitions. This simple application of W spin was pointed out by the author (among others) to Lipkin who confirmed the argument[9].

The comparison of the theory with the experimental data is shown in Fig 5.7. A slight asymmetry is observed which appears to spoil the fit. The claim that this is probably due to a statistical fluctuation is supported by the fact that the folded plot fits the M1 prediction quite well. The other couplings provide extremely bad fits to the data.

$M^2(\Lambda\pi^+)$ in $K^-p \rightarrow \Lambda\pi^+\pi^-$

for events with $M^2(\pi^+\pi^-) > 1.75$ GeV^2

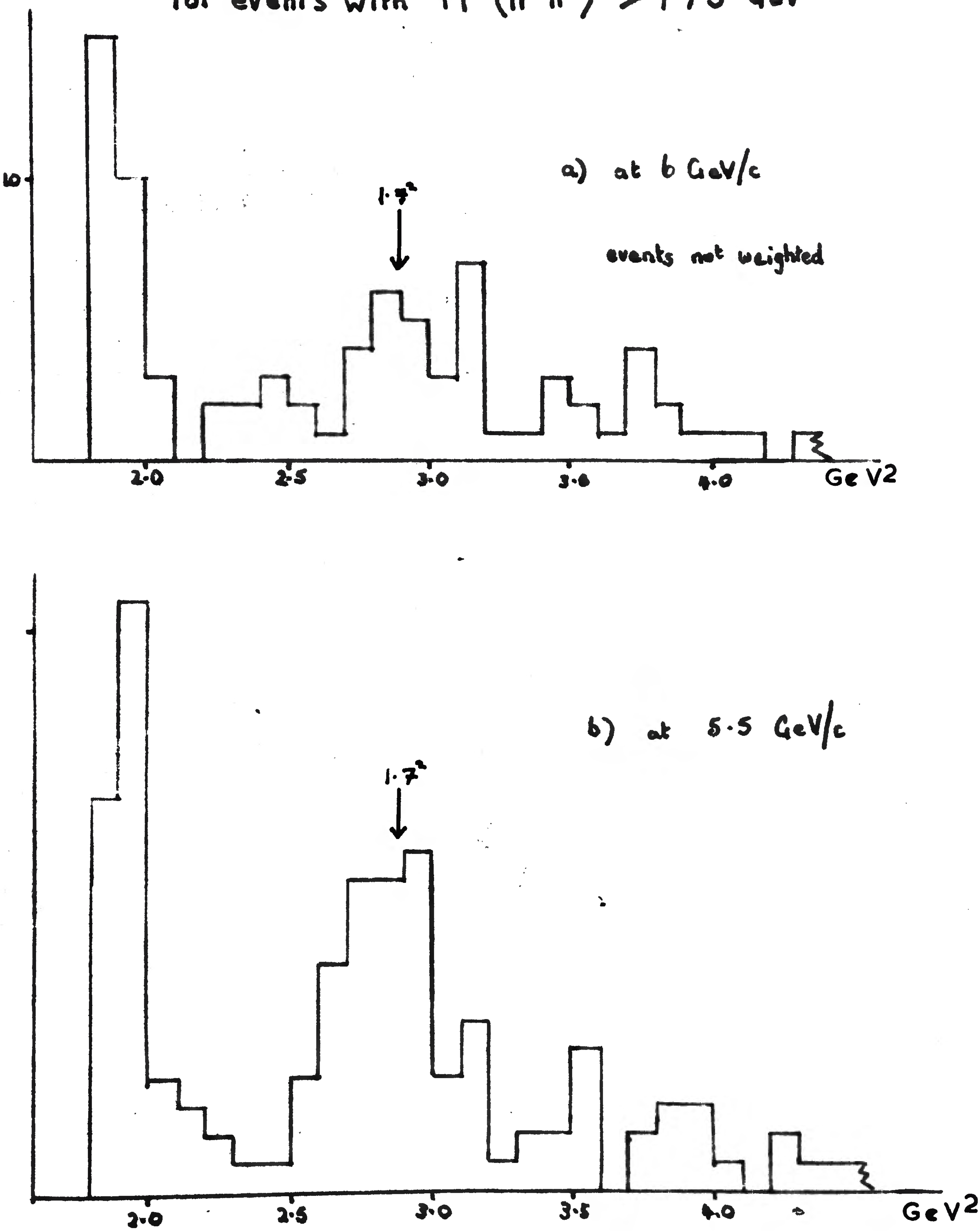

FIG.5.8

$Y_1^*(1680)^+\pi^-$

The $\Lambda\pi^+$ mass spectrum is examined further by excluding events in the ρ^0 and f^0 bands (i.e. taking events with $M^2(\pi^+\pi^-) > 1.75\ GeV^2$). The result is shown in Fig 5.8a.

A broad enhancement is observed between 1.61 and 1.79 GeV. 25 events are seen where 10 are expected. This corresponds to the much more significant enhancement seen at 5.5 GeV/c by the Argonne and Northwestern groups[10]. Their plot corresponding to 5.8a is shown in 5.8b. In Fig 5.9 the invariant mass of $(\Lambda\pi^+)$ is plotted for combinations with momentum transfer (-t) less than .5 GeV^2. Fig 5.10 shows the mass plots corresponding to other possible decay modes. None of them show large enhancements. As pointed out by Argonne the absence of $\Sigma\pi$ and $\Sigma\pi\pi$ decay modes strongly suggests that the enhancement is not the familiar $Y_1^*(1660)$ (for which the mass is too high anyway) but a new Y_1^*. Argonne claim a large branching ratio for this resonance into $Y_1^*(1385)\pi$. In fact examination of their evidence shows the presence of a bump in M $(\Lambda\pi\pi)$ at about 1700 MeV. The low Q value of this decay mode coupled with the width of $Y_1^*(1385)$ and its low Q value means that most events will have at least

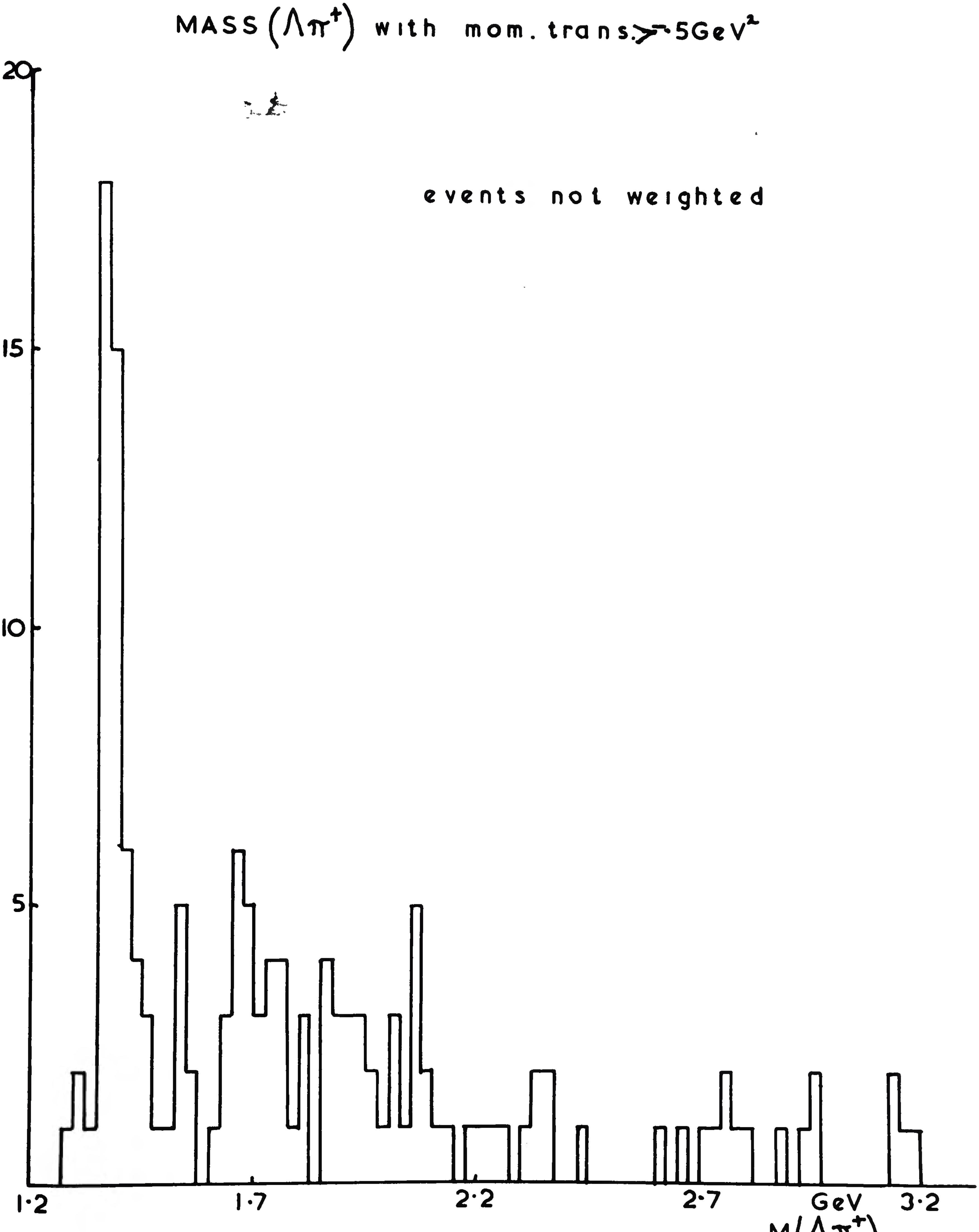

MASS ($\Lambda\pi^+$) with mom. trans. > .5GeV^2
events not weighted
20
15
10
5
1·2
1·7
2·2
2·7
GeV
3·2
M($\Lambda\pi^+$)

FIG. 5.9.

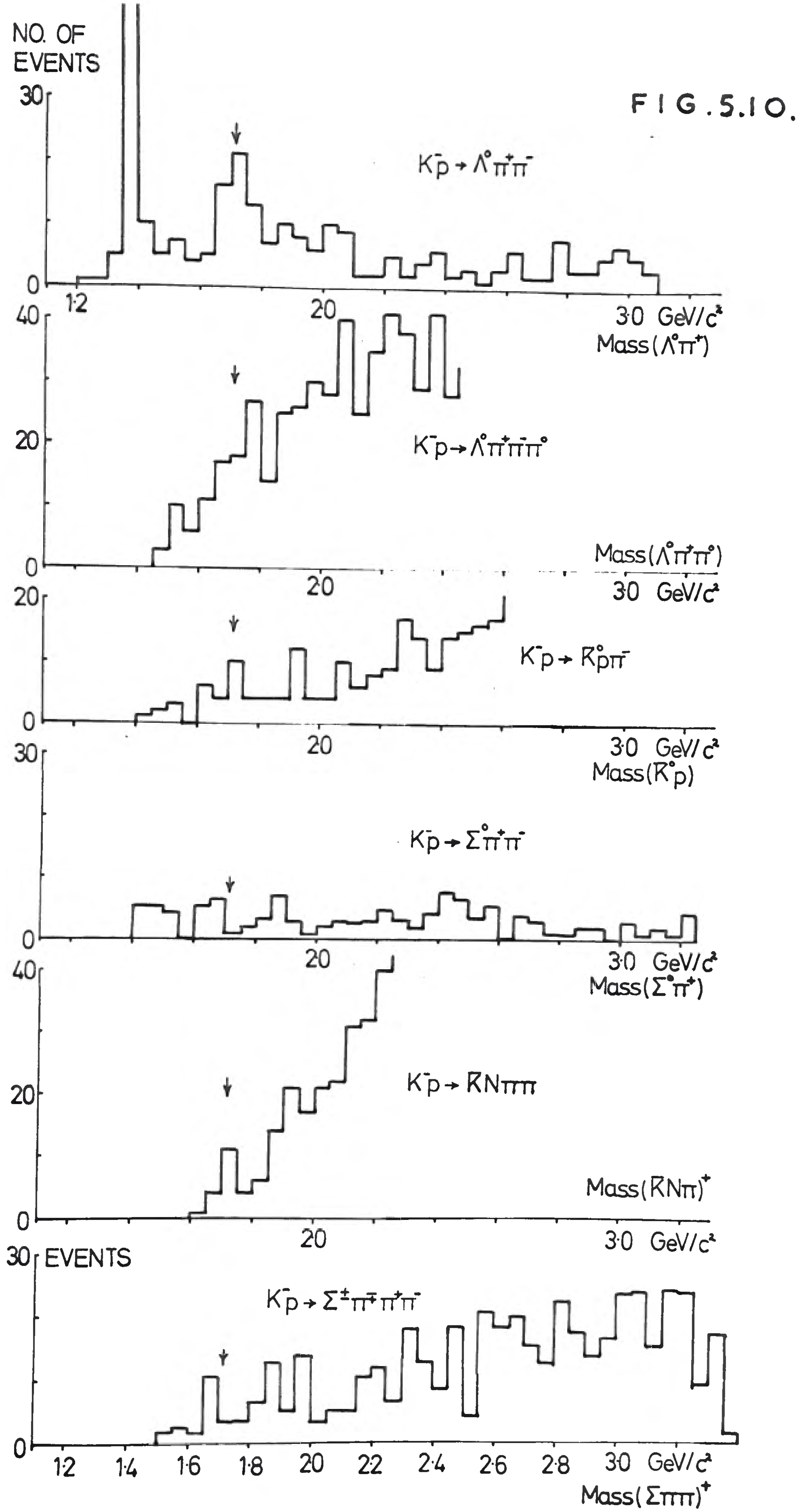

FIG. 5.10.
NO. OF EVENTS
K⁻p → Λ°π⁺π⁻
Mass(Λ°π⁺)
K⁻p → Λ°π⁺π⁻π°
Mass(Λ°π⁺π°)
K⁻p → K̄°pπ⁻
Mass(K̄°p)
K⁻p → Σ°π⁺π⁻
Mass(Σ°π⁺)
K⁻p → K̄Nππ
Mass(K̄Nπ)⁺
EVENTS
K⁻p → Σ±π∓π⁺π⁻
1·2
1·4
1·6
1·8
2·0
2·2
2·4
2·6
2·8
3·0 GeV/c²
Mass(Σππ)⁺

one ($\Lambda\pi$) combination in the 1385 MeV region. Their statement that 40% of the selections $Y^{*0}_{1385}\pi^{+}$ and $Y^{*+}_{1385}\pi^{0}$ overlapped indicates that on the basis of the data shown in their letter they are not in a position to distinguish whether the $Y_1^*(1700)$ decays through $Y_1^*(1385)$ or not. The best values for the mass and width of the feature in our data[11] are $M = 1715 \pm 12$ MeV and $\Gamma_{exp} = 100 \pm 35$ MeV compared with the Derrick result of $M = 1683(\pm 15)$ MeV.

<u>The forward [illegible]</u>

The events with forward Λs have a uniform distribution over the Dalitz plot. There is no indication either of hyperon or meson resonances. In particular there is no backward ρ^0 which Derrick claims to see ~~ff~~[12].

The cross sections for the $\Lambda\pi\pi$ final state are summarised in table 5.3

<u>TABLE 5.3</u>

<u>$\Lambda\pi^{+}\pi^{-}$ final state</u>

Λ(forward) $\pi^{+}\pi^{-}$	13 ± 3 μb
Λ(backward) $\pi^{+}\pi^{-}$	52 ± 11 μb
$Y^{*+}(1385)\ \pi^{-}$	13 ± 3 μb
$\Lambda\rho^{0}$	10 ± 3 μb
Λf^{0}	6 ± 2 μb
$Y^{*+}(1700)\ \pi^{-}$	6 ± 2 μb

Fig. 5.11. Longitudinal momenta in $\Lambda\pi^+\pi^-\pi^0$ for events with forward Λs.

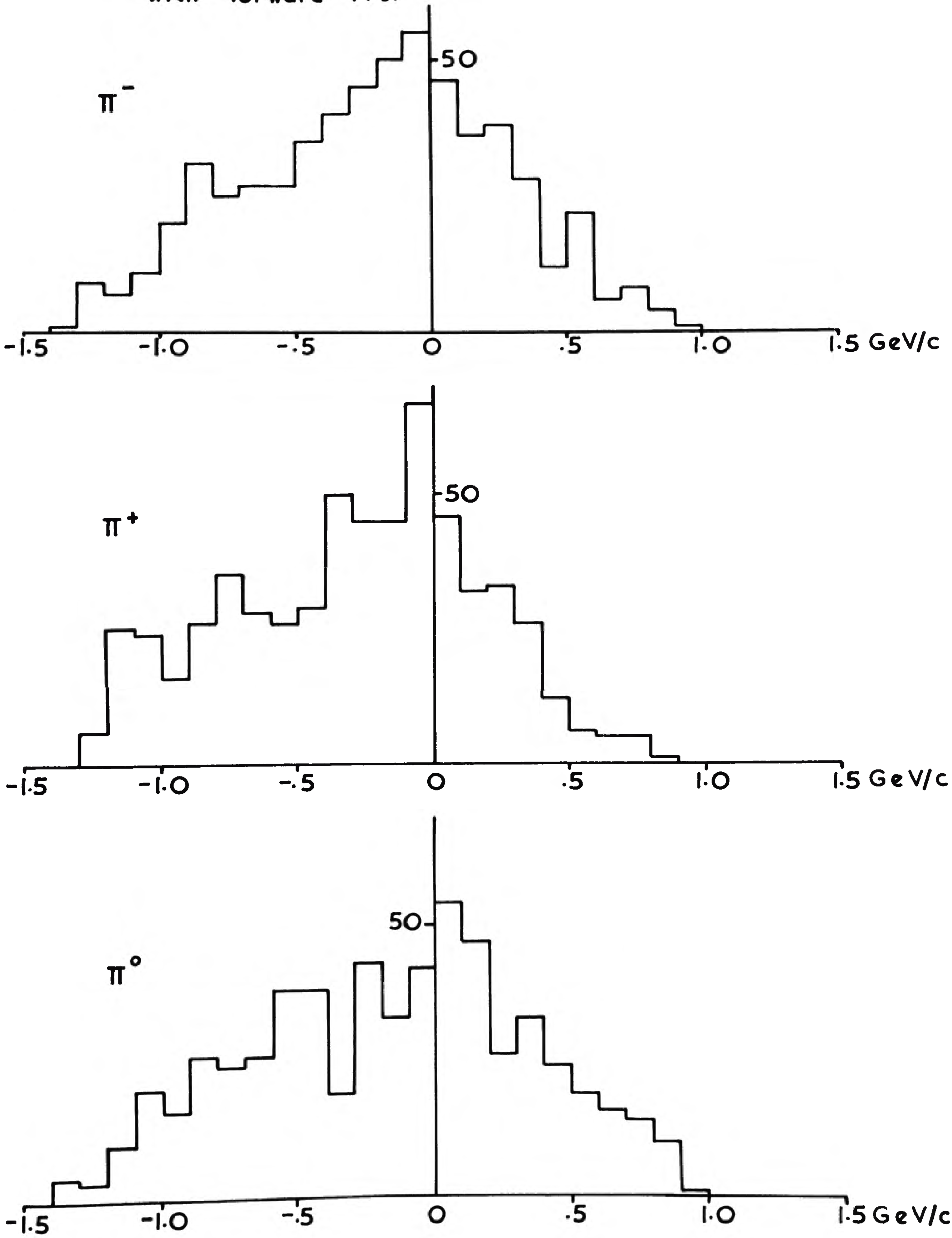

5.4 $\Lambda\pi^+\pi^-\pi^0$ final state

The separation between events with Λ in the forward hemisphere and those with Λ in the backward hemisphere is relatively clean as can be seen from Fig 5.1. 36% of the events with backward Λs involve resonance production but only 8% of those with forward Λs contain traces of resonances - in fact the cross sections for non resonant $\Lambda\pi^+\pi^-\pi^0$ are almost equal in the forward and backward hemispheres.

Backward Λ events

These have been discussed extensively elsewhere[13] and we have nothing further to add.

Forward Λ events

The longitudinal momenta of the particles in the total centre of mass is plotted in Fig 5.11 for the events with forward Λs. A slight backward peak for the π^+ is evident. Assuming that a pion is produced at low momentum transfer from the proton this suggests that the contribution due to $I = \frac{1}{2}$ exchange (nucleon) is more important than that due to $I = \frac{3}{2}$ exchange ($N^*(1238)$). This is shown in table 5.4.

TABLE 5.4

Charge of peripheral pion	Square of C.G. coefficient at top vertex for $I = \frac{1}{2}, \frac{3}{2}$ exchange		No. of πs with $-p_L^* > 1$ GeV/c
+	.667	.167	55
0	.333	.333	37
-	0.0	.500	28

Let us suppose that a Y^* resonance of isospin 2 exists. The orbital quark model(14) suggests that such states will not be found - it is therefore interesting to look for one. We assume that it is produced by an exchange process together with a pion and decays into $\Lambda\pi\pi$. It should therefore be observed in the $\Lambda\pi\pi\pi$ final state. I spin conservation demands that an $I = \frac{3}{2}$ object is exchanged. It would therefore be produced by N^* exchange and appear as an enhancement in forward going $(\Lambda\pi\pi)$ mass combinations. Furthermore since the total isospin of the state must be one

Invariant mass plots for combinations produced forwards ($\cos\Theta > .75$). $\Lambda\pi^+\pi^-\pi^0$ final state.

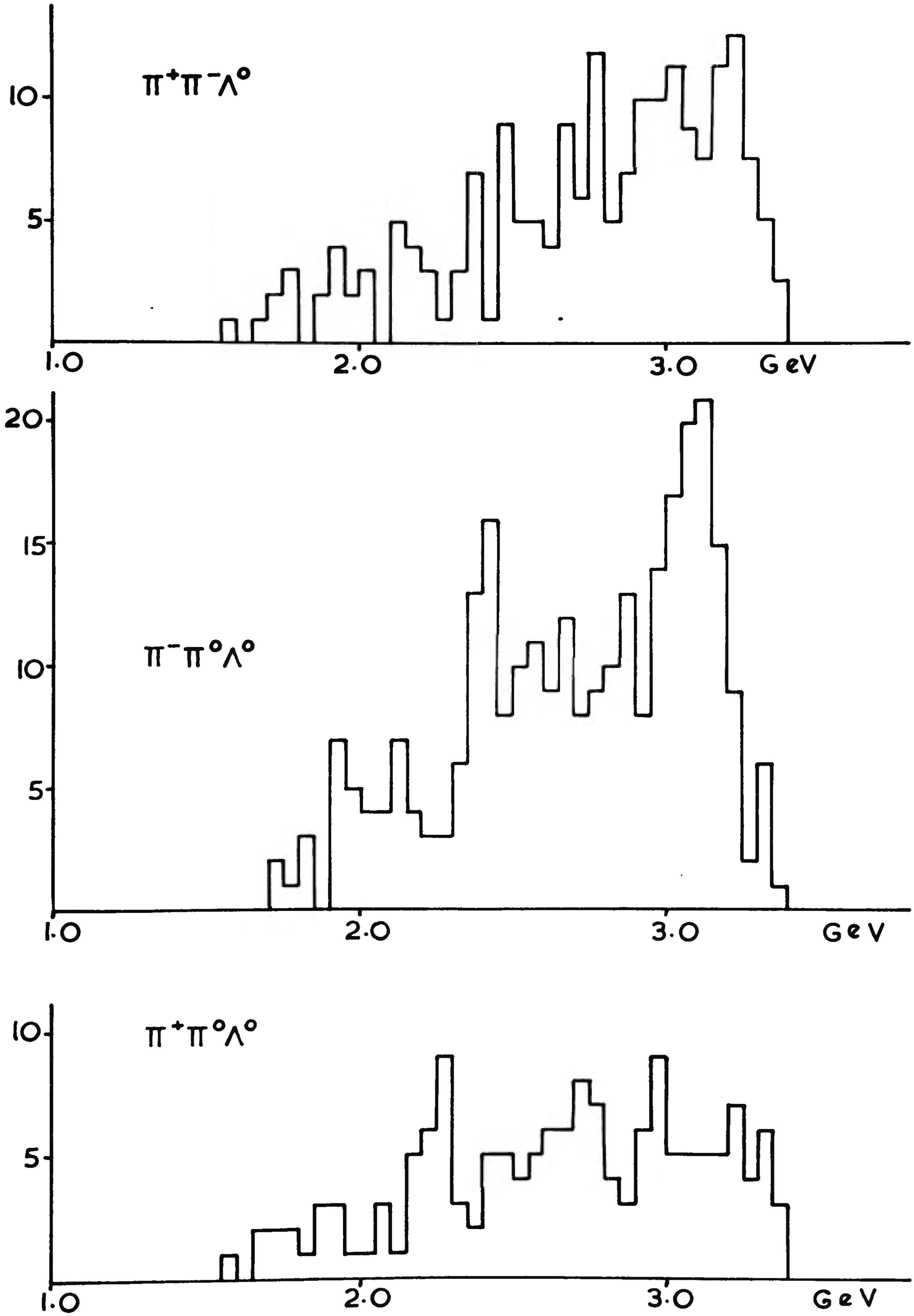

Fig. 5.12.

the charge ratios in which it should be produced may be computed exactly. The squared Clebsch Gordan coefficients give us:

$$Y_2^{*+} : Y_2^{*o} : Y_2^{*-} = 3 : 4 : 3$$

Fig 5.12 shows the mass plots for the three charge states of $\Lambda\pi\pi$ with cos $\theta^* > .75$. Our theory demands that any feature due to Y_2^* should appear in all plots - no such feature is observed.

The spectra of forward ($\Lambda\pi$) combinations have also been examined for evidence of I = 1 Y^*s produced by baryon exchange. None was found.

The only other feature of the events with forward Λ is the ω. This has been discussed elsewhere[13].

5.5 Lambda and four pions final state

The problem of isolating resonance contributions to multibody final states is complicated by three factors:

1) The appearance of each event two or four times in each plot - this amounts to an artificial increase of the "background" to any effect by a factor of two or four.

2) The general lack of precise dynamical properties associated with any resonance production. This means that

not only are the figures for the various resonance channels extremely hard to obtain but also it is very unclear what, if anything, can be deduced from them in our present state of knowledge. An approach to this problem for the special case of three body final states is the subject of chapter 6.

3) The very large number of variables that can be plotted. Thus considerable thought has to be given to what to plot and how to plot it. Much worse, since at least fifty plots are examined per final state the number of bins examined is of the order of thousands. Now the odds against even a three standard deviation effect are only 370:1. Therefore in looking for resonances we require effects to be at least 2½ standard deviations (1%) and to appear either in more than one final state or with precise dynamical properties (e.g. very low momentum transfer) or corresponding to well known resonances (ρ, ω, Y^* etc). Other three standard deviation effects are pointed out and, if no explanation is forthcoming, ignored.

The approach taken here is as follows. Since a large fraction of the baryons are produced in the forward or backward cones, the production dynamics is a function of

FIG. 5.13

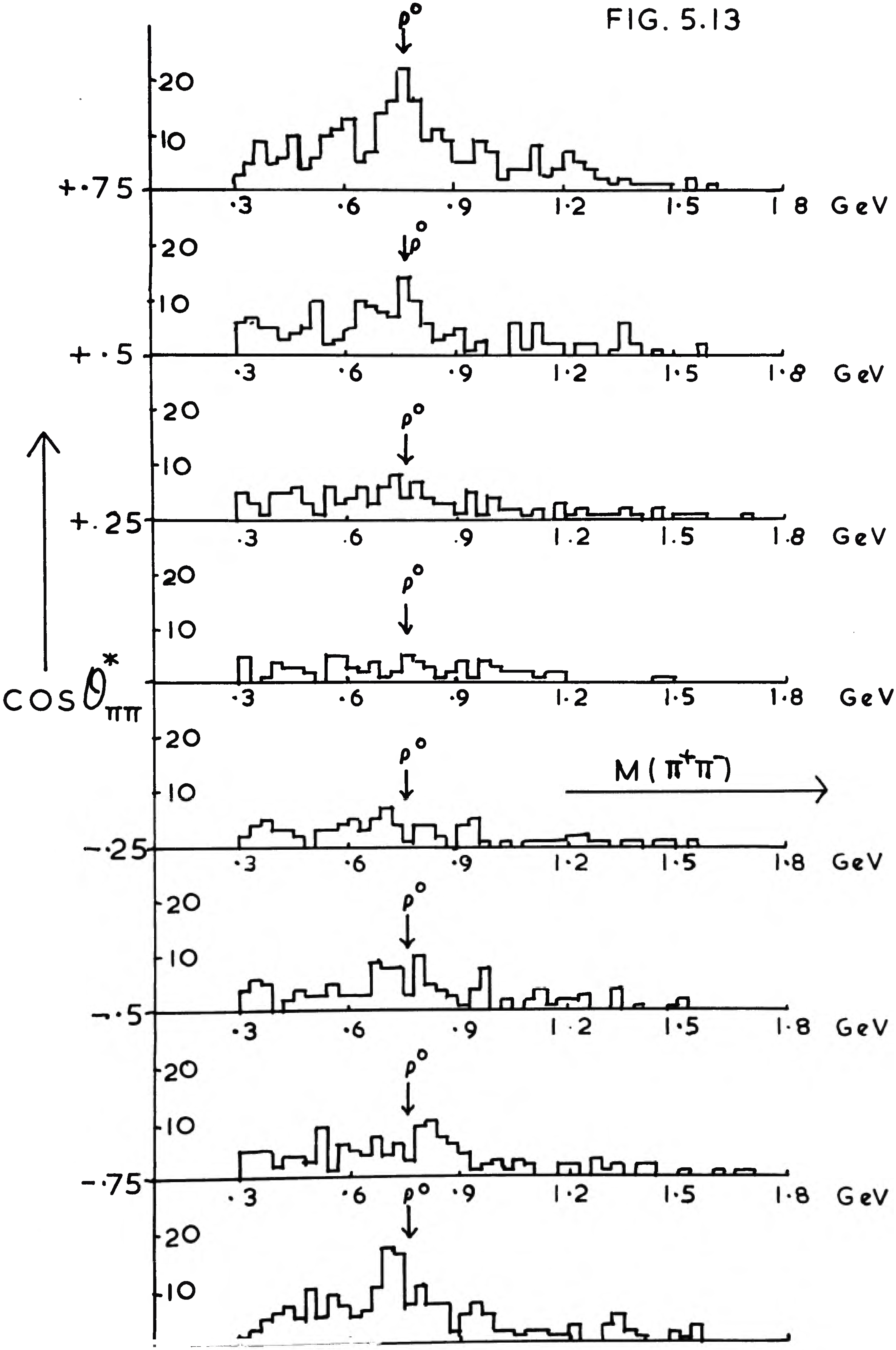

$\cos\theta^*$ (if nothing else). No other comparable general feature of the dynamics is seen. Since the decay of resonances can only tend to blur this angular dependence, we suppose that most resonances are produced peaked either forward or backward - irrelevant mass combinations on the other hand will tend to have a smoother production angle distribution. To take advantage of this scatter plots were made of the invariant mass of each particle combination against the centre of mass production angle of the combination. "Angle slices" of these plots showed the presence of resonances in the forwardmost and backwardmost "slices" and their general absence in between. Fig 5.15 shows a series of such slices for the $(\pi^+\pi^-)$ combination. Each event is plotted four times. Strong ρ^0 production is seen when $\cos\theta^*(\pi^+\pi^-)$ is greater than .75 or less than -.75. The very large number of such plots makes it impossible to show them all. Only the more interesting projections are reproduced here. The other $\pi\pi$ plots ($\pi^+\pi^+$ and $\pi^-\pi^-$) are featureless.

The $(\Lambda\pi)$ plots are dominated by the production of $Y^{*+}(1385)$. The angular distribution of this is peaked sharply backwards (see Fig 5.2). The mass spectrum of the most backward $(\Lambda\pi^+)$

MASS OF $(\Lambda\pi^+)$ FROM $\Lambda 4\pi$ FINAL STATE

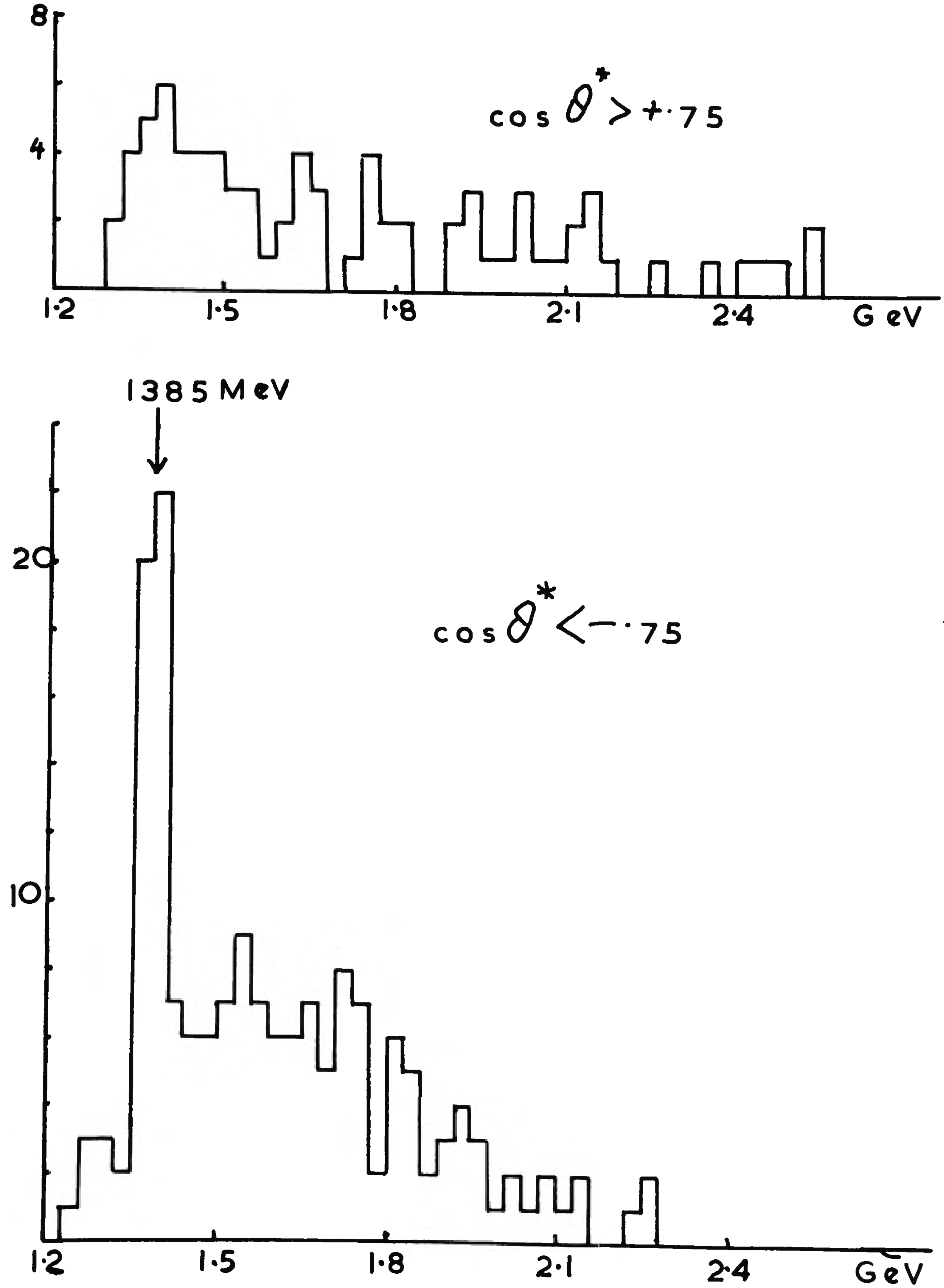

FIG 5.14.

MASS OF $(\Lambda\pi^-)$ FROM $\Lambda 4\pi$ FINAL STATE

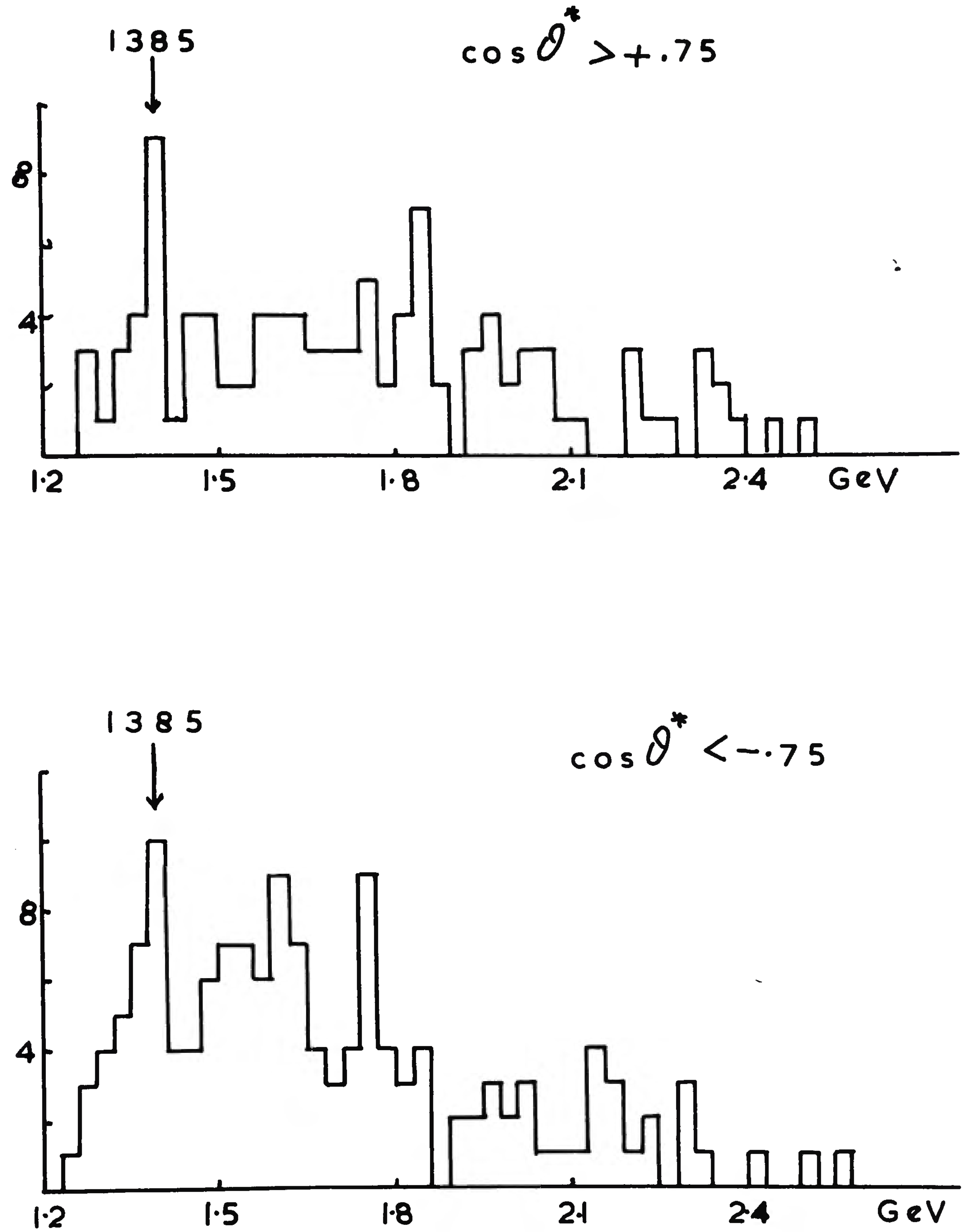

FIG.5.15.

$\Lambda 4\pi$ FINAL STATE

301×2 events

Shaded events for $M(\rho^0\pi^-)$

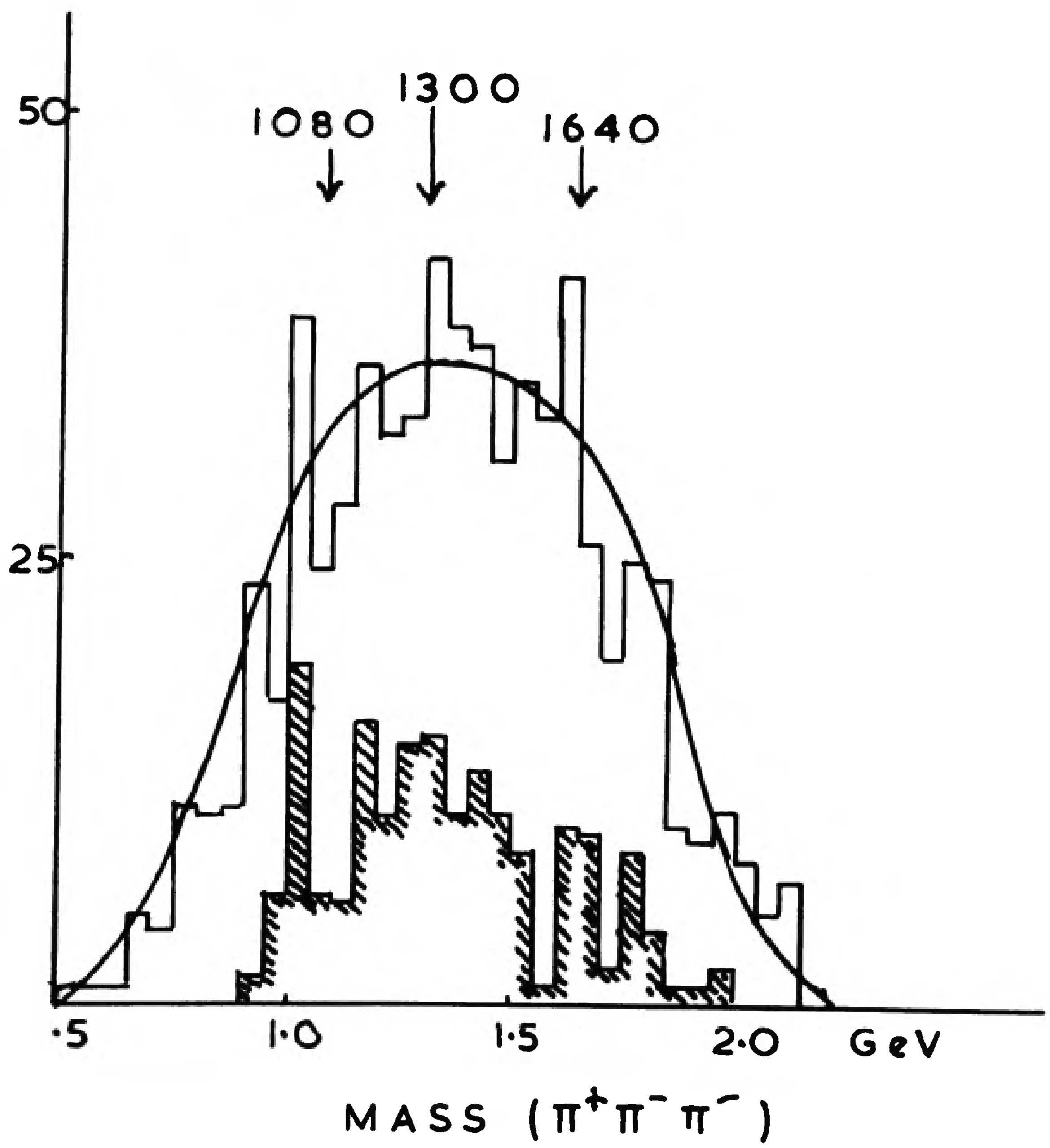

FIG.5.16.

$\Lambda 4\pi$ FINAL STATE

301×2 events

Shaded events for $M(\rho^\circ \pi^+)$

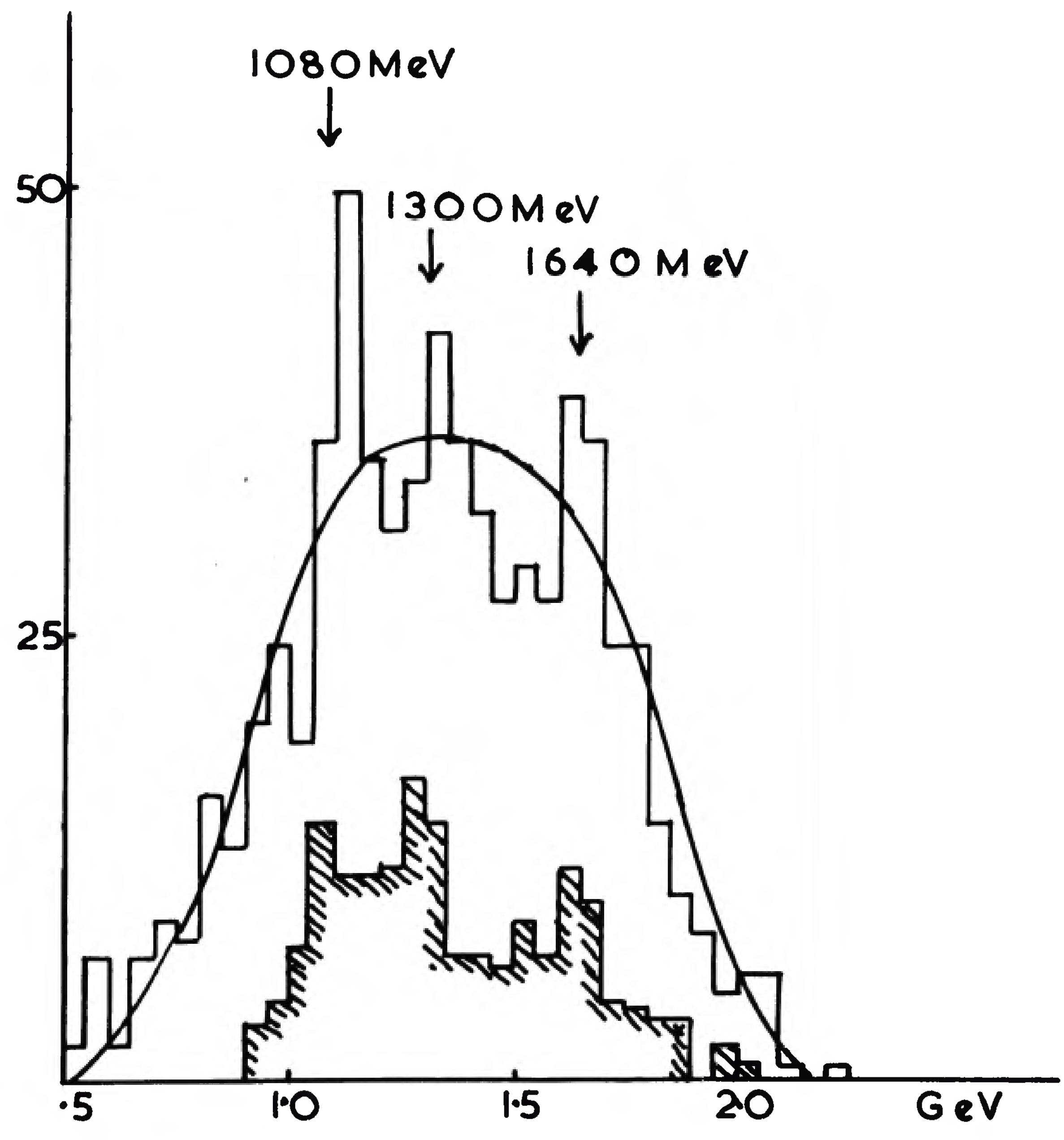

FIG. 5.17.

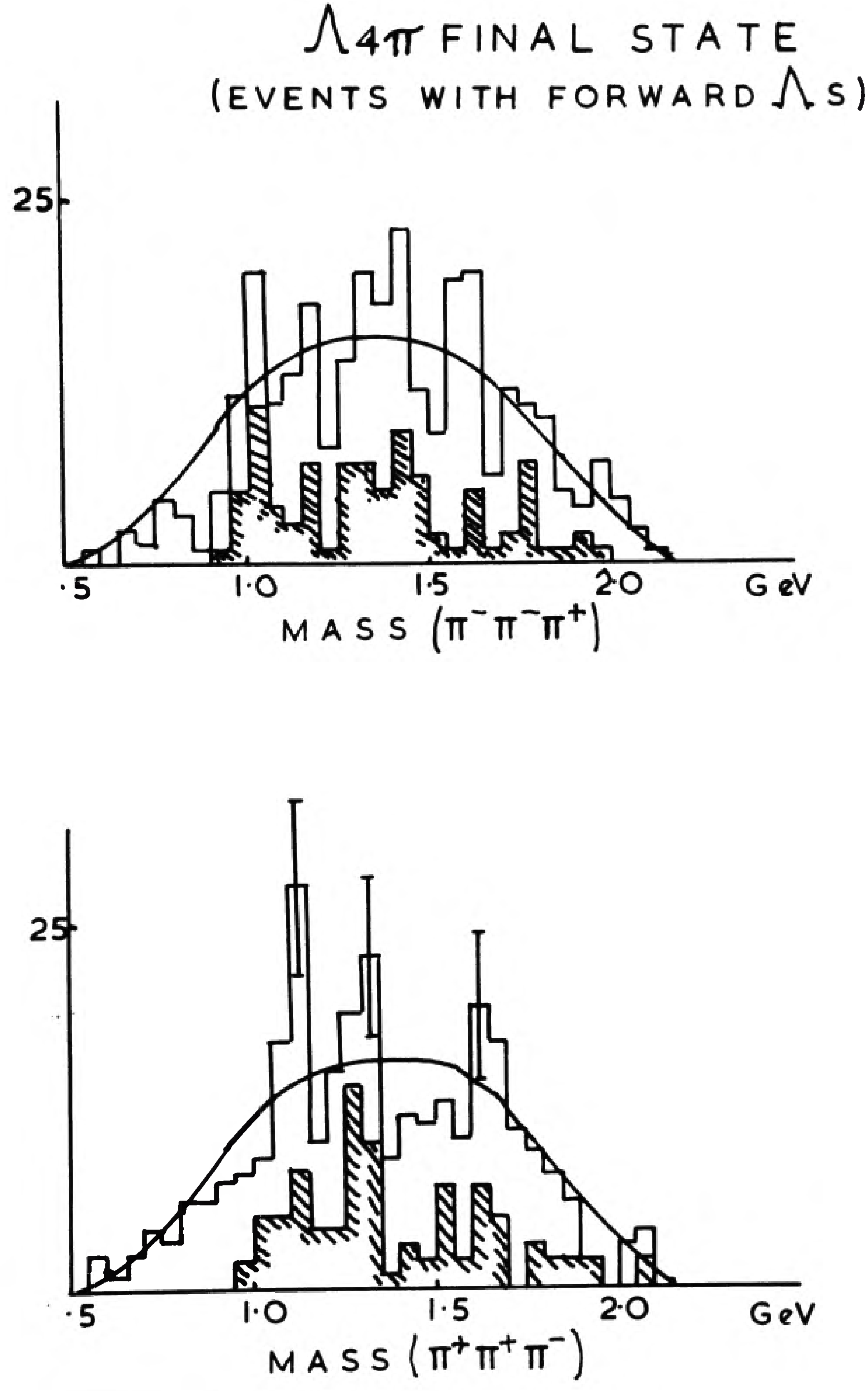

$\Lambda 4\pi$ FINAL STATE
(EVENTS WITH FORWARD Λs)
25
·5
1·0
1·5
2·0
GeV
MASS $(\pi^-\pi^-\pi^+)$
25
·5
1·0
1·5
2·0
GeV
MASS $(\pi^+\pi^+\pi^-)$

FIG.5.18.

slice is shown in Fig 5.14. The absence of the forward Y^* peak is clear from the mass plot of the forward slice also shown in Fig 5.14. No correlation was found between the production of ρ^0 and $Y^{*+}(1385)$ nor was there any evidence of the simultaneous production of two ρ^0s. Fig 5.15 shows the spectra of $\Lambda\pi^-$ - there is some indication of $Y_1^{*-}(1385)$ in both the forward and backward directions. The appearance of a slight enhancement in the region of 1765 MeV is probably spurious since this resonance does not appear in the positive charge state.

Figs 5.16 and 5.17 are the spectra of 3π masses. Each event is plotted twice - the shaded events are combinations of which a $(\pi^+\pi^-)$ pair has mass in the ρ^0 region (690 - 840 MeV). The curves drawn are the expectations of phase space normalised to the total number of events.

In the positive charge combinations there are three marked peaks above the phase space curve. This is made more dramatic by selecting events with forward Λ s only. The result is plotted in Fig 5.18. The three peaks are:

<u>1110 MeV</u>. This is consistent with the A_1. Its experimental width is about 100 MeV. There is an

excess of 25 events above a background of 20. Its correlation with ρ^0 does not look so good - less than half of these 25 contain ρ^0. The presence of a one bin ρ^0 correlated peak in the $(3\pi)^-$ mass spectrum at 1000 - 1050 MeV may be a fluctuation - certainly it is not correlated with the Λ angular distribution.

<u>1300 MeV</u>. This is consistent with the A_2. Its experimental width is about 100 MeV. There is an excess of some 20 events above 24 background. It shows strong correlation with ρ^0 and is consistent with pure $\rho^0\pi^+$ decay. This supports its identification with $A_2(1300)$.

<u>1640 MeV</u>. This is consistent with π (1640) state seen in πp collisions[15]. The apparent correlation with ρ^0 production could be due to the large ρ^0 background. No evidence that this state decays into $(\rho\pi)$ has been given before[16].

There is some evidence that the (1300) and (1640) effects are also produced in the negative charge state as can be seen from Fig 5.16. The selection of forward Λ s does not enhance the effects in the negative charge state.

The statistics of this channel are too low to investigate these features further. However we note:

1) The A_1 meson has only been observed before in reactions of the type: $\pi p \to \pi \pi \pi p$ where distortion of the (3π) mass spectrum by the "Deck" effect has thrown doubt on the interpretation of the peak at 1080 MeV as a resonant state[17]. On the basis of the $\Lambda 4\pi$ data alone the evidence for A_1 looks tenuous - especially in view of its rather weak correlation with ρ. However its appearance also in $\Lambda 5\pi$ removes any further doubt. It is interesting to not that $A_1^{\pm}$ (1080) was seen in $\Lambda 4\pi$ final state at 3.5 GeV/c[18]. Added together the two charge states gave a four standard deviation effect - again no correlation with ρ was seen.

2) The appearance of these resonances in the <u>positive</u> charge state with <u>forward</u> Λs suggests that the anomalous hyperon angular distributions in the $\Lambda 4\pi$ and $\Lambda 5\pi$ final states may be associated with the production of higher spin meson resonances in general. In section 5.7 we discuss a similar effect in the $\Lambda 5\pi$ final state.

$\Lambda 4\pi$ FINAL STATE

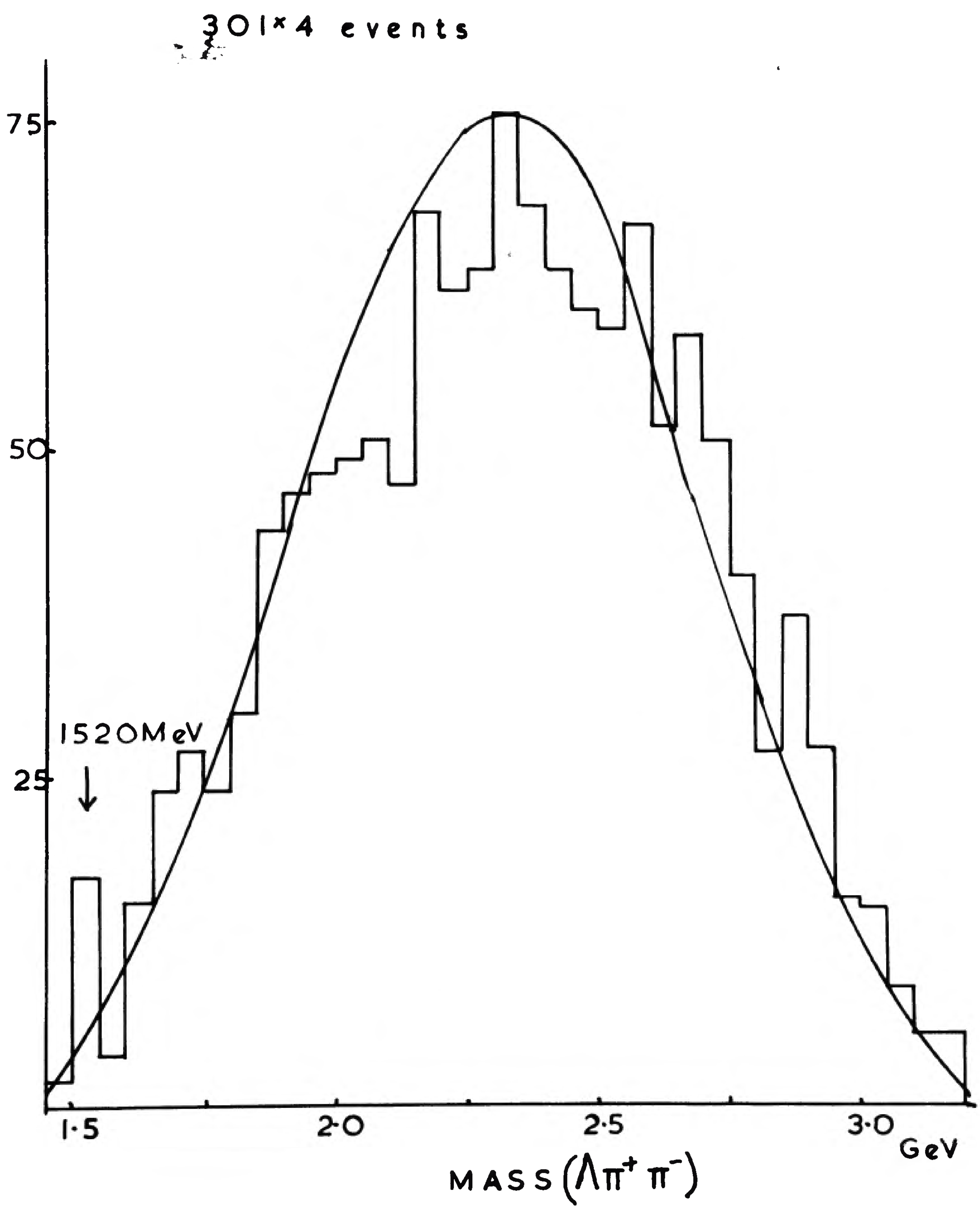

FIG. 5.19.

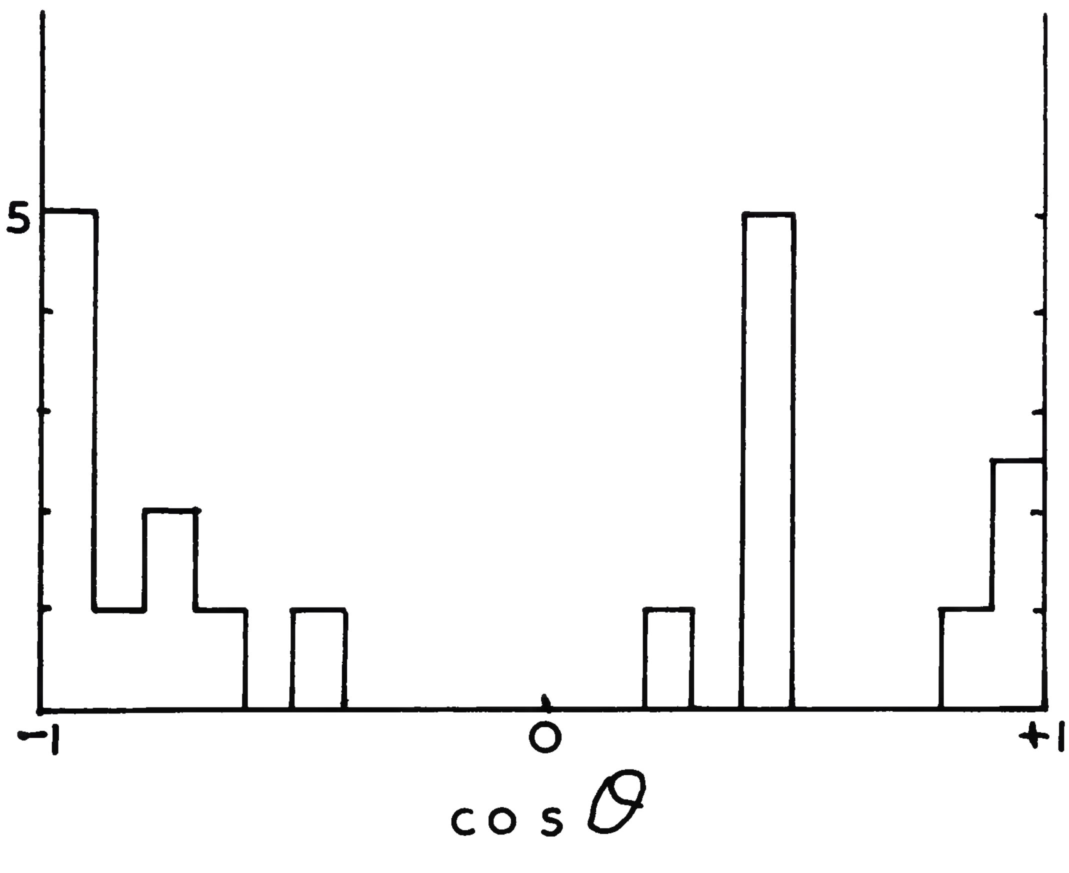

'roduction angle of $Y_0^*(1520)$ in $\Lambda 4\pi$ final state

FIG.5.20.

TABLE 5.5

$\Lambda 4\pi$ final state

		Cross section	Resonance decay mode seen
Total	$\Lambda\pi^+\pi^-\pi^+\pi^-$	107 ± 20 μb	
	$\Lambda\pi^+\pi^-\rho^0$	50 ± 20 μb	$\rho^0 \rightarrow \pi^+\pi^-$
	$Y^{*+}(1385)\pi^-\pi^+\pi^-$	32 ± 10 μb	$Y_1^{*+} \rightarrow \Lambda\pi^+$
	$Y^{*-}(1385)\pi^+\pi^+\pi^-$	17 ± 10 μb	$Y_1^{*-} \rightarrow \Lambda\pi^-$
	$Y^*(1520)\pi^+\pi^-$	16 ± 6 μb	$Y_0^* \rightarrow \Lambda\pi^+\pi^-$
	$\Lambda\pi^+A_1(1080)^-$	10 ± 10 μb	$A_1^- \rightarrow \rho^0\pi^-$
	$\Lambda\pi^+A_2(1300)^-$	10 ± 10 μb	$A_2^- \rightarrow 3\pi$
	$\Lambda\pi^+\pi\ (1640)^-$	10 ± 10 μb	$\pi(1640)^- \rightarrow 3\pi$
	$\Lambda\pi^-A_1(1080)^+$	9 ± 3 μb	$A_1^+ \rightarrow 3\pi$
	$\Lambda\pi^-A_2(1300)^+$	8 ± 3 μb	$A_2^+ \rightarrow \rho^0\pi^+$
	$\Lambda\pi^-\pi\ (1640)^+$	6 ± 3 μb	$\pi(1640)^+ \rightarrow 3\pi$ or $\rho\pi$?

The mass spectrum of ($\Lambda\pi^+\pi^-$) is shown in Fig 5.19. The only significant departure from the phase space curve is the appearance of $Y_0^*(1520)$ - its production angle is shown in Fig 5.20. It does not appear to be produced peripherally.

The invariant mass distributions of all other combinations were also examined as a function of production angle, lambda direction and association with the $Y^{*+}(1385)$ and ρ^0 features. No other significant enhancements were observed.

The $\Lambda 4\pi$ channel is summarised in table 5.5. The quoted errors take into account the large uncertainties in background subtraction.

5.6 Sigma zero and four pions final state

Table 2.3 shows that the cross section for the $\Sigma^0 4\pi$ final state is only 34 ± 8 μb as calculated from the Oxford data. This of course is the cross section for four charged pions. As in table 5.2 we can guess the $\Sigma^0 4\pi$ cross section for all π charge states using the statistical model(4). Multiplying by factor 3.2 we get

$$111 \pm 25 \ \mu b.$$

We compare this later with the $\Sigma^{\pm}4\pi$ cross sections. Note that $\Sigma^{0}\pi^{+}\pi^{-}\pi^{+}\pi^{-}$ cannot contain either $Y_0^*(1405)$ or $Y_0^*(1520)$ which are the main resonance channels in the $\Sigma^{\pm}4\pi$ final states. It follows that we expect the visible cross section to be small. Consequently the total number of events (67) is insufficient to show any interesting features.

5.7 <u>The lambda and five pions final state</u>

<u>$\eta'(958)$</u>. Fig 5.21 shows the mass spectrum of the five pions. The shaded events are those with forward hemisphere lambdas (i.e. backward going 5π combinations). The $\eta'(958)$ is completely isolated from the background. The poor mass resolution of this experiment is evident from the resolution of the width of this feature which is known to be less than 4 MeV. It is produced at very low momentum transfer to the K^-. Its decay to $\pi^+\pi^-(3\pi^0)$ has been seen in the no-fit 201 events[13]. However our resolution is insufficient to distinguish the $\eta\pi\pi$ decay mode from a five body phase space decay. Thus each $\eta'(958)$ gives rise to four $(\pi^+\pi^-\pi^0)$ combinations in the region of the $\eta(549)$ mass.

The other effect shown in Fig 5.21 is that events with backward Λs have a (5π) mass spectrum distributed according

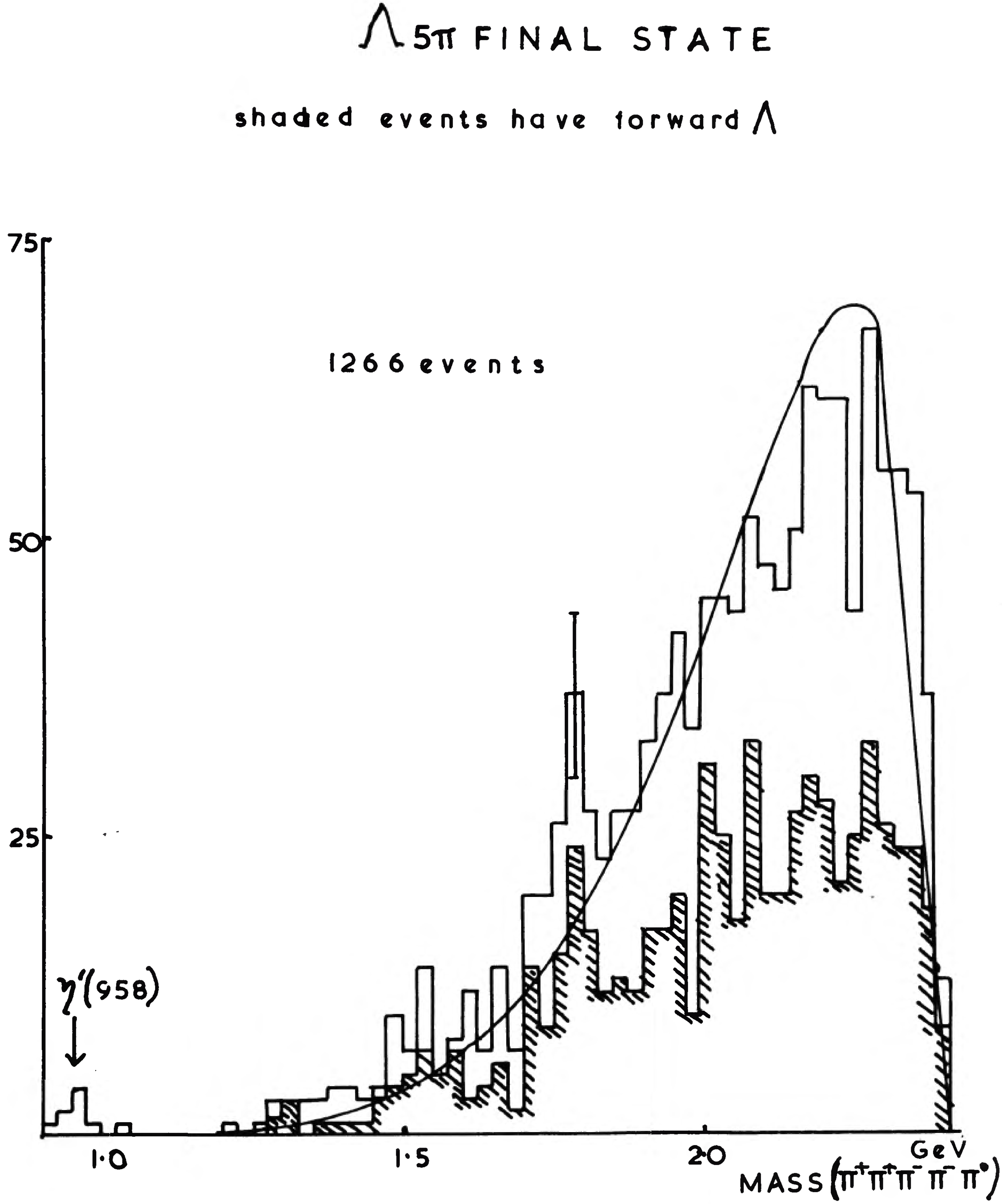

Λ5π FINAL STATE
shaded events have forward Λ
1266 events
75
50
25
η′(958)
1·0
1·5
2·0
GeV
MASS(π⁺π⁺π⁻π⁻π⁰)

FIG. 5.21.

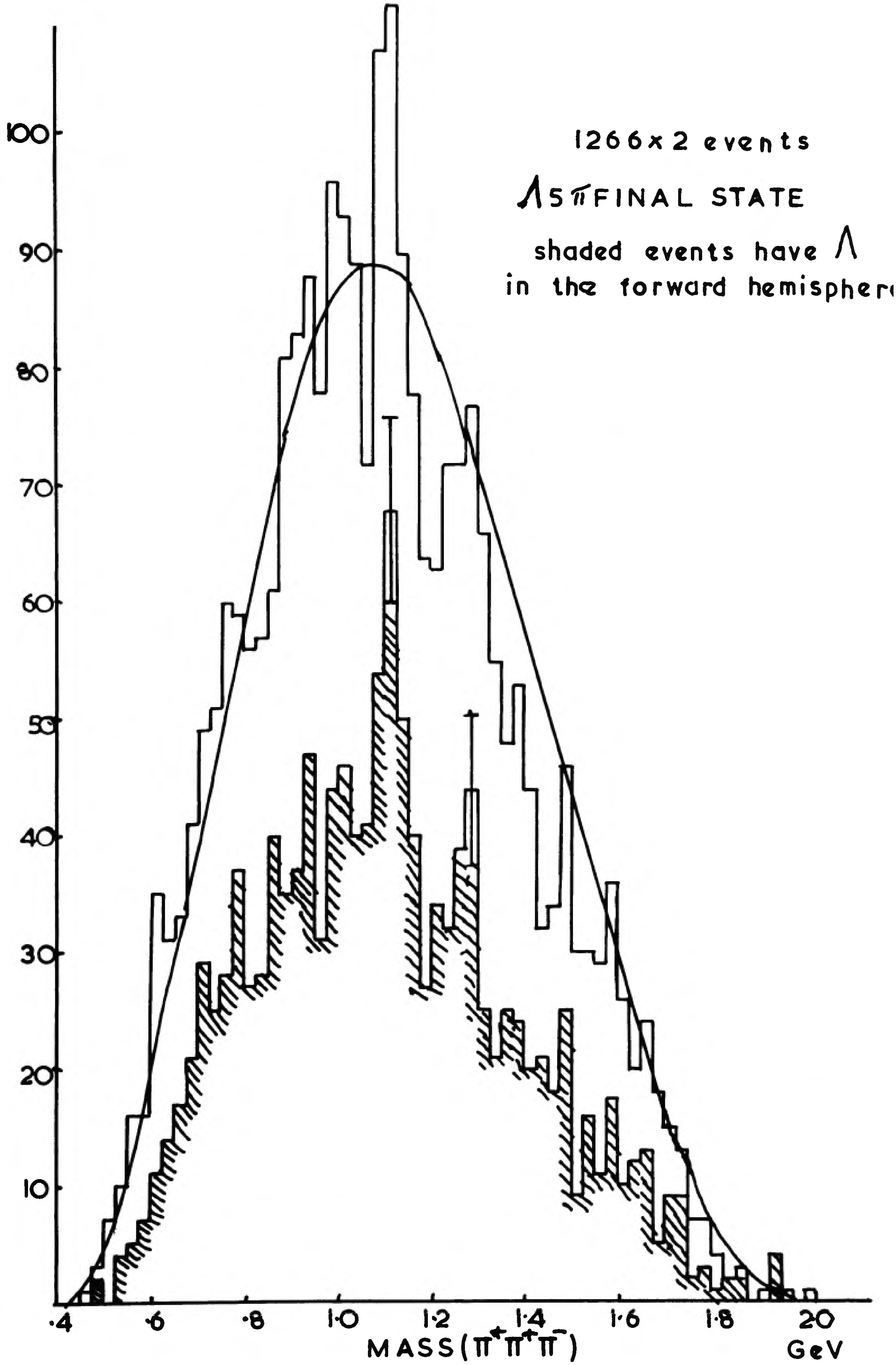

100
90
80
70
60
50
40
30
20
10
1266 x 2 events
Λ 5π FINAL STATE
shaded events have Λ
in the forward hemisphere
·4
·6
·8
1·0
1·2
1·4
1·6
1·8
2·0
MASS(π⁺π⁺π⁻)
GeV

FIG. 5.22.

$\Lambda\,5\pi$ FINAL STATE
(unweighted plots)

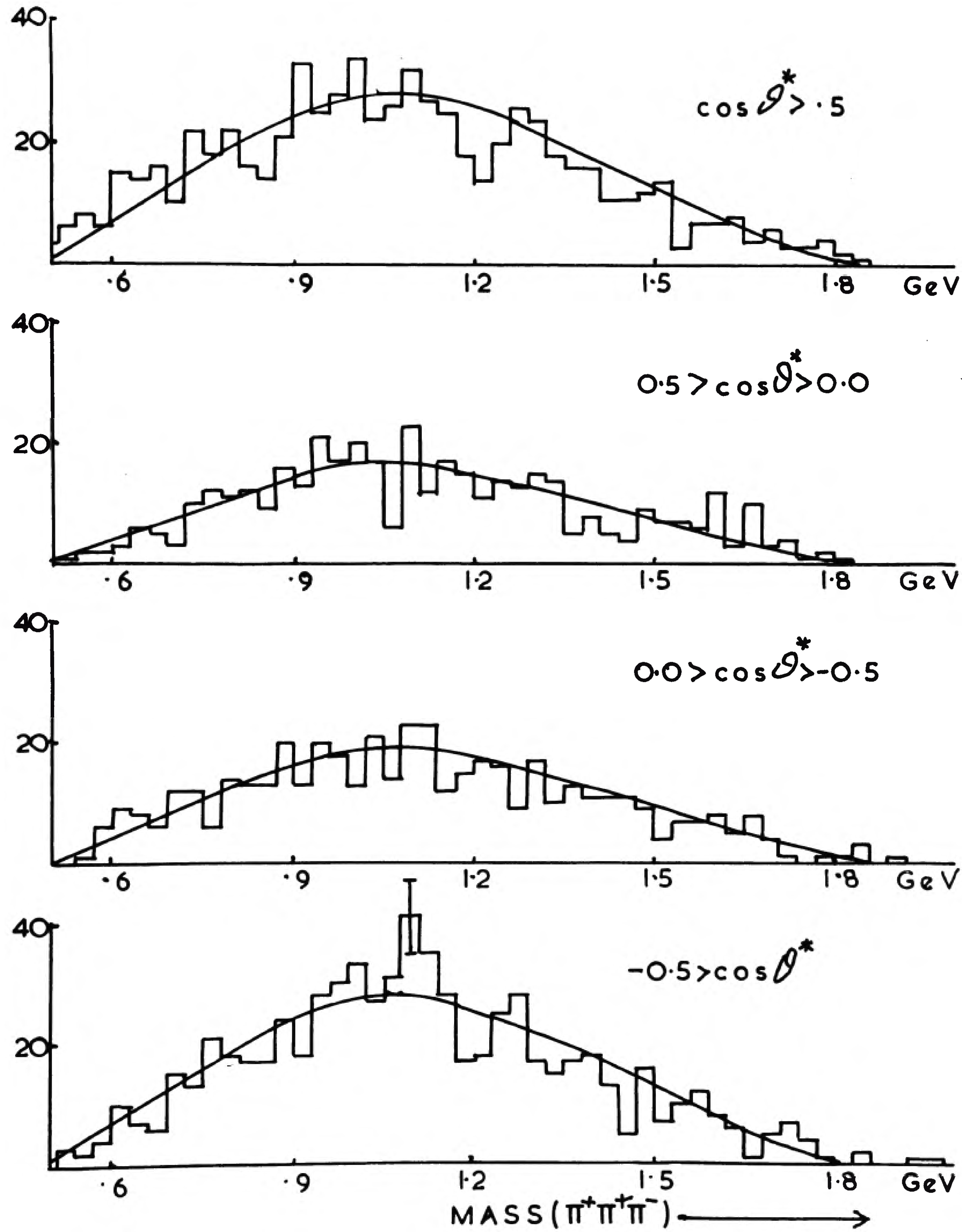

FIG.5.23.

to phase space (with the exception of the η') while events with forward Λ s have a spectrum shifted towards lower mass. This is in line with the general observation that forward lambda events are dominated by low and medium mass meson resonances while the backward lambda events contain large proportions of hyperon resonances. In the light of this the enhancement seen at 1790 MeV for forward lambda events is probably a fluctuation.

$A_1^+(1080)$ and $A_2^+(1300)$. Fig 5.22 shows the $(3\pi)^+$ invariant mass spectrum (forward Λ events shaded). As in the $\Lambda 4\pi$ final state strong A_1^+ and A_2^+ peaks are seen in association with forward lambdas. The A_1 effect is some three standard deviations above phase space. The A_2 enhancement does not appear to be so strong at first sight. However the general shift to lower mass relative to phase space for events with forward lambdas noted above tends to mask the A_2 peak. Fig 5.23 shows the mass plot divided into four regions of cos θ^*. The A_1^+ feature is prominent in the backward direction as expected. The statistics of the A_2^+ peak are not sufficiently robust to survive this form of dissection!

$Y^*(1385)$. The positive charge state is produced fairly, strongly backwards - the angular distribution is shown in Fig 5.2. The negative charge state is also seen in abundance. The neutral state is not seen. However the cross sections are difficult to estimate as phase space peaks sharply in this region.

$\rho(765)$. Again the problem of the rapidly varying phase space for two out of six bodies makes it very difficult to estimate the cross sections for ρ production. The neutral state is quite strong but still only appears as a shoulder on phase space. The negative rho is also seen. There may be some positive rho though the data is equally consistent with its absence. The very large background below the ρ^0 and below the $A_1^{\pm}$ and $A_2^{\pm}$ together with the ambiguities associated with permutations makes it impossible to check that the A mesons decay through ρ^0.

$\omega(783)$. Fig 5.24 shows the mass spectrum of $(\pi^+\pi^-\pi^0)$. The fit to phase space is good except in the region of $\omega(783)$ and $\eta(546)$. Examination of a scatter plot of mass against cos θ^* showed that the ω was produced in both forward and backward directions.

$\eta(546)$. This feature has to be distinguished from 3π combinations appearing in the $\eta'(958)$ discussed above. The latter appear shaded in Fig 5.24. It is clear that there is

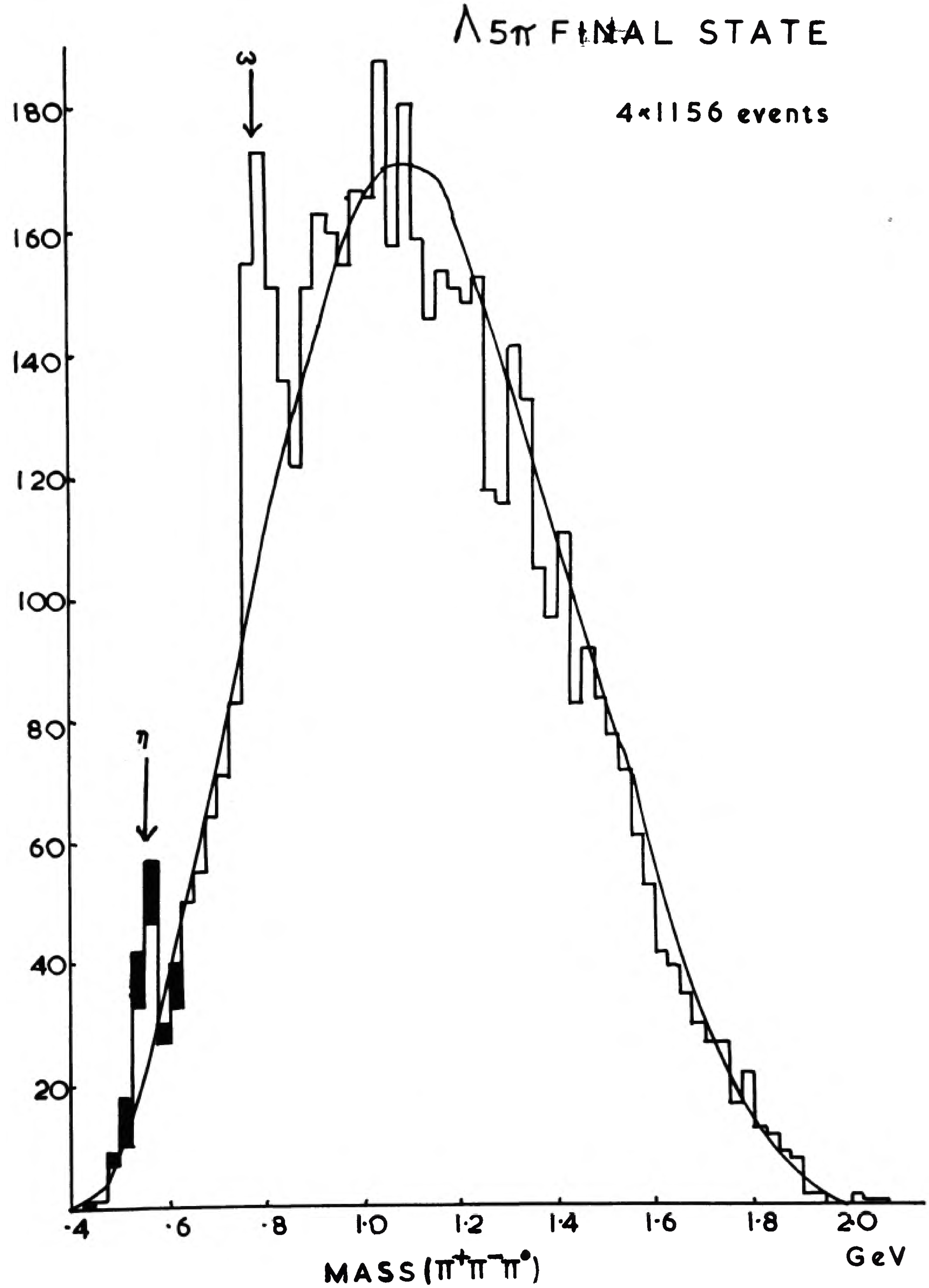
Λ5π FINAL STATE
4×1156 events
ω
η
180
160
140
120
100
80
60
40
20
·4
·6
·8
1·0
1·2
1·4
1·6
1·8
2·0
GeV
MASS(π⁺π⁻π⁰)

FIG. 5.24.

TABLE 5.6

Summary of $\Lambda 5\pi$ final state

		Decay mode observed
$\Lambda\pi^+\pi^-\pi^+\pi^-\pi^0$	$345(\pm 30)\mu b$	
$\Lambda\,\eta'(958)$	$2.5(\pm 1)\mu b$	$\eta' \rightarrow 2\pi^+2\pi^-\pi^0$
$Y^{*+}(1385)\pi^-\pi^+\pi^-\pi^0$	$45(\pm 15)\mu b$	$Y^{*+} \rightarrow \Lambda\pi^+$
$Y^{*-}(1385)\pi^+\pi^-\pi^+\pi^0$	$28(\pm 15)\mu b$	$Y^{*-} \rightarrow \Lambda\pi^-$
$\rho^0\Lambda\pi^+\pi^-\pi^0$	$50(\pm 20)\mu b$	$\rho^0 \rightarrow \pi^+\pi^-$
$\rho^-\Lambda\pi^+\pi^+\pi^-$	$10(\pm 5)\mu b$	$\rho^- \rightarrow \pi^0\pi^-$
$\omega\Lambda\pi^+\pi^-$	$42(\pm 7)\mu b$	$\omega \rightarrow \pi^+\pi^-\pi^0$
$\eta\Lambda\pi^+\pi^-$	$8.5(\pm 4)\mu b$	$\eta \rightarrow \pi^+\pi^-\pi^0$
$A_1^+\Lambda\pi^-\pi^0$	$15(\pm 5)\mu b$	$A_1^+ \rightarrow \pi^+\pi^+\pi^-$
$A_2^+\Lambda\pi^-\pi^0$	$5(\pm 4)\mu b$	$A_2^+ \rightarrow \pi^+\pi^+\pi^-$

The errors on these cross sections are intended to cover the large uncertainties in background subtraction.

production of $\eta(546)$ which is not associated with $\eta'(958)$. Like the $\omega(783)$, the $\eta(546)$ is observed in both forward and backward hemispheres.

The mass spectra of the 56 combinations in this final state were carefully scanned and correlations with production angle and lambda production angle examined. No other features were distinguished. In particular no $Y_0^*(1520)$ decaying to $\Lambda\pi^+\pi^-$ was seen. In only two cases was the mass of any $(\Lambda\pi^+\pi^-\pi^0)$ combination below 1700 MeV. This rules out production of the $Y_0^*(1670)$ which is meant to decay into $\Lambda\eta(546)$.

Table 5.6 gives rough estimates of the cross sections for the various channels.

5.8 Charged sigma and three pions final state

The heavy scanning and fitting losses discussed in chapter 4 make the analysis of these channels very difficult with the limited statistics available. Three types of sample in each channel were examined:

a) Unweighted without cuts. This is the raw data. It is best statistically but is biassed and contaminated. Scatter plots of Cos θ^* versus mass (of the type discussed for

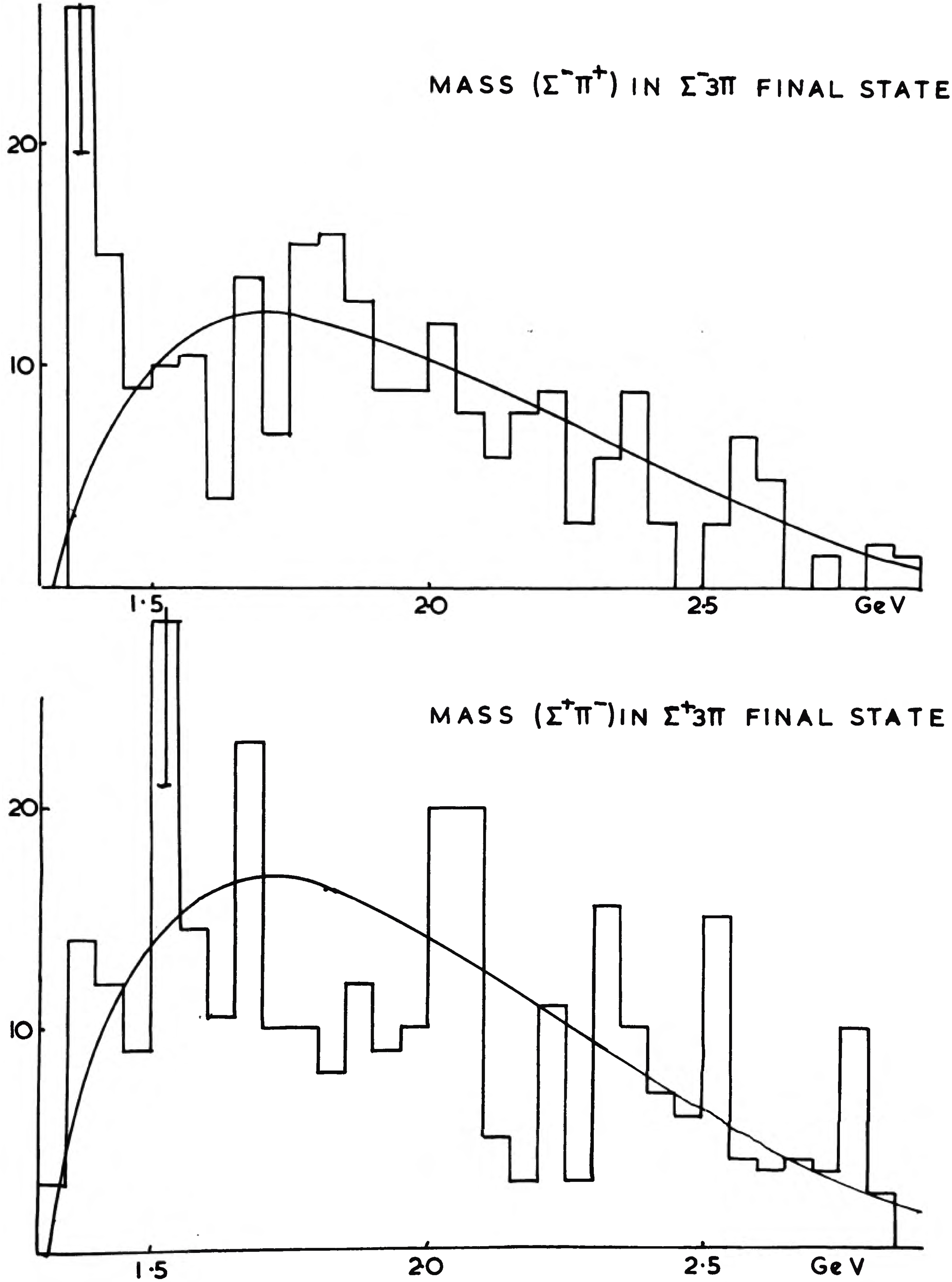
MASS $(\Sigma^-\pi^+)$ IN $\Sigma^-3\pi$ FINAL STATE
20
10
1·5
2·0
2·5
GeV
MASS $(\Sigma^+\pi^-)$ IN $\Sigma^+3\pi$ FINAL STATE
20
10
1·5
2·0
2·5
GeV

FIG. 5.25.

lambda final states) were made for every combination using this sample.

b) Unweighted with cuts. This is the purest sample of data. However it is statistically poor and very biassed.

c) Weighted with cuts. This is the least biassed sample of data. However the fluctuations tend to be very large. For this reason it is often necessary to compare with samples a) and b) to assess the significance of features.

In table 5.7 we show the number of events in each sample for the four sigma channels considered here.

Channel	(a)	(b)	(c)
$\Sigma^+_\pi\ \pi^-\pi^+\pi^-$	113 events	89 events	170 events
$\Sigma^+_\pi\ \pi^-\pi^+\pi^-\pi^0$	368 events	316 events	585 events
$\Sigma^-\ \pi^+\pi^-\pi^+$	94 events	79 events	124 events
$\Sigma^-\ \pi^+\pi^-\pi^+\pi^0$	554 events	493 events	753 events

TABLE 5.7

It is clear from the number of events that very few features may be discerned with certainty in the sigma and three pion channels. Fig 5.25 shows the mass spectra of the neutral ($\Sigma\pi$) combinations. The sigma plus data is taken from the charged pion decay mode only. The curves drawn are the phase space curves normalised to the total number of events. The plots are of type c) described above. Any resonance observed in one plot should also be seen in the other in the ratio

$$(\Sigma^-\pi^+) : (\Sigma^+_\pi\pi^-) = 2 : 1$$

by charge symmetry (assuming that no strong interference is present). This does not appear to be the case. Enhancements in the regions of $Y_o^*(1405)$ in $(\Sigma^-\pi^+)$ and $Y_o^*(1520)$ in $(\Sigma^+\pi^-)$ do not appear very strongly in the other charge combinations. No strong peaks are observed in the regions of Y_1^{*o} (1660), Y_o^* (1815) or Y_1^{*o}(2035) although the data are so poor as to be consistent also with quite strong production of these and other resonances. The lack of evidence for the final state $Y_1^{*+}(1660)\pi^-$ in which the Y^* decays to $\Sigma\pi\pi$ has already been discussed in section 5.3 and the mass plot shown in Fig 5.10.

5.9 Charged sigma and four pions final state

In Fig 5.26 are shown the mass plots for neutral $(\Sigma\pi)$ combinations. The better statistics in these channels enables the $Y_o^*(1405)$ and $Y_o^*(1520)$ resonances to be identified. The plots are weighted.

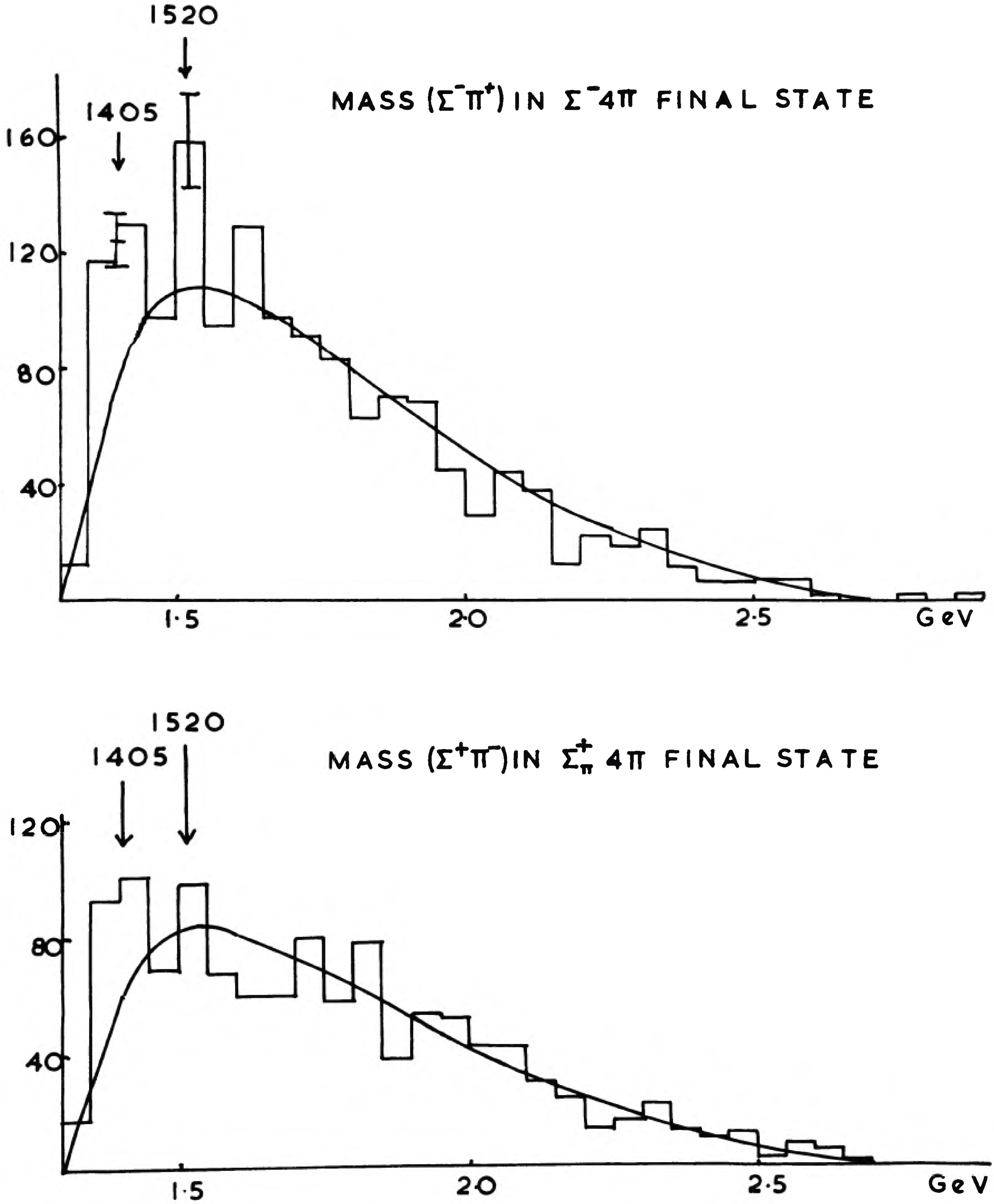

1520
1405
MASS ($\Sigma^-\pi^+$) IN $\Sigma^-4\pi$ FINAL STATE
160
120
80
40
1·5
2·0
2·5
GeV
1520
1405
MASS ($\Sigma^+\pi^-$) IN $\Sigma^+_\pi 4\pi$ FINAL STATE
120
80
40
1·5
2·0
2·5
GeV

FIG. 5.26.

TABLE 5.8

	$(\Sigma^{+}_{\pi}\pi^{-})$	$(\Sigma^{-}\pi^{+})$	
$Y_0^*(1405)$	90(±20)	100(±14)	events
$Y_0^*(1520)$	16(±10)	50(±10)	events

Table 5.8 shows the approximate numbers of events in the two resonances. They are not irreconcilable with the expected branching ratios. Excluding these events we are left with 603 $\Sigma^-\pi^+\pi^-\pi^+\pi^0$ and 479 $\Sigma^+_{\pi}\pi^-\pi^+\pi^-\pi^0$ corresponding to cross sections of 141 μb and 238 μb. We now apply the statistical charge model(4) discussed in section 5.6 to derive the cross sections:

$\Sigma^-4\pi$	188 μb	(Correction factor 1.3 for $2\pi^0$ cases)
$\Sigma^0 4\pi$	111 μb	(from section 5.6)
$\Sigma^+4\pi$	318 μb	(Correction factor 1.3 for $2\pi^0$ cases)

The agreement between these is very reasonable taking into account a) the contamination of Σ^- cross sections with final states containing $n\pi^0$, $n = 0, 2\ldots$ b) the probable loss of $\Sigma^0 4\pi$ events into the $\Lambda 5\pi$ channel as was found in the case of $\Sigma^0 2\pi$ (see chapter 4); c) the peripheral effect on the sigma charge which favours $\Delta Q = 0, 1$ transitions of the

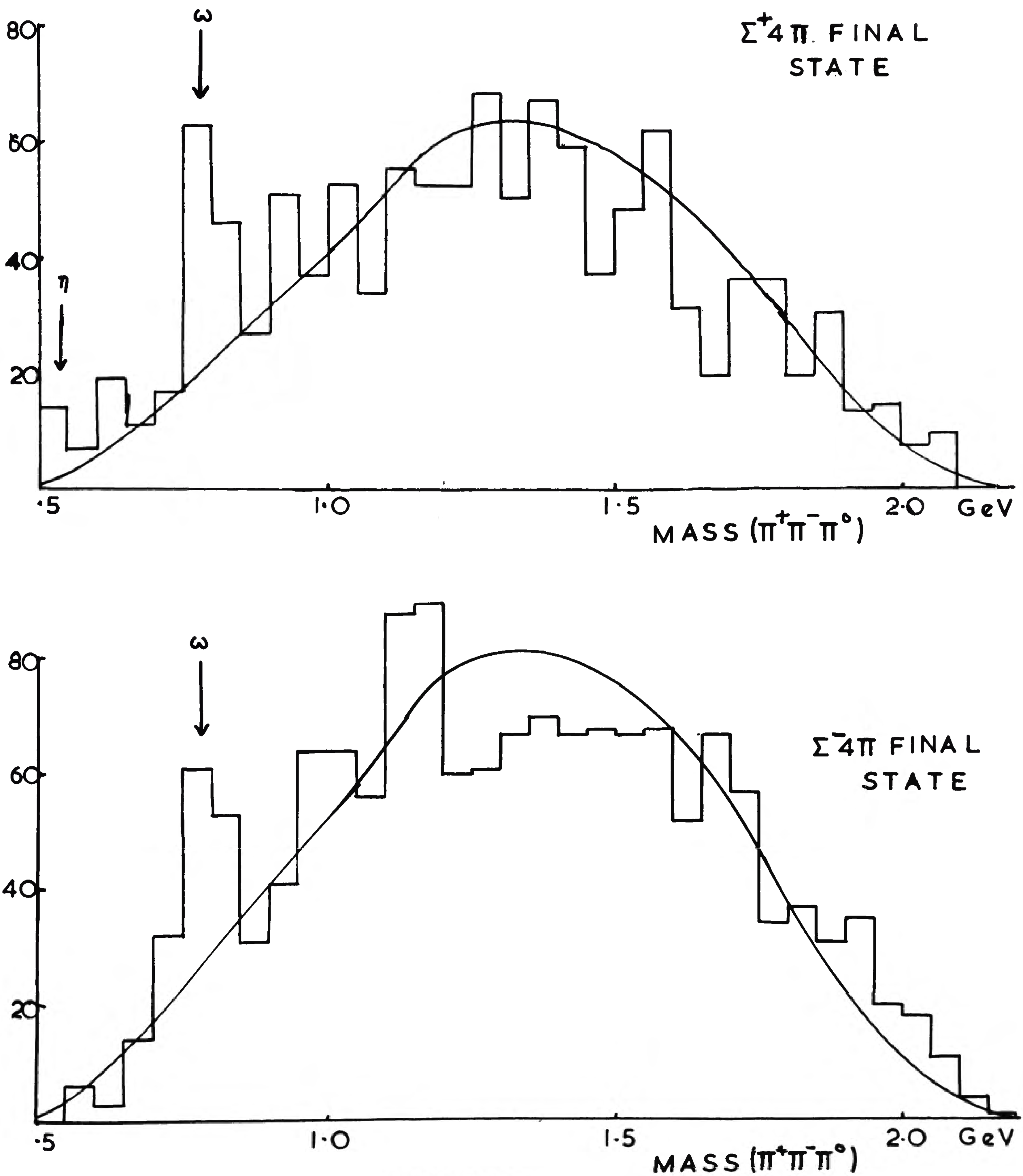

80
60
40
20
ω
η
Σ⁺4π FINAL STATE
·5
1·0
1·5
2·0
GeV
MASS (π⁺π⁻π°)
80
60
40
20
ω
Σ⁻4π FINAL STATE
·5
1·0
1·5
2·0
GeV
MASS (π⁺π⁻π°)

FIG. 5.27.

baryon state. The $Y_0^*(1405)$ and $Y_0^*(1520)$ have angular distributions with sharp backward peaks - they cannot be seen above background in the forward hemisphere.

Small excesses above phase space in the $(\pi^+\pi^0)$ and $(\pi^-\pi^0)$ plots in the 750 MeV region are attributed to weak ρ production. They occur in both Σ^+ and Σ^- final states. No ρ^0 is seen.

Fig 5.27 shows the $(\pi^+\pi^-\pi^0)$ mass spectra for weighted events of each channel. Strong ω production is seen in both cases. The cos θ^* versus mass plot shows that the ω is peaked forward although it is produced weakly in the backward hemisphere also. The Σ^+ final state also shows some indication of $\eta(546)$. The experimental width of the ω peak (full width 100 MeV) shows how poor the experimental resolution is in these weakly constrained final states.

This lack of experimental resolution coupled with the systematic loss of events tends to reduce confidence in the [illegible]. However quantities that depend on the variables of tracks whose momenta are determined from curvature have a considerably sharper resolution. Such a variable is the invariant mass of $(\pi^-\pi^-\pi^+)$ from the Σ^+ events or $(\pi^+\pi^+\pi^-)$ from the Σ^- events; these are shown in the lower plots of

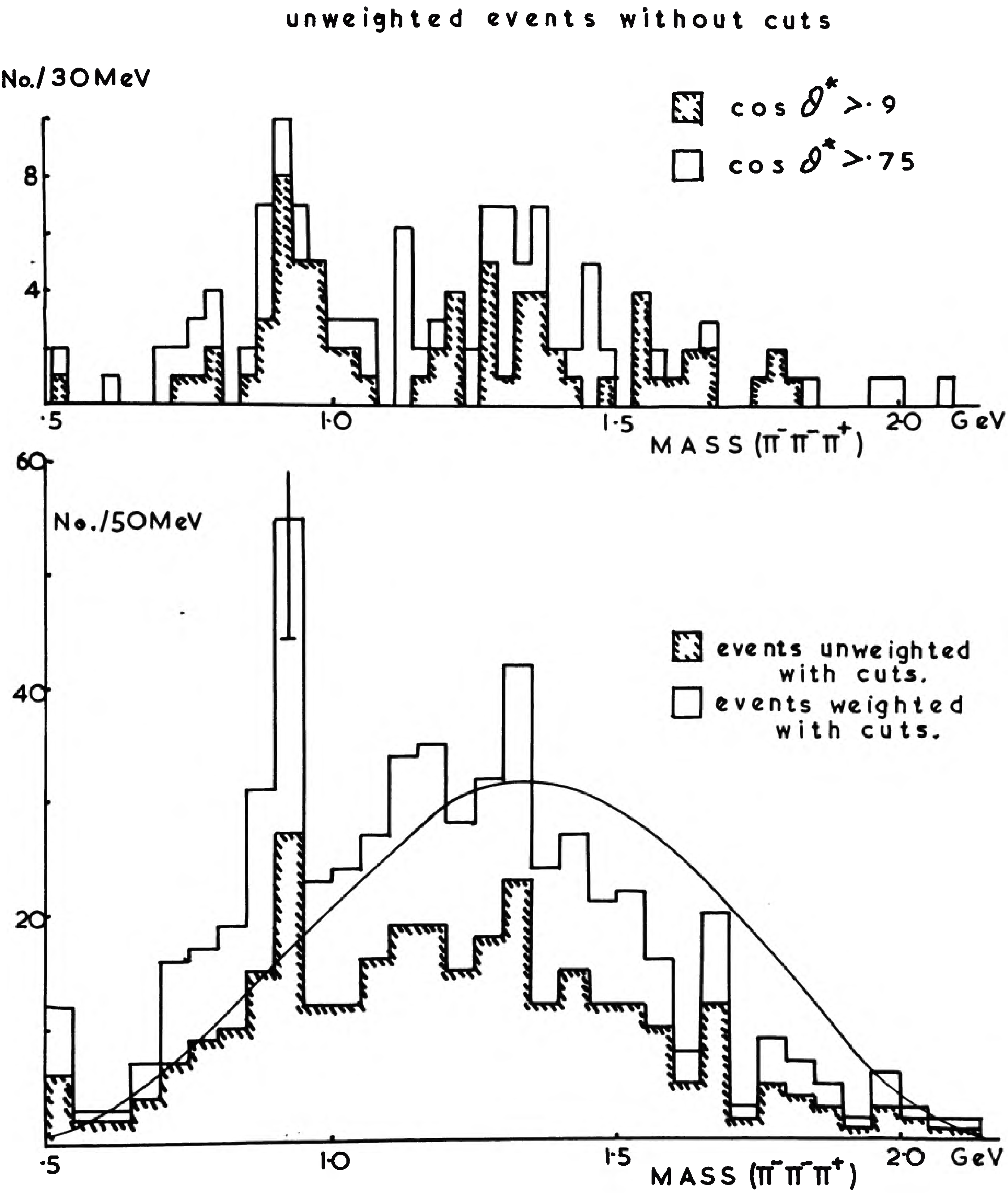

$\Sigma_\pi^+ \pi^-\pi^+\pi^-\pi^0$ FINAL STATE

FIG. 5.28.

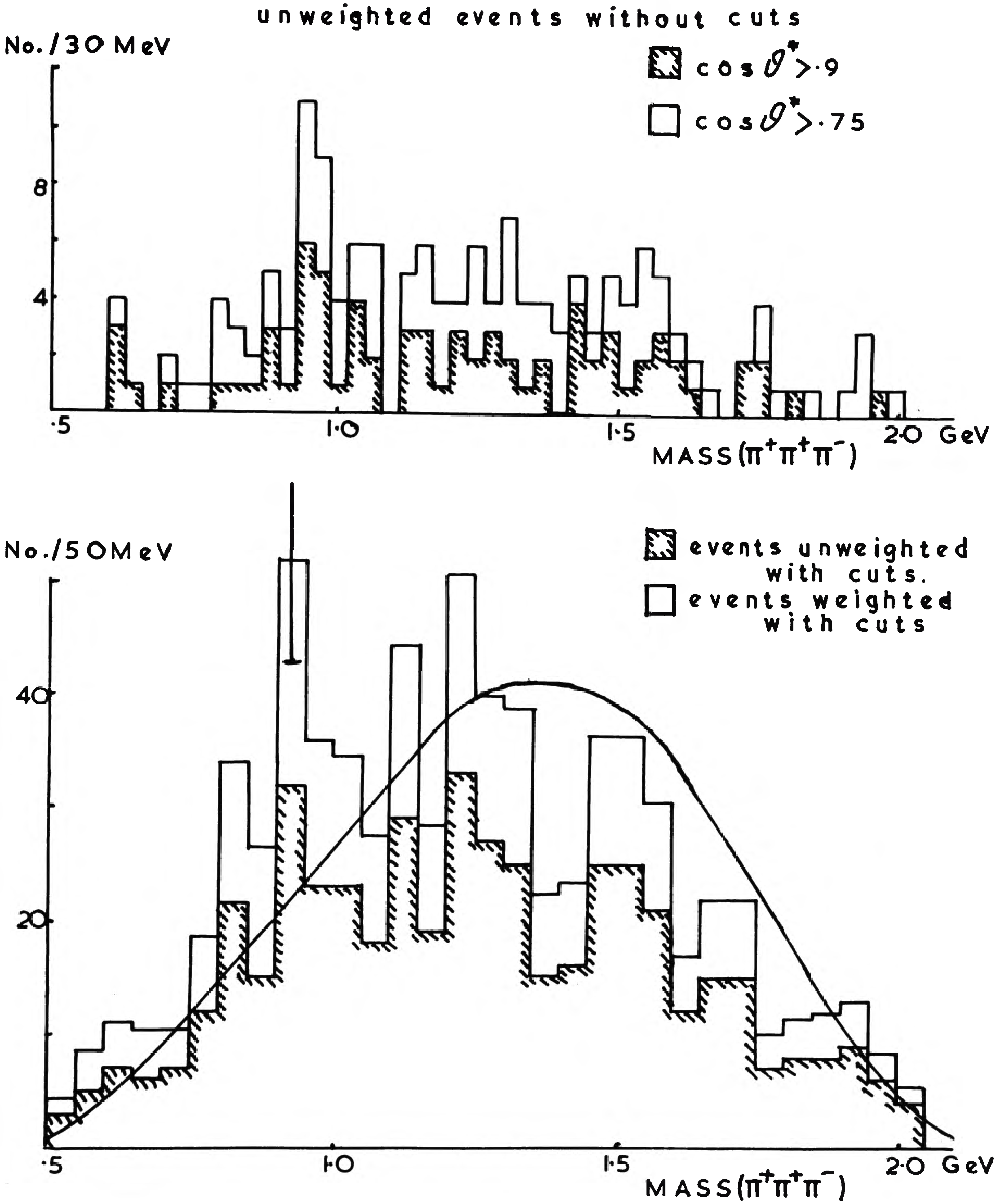

$\Sigma^-\pi^+\pi^-\pi^+\pi^0$ FINAL STATE

FIG. 5.29.

Figs 5.28 and 5.29. The upper outline on the histograms is the spectrum of weighted events (type (c)). The cross hatched histogram below is the plot of unweighted events (type (b)). The upper histograms in both figures are those for raw data (type (a)). The area under the cross hatched histogram is for track combinations with cos $\theta^* > .9$ and that under the upper line for combinations with cos $\theta^* > .75$. In all cases shown and in both charge states a very pronounced enhancement is seen in the region 900 - 950 MeV. The curve drawn on the lower plots is phase space normalised to the area of the weighted histogram. In the Σ^+ case the peak is 3.5 standard deviations above phase space and more than 2.5 above the highest reasonable background curve. In the Σ^- case the factors are 3.2 and 2.0 respectively. The enhancements are not due to peculiar weights as can be seen from the cross hatched histograms. The cos θ^* versus mass plots showed strong forward peaks in this mass region - the effect is shown by the upper histograms in Fig 5.28 and 5.29. Rebinning the histograms in 100 MeV wide bins we have calculated the χ^2 for a fit to phase space for these two forward cones. In table 5.9 we give two probabilities in each case - P_1, for all bins fitted to normalised phase space and P_2 for all

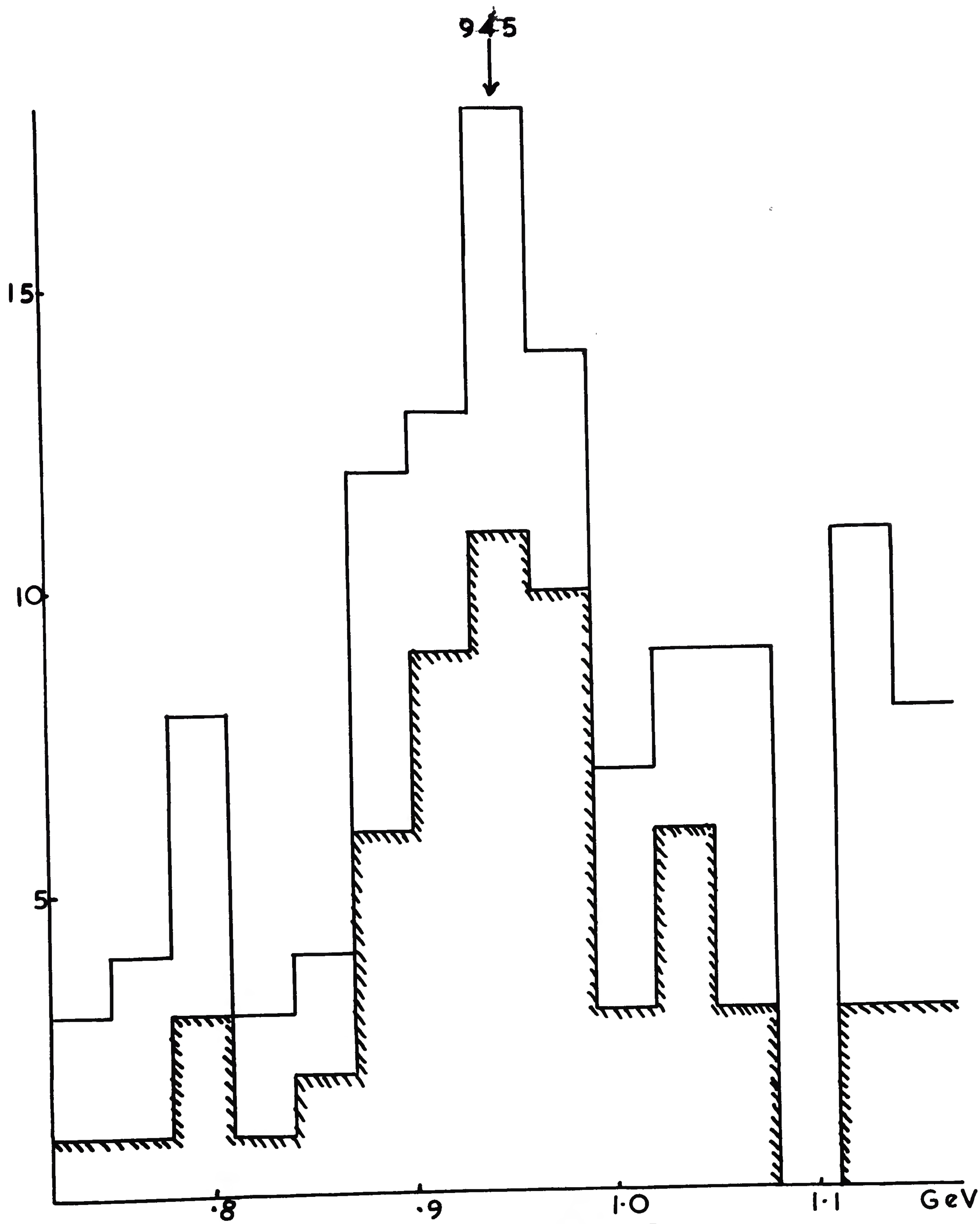

MASS $(3\pi)^{+}$ & $(3\pi)^{-}$ IN $\Sigma 4\pi$ FINAL STATES.

SUM OF UPPER HISTOGRAMS OF FIGURES 5.28 & 5.29.

FIG. 5.30.

bins except 900 - 1000 MeV fitted to the same phase space.

TABLE 5.9

χ^2 Probabilities for fit of (3π) mass spectrum to normalised phase space

		P_1	P_2
$\Sigma^+\pi^0\ (3\pi)^-$	$\cos\theta^* > .9$	$< 10^{-4}$	.55
"	$\cos\theta^* > .75$	$< 10^{-4}$	.06
$\Sigma^-\pi^0\ (3\pi)^+$	$\cos\theta^* > .9$	.01	.4
"	$\cos\theta^* > .75$	.002	.3

The question remains as to what this resonance is. A very similar object has been seen in πp and pp interactions in hydrogen bubble chamber and missing mass spectrometer experiments[19] - it is called $\delta(965)$. Fig 5.30 shows the two upper histograms added together. The eye-fit centre is 945 ($\pm$15) MeV and the full width 90 MeV. This is compatible with the parameters for δ of 965 MeV with a small width. We note that the $\Sigma^-\delta^+\pi^0$ final state is not as peripheral as the $\Sigma^+\delta^-\pi^0$ case. The peripheral production of this channel by meson exchange would involve the exchange of an $I = \frac{3}{2}$ K^* meson whose existence is forbidden by the orbital quark model[14].

TABLE 5.10

Channel	$\sigma(\mu b)$	$\Delta\sigma$	Resonance decay mode
$\Sigma^+\rho^+\pi^-\pi^-$	11	$\pm$ 7	$\rho^+ \to \pi^+\pi^0$
$\Sigma^+\rho^-\pi^+\pi^-$	10	$\pm$ 8	$\rho^- \to \pi^-\pi^0$
$Y_0^*(1405)\pi^+\pi^-\pi^0$	65	$\pm$ 20	$Y^* \to \Sigma^\pm\pi^\mp$
$Y_0^*(1520)\pi^+\pi^-\pi^0$	19	$\pm$ 4	$Y^* \to \Sigma^\pm\pi^\mp$
$\Sigma^+\pi^-\omega$	31	$\pm$ 7	$\omega \to \pi^+\pi^-\pi^0$
$\Sigma^+\pi^-\eta$	6	$\pm$ 4	$\eta \to \pi^+\pi^-\pi^0$
$\Sigma^+\pi^0\delta^-(965)$	20	$\pm$ 5	$\delta^- \to \pi^+\pi^-\pi^-$
$\Sigma^-\rho^+\pi^+\pi^-$	6	$\pm$ 5	$\rho^+ \to \pi^+\pi^0$
$\Sigma^-\rho^-\pi^+\pi^+$	7	$\pm$ 5	$\rho^- \to \pi^-\pi^0$
$\Sigma^-\pi^+\omega$	14	$\pm$ 4	$\omega \to \pi^+\pi^-\pi^0$
$\Sigma^-\pi^+\eta$	0	$\pm$ 4	$\eta \to \pi^+\pi^-\pi^0$
$\Sigma^-\pi^0\delta^+(965)$	6	$\pm$ 3	$\delta^+ \to \pi^+\pi^+\pi^-$
Total $\Sigma^+\pi^+\pi^-\pi^-\pi^0$	290	$\pm$ 40	
$\Sigma^-\pi^+\pi^+\pi^-\pi^0$	176	$\pm$ 15	

Cross sections refer to both Σ^+ decay modes

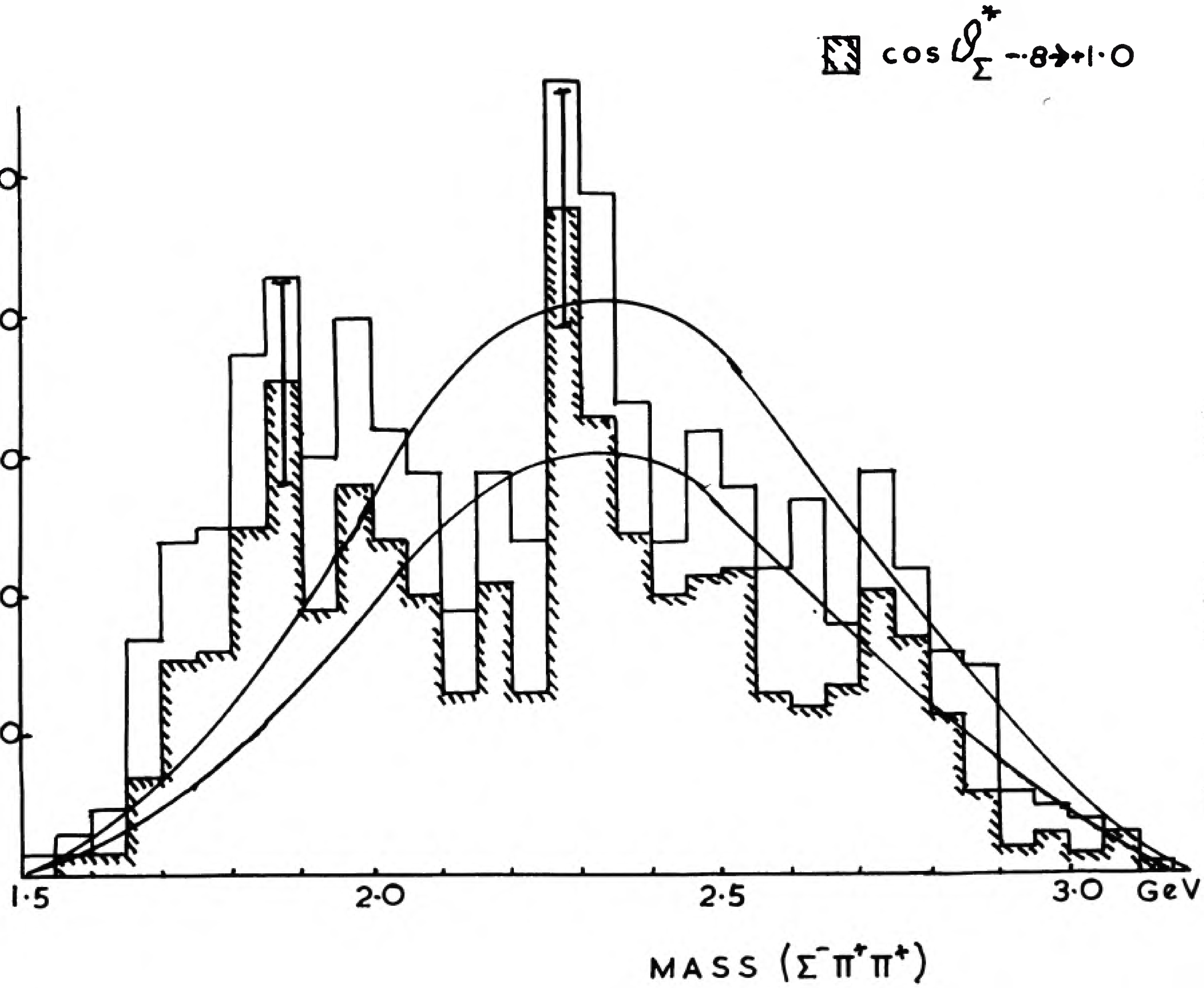

$\Sigma^-\pi^+\pi^+\pi^-\pi^0$ FINAL STATE

FIG. 5.31.

Examination of the mass plots and cos θ^* versus mass scatter plots showed other departures from phase space. The most significant of these is in the spectrum of $(\Sigma^- \pi^+ \pi^+)$ shown in Fig 5.31. The shaded area represents non peripheral Σs. The two curves are phase space curves for the two histograms. It is difficult to know which of the peaks correspond to resonances. None of them is seen in the $(\Sigma^+ \pi^- \pi^+)$ mass plot which would be surprising if any of the peaks were a resonance; furthermore the enhancement appears to be uniformly distributed with respect to cos θ^* $(\Sigma^- \pi^+ \pi^+)$. In accordance with the criteria outlined in section 5.5 we ignore this feature.

The cross sections for these channels are given in table 5.10.

REFERENCES TO CHAPTER 5

(1) G. Czyzewski: Report presented to the Berkeley Conference (1966) and CERN/TC/Physics 66-28.

(2) . Goldsack and D. Morrison: Private communication.

(3) R. Hemingway and D. Sumner: Private communication.

(4) Ref (1) and

K. Zalewski and J.A. Danysz: TH 747 CERN (1967).

(5) J.D. Bronzan and F.E. Low: Phys. Rev. Letters **12**, 522(1964).

(6) See Ref (4), chapter 6.

(7) Lipkin and Meshkov: Phys. Rev. Letters **14**, 670 (1965).

(8) Stodolsky and Sakurai: Phys. Rev. Letters **11**, 90 (1963).

(9) Lipkin: Private communication.

(10) M. Derrick et al: Phys. Rev. Letters **18**, 266 (1967).

(11) "Production of $Y_1^*(1700)$ in K^-p collisions at 6 GeV/c" (Letter in preparation).

(12) J. Mott et al: Phys. Rev. Letter **18**, 355 (1967).

(13) D. Locke: D.Phil. thesis (Oxon) 1966.

(14) See section 3.3.

(15) G. Goldhaber: see Review on Mesons, 1966, Berkeley Conference. Seen in almost all π^+p experiments above 6 GeV/c.

(16) The branching ratio to $\rho\pi$ is known to be less than 40%.

A.H. Rosenfeld et al: Rev. Mod. Phys. **39**, 1 (1967).

(17) G. Goldhaber: Review of Mesons, 1966, Berkeley Conference.

(18) J.H. Field: D.Phil. thesis (Oxon) 1964.

(19) Oostens et al: Phys. Lett. <u>22</u>, 708 (1966).

See also Ref (17).

C H A P T E R 6

THE DOUBLE PERIPHERAL MODEL

6.1 Introduction

In recent years intensive study of two body final states has increased our understanding of strong interactions. With increasing beam energy, however, the cross sections for inelastic two-body reactions decrease dramatically compared with those for multibody final states. It is clearly of interest to extend the analyses used for two-body reactions to final states of higher multiplicity.

An extension of the Regge pole formalism to three body final states has been discussed by Chan[1,2]. In this chapter we look at the phenomenology of various three body final states in our data. Two of these reactions are considered in detail and considerable care is taken to distinguish dynamic from kinematic effects. This in itself is a sufficiently complicated problem to cast doubt on the wisdom of analysing the data in terms of any but the simplest model. The single particle exchange model applied to two body processes is known to be in violent disagreement with

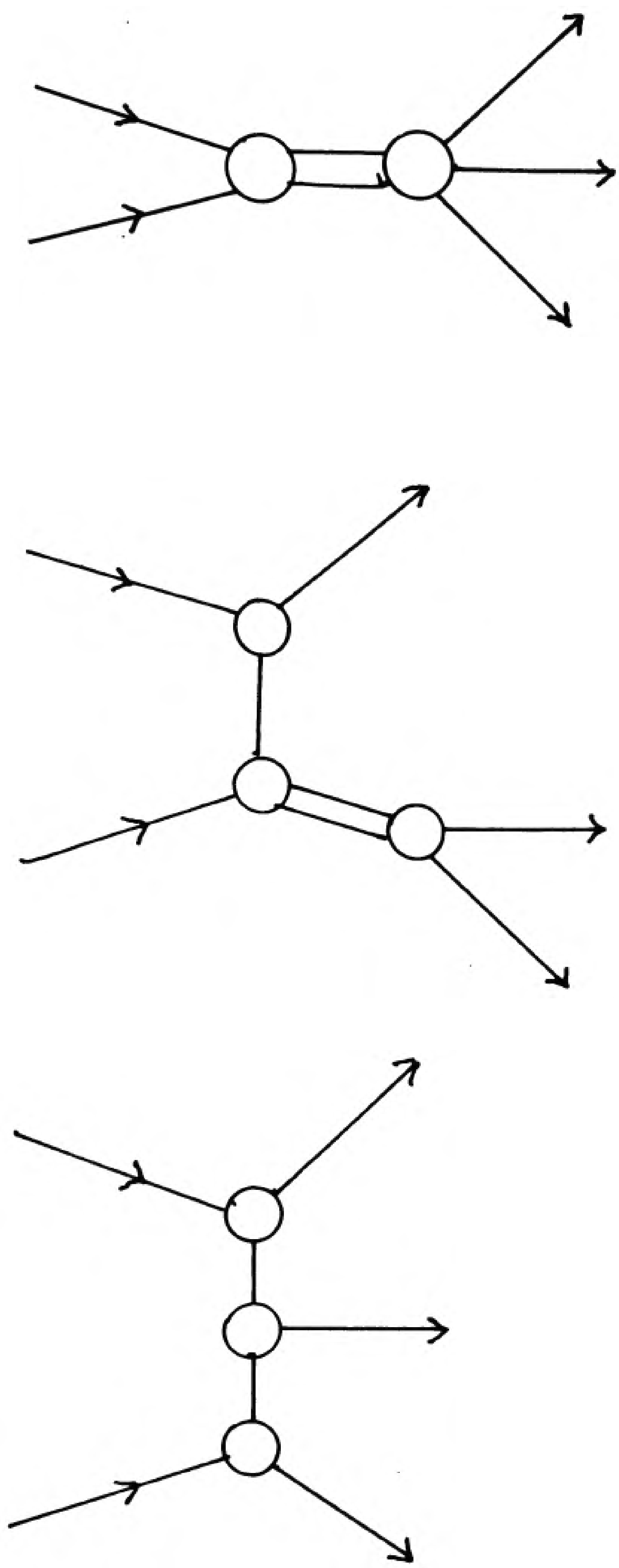

(a)

(b)

(c)

fig 6.1

experiment as far as momentum transfer and centre of mass energy dependence are concerned. This is particularly true for the exchange of particles with spin. However the analysis of chapter 5 and appendix F shows that the predicted dependence of the matrix element on other variables (such as resonance decay angles) provides a good fit to the data. We therefore consider a model of three body production using pseudoscalar and vector exchanges and concentrate on those features which are not too sensitive to the effects of absorption. In appendix G explicit matrix elements are derived for two cases of interest.

6.2 Three body final states

The three body final states which are most likely to be analysable are those which simplify in one of the following ways:

1) s-channel resonance (Fig 6.1a)
2) quasi 2-body final state produced by an exchange process (Fig 6.1b)
3) 3-body final state produced by a double exchange process (Fig 6.1c)

Cases 1 and 2 may be treated in terms of well established models. We are concerned with case 3.

Consider the reaction:

$$K^-p \rightarrow K^{*-}\pi^+n;\quad K^{*-} \rightarrow \overline{K}^o\pi^- \qquad 6.1$$

This channel occurs in events fitted to the hypothesis $\overline{K}^o\pi^+\pi^-n$ and was selected as shown in Table 6.1. The cross sections there have been corrected for other resonance decay modes; "background" includes (i) non resonant mass combinations in the selected mass region and (ii) quasi two body reactions.

TABLE 6.1

Reaction	Cross Section μb	Selection Criteria	Background
$K^{*-}\pi^+n$	225±25	$.83<M(\overline{K}\pi)<.95$	25%
$K^{*-}\pi^-N^{*++}$	172±45	$1.15<M(p\pi^+)<1.35$	30%
$K^{*o}\pi^-p$	255±110	$.83<M(\overline{K}\pi)<.95$	30%
$K^{*-}\pi^op$	346±40	$.83<M(\overline{K}\pi)<.95$	30%
$\rho^{\bar{o}}_{\pi}{}^{\overset{+}{o}}\Lambda$	92±20	$\left\{ \begin{array}{l} .625<M(\pi\pi)<.875 \\ t_{K,\rho} \leqslant 1.2\ \mathrm{GeV}^2 \end{array} \right.$	25%

The main source of background came from $K^*(1400)n$ and a little from $K^{*-}N^{*+}$. Fig 6.2a shows the scatter plot of transverse against longitudinal momentum for each particle in the overall centre of mass. The distinctive features are

FIG.6.2(a).

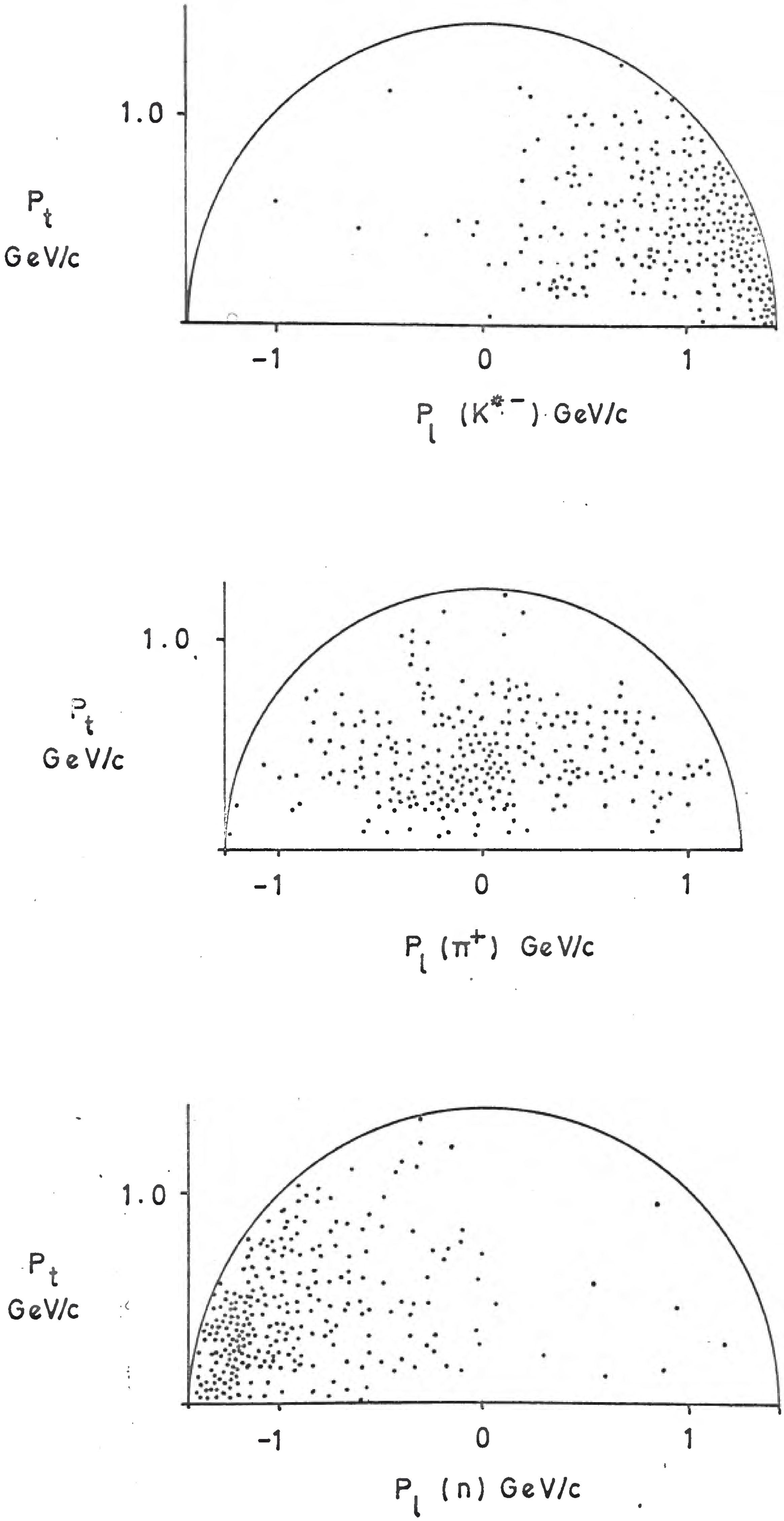
1.0
P_t
GeV/c
-1
0
1
P_l (K^{*-}) GeV/c
1.0
P_t
GeV/c
-1
0
1
P_l (π^+) GeV/c
1.0
P_t
GeV/c
-1
0
1
P_l (n) GeV/c

FIG.6.2(b).

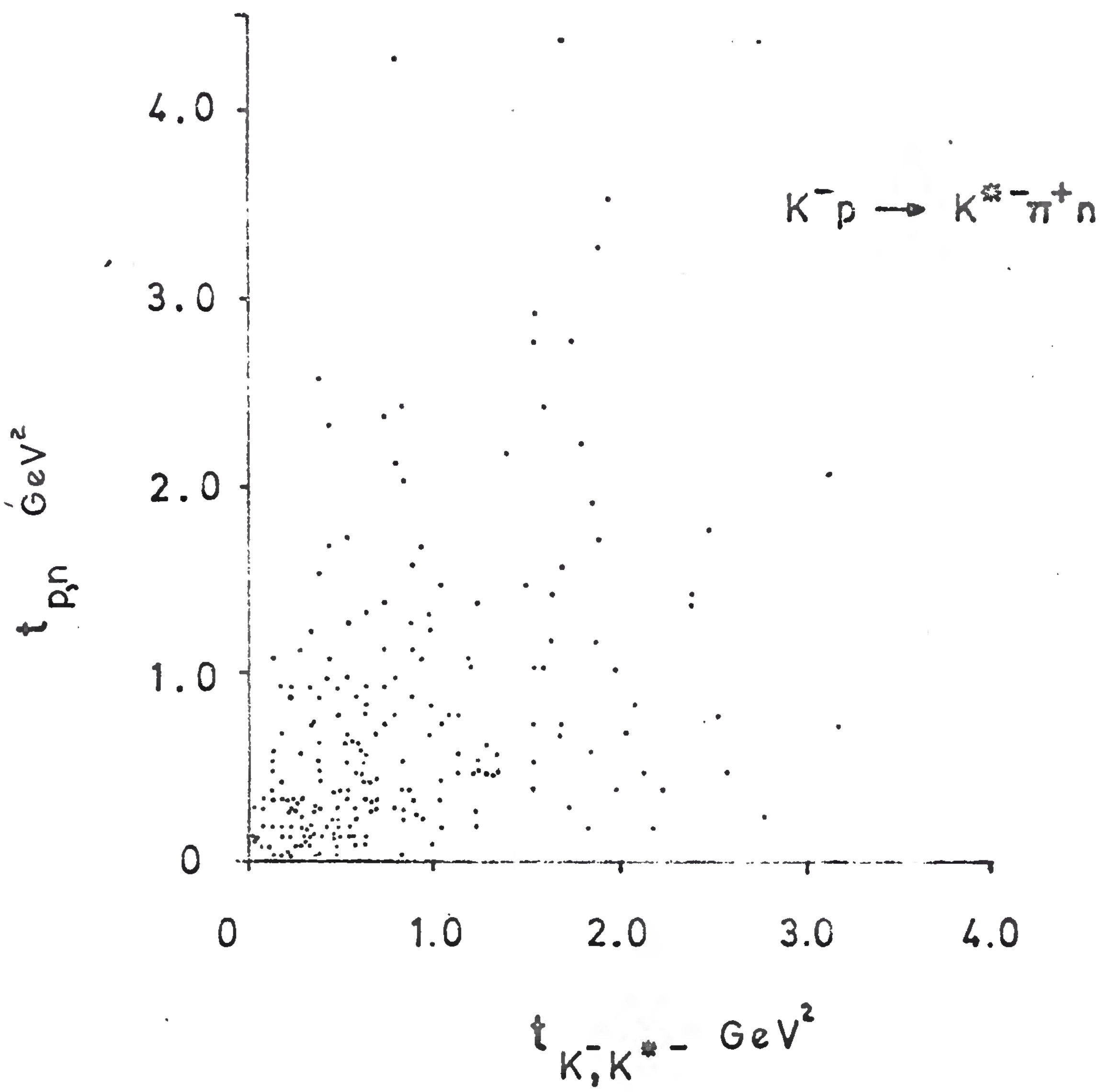

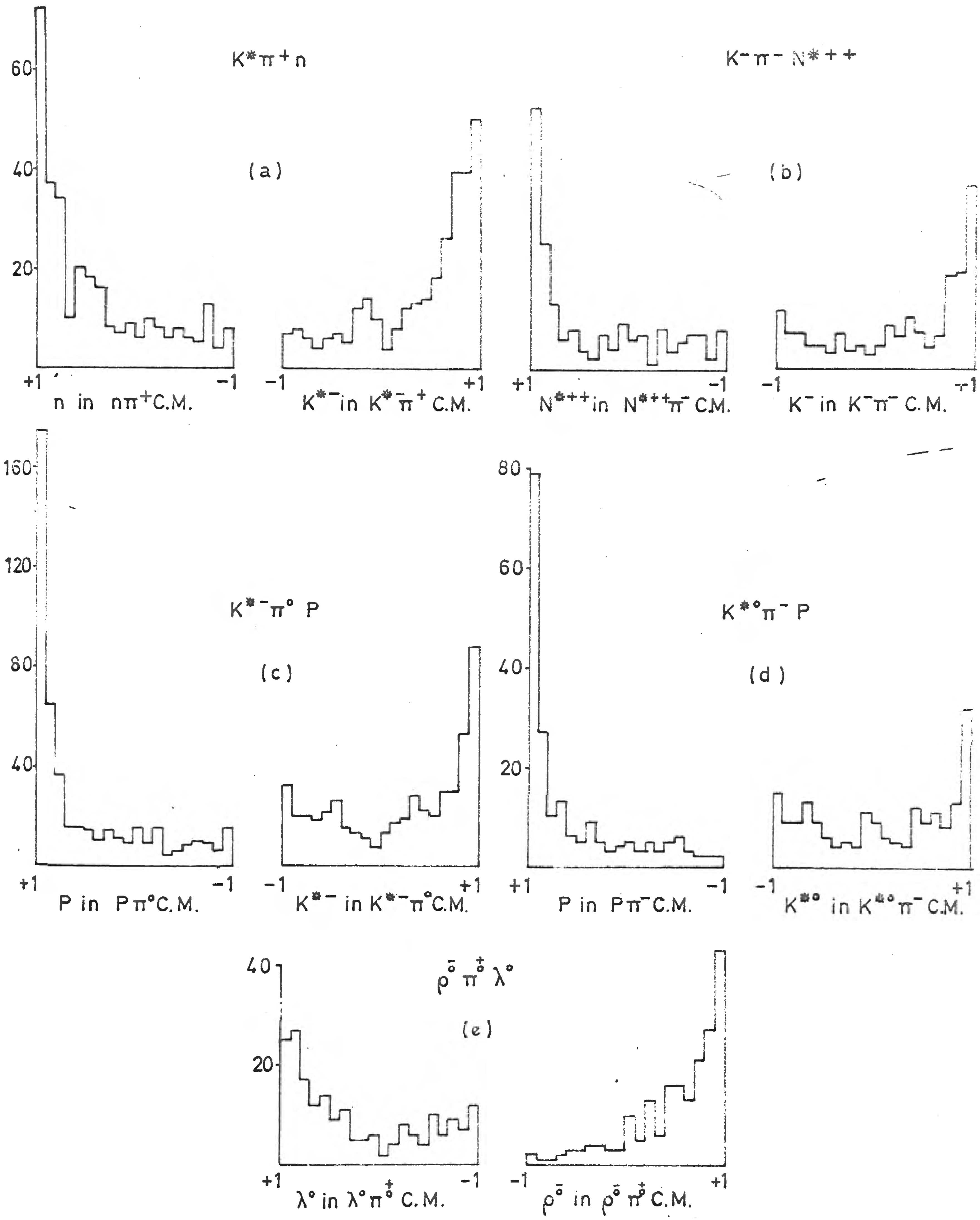

60
40
20
$K^{*}\pi^{+}n$
(a)
+1
-1
n in $n\pi^{+}$C.M.
-1
+1
K^{*-}in $K^{*-}\pi^{+}$ C.M.
$K^{-}\pi^{-}N^{*++}$
(b)
+1
-1
N^{*++}in $N^{*++}\pi^{-}$ C.M.
-1
+1
K^{-} in $K^{-}\pi^{-}$ C.M.
160
120
80
40
$K^{*-}\pi^{\circ}$ P
(c)
+1
-1
P in $P\pi^{\circ}$C.M.
-1
+1
K^{*-} in $K^{*-}\pi^{\circ}$C.M.
80
60
40
20
$K^{*\circ}\pi^{-}$ P
(d)
+1
-1
P in $P\pi^{-}$C.M.
-1
+1
$K^{*\circ}$ in $K^{*\circ}\pi^{-}$C.M.
40
20
$\rho^{\bar{o}}\pi^{\pm}\lambda^{\circ}$
(e)
+1
-1
λ° in $\lambda^{\circ}\pi^{\pm}$ C.M.
-1
+1
$\rho^{\bar{o}}$ in $\rho^{\bar{o}}\pi^{\pm}$C.M.

FIG. 6.3.

FIG. 6.4.

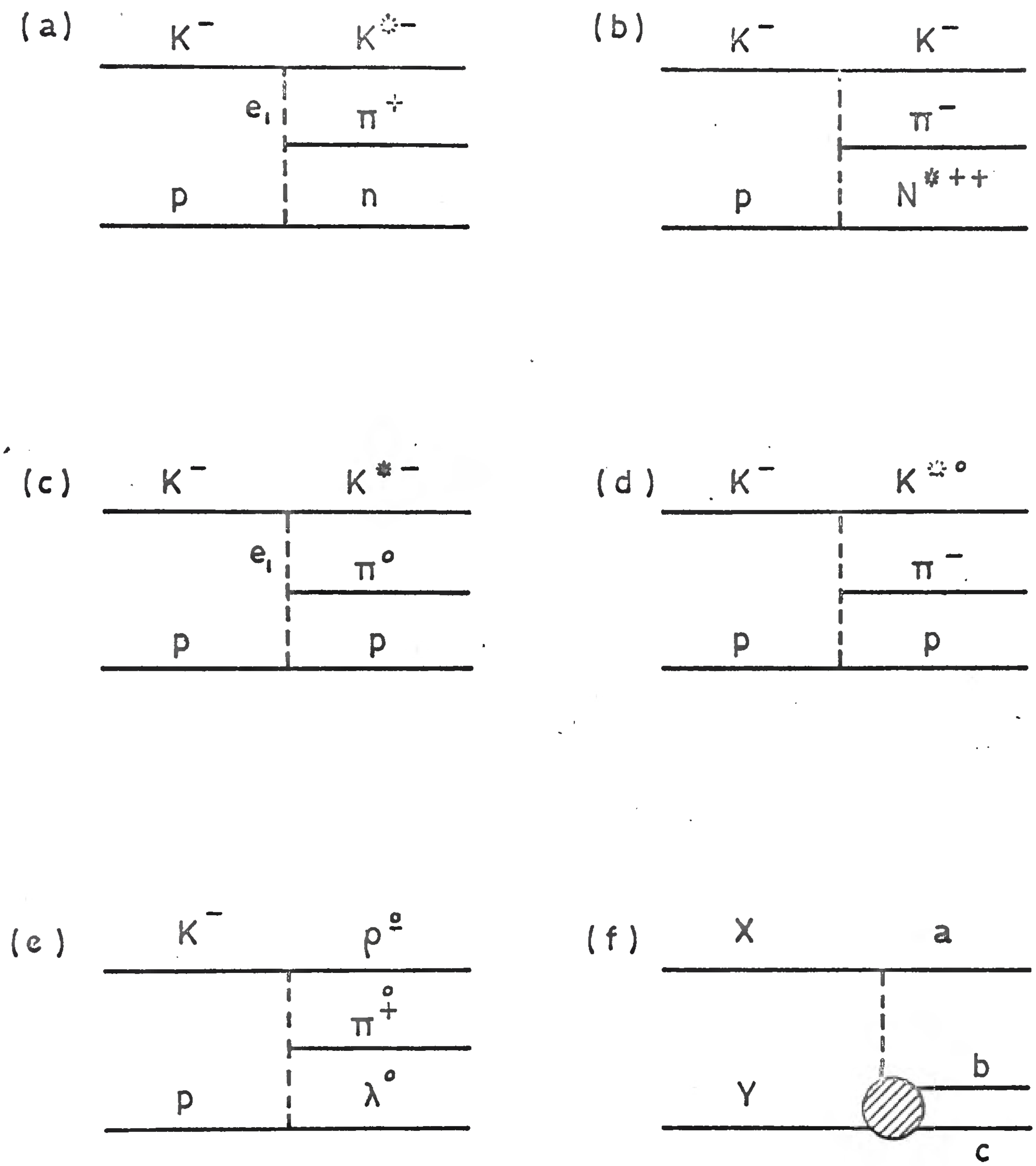

that the K^{*-} and neutron are mostly produced at small momentum transfers with respect to the K^- and proton respectively, and that the π^+ is produced isotropically with small momentum. These distributions suggest that the process might be dominated by an exchange diagram of the type shown in Fig 6.4a. However momenta have to be treated with caution in a multibody final state. The real test should be the angles in the $(K^{*-}\pi^+)$ centre of mass and in the $(n\pi^+)$ centre of mass - these angles are related by ~~the~~ Lorentz transformations to the angles and velocities in the overall centre of mass. In short, momenta are all important in the correct centre of mass in determining matrix elements and density of states factors but viewed from another centre of mass their mass dependent transformation properties can completely distort the picture.

Fig 6.3a shows the scattering angle of the K^{*-} with respect to the incident K^- in the $K^{*-}\pi^+$ centre of mass. The distribution is strongly peaked forwards. Also shown is the neutron scattering angle in the $n\pi^+$ centre of mass which is strongly peaked backwards. To show that these peaking effects are simultaneous we have made a scatter plot of the two momentum transfers. This is shown in Fig 6.2b. A strong concentration of events in the region where both momentum transfers are small is seen. These are the features we would expect of the graph 6.4(a). We now consider whether the other channels of Table 6.1 might be described by graphs 6.4(b) to 6.4(e). Scatter plots of transverse against longitudinal momentum for each particle of these four reactions shown the same features as observed in $K^{*-}\pi^{+}n$. The scattering angles in the appropriate "local centre of mass systems" are shown in Figs 6.3(b) to 6.3(e). These distributions show the same collimation as Fig 6.3(a). The four momentum transfer cut used in the ρ selection (Table 6.1) was applied to reduce background. The number of ρ events outside this cut off is small and hence the distributions shown in the text for these channels are not significally biassed.

6.3 Production angular distributions

To investigate the model further we choose a channel with the simplest final state spin-wise; e.g.

$$K^{-}p \rightarrow \Sigma^{0}\pi^{+}\pi^{-} \qquad 6.2$$

we consider a series of production angular distribution tests which can tell us about the nature of the exchanges.

Total centre of mass planar effect.

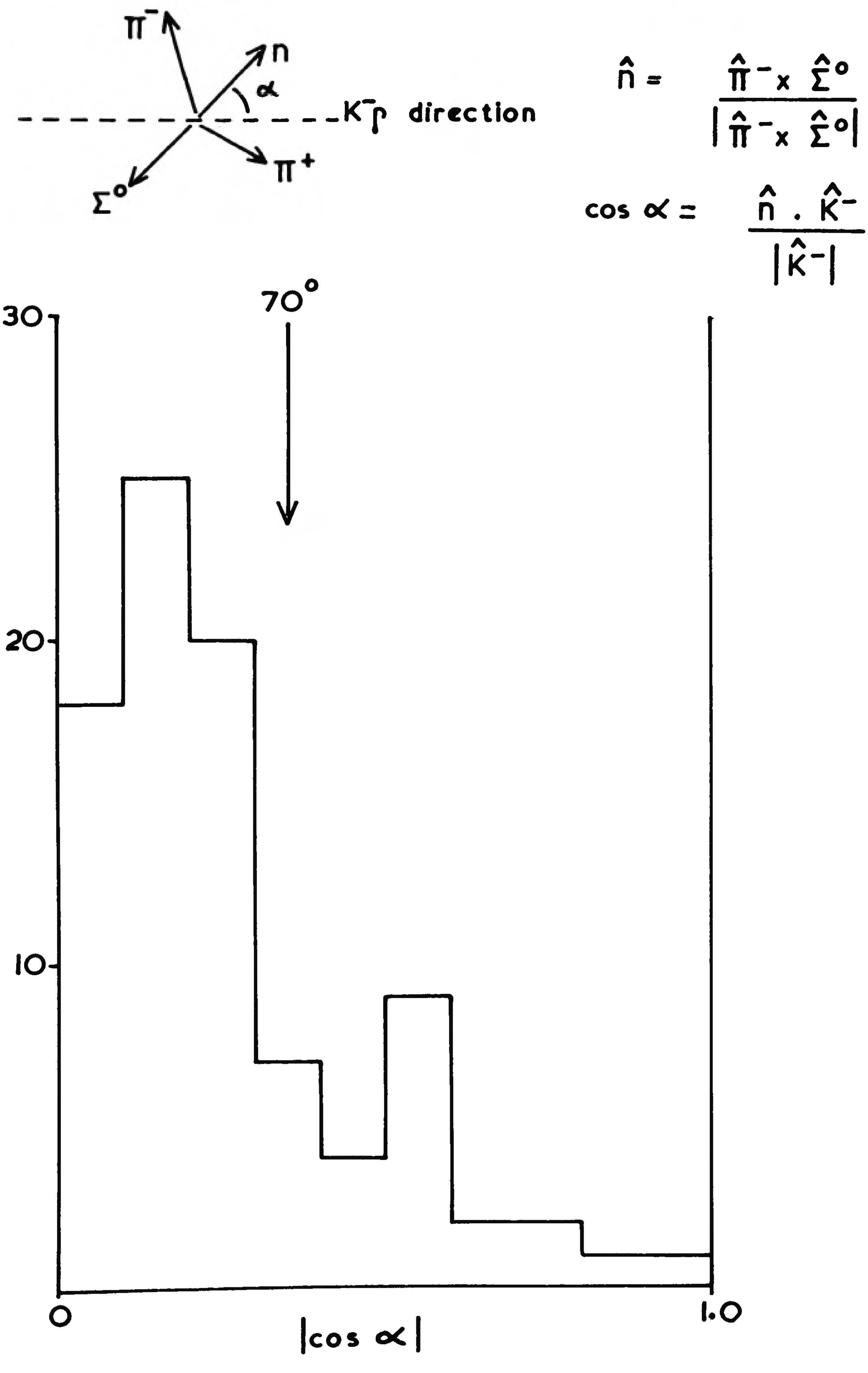

Fig. 6.5.

FIG. 6.6.

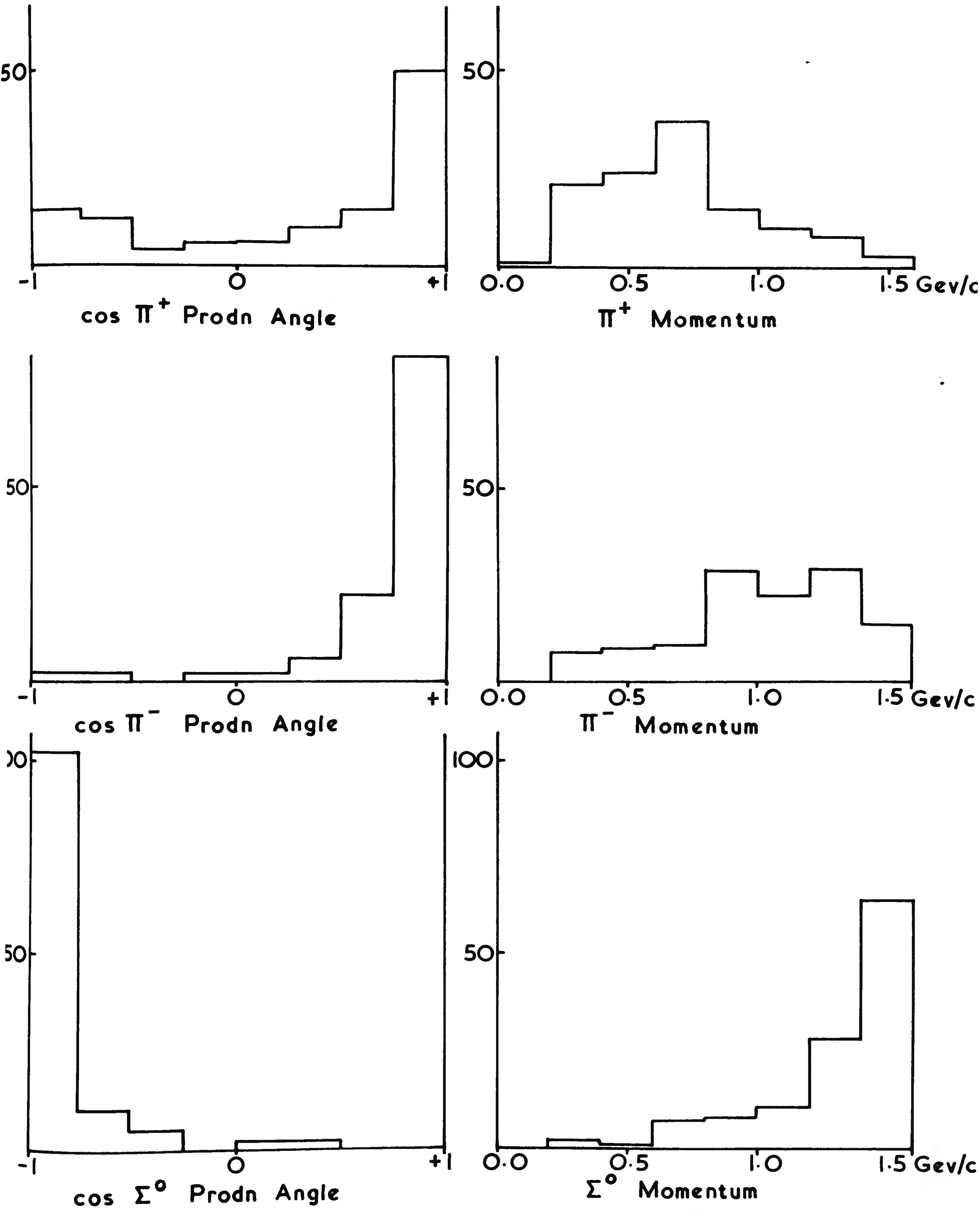
50
-1
0
+1
cos π⁺ Prodn Angle
50
0.0
0.5
1.0
1.5 Gev/c
π⁺ Momentum
50
-1
0
+1
cos π⁻ Prodn Angle
50
0.0
0.5
1.0
1.5 Gev/c
π⁻ Momentum
00
50
-1
0
+1
cos Σ⁰ Prodn Angle
100
50
0.0
0.5
1.0
1.5 Gev/c
Σ⁰ Momentum

a) <u>Total centre of mass planar effect</u>

In the total centre of mass the three outgoing particles move in a plane. Let the normal to this plane be $\hat{\underline{n}}$ (see Fig 6.5) and let the initial state axis lie at an angle α to $\hat{\underline{n}}$. If the final state had no memory of the initial state (phase space) the distribution of cos α would be flat. If however <u>any</u> of the final state particles is produced at low momentum transfer then the angle between the final state plane and the beam direction will be small i.e. α will be peaked at 90° (cos α = 0). A two-body peripheral process tends to be collinear - a three body peripheral process tends to be coplanar in the total centre of mass. Fig 6.5 shows the histogram of cos α for reaction 6.2. We conclude that there is strong peripheral production of some kind. This coplanarity effect must be distinguished from the coplanarity observed in the π^+ centre of mass discussed later. The latter is a kinematic effect present in phase space generated events while the former is purely dynamic.

b) <u>Total centre of mass production angles</u>

In Fig 6.6 we show the centre of mass angles and momenta of the three final state particles. Both the Σ^0 and π^-

The invariant mass spectra of the final state

$\Sigma^{0}\pi^{+}\pi^{-}$

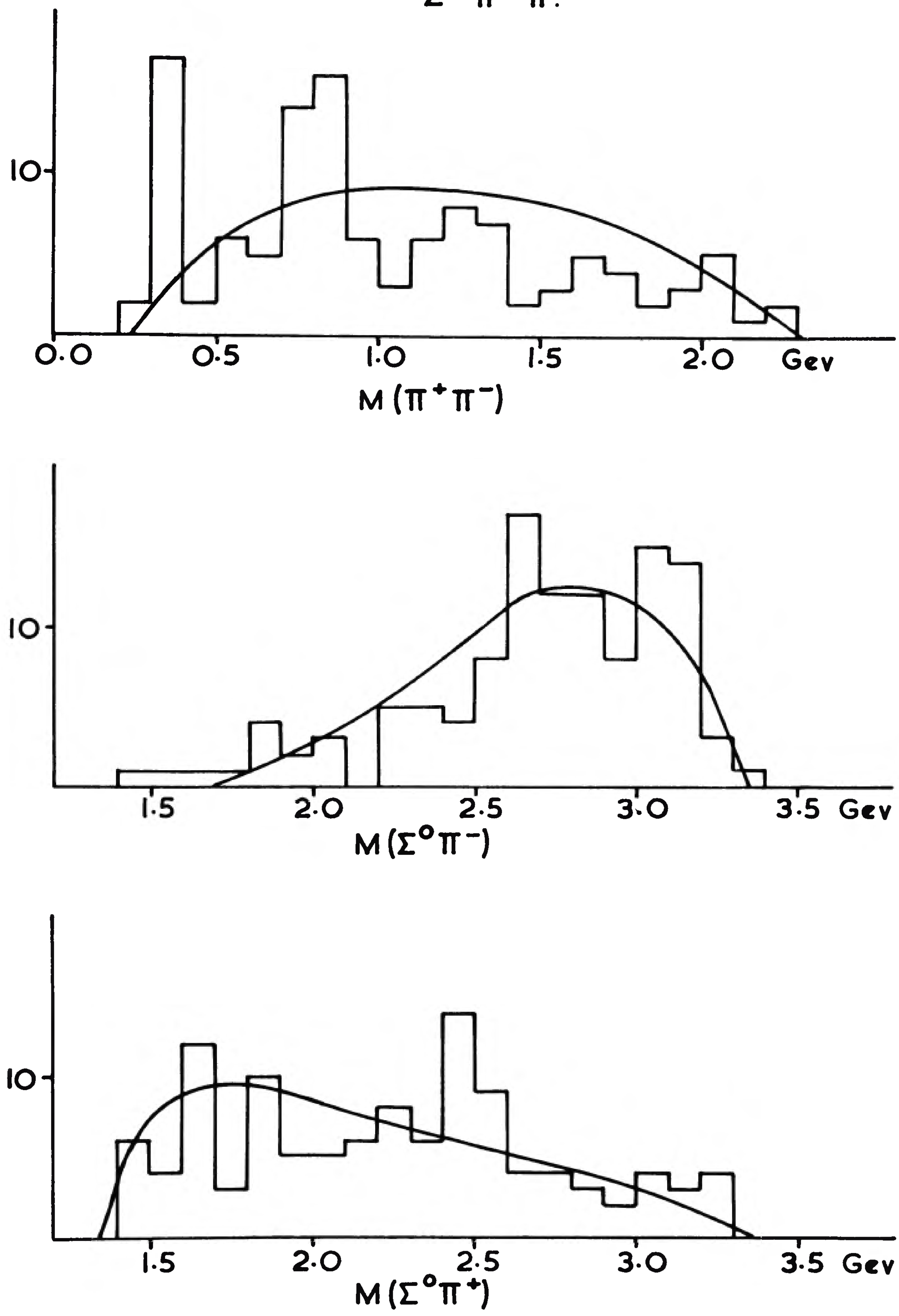

Fig. 6.7.

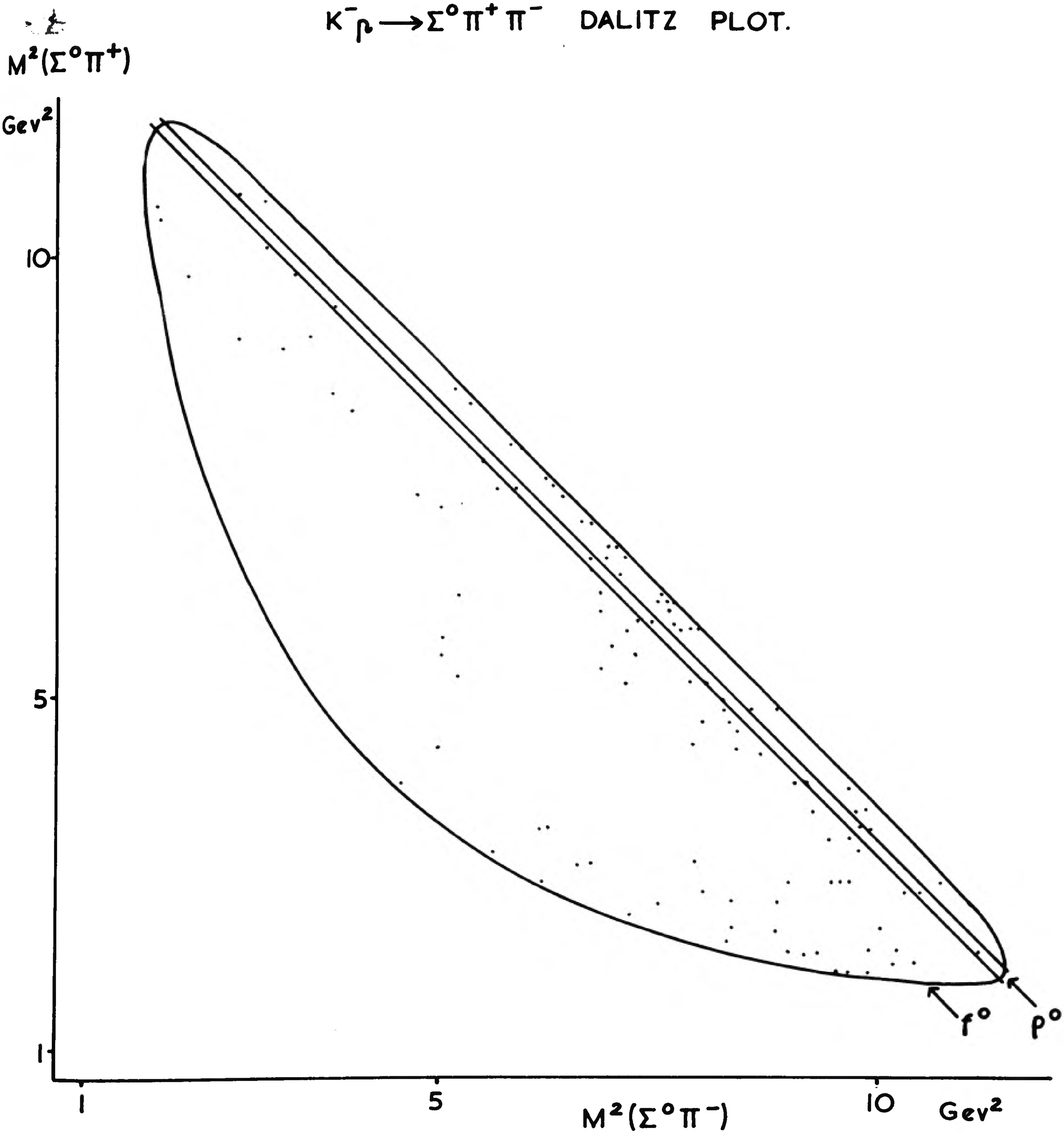

$K^-p \longrightarrow \Sigma^o\pi^+\pi^-$ DALITZ PLOT.
$M^2(\Sigma^o\pi^+)$
Gev²
10
5
1
1
5
10
Gev²
$M^2(\Sigma^o\pi^-)$
f°
ρ°

Fig. 6.8.

show the strong collimation associated with peripheral production - high momenta and peaked angular distributions. The forward peak of π^+ is due to resonance production and is removed later but otherwise the π^+ have low momenta and a flat angular distribution. To isolate the effects of quasi two body processes the mass distributions were examined as follows.

The Σ^0 and π^- angular distributions were used as weighting factors to generate double peripheral $\Sigma^0\pi^+\pi^-$ "events" with the Monte Carlo programme FAZALL. These phase space curves are superimposed on the mass spectra in Fig 6.7. The curves fit the data except for peaks in the $(\pi\,\pi)$ distribution at 800 MeV and below 400 MeV. The latter is attributed to events of the type $\Sigma^0\phi$ or $\Lambda\phi$ where the ϕ decays to K^+K^-. These kaons would have a high momentum in the laboratory and would be indistinguishable from pions. Since ambiguities of this type were assigned to the common hypothesis, contamination of this kind is to be expected (see chapter 4). The peak at 800 MeV is identified as the ρ^0. Fig 6.8 shows the Dalitz plot for this final state. The reflection of the "ϕ" events on the $\Sigma^0\pi^+$ and $\Sigma^0\pi^-$ mass distributions accounts for the excess of events in the region 2.5 - 2.6 GeV in both cases. No other significant resonances are observed. In particular $Y^{*+}(1660) \rightarrow \Sigma^0 \pi^+$ accounts for 4 ± 4 events. This is consistent with the number seen in the $\Sigma \pi\pi$ decay mode (chapter 5). It is possible that a few f° are produced. The observed angular distributions correspond to configurations which are nearly collinear and in which the Σ^0 and π^- travel in opposite directions. The locus of collinear configurations on a Dalitz plot is the boundary and, if Σ^0 and π^- move in opposite directions, they will have a high invariant mass. So we expect that events should congregate in a broad band adjoining the boundary in the right hand, high $M(\Sigma^0\pi^-)$, half of the Dalitz plot. Almost all events are seen to be in this band. Furthermore most of the events with <u>low</u> $M(\Sigma^0\pi^-)$ can be attributed to the ρ^0, "ϕ" and possible f° $(\pi\,\pi)$ invariant mass bands. We would emphasize that the Dalitz plot picture of double peripheral processes is just another way of looking at the problem and, while highlighting certain effects, does not produce anything which is not implicit in the angular distribution analysis. One such effect is the general depopulation of the centre of the Dalitz plot. This is discussed by Chan[1,2]. In all that

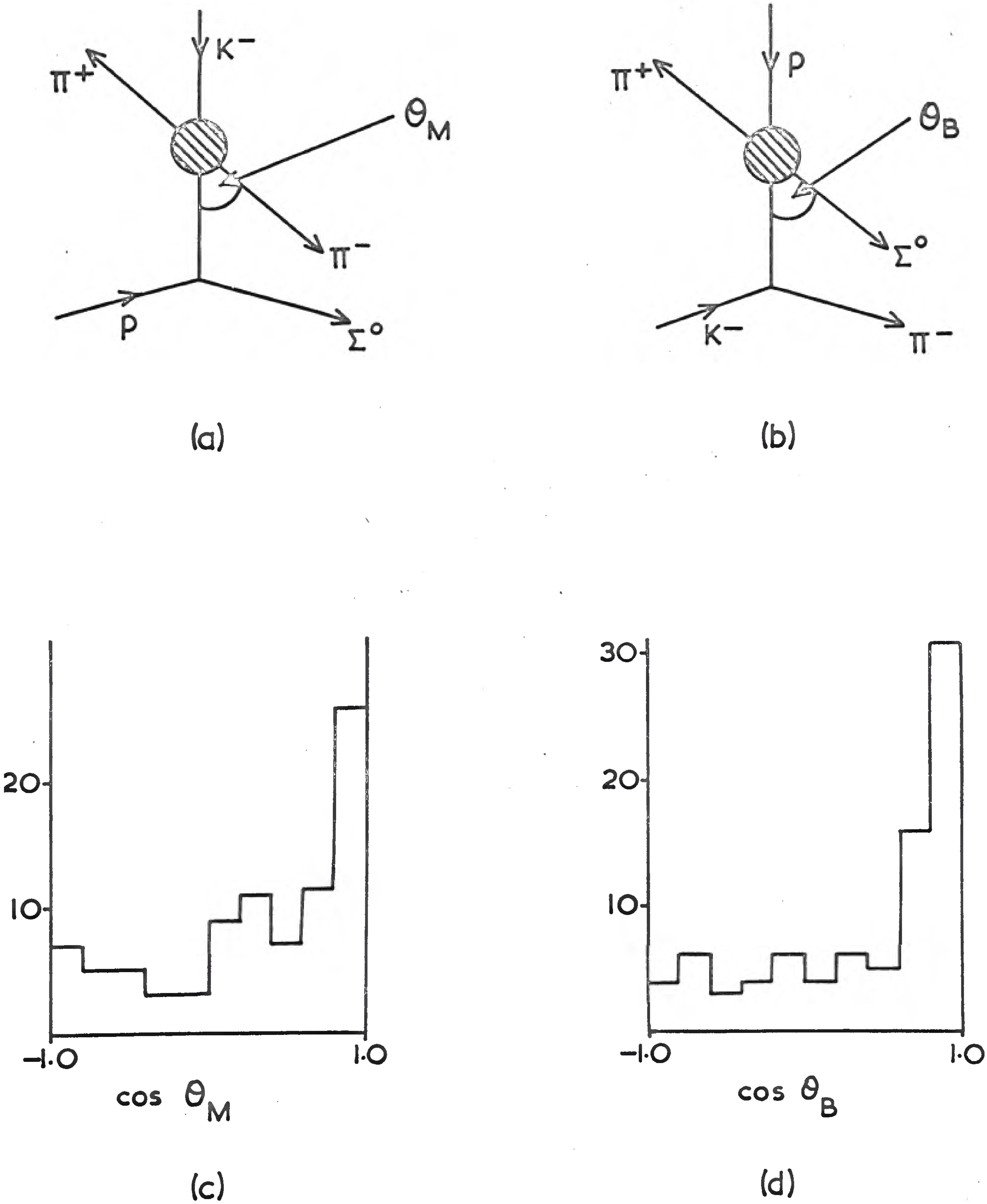

Fig 6.9.

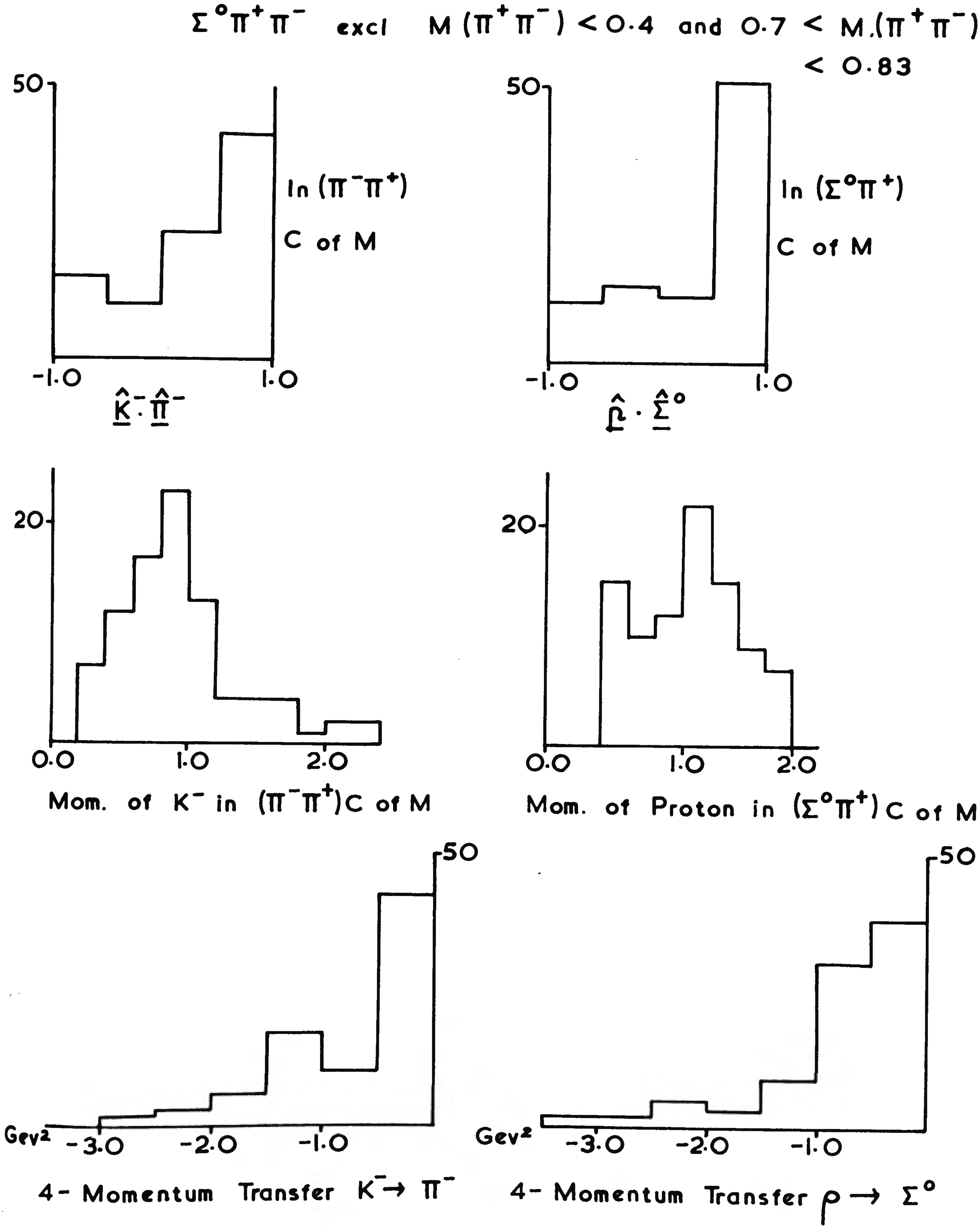

$\Sigma^0\pi^+\pi^-$ excl $M(\pi^+\pi^-) < 0.4$ and $0.7 < M(\pi^+\pi^-) < 0.83$
50
In $(\pi^-\pi^+)$
C of M
-1.0
1.0
$\hat{K}^- \cdot \hat{\pi}^-$
50
In $(\Sigma^0\pi^+)$
C of M
-1.0
1.0
$\hat{p} \cdot \hat{\Sigma}^0$
20
0.0
1.0
2.0
Mom. of K^- in $(\pi^-\pi^+)$ C of M
20
0.0
1.0
2.0
Mom. of Proton in $(\Sigma^0\pi^+)$ C of M
50
Gev²
-3.0
-2.0
-1.0
4- Momentum Transfer $K^- \rightarrow \pi^-$
50
Gev²
-3.0
-2.0
-1.0
4- Momentum Transfer $p \rightarrow \Sigma^0$

Fig. 6.10.

follows events in the "ϕ" band and in the ρ^0 band have been excluded from the data leaving 81 events (90 weighted). The same cuts have been made on all the Monte Carlo samples with which the data are compared. Taking into account the loss of events into the $\Lambda\pi^+\pi^-\pi^0$ fits discussed in chapter 4 the cross section for non resonant $\Sigma^0\pi^+\pi^-$ production is estimated to be 30 ± 10 μbarns - systematic effects of this loss are discussed later.

c) <u>Local centre of mass scattering angles θ_m and θ_B</u>

The angle θ_m is defined as the scattering angle of π^- in the $(\pi^-\pi^+)$ centre of mass; i.e. $\cos\theta_m = \underline{K}^-.\underline{\pi}^-$, as shown in Fig 6.9(a). Similarly θ_B is defined by $\cos\theta_B = \underline{p}.\underline{\Sigma}^0$ in the $(\Sigma^0\pi^+)$ centre of mass (Fig 6.9(b)). If the production process is dominated by a double peripheral mechanism, then the distributions should peak at $\cos\theta = +1$. In two body final states the scattering angle distributions are strongly affected by absorption; consequently in this case we do not attempt to fit these features quantitatively on the one particle exchange model. These angular distributions are shown in Fig 6.9(c) and (d), and support the double peripheral diagram of Fig 6.12(a). We note that, if we consider the

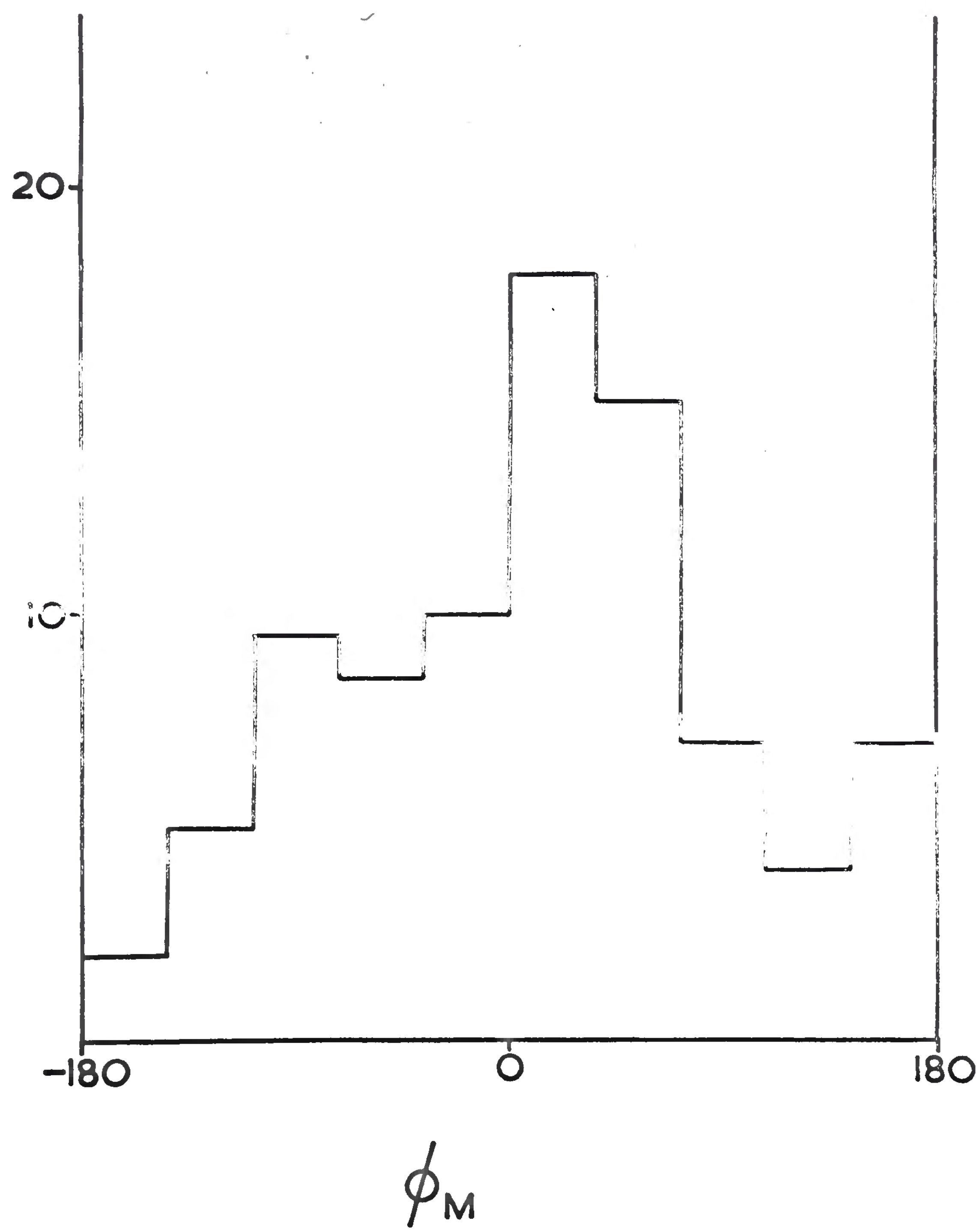

Fig 6.11.

exchange of only meson nonets, no other double peripheral diagram may be drawn. In the lower four plots of Fig 6.10 are shown the four momentum transfers of the two propagators and the initial state local centre of mass momenta. The former are peaked in the region near $t = 0$ as expected; the latter show that even in the local centres of mass the momenta are sufficiently high for peripheral interactions to dominate.

Next we attempt to identify the spins and parities of these exchanges:

d) <u>Local centre of mass production azimuths ϕ_m and ϕ_B</u>

The azimuth ϕ_m is the angle between the $\underline{K}^- \times \underline{\pi}^-$ and the $\underline{p} \times \underline{\Sigma}^0$ planes in the $(\pi^-\pi^+)$ centre of mass. This is identical with the Treiman-Yang angle which is normally considered when ~~with~~ $(\pi^-\pi^+)$ form a resonance. If the exchanged particle e_2 in Fig 6.12(b) is pseudoscalar the original Treiman-Yang argument(3) requires an isotropic ϕ_m distribution, regardless of whether the $(\pi^-\pi^+)$ system resonates or not. The distribution in ϕ_m (Fig 6.11) exhibits (a) symmetry about 180°, as required by parity conservation, and (b) anisotropy, indicating at most only a small contribution from pseudoscalar exchange (for e_2). The lack of symmetry

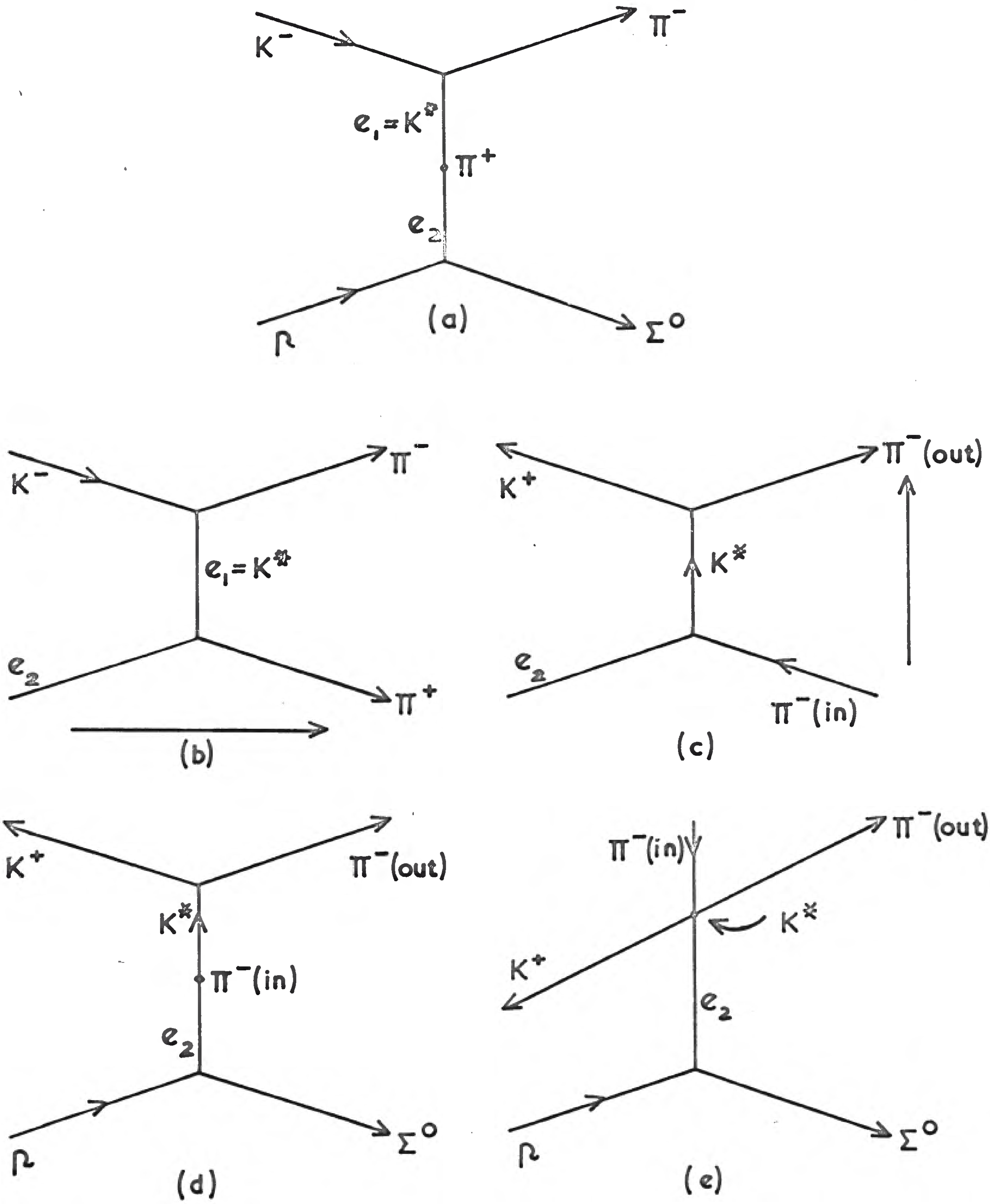

K⁻
π⁻
e₁ = K*
π⁺
e₂
p
Σ⁰
(a)
K⁻
π⁻
e₁ = K*
e₂
π⁺
(b)
K⁺
π⁻(out)
K*
e₂
π⁻(in)
(c)
K⁺
π⁻(out)
K*
π⁻(in)
e₂
p
Σ⁰
(d)
π⁻(in)
π⁻(out)
K*
K⁺
e₂
p
Σ⁰
(e)

Fig 6.12.

about 90° arises from the mixing of parity states in the $(\pi^-\pi^+)$ system which is not restricted.

The azimuth ϕ_B is defined analogously as the angle between the $\underline{p} \times \underline{\Sigma}^0$ and $\underline{K}^- \times \underline{\pi}^-$ planes in the $(\Sigma^0\pi^+)$ centre of mass, and anisotropy in its distribution could provide information about the spin parity of e_1. In fact no anisotropy is observed in this case. Pseudoscalar exchange is however forbidden by spin parity conservation at the top vertex, so that, within the limitations of our assumptions, we can identify e_1 as $K^*(890)$ and e_2 as predominantly $K^*(890)$.

e) <u>The production azimuth ϕ in the π^+ rest frame</u>

The angle ϕ is defined as the angle between the planes $\underline{p} \times \underline{\Sigma}^0$ and $\underline{K}^- \times \underline{\pi}^-$ in the π^+ rest system. The vectors appear as shown in Fig 6.12(a) and

$$\cos \phi = \frac{(\underline{p} \times \underline{\Sigma}^0) \cdot (\underline{K}^- \times \underline{\pi}^-)}{|\underline{p} \times \underline{\Sigma}^0| \; |\underline{K}^- \times \underline{\pi}^-|} \qquad 6.3$$

The effect of crossing the incoming K^- with the outgoing π^+ in the part of the diagram shown in Fig 6.12(b) is to convert it into 6.12(c). This crossing operation on Fig 6.12(a) thus produces the situation shown in 6.12(d) which describes the two body reaction:

$$K^-p \to \Sigma^o K^{*o}; \qquad K^{*o} \to K^+\pi^- \qquad 6.4$$

Various experiments show that this reaction proceeds by a mixture of K and K^* exchange with the latter being dominant(4). A Lorentz transformation along the K^* direction into its rest frame (Fig 6.12(e)), which does not affect the value of ϕ, results in ϕ being identified with the conventional Treiman-Yang decay angle of the K^* for this two body process. Thus, if e_2 is the same for both reactions, then so is the ϕ dependence of the matrix element. (The dependence on the polar angle θ of the decay of the K^* in reaction 6.4 becomes a dependence on β_1 (defined in appendix G) for reaction 6.2. The resulting s and t behaviour is strongly modified by absorption as discussed in appendix F and therefore not compared with experiment.) The dependence of the square of the matrix element on ϕ is thus of the form:

a) constant for $e_2 = K$

b) $1 - x + 2x \sin^2\phi$ for $e_2 = K^*(890)$ 6.5

Here x = 1 for spin non flip coupling at the baryon vertex, and $x = \rho_{1-1}/\rho_{11}$ for spin flip coupling, where ρ_{ij} is the density matrix of the K^* in the crossed channel. An

Monte Carlo calculations of ϕ distribution.

Low energy $\pi\pi$ bands excluded

Smooth curve from 5572 random events

Histogram from 409 collimated events.

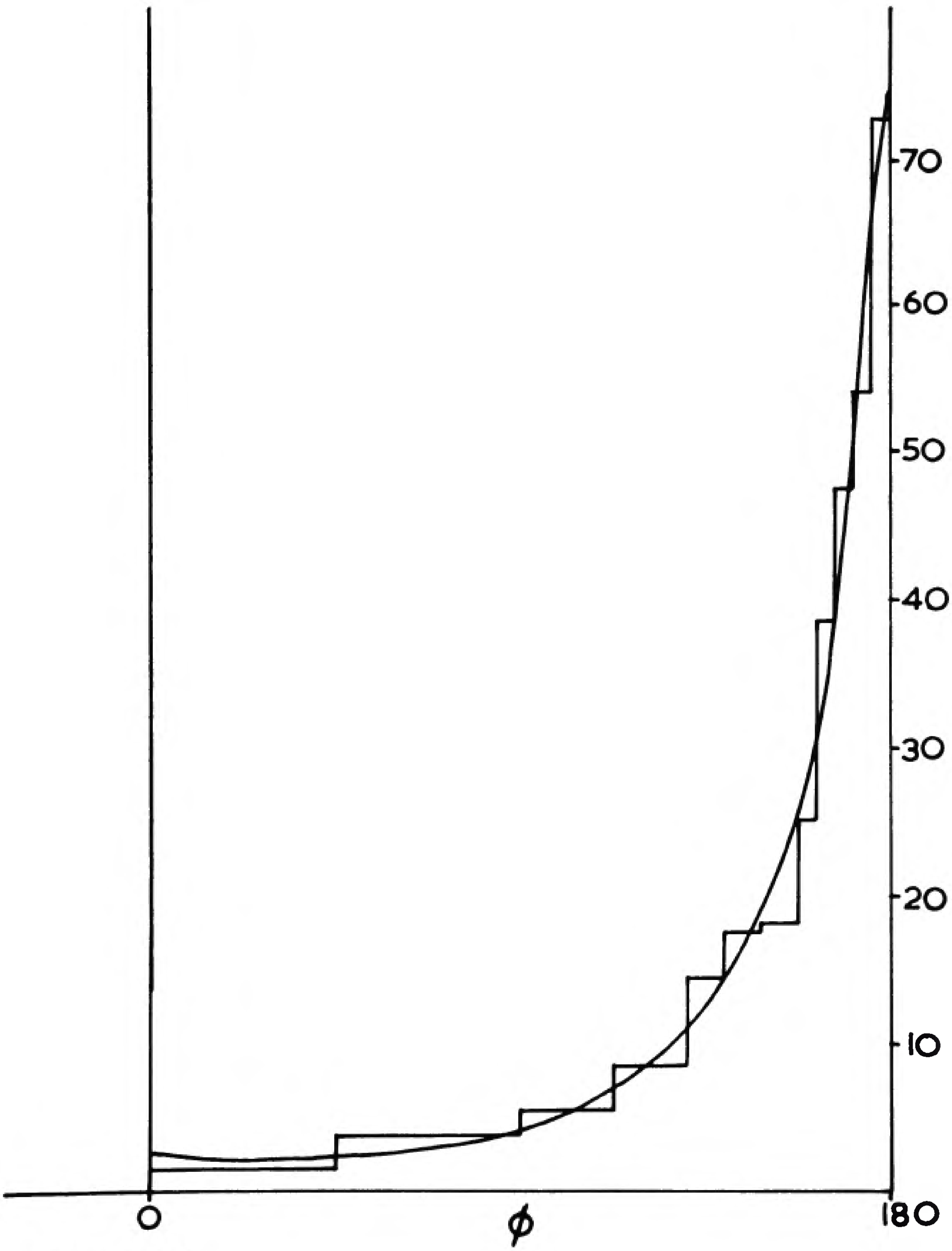

Fig. 6.13.

alternative derivation of these results without the use of crossing symmetry is given in appendix G.

All this time we have spoken of matrix elements and ignored the density of states factor. In decay correlations such as those of the K^* in reaction 6.4 the density of states is spherically symmetric for the decay of the K^* in its rest frame - that is the δ-function ensuring overall energy-momentum conservation is satisfied quite independently of how the K^* decays. In the crossed reaction $K^- p \rightarrow \Sigma^0 \pi^+ \pi^-$ the δ-function is very different and the density of states can be a function of ϕ. The smooth curve in Fig 6.13 represents the ϕ distribution for $\Sigma\pi\pi$ "events" generated according to phase space. The histogram is the distribution for 409 "events" obtained by weighting the phase space "events" with the experimental angular distributions as earlier. The agreement between the two is impressive. It suggests that the collimation of the polar angular distributions does not affect the ϕ distribution and consequently that the effects of absorption on ϕ should be slight. We use the curve as the ϕ dependence of the density of states, $\rho(\phi)$. Fig 6.14(a) shows an experimental histogram of x calculated as shown in appendix G. By folding this experimental histogram

Experimental plot of $x = (\cos^2\beta_2 - 1)/(\cos^2\beta_2 + 1)$ where β_2 is the scattering angle in the cross channel for the lower propagator.

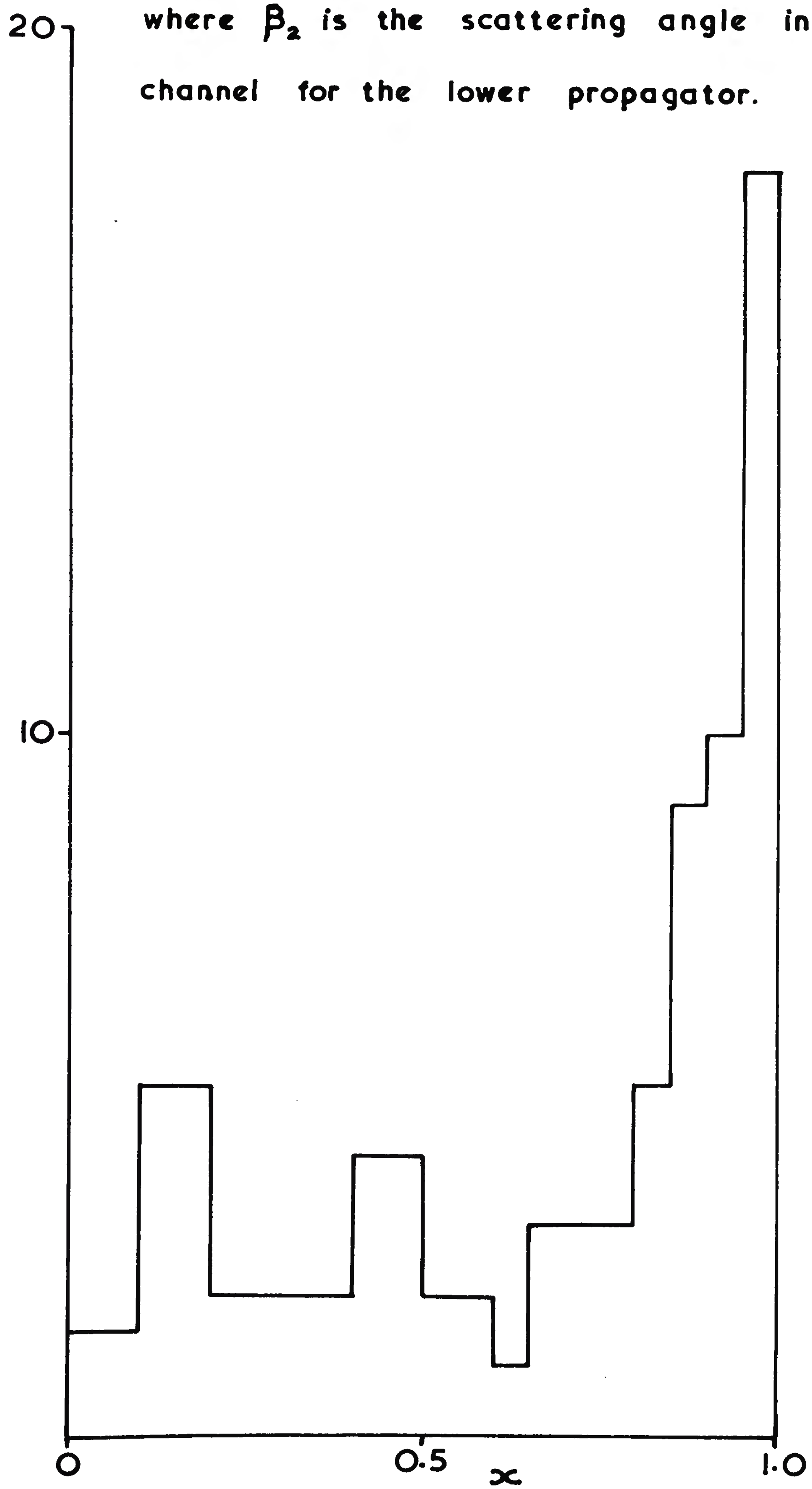

Fig. 6.14(a).

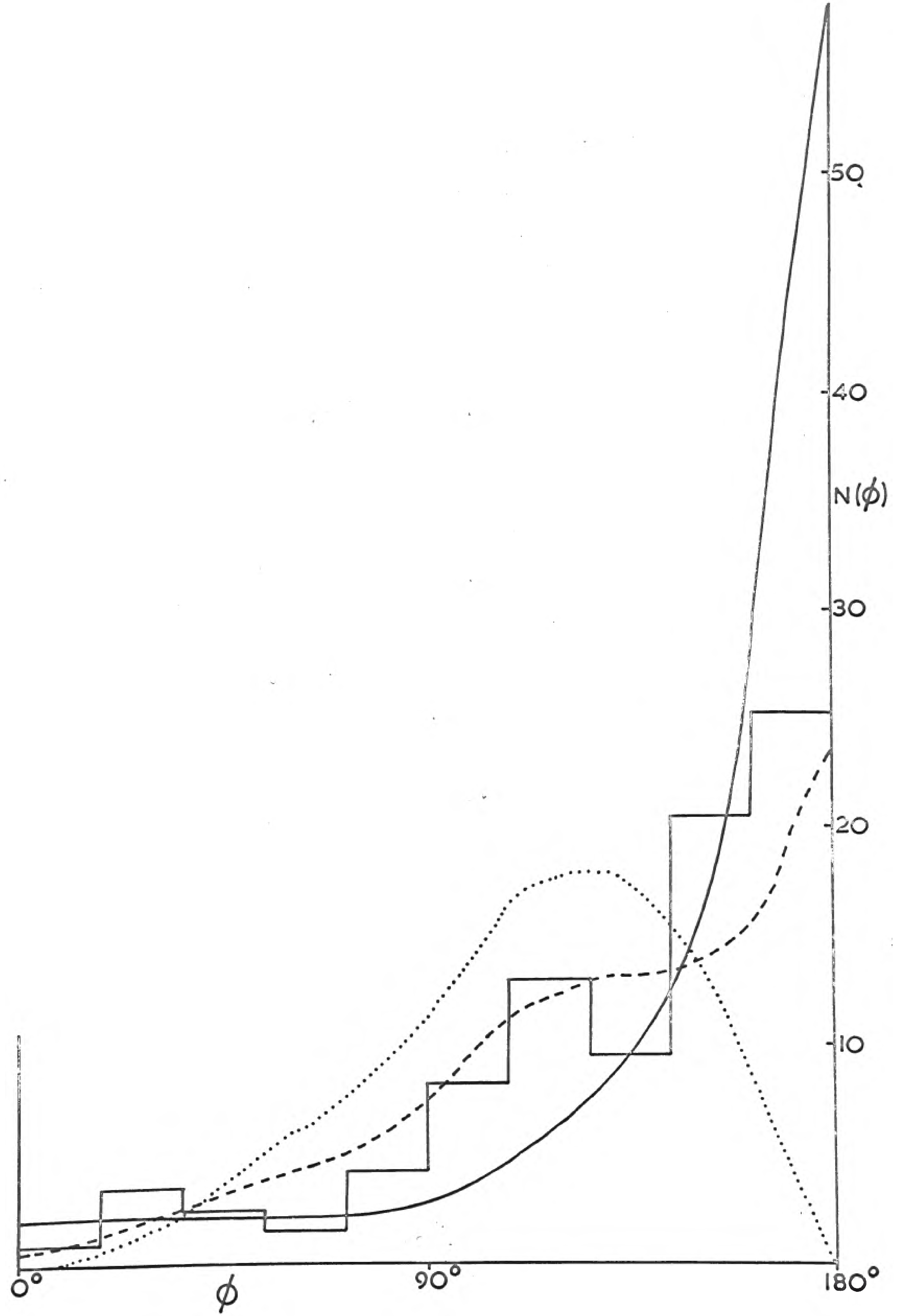

Fig 6.14(b)

into equation 6.5 we can get a prediction for the spin flip matrix element.

Fig 6.14(b) shows the experimental histogram in ϕ. The curves are calculated from:

$$N(\phi) \sim \rho(\phi) \times (\text{matrix element})^2 \qquad 6.6$$

All the curves are normalised to the total number of events. The spin flip curve was calculated from the distribution in Fig 6.14(a) so that each event is normalised to one event in the ϕ distribution:

$$N(\phi) = \sum_{\substack{i\ \text{all} \\ \text{events}}} n_i(\phi) \sim \sum_i \rho(\phi) \times (1 - x_i + 2x_i \sin^2\phi) \qquad 6.7$$

where x_i is the value of x for the i^{th} event and where $\int n_i(\phi)d\phi = 1$ for each event.[5] The sensitivity of the test relies on the fact that terms in $\sin^2\phi$ vanish where phase space is a maximum.

The losses, biasses and ambiguities affecting this final state are discussed in chapter 4. It is shown there that about 25% of the $\Sigma^0\pi^+\pi^-$ events are to be found in the $\Lambda\pi^+\pi^-\pi^0$ "fits" with $(\Lambda\pi^0)$ invariant mass less than 1350 MeV. We have treated these events in parallel by treating the four vector of the $(\Lambda\pi^0)$ system as the "Σ^0" in our analysis. The azimuthal distribution ϕ_m corresponding to Fig 6.11 for

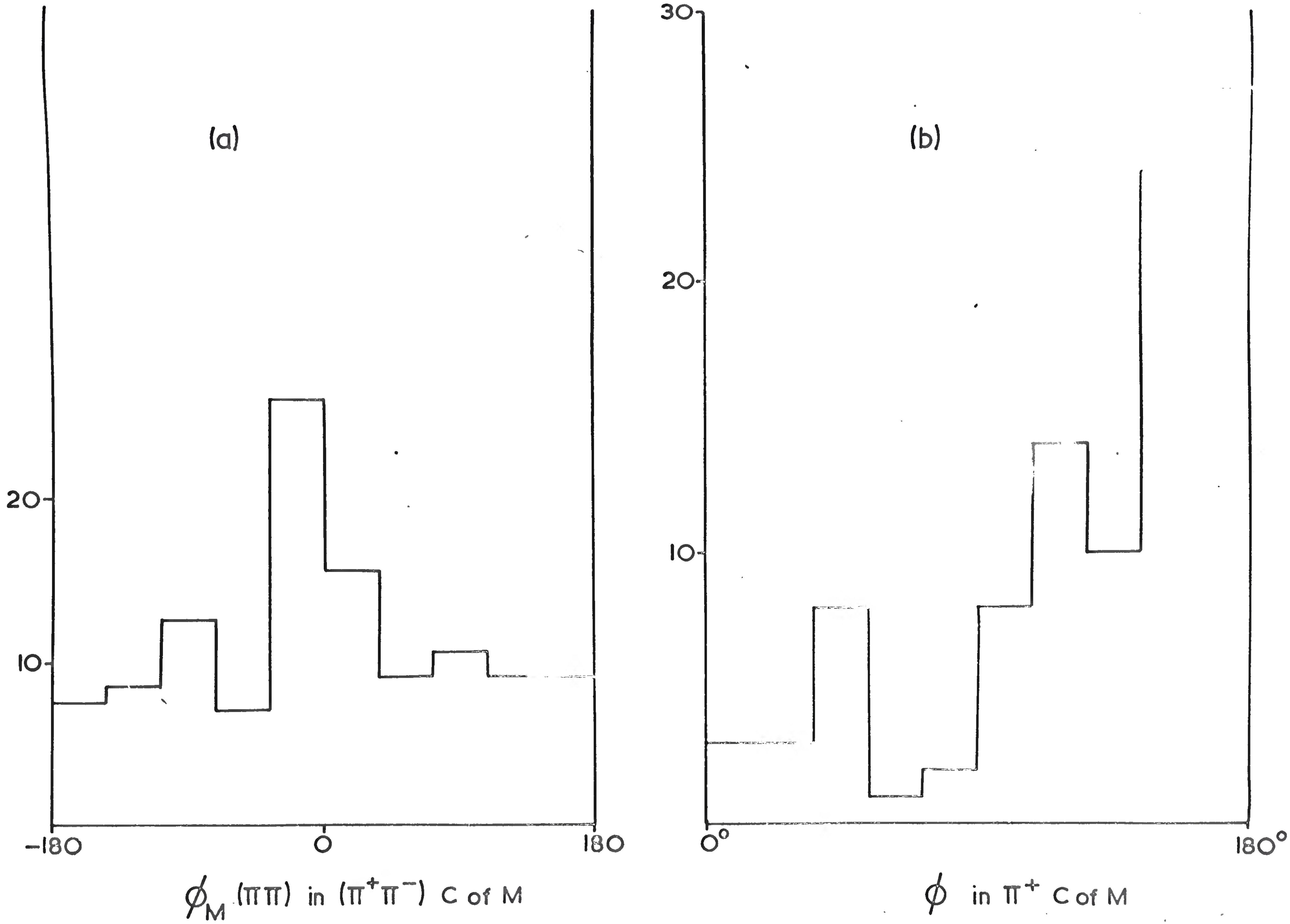

(a)
20
10
-180
0
180
ϕ_M ($\pi\pi$) in ($\pi^+\pi^-$) C of M
(b)
30
20
10
0°
180°
ϕ in π^+ C of M

Fig 6.15.

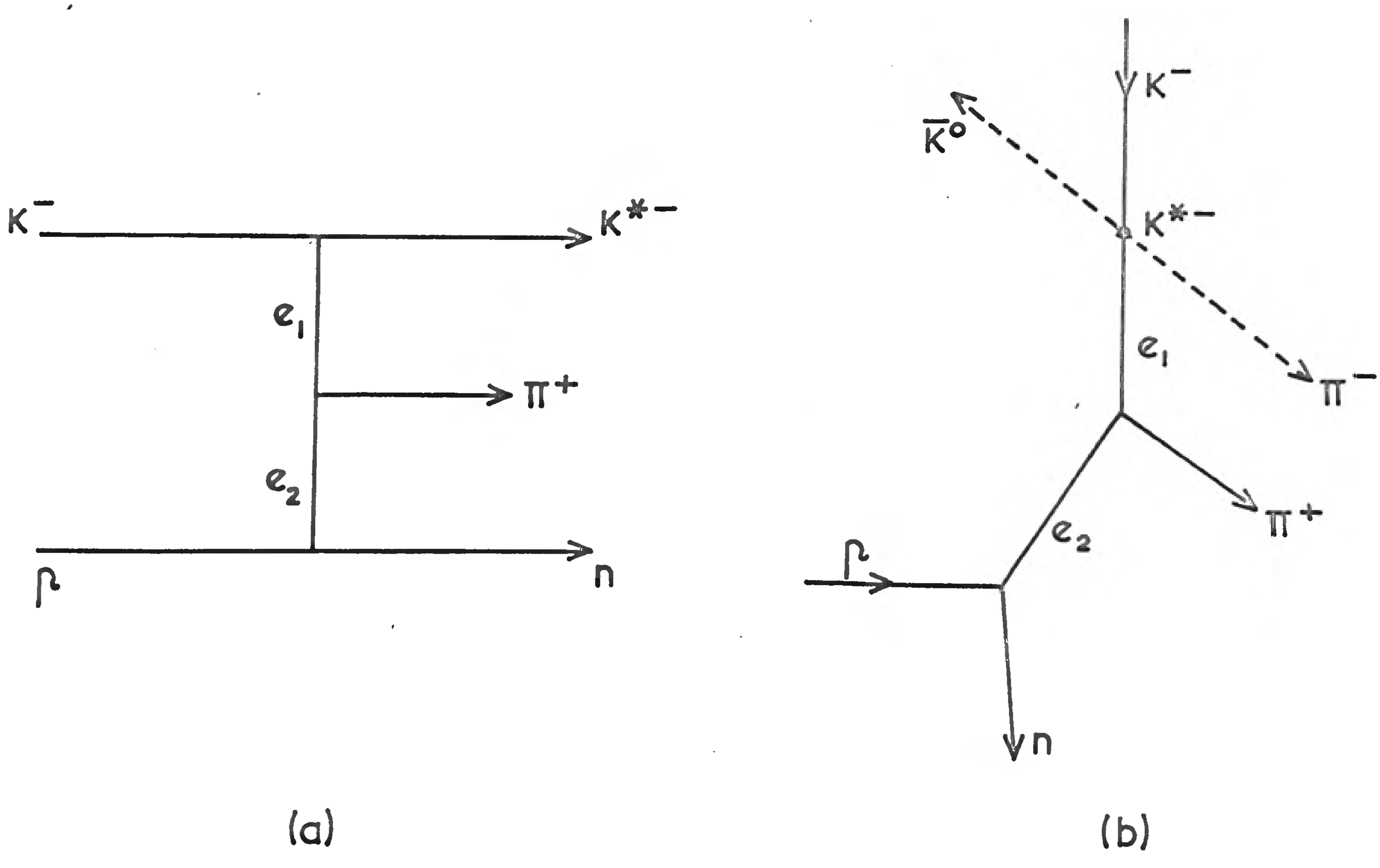

Fig 6.16.

these events is shown in Fig 6.15(a). The ϕ distribution corresponding to Fig 6.14(b) is shown in 6.15(b). They are seen to contain the same features as the $\Sigma\pi\pi$ fits. We conclude that our $\Sigma\pi\pi$ sample is not significantly biassed by the loss of events into the $\Lambda\pi^+\pi^-\pi^0$ channel.

Although this loss of events prevents our drawing any firm conclusion from Fig 6.14(b) regarding K exchange, it is clear that the data rule out pure K^* spin non flip exchange. Combining this with the evidence of the other distributions discussed above we conclude that the data for this reaction are consistent with the diagram shown in Fig 6.10 in which both exchanged particles are K^*s and the spin of the baryon current is flipped. The data are equally consistent with a combination of K and K^* (with no spin flip) in the lower propagator e_2. This is in reasonable agreement with the results for the reaction $\pi^-p \rightarrow \Sigma^0K^{*(4)}$.

6.4 Decay Angular Distributions

In reaction 6.1 additional information can be derived from the decay of the K^*. Fig 6.16(a) shows the double peripheral diagram suggested by the analysis of the production angles. In the K^* centre of mass the vectors appear as

$K^-p \rightarrow K^{*-}\pi^+n$

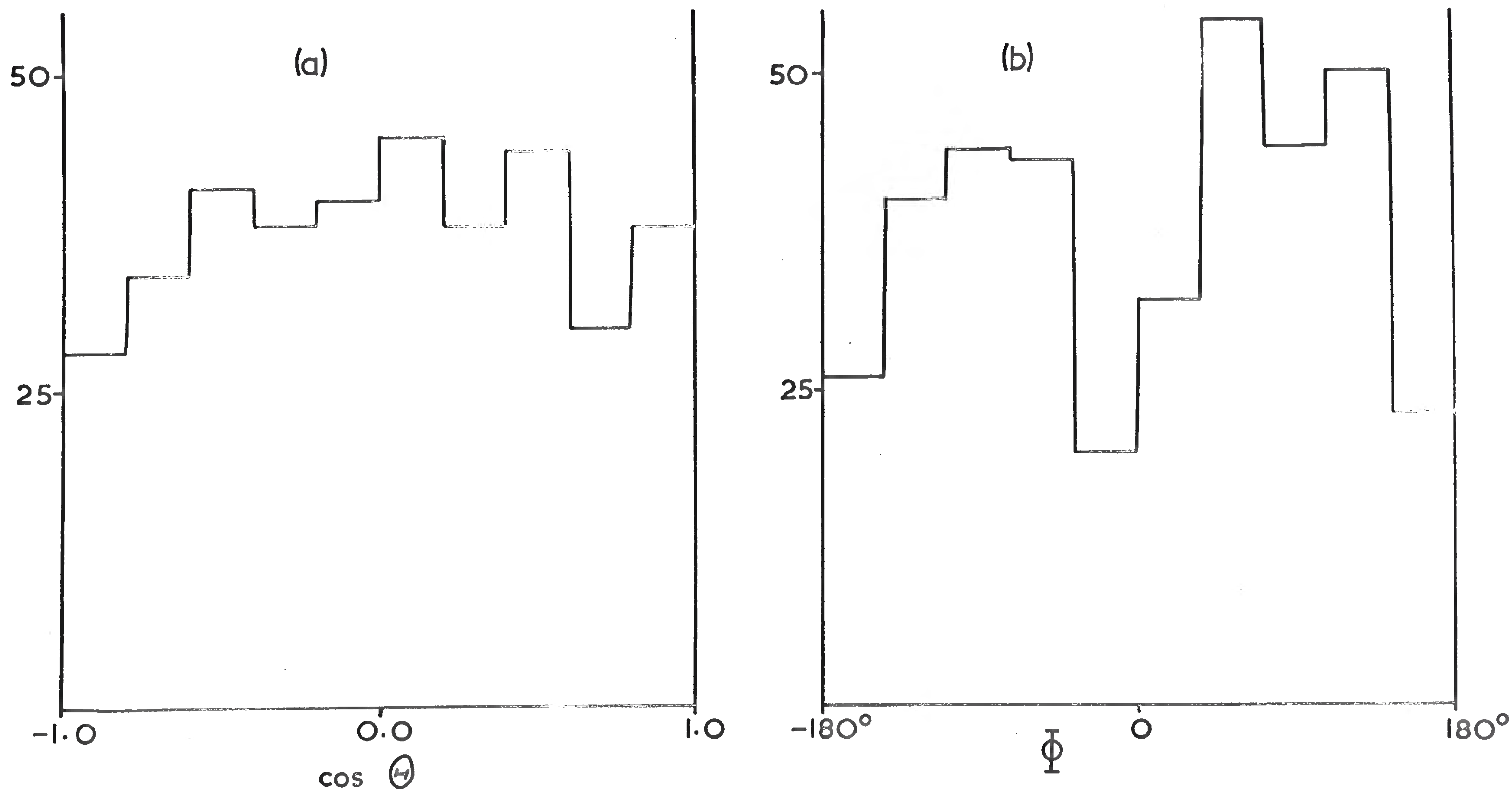

Fig 6.17.

shown in Fig 6.16(b). The decay angles are defined as follows:

<u>The polar angle Θ</u> : $\cos \Theta = \underline{K}^{-}.\underline{K}^{o}$ 6.8

in the rest frame of K^{*}. The experimental histogram is shown in Fig 6.17(a).

<u>The azimuthal decay angle Φ</u>. This is the angle between the $\underline{K}^{-} \times \underline{\pi}^{-}$ and the $\underline{K}^{-} \times \underline{\pi}^{+}$ planes in the K^{*} centre of mass. The experimental histogram is shown in Fig 6.17(b) and exhibits a strong $\sin^2 \Phi$ dependence. We also define the production azimuth $\emptyset$ as in equation 6.3:

$$\cos \emptyset = \frac{(\underline{K}^{-} \times \underline{K}^{*-}) \cdot (\underline{p} \times \underline{n})}{|\underline{K}^{-} \times \underline{K}^{*-}| \; |\underline{p} \times \underline{n}|} \qquad 6.9$$

Again we denote the density of states factor by $\rho(\emptyset)$ which is independent of $\cos \Theta$ and Φ.

When e_1 is pseudoscalar the angular distribution is given by:

$$W (\cos \Theta, \Phi, \emptyset) \sim \cos^2 \Theta \, \rho(\emptyset) \qquad 6.10$$

as derived in appendix G. Clearly the histograms of Fig 6.17 are inconsistent with this.

If e_1 is vector, the distribution depends also on the spin of e_2. When the latter is pseudoscalar, we have:

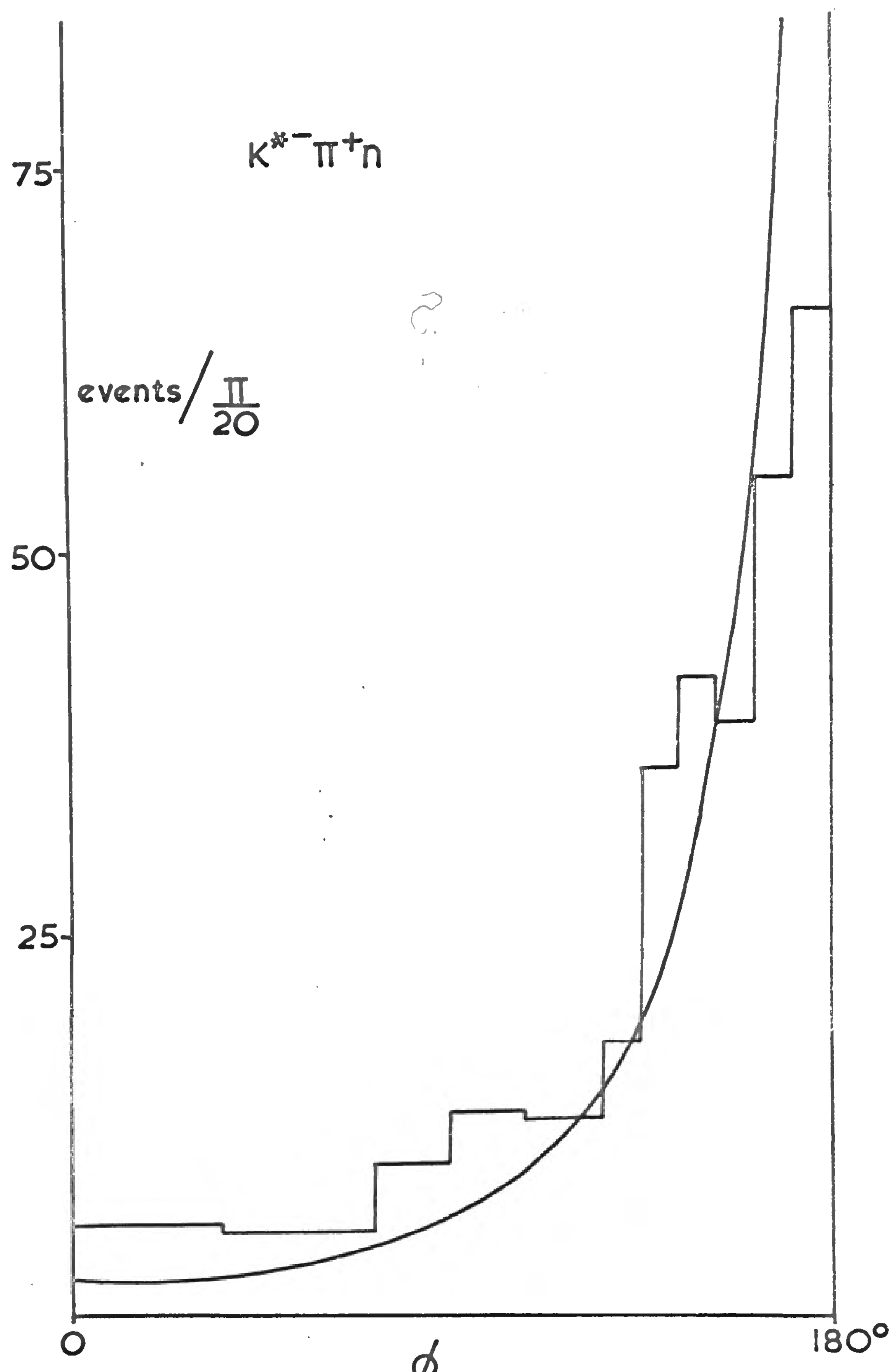

Fig 6.18.

$$W(\cos\Theta, \Phi, \phi) \sim \sin^2\Theta \sin^2\Phi\, \rho(\phi) \qquad 6.11$$

Our data are consistent with a strong contribution from this assignment (see also Fig 6.18).

The distributions for $e_1 = e_2$ = vector derived in appendix C for both the spin flip and non flip cases have a complicated ϕ dependence. When they are averaged over the other variables, the coefficients of $\cos^2\phi\, \rho(\phi)$ and $\sin^2\phi\, \rho(\phi)$ are both important. Thus, even in these cases, no strong deviations from $\rho(\phi)$ are expected. On the other hand, in contrast with equation 6.11, when the expression C21 or C28 is averaged to obtain the predicted Φ distribution, both strong $\sin^2\Phi$ and $\cos^2\Phi$ terms are retained. The predominantly $\sin^2\Phi$ behaviour observed is thus incompatible with e_2 being vector.

Summarising we find that our data for reaction 6.1 are consistent with, though not conclusive evidence for, the assignment e_1 = vector e_2 = pseudoscalar.

In the early stages of the analysis of this data it was shown that the K^* decay exhibited a strong $\sin^2$ dependence in azimuth very similar to the plot 6.17(b) when azimuth was defined with respect to the $\underline{K}^- \times \underline{p}$ plane in the K^{*-} rest frame. This is due to the small angle between the $\underline{K}^- \times \underline{p}$

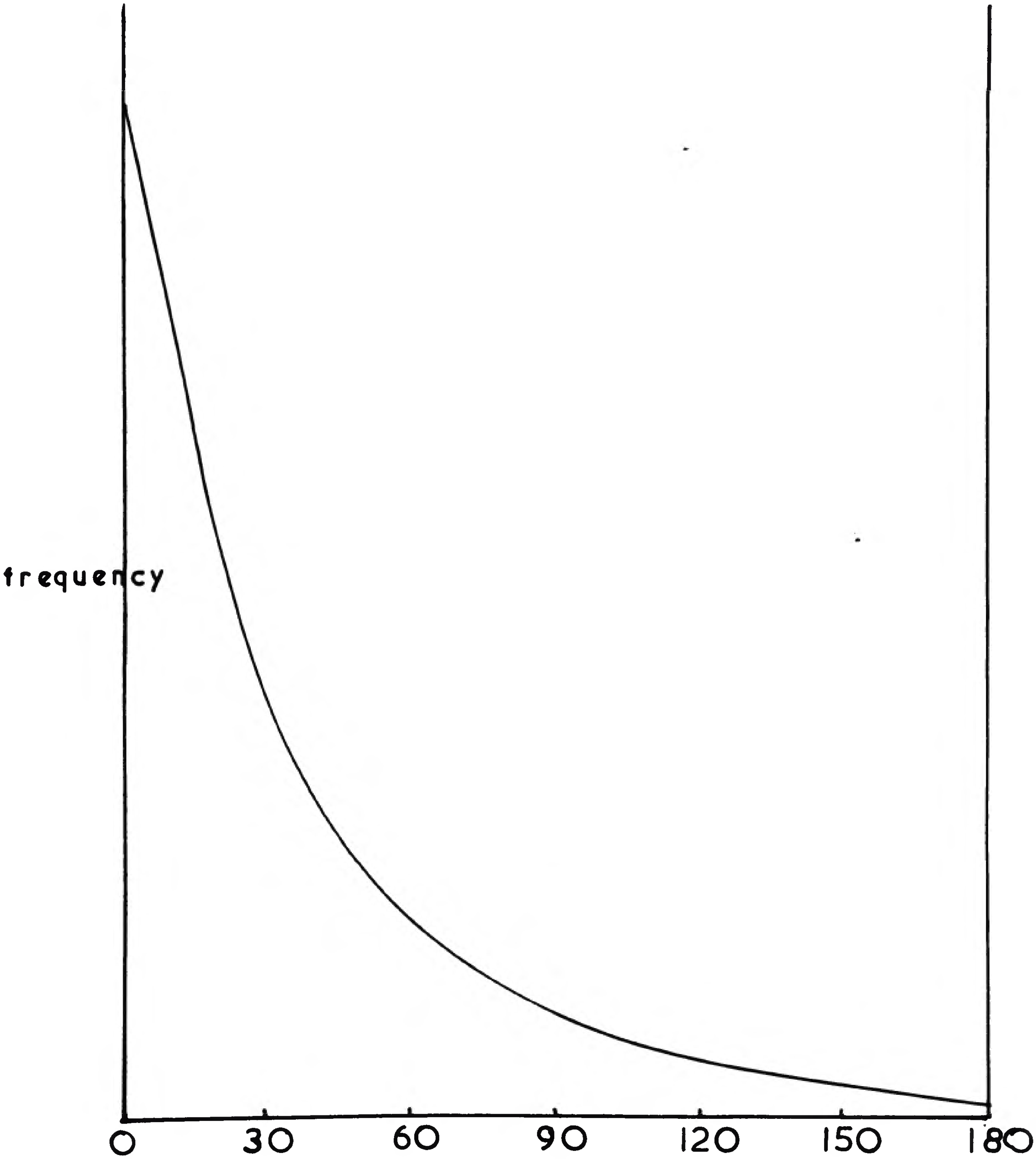

The angle between the two azimuth defining planes for phase space "events".

fig 6.19

and K^- x π^+ planes in the K^{*-} centre of mass. This is shown in Fig 6.19 for phase space events. The effect of folding this smearing into a $\sin^2$ distribution is small. We therefore regard the early correlation as rather misleading.

REFERENCES TO CHAPTER 6

(1) H.M. Chan et al: CERN preprint (1966) TH 679.

(2) H.M. Chan et al: CERN preprint (1966) TH 719.
Chan also discusses the azimuthal angle ∅.

(3) S.B. Treiman and C.N. Yang: Phys. Rev. Lett. **8**, 140 (1962).

(4) G. . mith et al: Phys. Rev. Lett. **10**, 138 (1963);
D.H. Miller et al: Phys. Rev. **140**, B360 (1965);
J. Bartsch et al: Nuovo Cim. **43**, 1010 (1966);
T.P. angler et al: Phys. Rev. **137**, B414 (1965).

(5) The use of the experimental values of x in predicting the angular distributions is discussed in a note at the end of Appendix .

APPENDIX A

Calculation of projected decay angle spectrum for charged sigmas

A change in the component of sigma momentum perpendicular to the front glass has no effect on the projected decay angle distribution. It is therefore sufficient to consider a sigma with momentum, **P**, in the plane of the front glass - the results will hold good also for sigmas with any component of momentum perpendicular to the front glass. Denote the sigma mass by M and the mass of the charged decay product by m. Let the momentum of the decay product in the sigma centre of mass be **p**. We use spherical polar co-ordinates in the sigma centre of mass with **P** as the polar axis, $\theta = 0$, and the plane $\phi = 0$ parallel to the front glass. The 4-vector momentum of the charged decay product is then:

$$\begin{pmatrix} p \sin\theta \cos\phi \\ p \sin\theta \sin\phi \\ p \cos\theta \\ \sqrt{p^2+m^2} \end{pmatrix}$$

When we transform this to the lab along **P** we get:

$$\begin{pmatrix} p \sin\theta \cos\phi \\ p \sin\theta \sin\phi \\ \sqrt{1 + P^2/M^2}\, p \cos\theta + \frac{P}{M}\sqrt{p^2 + m^2} \\ \frac{P}{M}\, p \cos\theta + \sqrt{1 + P^2/M^2}\,.\sqrt{p^2 + m^2} \end{pmatrix}$$

The front glass is the x - z plane so that the projected decay angle γ between $\underline{P}$ (z-axis) and the decay product is given by:

$$\tan\gamma = \frac{\sin\theta\cos\phi}{A\cos\theta + B}$$

where $A = \sqrt{1 + P^2/M^2}$ and $B = \frac{P}{M}\sqrt{1 + m^2/p^2}$.

Now since the decay product can be considered to be produced isotropically in the sigma centre of mass (see section 4.2) all elements $d\phi d(\cos\theta)$ are equally probable. We consider therefore a plot of $\cos\theta$ against ϕ, equal areas representing equal probabilities. This is simply an equal-area projection of the (θ, ϕ) sphere. Lines of constant γ given by the above equation on the sphere may be plotted on the projection by inverting the above equation

$$\cos\theta = \frac{-A\,B\tan^2\gamma + \cos\phi\sqrt{(A^2 - B^2)\tan^2\gamma + \cos^2\phi}}{A^2\tan^2\gamma + \cos^2\phi}$$

if $A > B$

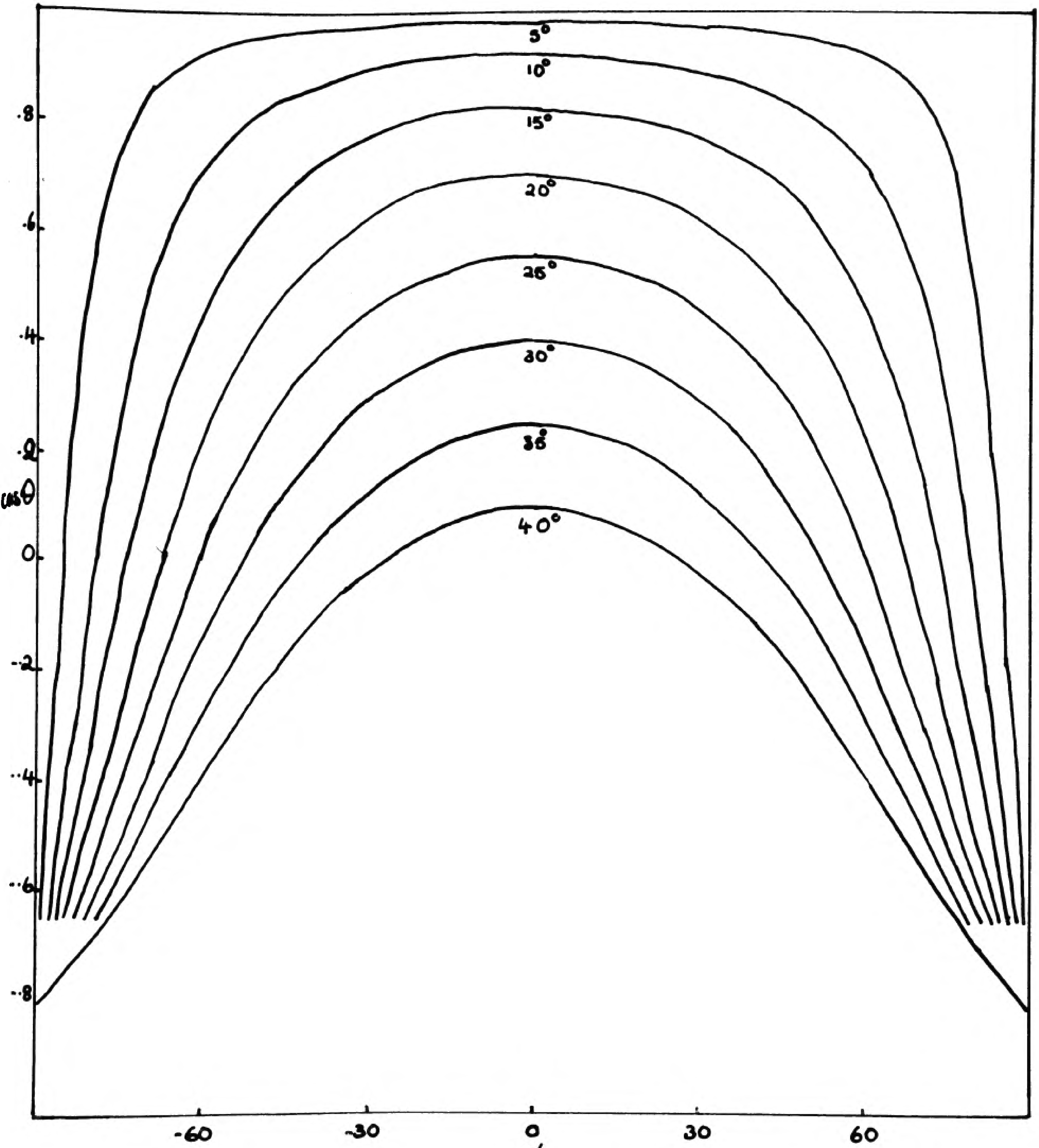

PROJECTED DECAY ANGLE PLOT FOR Σ^{+}_{π} DECAYS AT 1 GeV/c.

FIG. A1(a).

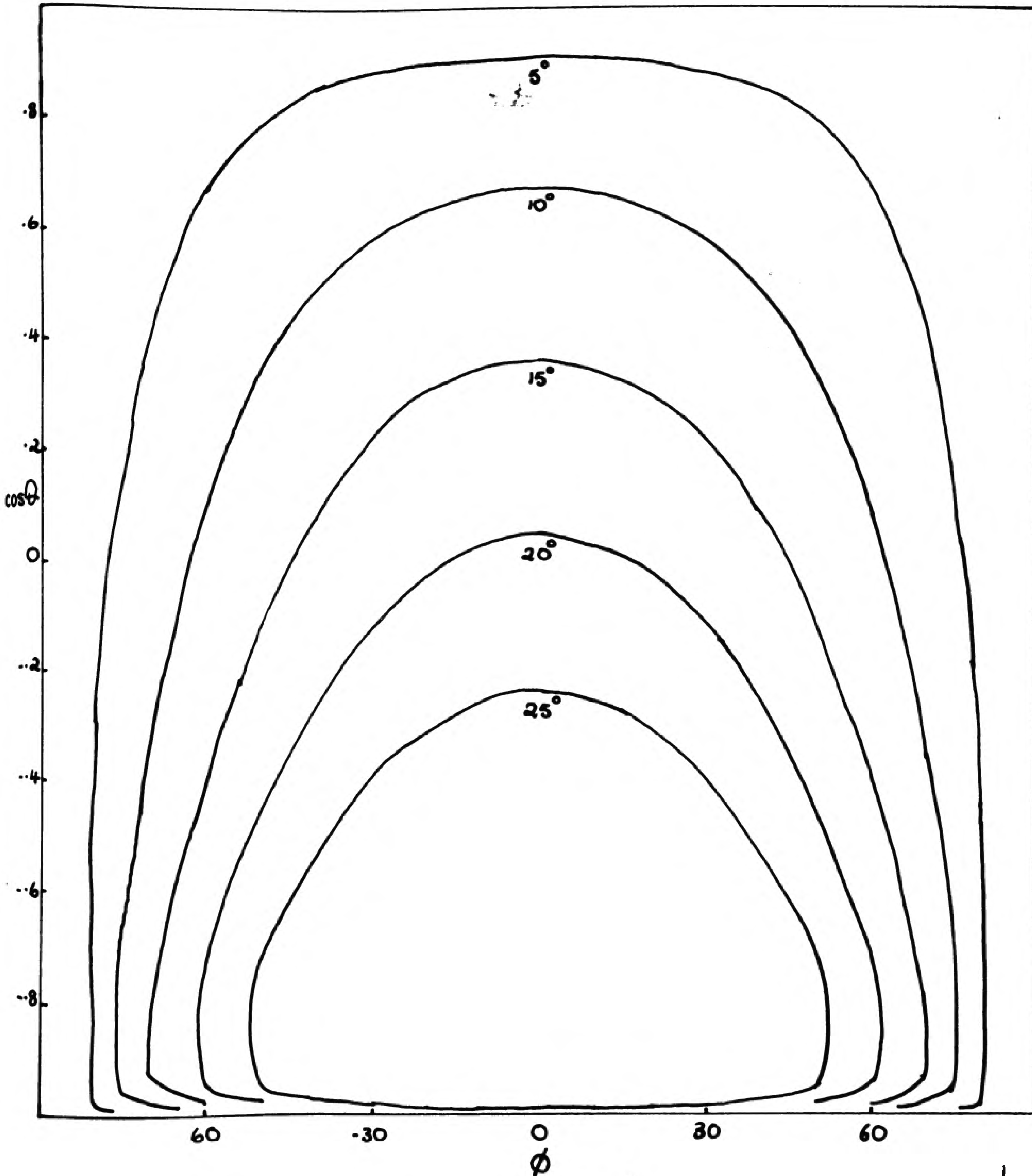

PROJECTED DECAY ANGLE PLOT FOR Σ^{+}_{π} DECAYS AT 2·5 GeV/c.

FIG. A1(b).

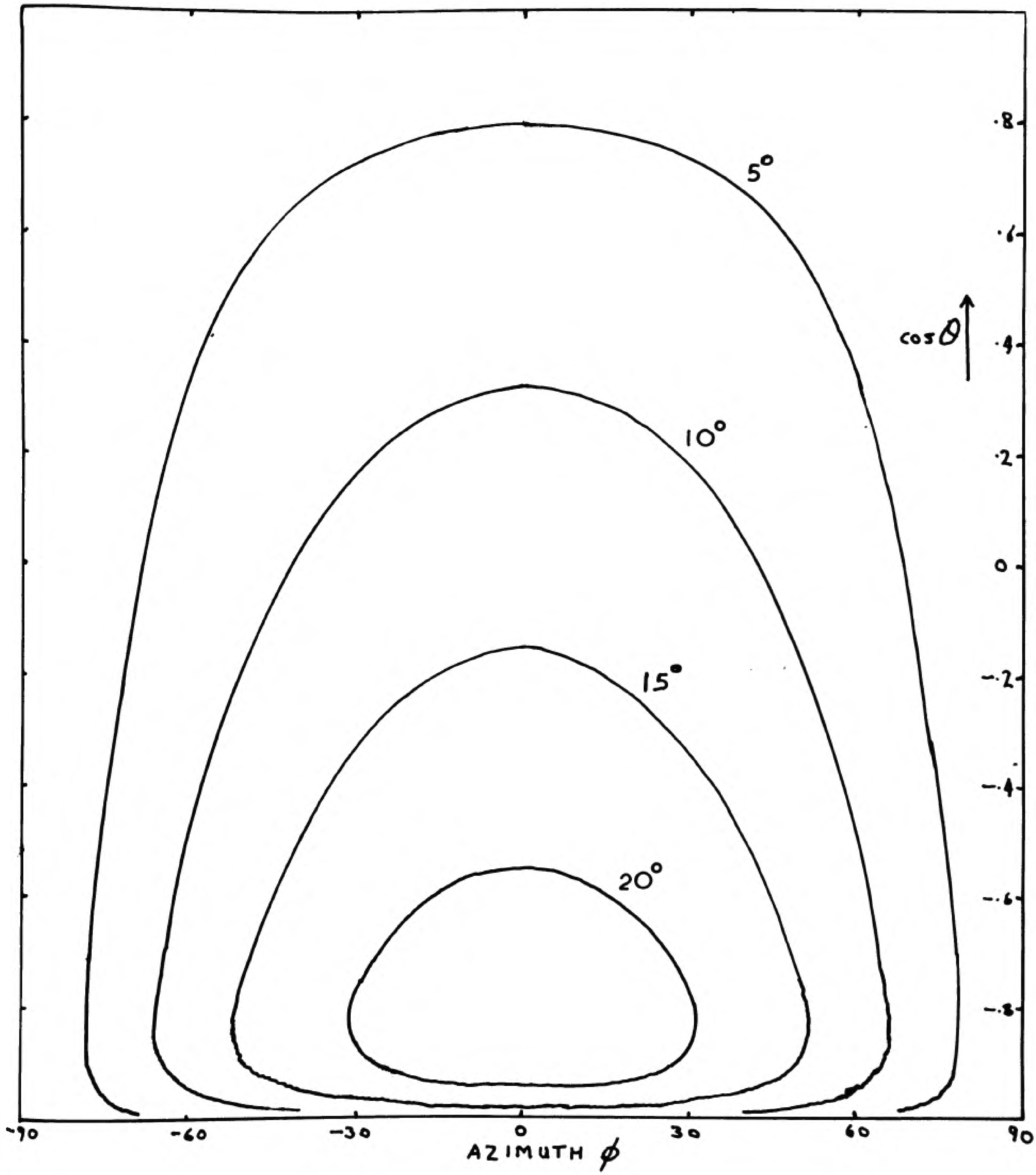

$\Sigma^+ \rightarrow n\pi^+$. $P = 4$ GeV/c . $\lambda = 0°$.

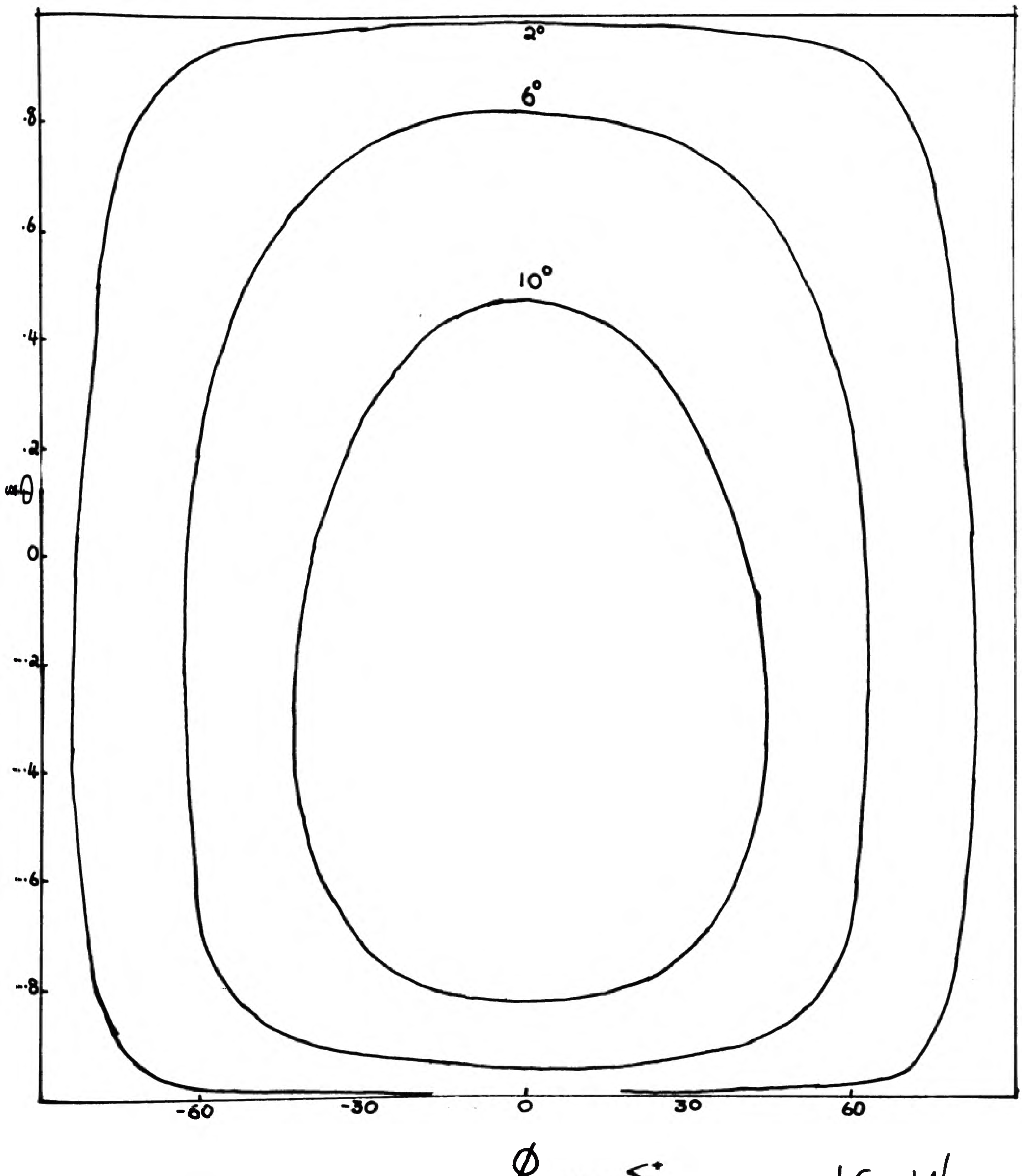

PROJECTED DECAY ANGLE PLOT FOR Σ^+_p DECAYS AT 1 GeV/c.

FIG. A1(d).

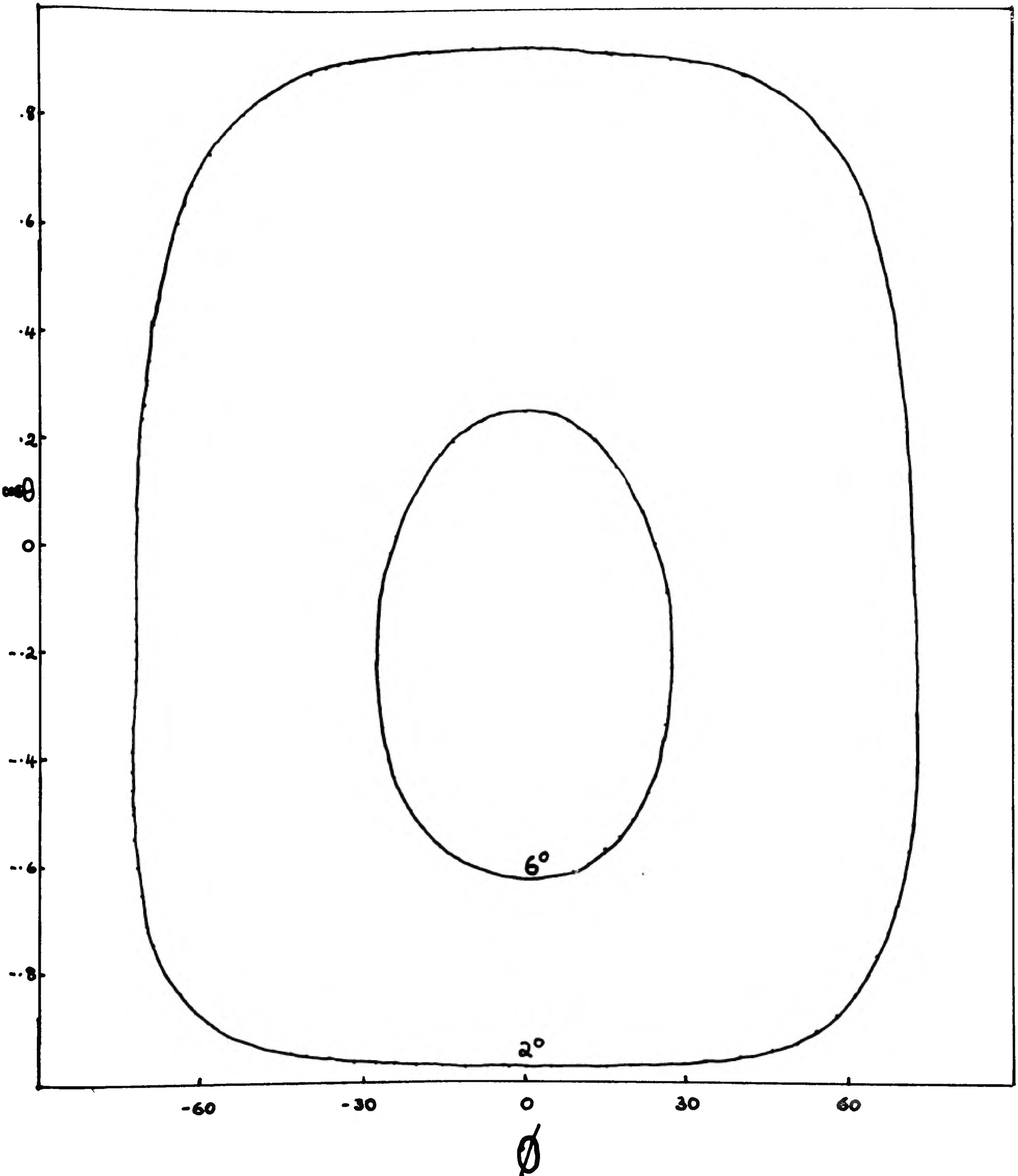

PROJECTED DECAY ANGLE PLOT FOR Σ_p^+ DECAYS AT 2 GeV/c.

FIG. A1(e).

$A > B$ (i.e. $v > V$).

ONE VALUE OF θ, CENTRE OF MASS ANGLE, FOR EACH VALUE OF ψ, LABORATORY DECAY ANGLE.

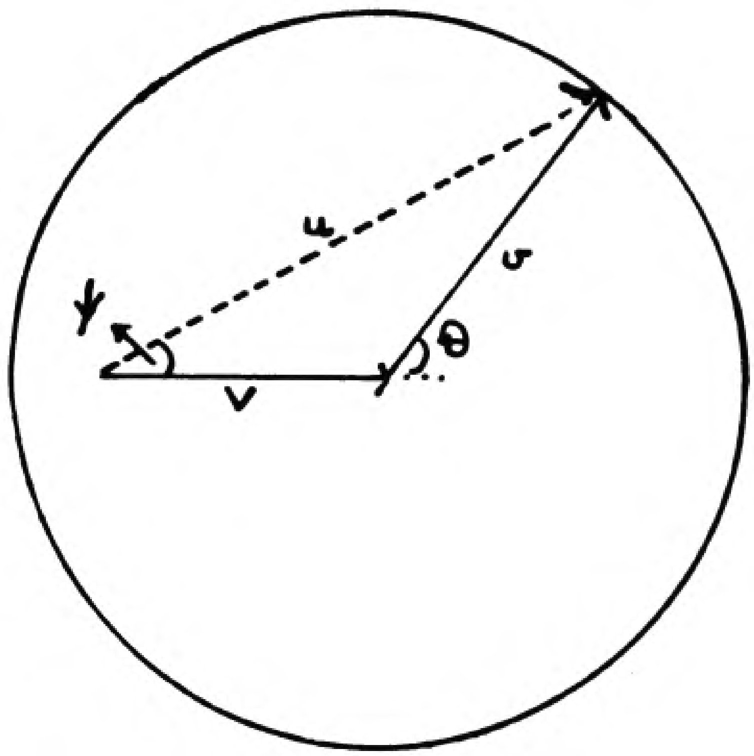

$A < B$ (i.e. $v < V$).

TWO VALUES OF θ, CENTRE OF MASS ANGLE, FOR EACH VALUE OF ψ, LAB. DECAY ANGLE.

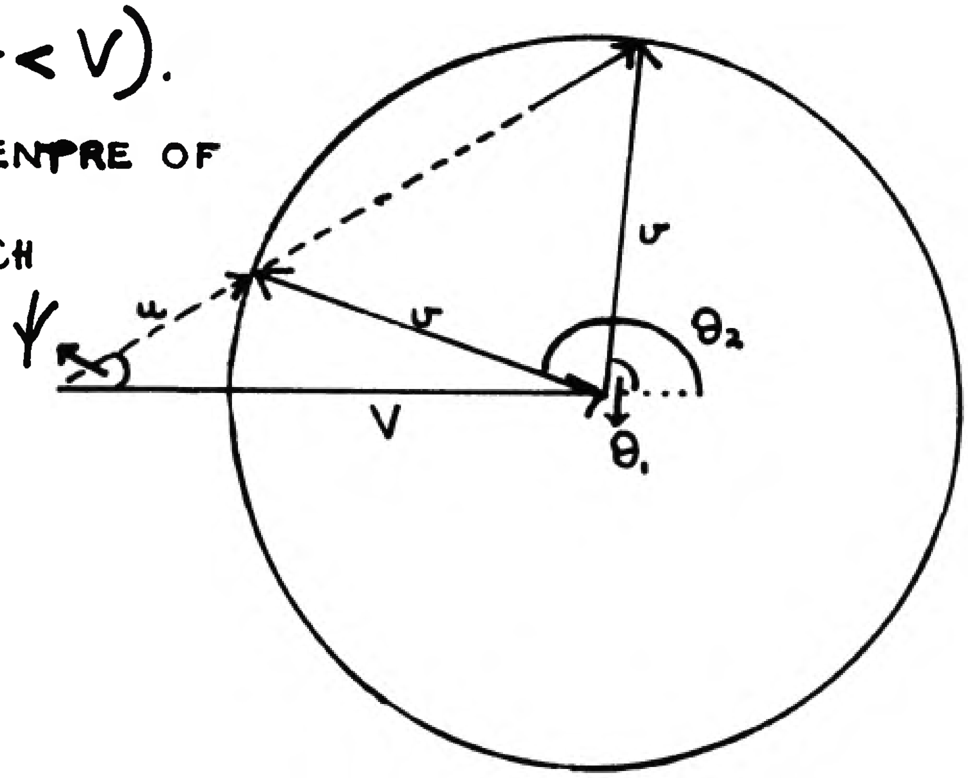

$V = \Sigma$ VELOCITY VECTOR IN LABORATORY

v = CHARGED DECAY PRODUCT VELOCITY VECTOR IN Σ CENTRE OF MASS.

u = DECAY PRODUCT VELOCITY VECTOR IN LABORATORY.

N.B. THIS DIAGRAM IS NON RELATIVISTIC AND THEREFORE ONLY QUALITATIVELY CORRECT.

Fig. A.2.

[illegible]

and $$\cos\theta = \frac{-A\,B\tan^2\psi \pm \cos\phi\sqrt{(A^2 - B^2)\tan^2\psi + \cos^2\phi}}{A^2\tan^2\psi + \cos^2\phi}$$

if $A < B$.

If A is greater than B the velocity of the decay product in the sigma rest frame is greater than the velocity of the sigma in the laboratory. Several typical plots are shown in Fig.A.1. In the low momentum plots ($A > B$) the point at which all the contours intersect corresponds to the case in which the decay product momentum is perpendicular to the plane of the front glass. When $A < B$ this is no longer possible and two solutions for each value of ϕ are found. The change from single to double solution may be understood with the help of Fig.A.2. The plots in Fig.A.1 are for one half of the sphere only; the other half is related to it by a symmetry plane perpendicular to the front glass.

To calculate the projected decay angle spectrum the appropriate areas of the plot are found by numerical integration with respect to ϕ.

APPENDIX B

The use of the concept of 'noise' in histograms

The behaviour of data in a histogram bin is very similar to that of an electronic device.

In the latter there is a 'signal' which is the mean response of the device taken over an infinite sample of pure stimuli. There is the Shott noise level which is due to statistical fluctuations on the number of response quanta. Thirdly there is background noise which originates from unwanted stimuli.

In the case of the contents of a bin in a histogram which has been subjected to some attempted selection we have by analogy the ideal mean bin content, the $\sqrt{N}$ statistical fluctuations thereon and the contamination contribution due to imperfect selection. By maximising the signal to noise ratio as a function of the selection criteria and final bin size we achieve the best demonstration of the desired effect in the histogram.

The process is far from rigorous due to interference between the signal and the background, unequal bin population, non random background behaviour, uncertainty in the estimation of background and the problem of how to add the Shott noise to the background noise. Despite these drawbacks the idea provides a guide to the best way of selecting and anti-selecting resonances, choosing bin widths and deciding in advance whether plots are likely to contain useful information.

Example

To select a (J = 1) resonance from a mass plot in order to examine its decay distribution for evidence of alignment.

A vector particle cannot have a decay distribution with powers of cos θ or ∅ greater than 2. Therefore 5 bins in a decay angle plot is the minimum required to show the alignment. The Shott noise in each bin of this plot is equally positive and negative whereas the contamination noise is always positive. Therefore they are orthogonal and should be added in quadrature. We assume that a phase space or other background curve can be drawn on the mass plot below the resonance. Then for a certain pair of selection limits we have an estimated N_R resonant and N_B background events. If we divide our decay angle plot into n bins (minimum 5), the noise will be $\sqrt{N_R/n + N_B^2/n^2}$.

and the signal N_R/n giving a signal-to-noise ratio:

$$R \sim \frac{N_R}{\sqrt{nN_R + N_B^2}}$$

The selection criteria should then be moved to maximise R. If R is less than one it is very unlikely to be a useful plot. If the background is high the mass selection should be narrow; if low, wide. n should be as small as possible - any folding permitted by an unequivocal symmetry principle can help.

APPENDIX C

The estimation of scanning efficiency from N scans

In the majority of experiments the film is scanned only twice. To estimate the number of events that have been missed altogether it is necessary to make assumptions which are rather implausible. It is assumed that every event has the same observability a. The observability of an event is defined as:

$$a = \underset{N \to \infty}{\mathrm{Lt}} \left(\frac{\text{Number of times it is seen in N scans}}{N} \right)$$

It follows that the number of events seen on one of the scans only is $n_1 = 2Ma(1-a)$ and on both is $n_2 = Ma^2$ where M is the total number of events. It follows that the number missed altogether is

$$n_0 = M(1-a)^2 = n_1^2 / 4n_2.$$

In practice some events are easier to see than others and the above calculation gives rise to a systematic underestimate of the total number of events.

When the film is scanned more than twice the above assumption can be dropped. We continue to assume that every scan has the same efficiency. We therefore have N numbers as input - the numbers of events seen on N, N-1,.....2, 1 scans out of N. We may therefore have N adjustable parameters describing the observability of the events. We consider two ways of defining these parameters:

a) <u>Method of variable observability.</u>

In this case we suppose that there are $\frac{N+1}{2}$ classes of events if N is odd and $^N/_2$ classes if N is even. The unknown parameters are n_i the number in each class of observability a_i. We then have N equations of the form:

$$m_r = {}^N C_r \sum_i a_i^{\,r} (1 - a_i)^{N - r} n_i$$

where m_r is the number of events seen on r scans out of N. This method has two disadvantages; firstly the equations are nonlinear in a_i, so that for $N \geqslant 4$ they are not soluble analytically; secondly if N is odd there are too many unknown parameters. This can be overcome by tabulating the results as a function of the observability of the class with highest a, a_1. It is often found that the total number of events estimated

$$\sum_i n_i$$

does not vary much over the range where a_1 is reasonable. For the case N = 3 after some tedious algebra we find

$$N_1 = \frac{3m_1m_3 - m_2^2}{3m_1a_1^3 + 9m_3a_1(1 - a_1)^2 - 6m_2(1 - a_1)a_1^2}$$

$$N_2 = \frac{m_3 - N_1a_1^3}{a_2^3} \qquad \text{where } a_2 \text{ is given by}$$

$$a_2 = \frac{m_2 - 3N_2(1 - a_1)a_1^2}{m_1 + m_2 - 3N_2(1 - a_1)a_1}$$

The total number of events is then estimated to be $(N_1 + N_2)$. If $N > 3$ the algebra becomes impossible and the second method is probably more appropriate anyway.

b) <u>Method of fixed observability.</u>

If N is large enough we consider N classes of events with suitably chosen observabilities a_j. This has the tremendous advantage of making the equations linear. We have $m_i = \sum_j A_{ij}n_j$ or $M = AN$ so that $N = A^{-1}M$ where $A_{ij} = {}^NC_i a_j^i(1 - a_j)^{N-i}$. We invert the square matrix A to evaluate the n_j - the number in the class of observability a_j.

Of course there is considerable ambiguity as to how a_j should be chosen, but it was found with $N = 5$, for example, that the requirement that all n_j be positive was very restrictive on possible sets of a_j. This extra condition fixed the value of $\sum_j n_j$ to within a very small range. With $N = 3$ on the other hand the ambiguity was much greater and method a) gave more consistent results.

Once the characteristics (a_js and relative values of n_j) of the particular event type have been found from part of the film scanned many times they may be used to make a better estimate for parts of the film which have been scanned only a few times.

The error on the estimate of the number of events consists of a statistical error on the number seen and an error also of statistical origin on the number unseen. Since the number unseen is calculated from the number seen their errors will be correlated - we add them in phase rather than quadrature.

$$\Delta = \sqrt{\text{total seen}} + \sum_j (1 - a_j)^N \sqrt{n_j}$$

APPENDIX D

BABEL - A computer based scanning system[1]

BABEL is a system designed to maintain a library of scanned events on magnetic tape and to produce from this library master lists and measuring lists suitable for direct input on 8 channel paper tape into the on-line measuring machines[2]. The scans are made at the scan table on special Mark Sense cards. Pencil marks in appropriate positions on these cards are transformed into punch holes on an IBM 519. These punched cards provide the input to the KDF9 programme.

Each scan (of up to 800 cards) is checked and, when found to be fault-free, it is written up to a magnetic tape. Stored in this way more than 500,000 scanned events may be kept on one magnetic tape. Each scan is preceded by cards giving the necessary identifying information together with a list of topologies being scanned for. The scans on tape may be compared and the resulting listing used as a basis for a comparison scan. The comparison scan itself is also recorded on cards and is used to construct a master list which is

Fig. D1. Some BABEL operations.

Loading a scan

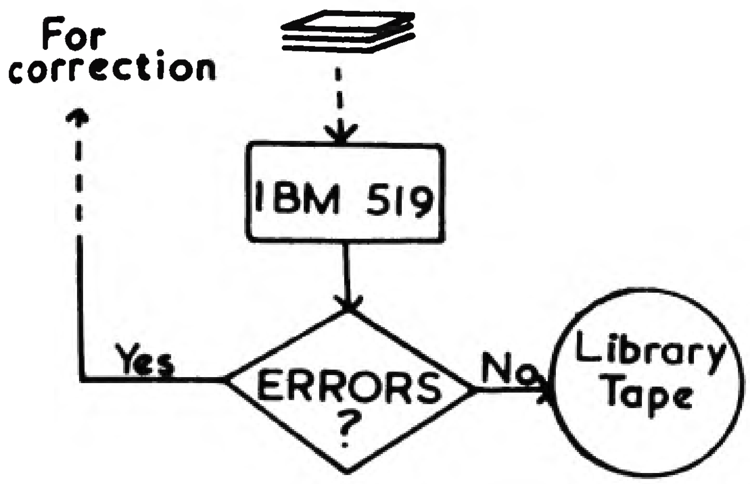

Comparing two scans

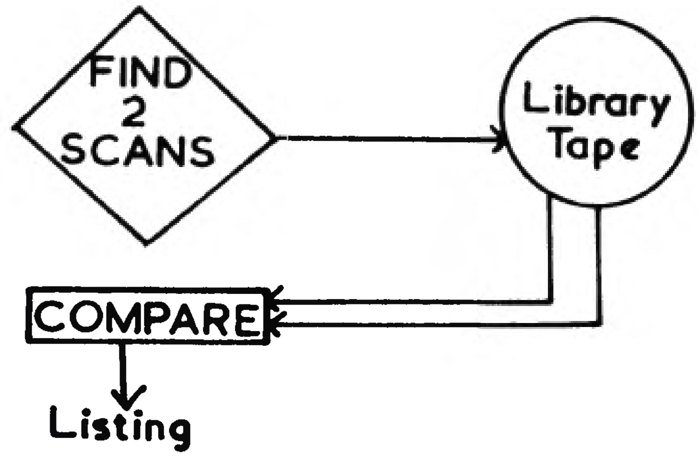

Loading a comparison scan & making a master list.

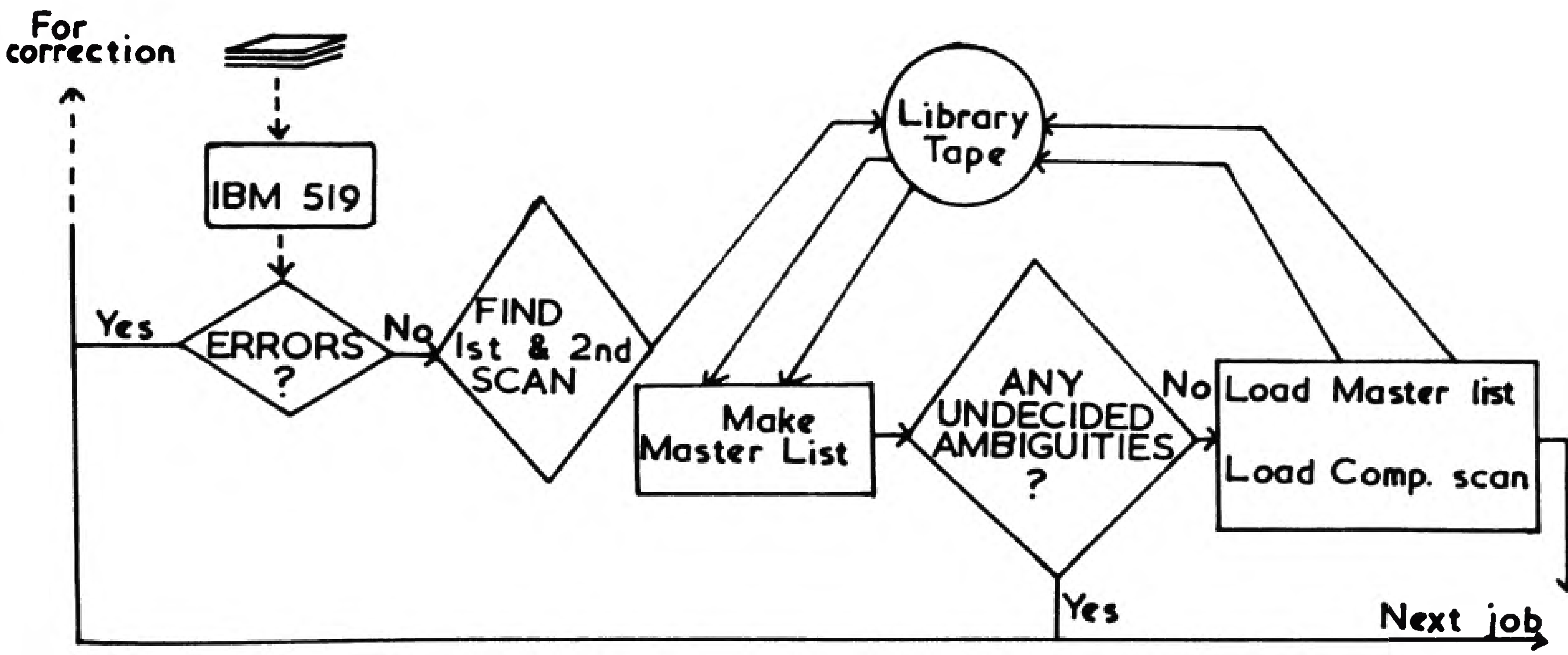

Making a measuring list.

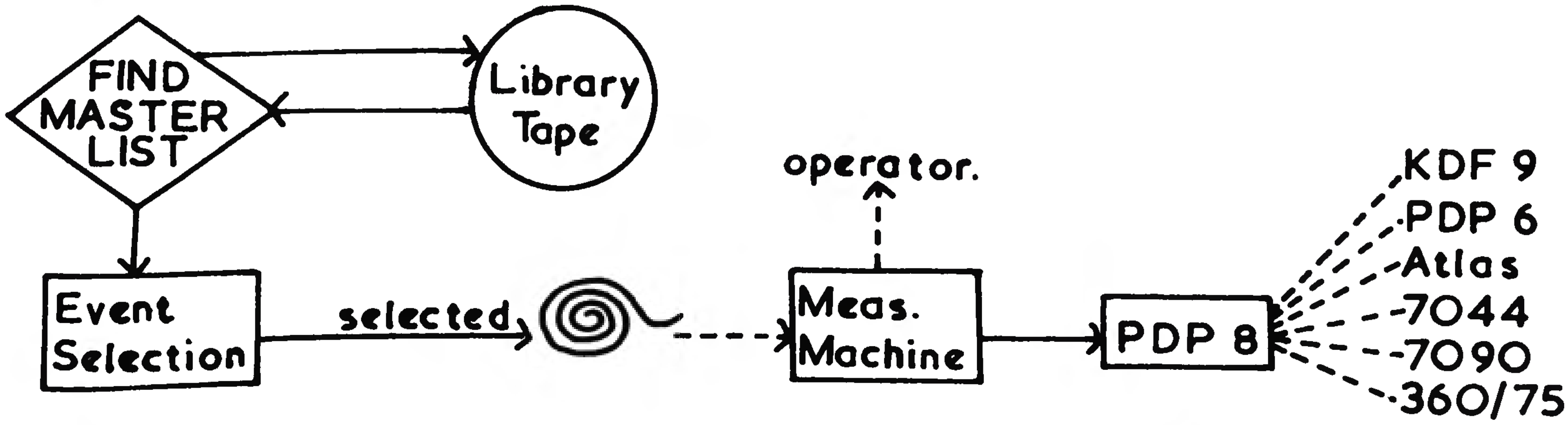

NB: Solid lines are computer connections. Dashed lines are off line operations.

Fig. D2. A Mark Sense scan card.

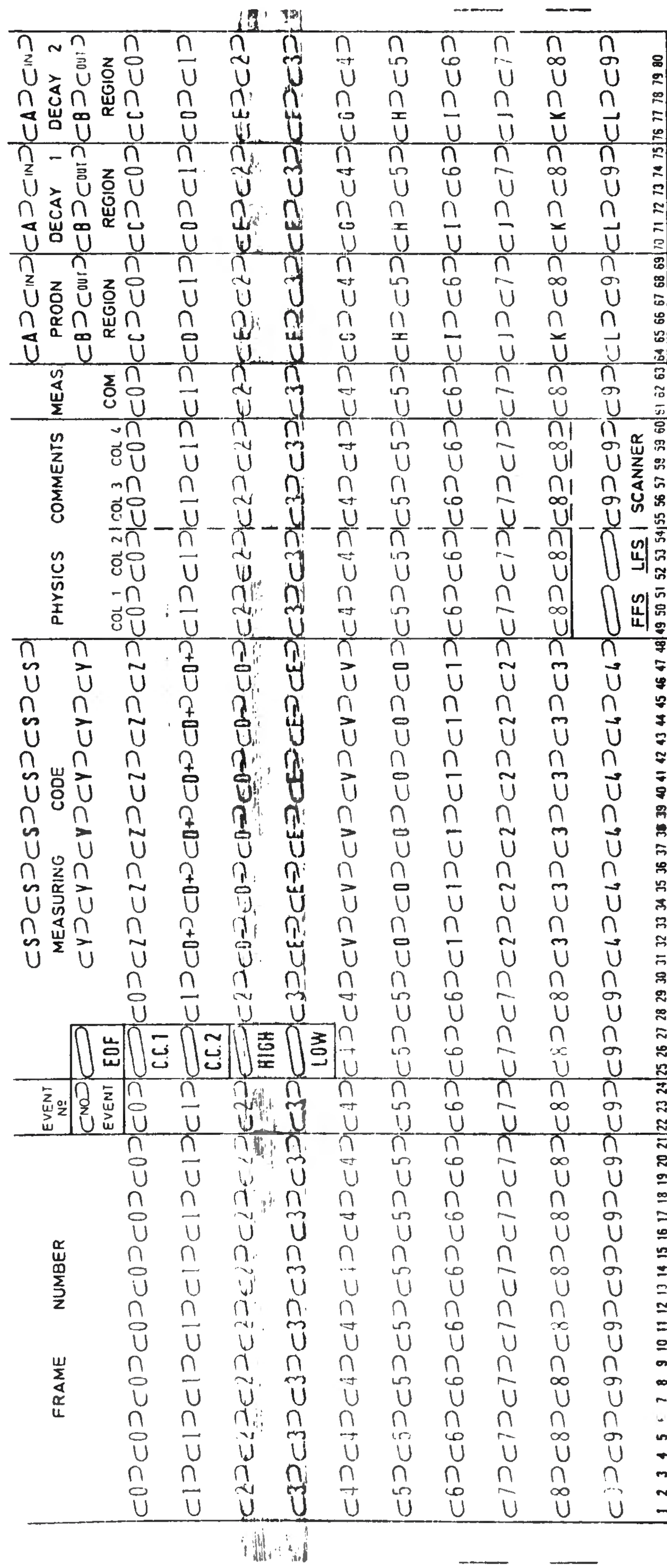

held on magnetic tape in a format similar to normal scans. The scans or master lists on tape may be listed or used to punch out the pre-set information required by the on-line measuring machines; general selection data may be used to select or antiselect on any desired feature or combination of features on the scan card. A full printing format is available for easy filing and checking. Facilities are provided for summarising scans, editing, rescuing and updating duplicate tapes. The programme is supplied with its own fully time sharing input and output buffers[3].

The coding of comments and use of grid references are options that may be changed from experiment to experiment to suit the physics and bubble chamber concerned. The comments may be transmitted through the on-line programme to the RHEL programmes[4], where they may be printed out to assist in the problem of choosing the correct hypothesis.

The use of special job cards allows any number of operations to be obeyed sequentially. The format of these has been designed so that the entire system can be organised by scanners without physicist supervision.

REFERENCES TO APPENDIX D

(1) BABEL: W.W.M. Allison.

(2) PDP8 SYSTEM: D.E. Lawrence.

(3) BABEL Mark 3: W.W.M. Allison.

(4) JOKING SYSTEM: E.C. Sedman.

APPENDIX E

The process of kinematic fitting and its interpretation

Particle Identification

It is an unfortunate feature of the analysis of bubble chamber events that the question: "what particles correspond to the tracks in this event?" cannot be answered directly. In particular the probability output by the kinematics programme which attempts to satisfy energy and momentum conservation for mass assignments corresponding to a certain hypothesis does not represent the probability that these mass assignments are correct. Misconceptions about kinematic fitting have in the past produced some highly dubious selection criteria for events fitting more than one hypothesis.

Geometrical reconstruction

In the geometrical reconstruction of each track the values of 1/momentum, tangent of the dip and the azimuth are derived by minimising the sum of the squares of the distances of each measured point from the reconstructed path as seen on each view. These variables are chosen because they correspond most closely to the quantities actually measured and are therefore most likely to have normally distributed deviations. From the goodness of the least squares fit an error is calculated. It is known that these errors should have a certain lower limit associated with the known accuracy of track and vertex measurements - a fixed standard error is therefore used when the calculated error is small. Some of the variables such as the momentum of a straight track or variables of unseen neutral tracks are not known at this stage.

<u>The meaning of the probability of a fit to a hypothesis</u>

Let us assume that we try to fit an event or part of an event to a particular set of mass assignments. Let the number of vertices be N, the number of tracks be n, and the number of unknown track variables be m. The conservation of 3-momentum and energy at each vertex gives 4N equations to be satisfied so that there are (4N-m) constraints on the measured variables when the unknowns have been calculated. Due to finite measurement errors these constraints will not be satisfied exactly. The fitting process attempts to answer the following question:

"Assuming that the variables measured are a random sample of a statistical population whose means satisfy the constraint equations and whose dispersion is given by the measured error matrix; what are the values of these means when the proportion of the population with sets of variables less likely than those measured is largest?"

Let us consider a one dimensional example. A variable has a measured value x and estimated variance σ and by hypothesis is constrained to have the true value X. Therefore it is supposed that an infinite sample of measurements x would give rise to the frequency distribution

$$f(x') \sim \exp\left[-(X-x')^2/2\sigma\right]$$

and the proportion worse than our x would be:

$$\underset{\text{for } x > X}{P(x)} \sim \int_x^\infty \exp\left[-(X-x')^2/2\sigma\right] dx' + \int_{-\infty}^{2X-x} \exp\left[-(X-x')^2/2\sigma\right] dx'$$

or a similar expression if $x < X$.

If on the other hand X may be varied the proportion or "probability" may be made 100% and the hypothesis is trivial.

To establish a picture in the multidimensional case encountered in fitting processes, we imagine a configuration space of all the measured variables (3n-m) dimensions). Each measured normally distributed variable has its own orthogonal axis. The measurement of one particular event is represented by a point in this space. Each constrained hypothesis appears as a subspace which obeys the constraint equations. So we imagine our point in the midst of a series of lines, surfaces etc. each representing the locus of configurations satisfying a given hypothesis. The highly constrained hypotheses correspond to "small" subspaces like lines whereas less constrained ones have more degrees of freedom like surfaces.

Consider the measurement of an event as the position vector y in this space with error matrix E and let a point on a nearby hypothesis locus be Y. Then if, by hypothesis, y differs from Y only by virtue of the dispersion, (E), the probability of measurements of Y in the neighbourhood of y is

$$\sim \exp\left[-\frac{(Y - y)\, E^{-1}\, (Y - y)^{T}}{2}\right] d\Omega$$

where T represents transposition of the vector and $d\Omega$ represents the volume of an element of the configuration space. The quantity $(Y - y)\, E^{-1}\, (Y - y)^{T}$ is known as χ^2. In fact Y is not completely fixed. As can be seen from our one dimensional example any dimension in which it may be varied does not contribute to the probability. Thus it is only necessary to integrate with respect to dimensions perpendicular to the locus - the number of these is equal to the number of constraints, N_c. Therefore

$$P(\chi^2, N_c) \sim \iint \cdots \int e^{-x^2/2} \, d\Omega_c$$

integration over all elements of perpendicular subspace, Ω_c, for which $x^2 = (Y - y^1)\, E^{-1}\, (Y - y^1)$ is greater than χ^2. It is clear that the highest probability corresponds to the smallest value of χ^2. To minimise χ^2 the kinematics programme calculates the derivatives of χ^2 with respect to each component of Y so as to converge by iteration on the best fit.

<u>Comparing fits to different hypotheses</u>

Suppose that an event is fitted to two hypotheses A and B and the associated "probabilities" P_A and P_B obtained. Now the fitting process as we have seen assumes the correctness of the hypothesis being tried so that, if hypothesis A is correct, P_A is meaningful and P_B meaningless; conversely if B is correct. If neither is correct, neither is meaningful. So that under no circumstances can it be valid to compare P_A and P_B as if they were both quantitatively correct. However in the space picture we see that if the event (point) is not associated with the hypothesis (locus) it will probably be a great way from it and therefore give rise to a small probability when the fit is attempted. The more constrained the hypothesis

Fig. E 1. Configuration space for two measured variables.

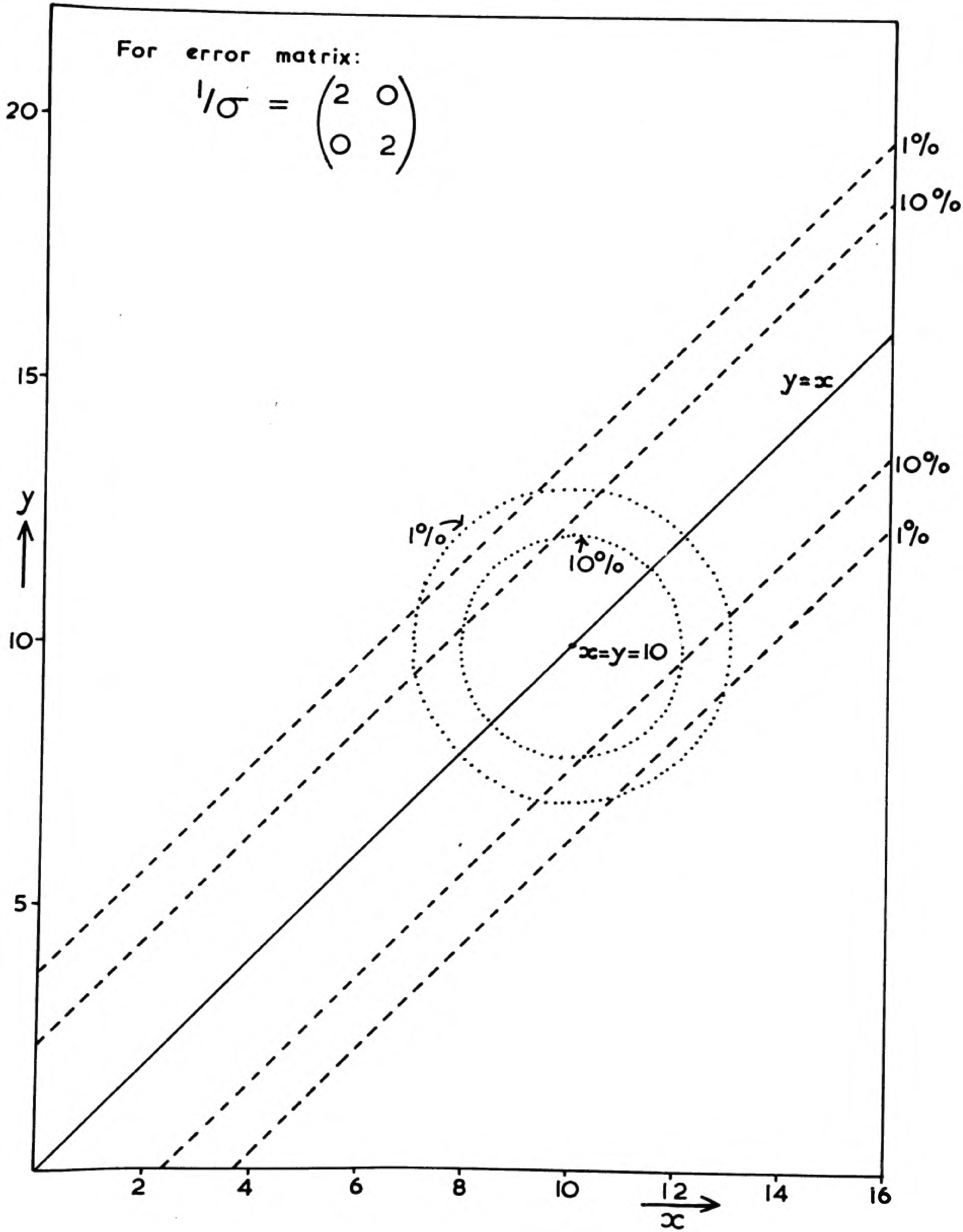

the further away the average unrelated event will be, so that all fits with a probability less than a certain cut off are best rejected as "no-fits". By extension, if an event is within errors of the loci of two hypotheses, it is much more likely that it is genuinely associated with the more highly constrained of the two. In chapter 4 this is shown to be the case for ambiguities between $\Sigma^0\pi^+\pi^-$ and $\Lambda^0\pi^+\pi^-$. In chapter 2 similar results have been assumed. No mention has been made above of the physical regions of variables - in practice these play an important part and act in effect like extra constraints.

To demonstrate the principle graphically we show in Fig.E.1 the two dimensional configuration space corresponding to two measured quantities x and y. We consider three "hypotheses":

a) $x = y = 10$

b) $x = y$

c) No constraints on x and y

If the expected number of cases of a), b) and c) are not too unequal and the physical regions of x and y are as shown, then we will not be too far wrong if we take any fit to a) in preference to b) or c) and any fit to b) in preference to c) (accepting fits at the 1% level).

Then if ℓ, m and n are the numbers of a), b) and c) events the selected samples will be made up as follows:

Selected "a"	$.99\ell$,	.25m,	.1n
Selected "b"	$.005\ell$,	.74m,	.2n
Selected "c"	$.005\ell$,	.01m,	.7n

This separation could be improved by reducing the errors compared with the size of the allowed physical region. It would also be much improved if the hypotheses had different physical regions (as is usually the case in practice).

APPENDIX F

The angular momentum algebra of peripheral processes

There are three main approaches to the dynamics of peripheral processes. The most straight forward is the single particle exchange model. This essentially corresponds to evaluating the simplest Feynman diagram. The decay correlations deduced from the model are well obeyed in general but the predicted momentum transfer dependence is always far too broad. The dependence of the cross section on total centre of mass energy is utterly wrong. Form factors[1] may be introduced to modify the momentum transfer dependence in an ad hoc fashion:

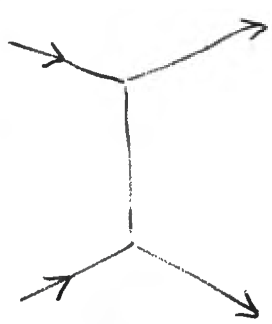

Lowest diagram

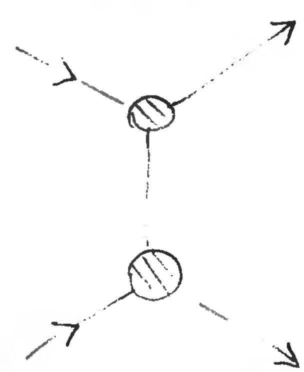

Effect of form factors

However the form factors needed are such steep functions of momentum transfer that the explanation is rather unconvincing. The Stodolsky-Sakurai model[2] for isobar production by vector meson exchange predicts decay correlations which are in excellent agreement with experiment over a very wide range of incident momenta[3]. The second approach is the absorption model[4] which is a modification of single particle exchange taking into account the effect of other channels. Other processes deplete the incoming wave - especially the part of it with small impact parameter or low angular momentum. This means that the incoming wave is not a plane wave. Similarly the principle of unitarity demands that the outgoing particles can rescatter - this modifies the shape of the outgoing wave. Difficulty arises from our ignorance of the scattering parameters involved in many cases. However the model has had notable successes in accounting for the shapes of momentum transfer distributions. The predicted dependence of the cross section on total centre of mass energy is still in bad disagreement with the data. The third model, the Regge pole model[5], is aimed primarily at predicting the 's' and 't' dependence of the amplitudes and relating the cross sections for different channels. In this it has had great success. Relatively little discussion has been devoted to its predictions for decay correlations.

The successes of the models are summarised below:

Model	Decay Correlations	t-dependence	s-dependence
Single particle	✓	X	X
Absorption	✓	✓	X
Regge-pole		✓	✓

The absorption and Regge models contain parameters referring to unknown scattering processes and unknown particle states respectively. It seems wiser therefore to develop the theory of double peripheral processes discussed in chapter 6, through the successes of single particle exchange as a first step. In the rest of this appendix we give a detailed investigation of the decay correlations implied by the model for single peripheral processes. In particular we examine the data for the reaction:

$$K^- p \rightarrow \Lambda \rho^0$$

In chapter 6 we relate the correlations in this final state to certain variables in the reaction:

$$K^- p \rightarrow \Sigma^0 \pi^+ \pi^-$$

A similar general treatment of isobar production by vector exchange is already in the literature(6).

<u>Derivation of decay correlation predictions in single particle exchange processes</u>

Consider the process: $A + C \rightarrow E \rightarrow B + D$

which occurs through the formation of a state Ξ of spin J in the s-channel:

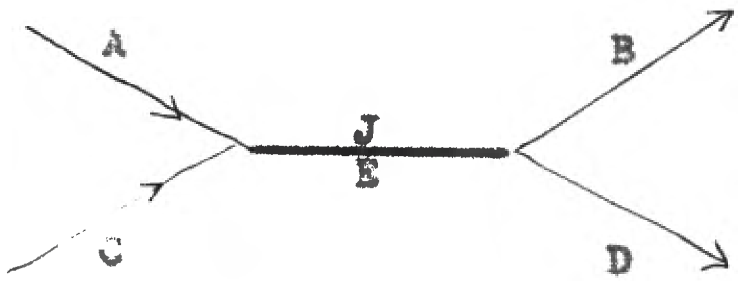

F.1

Then the square of the total centre of mass energy is given by:

$$s = a + c + 2(a + p^2)^{\frac{1}{2}} (c + p^2)^{\frac{1}{2}} + 2p^2 \qquad \text{F.2}$$

and by:

$$s = b + d + 2(b + p'^2)^{\frac{1}{2}} (d + p'^2)^{\frac{1}{2}} + 2p'^2 \qquad \text{F.3}$$

where

a, b, c, d are M_A^2, M_B^2, M_c^2 and M_d^2

p is the initial state centre of mass momentum

and p' is the final state centre of mass momentum.

Now the distribution of the production angle of B is determined by J - we are taking A, B, C and D to be spinless at this stage. In the centre of mass taking the direction of A as quantisation axis the angular momentum coupling is trivial - only the initial state with orbital angular momentum J can contribute and the final state must have pure L = J. The axial symmetry of the initial state implies that the angular distribution of B must be $P_J^o(\cos\theta)$ where θ is the centre of mass scattering angle. We can express $\cos\theta$ in terms of t the square of the four momentum transfer from A to B:

$$t = a + b - 2(a + p^2)^{\frac{1}{2}} (b + p'^2) + 2p\,p' \cos\theta \qquad \text{F.4}$$

From F.2 and F.3 we can find p and p' :

$$p^2 = \frac{(s - a - c)^2 - 4ac}{4s} \qquad \text{F.5}$$

$$p'^2 = \frac{(s - b - d)^2 - 4bd}{4s} \qquad \text{F.6}$$

Substituting F.5 and F.6 in F.4 we get:

$$\cos\theta = -\frac{(c-a)(b-d) + s(a+b+c+d) - s^2 - 2st}{((s-a-c)^2 - 4ac)^{\frac{1}{2}}\,((s-b-d)^2 - 4bd)^{\frac{1}{2}}} \qquad \text{F.7}$$

Thus the matrix element contains the factor:

$$P_J^o\left(-\frac{(c-a)(b-d) + s(a+b+c+d) - s^2 - 2st}{((s-a-c)^2 - 4ac)^{\frac{1}{2}}\,((s-b-d)^2 - 4bd)^{\frac{1}{2}}}\right) \qquad \text{F.8}$$

It also contains the factors $gg' \dfrac{S}{S - m^2}$ where g and g' are the coupling constants for the two vertices, and m is the mass of the intermediate particle of spin J (a complex number of the form M + i $\Gamma/2$ where M is the rest mass and Γ

the width). These last factors come from field theory as opposed to the simple arguments of angular momentum conservation. Consequently they are not so reliable. (We have omitted the overall energy-momentum conservation δ-function, normalisation factors etc). This matrix element is a relativistic invariant - i.e. it is invariant under all proper Lorentz transformations. The hypothesis that it is still correct for reactions of the type:

$$A + \bar{B} \rightarrow \bar{C} + D$$

going by the exchange processes:

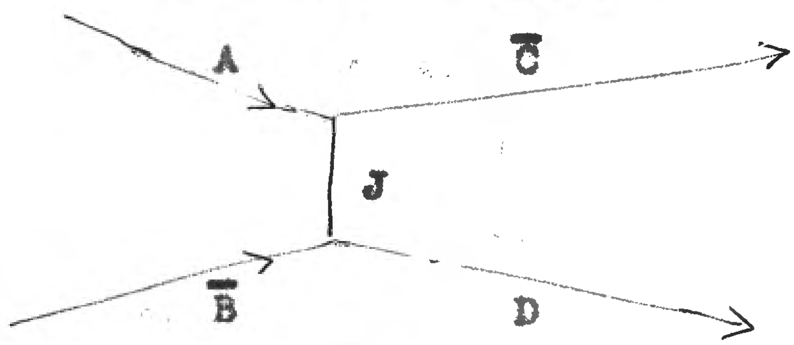

F.9

is known as "crossing symmetry" and is a basic assumption in nearly all theories of elementary particle interactions. In interpreting the meaning of F.8 for the process F.9 we note that the four vector q_B is reversed and so is q_C.

$$q_{\bar{B}} = - q_B$$
$$q_{\bar{C}} = - q_C \qquad \text{F.10}$$

so that the meanings of 's' and 't' are reversed. Thus the matrix element for F.9 contains the terms:

$$P_J^0(\cos\beta) = P_J^0\left(- \frac{(c-a)(b-d) + t(a+b+c+d) - t^2 - 2at}{((t-a-c)^2 - 4ac)^{\frac{1}{2}}((t-b-d)^2 - 4bd)^{\frac{1}{2}}} \right) \quad \text{F.11}$$

In fact this corresponds to an imaginary value of β, the scattering angle in the rest frame of the exchange particle.

Let us now look at the general problem of the peripheral scattering of particles with spin. We use the fact that the argument of P_J in F.11 is still the cosine of the scattering angle in the rest frame of E - that is the angle between A and $\bar{B}$. At each vertex we have four angular momenta - if we work in the rest frame of one of the particles at the vertex the magnetic substate of the orbital motion at the vertex is zero. However four angular momenta do not couple uniquely in general and a sum over possible couplings (as well as over possible values of the orbital angular momentum) with arbitary coefficients has to be introduced.

$$a_\lambda^E = \sum_\eta \sum_\ell f_\eta(\ell, j_A, j_C, j_E, \lambda_A, \lambda_{\bar{C}}, \lambda)\, \delta(\lambda - \lambda_{\bar{C}} - \lambda_A) \quad \text{F.12}$$

where a_λ^E is the amplitude of the helicity state λ of E as seen from the rest frame of A. f_η contains the arbitary coefficient and product of Clebsch Gordon coefficients for coupling scheme η . A Lorentz transformation to the centre of mass of E does not alter its helicity state λ . Using the rotation matrices for spin J $d^J_{\lambda'\lambda}(\theta)$ we derive:

$$b^E_{\lambda'} = \sum_{\lambda} d^J_{\lambda'\lambda}(\theta)\; a^E_\lambda \qquad \text{F.13}$$

for the substate λ' of E in its rest frame with respect to the direction of $\overline{D}$. A Lorentz transformation to the centre of mass of $\overline{E}$ leaves F.13 invariant. We then couple the angular moments for the lower vertex to get:

$$\sum_{\lambda,\lambda'} \Big(\sum_{\xi}\sum_{L} g_\xi\Big)_{\lambda'}\; d^J_{\lambda'\lambda}(\theta)\; \Big(\sum_{\eta}\sum_{\ell} f_\eta\Big)_\lambda \qquad \text{F.14}$$

where the first bracket represents the equivalent of F.12 for the lower vertex. In principle this contains all the information about the spin states of A,$\overline{B}$,$\overline{C}$ and D which is implied by angular momentum conservation and the exchange of E.

Clearly the general case contains too many arbitary parameters to be particularly interesting. We consider some specific cases relevant to the data analysed here in which the sums in F.14 simplify. We see that we recover F.11 from F.14 by noting that $\lambda = \lambda' = 0$ and $d^J_{00}(\theta) \sim P^0_J$ (cos θ).

Consider the reaction:

$$K^- p \rightarrow \Lambda^0 \rho^0 \qquad \text{F.15}$$

Let us assume that the reaction is dominated by <u>pseudoscalar</u> exchange (K-exchange):

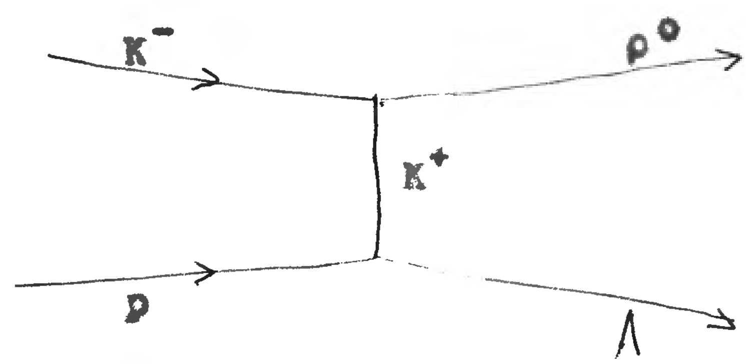

F.16

We know from parity conservation that the orbital motion at both vertices must be odd and from angular momentum conservation that it must be less than or equal to one. Therefore we have $\ell = 1$ in both cases. Since J = 0 the rotation matrix d(θ) is unity. In the centre of mass of K^- we have that $\lambda_\rho = 0$ since it must equal the magnetic substate of the orbital motion. Similarly at the other vertex the helicities of the proton and Λ must be equal so that F.14 reduces to:

$$\delta_{\lambda_\rho 0}\, \delta_{\lambda_\rho \lambda_\Lambda} \qquad \text{F.17}$$

The production and decay of the ρ are very similar indeed to the production and decay of E in F.1 in which J = 1. The fact that K^+ is off the mass shell does not influence its angular momentum properties. We have $K^+ + \overline{K}^- \rightarrow \rho^0 \rightarrow \pi^+ + \pi^-$ so that as derived earlier the angular distribution of the πs in the rest frame of ρ with respect to the K^- direction is:

$$f(\theta) \sim \left| P_1^0 (\cos\theta) \right|^2 \sim \cos^2\theta \qquad \text{F.18}$$

Reference to Fig.5.6 shows that this is definitely __not__ the case.

Let us try K^*_{890} exchange:

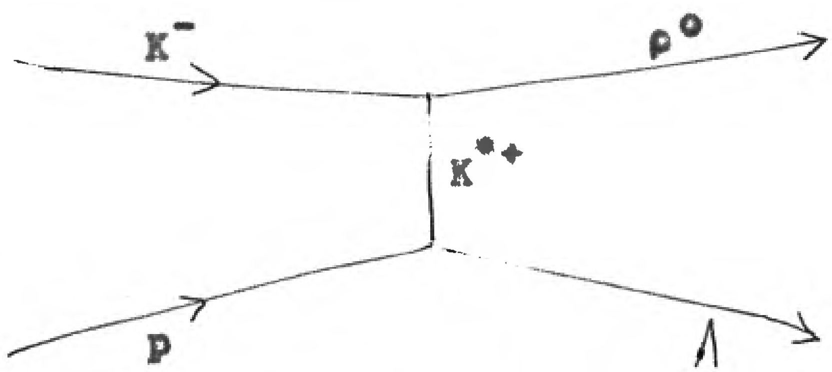

F.19

We still have $\ell = 1$ at both vertices. We start in the proton rest frame. There are four angular momenta at the lower vertex and so we must consider two different amplitudes which will be taken as the baryon spin flip and spin non flip amplitudes.

Spin non flip: $b_N \langle 1\lambda 1 0 \| 0 0\rangle \langle \tfrac{1}{2}\lambda_\Lambda 0 0 \| \tfrac{1}{2}\lambda_p\rangle$

F.20

Spin flip: $b_F \langle 1\lambda 1 0 | 1\lambda\rangle \langle \tfrac{1}{2}\lambda_\Lambda 1\lambda \| \tfrac{1}{2}\lambda_p\rangle$

which on dropping irrelevant numerical factors reduces to

$$a_\lambda = b_F\,\delta_{\lambda 1}\,\delta_{\lambda_\Lambda -\frac{1}{2}}\,\delta_{\lambda_p \frac{1}{2}} + b_F\,\delta_{\lambda -1}\,\delta_{\lambda_\Lambda \frac{1}{2}}\,\delta_{\lambda_p -\frac{1}{2}} + b_N\,\delta_{\lambda_\Lambda \lambda_p}\,\delta_{\lambda 0} \qquad \text{F.20}$$

where λ is the helicity of K^* in the proton rest frame, and b_F and b_N are constants describing the strengths of the spin flip and spin non flip coupling respectively. Now the Lorentz transformation to the K^* rest frame is trivial and is followed by the rotation β. The rotation matrix $d^1_{mm'}(\beta)$ is given by:

$$\begin{bmatrix} (1+\cos\beta)/2 & -\sin\beta/\sqrt{2} & (1-\cos\beta)/2 \\ \sin\beta/\sqrt{2} & \cos\beta & -\sin\beta/\sqrt{2} \\ (1-\cos\beta)/2 & \sin\beta/\sqrt{2} & (1+\cos\beta)/2 \end{bmatrix} \qquad \text{F.21}$$

Therefore, after another Lorentz transformation to the rest frame of ρ, we have K^* helicity amplitude:

$$\psi_{\lambda'} = \sum_\lambda d^1_{\lambda'\lambda}(\beta)\, a_\lambda$$

Finally the angular momentum coupling at the top vertex yields $\chi_{\lambda'}$ the ρ helicity amplitude:

$$\chi_{\lambda'} = \sum_\lambda \langle 1\lambda' \| 1 0 1 \lambda'\rangle\, d^1_{\lambda'\lambda}(\beta)\, a_\lambda \qquad \text{F.22}$$

If (θ,ϕ) are the decay angles of the Λ in the decay:

$$\Lambda \rightarrow p + \pi^-$$

then each helicity state of Λ decays as follows:

$$\psi^{\Lambda}_{\frac{1}{2}} \longrightarrow s\psi^{p}_{\frac{1}{2}} + p\left[-\frac{1}{\sqrt{3}}\psi^{p}_{\frac{1}{2}}Y^0_1(\theta,\phi)+\sqrt{\tfrac{2}{3}}\,\psi^{p}_{-\frac{1}{2}}Y^1_1(\theta,\phi)\right]$$

$$\psi^{\Lambda}_{-\frac{1}{2}} \longrightarrow s\psi^{p}_{-\frac{1}{2}} + p\left[\frac{1}{\sqrt{3}}\psi^{p}_{-\frac{1}{2}}Y^0_1(\theta,\phi)-\sqrt{\tfrac{2}{3}}\,\psi^{p}_{\frac{1}{2}}Y^{-1}_1(\theta,\phi)\right]$$

where s and p are the s and p wave decay amplitudes. ψ^{p}_{λ} is the helicity of the final state proton - this is not observed and we take the trace over this helicity index. We also take $|s|^2+|p|^2 = 1$ and $2\mathrm{Re}(s^*p) = \alpha$. The density matrix elements of the lambda are given by:

$$\rho^{\Lambda}_{11} = \tfrac{1}{2}(1 - \alpha\cos\theta) \qquad \rho^{\Lambda}_{1-1} = -\tfrac{1}{2}\alpha\sin\theta e^{i\phi}$$

$$\rho^{\Lambda}_{-11} = -\tfrac{1}{2}\alpha\sin\theta e^{-i\phi} \qquad \rho^{\Lambda}_{-1-1} = \tfrac{1}{2}(1 + \alpha\cos\theta) \qquad \text{F.23}$$

If subsequently we wish to look at a correlation not involving the Λ decay we take the trace of this matrix or (equivalently) set $\alpha = 0$.

We now examine the density matrix of the ρ $\left(= \chi_\lambda \chi^{\dagger}_{\lambda'}\right)$ after taking the trace over initial proton spin states and substituting F.23 for the lambda density matrix elements F.22 yields diagonal elements:

$$\rho_{11} = \frac{1}{4}(1 + \cos^2\beta)b_F^2 + \frac{(\cos^2\beta - 1)b_N^2}{2} + \frac{1}{4}b_F^2 \cos\beta\,\alpha \cos -$$
$$- \frac{(\cos^2\beta - 1)^{\frac{1}{2}}}{\sqrt{2}} \cos\beta\, b_N\, b_F\, \alpha \sin\theta \sin\phi$$

$$\rho_{oo} = 0$$

$$\rho_{-1-1} = \frac{1}{4}(1 + \cos^2\beta)b_F^2 + \frac{(\cos^2\beta - 1)b_N^2}{2} - \frac{1}{4}b_F^2 \cos\beta\,\alpha \cos -$$
$$- \frac{(\cos^2\beta - 1)^{\frac{1}{2}}}{\sqrt{2}} \cos\beta\, b_N\, b_F\, \alpha \sin - \sin\phi \qquad \text{F.24}$$

To derive the Λ decay asymmetry we take the trace over the rho density matrix. The last term above will contribute a strong up-down asymmetry from the interference of the spin flip and spin non flip amplitudes. If however b_N or $b_F = 0$ the asymmetry will vanish.(7) The above calculation could be continued to derive the complete angular correlation function - instead we will neglect the Λ decay from here on. The non vanishing elements of the ρ density matrix become

$$\rho_{11} = \rho_{-1-1} = \frac{1}{4}(1 + \cos^2\beta)b_F^2 + \frac{(\cos^2\beta - 1)b_N^2}{2}$$
$$\rho_{1-1} = \rho_{-11} = \frac{b_F^2 + 2b_N^2}{4}(\cos^2\beta - 1) \qquad \text{F.25}$$

We note that there is no interference between the two amplitudes when the Λ decay is neglected. We can therefore treat the two separately. For the non spin flip case we divide by the trace to get a normalised state:

$$\rho \text{ non spin flip} = \begin{pmatrix} \frac{1}{2} & 0 & \frac{1}{2} \\ 0 & 0 & 0 \\ \frac{1}{2} & 0 & \frac{1}{2} \end{pmatrix} \qquad \text{F.26}$$

which gives the decay distribution:

$$W_N(\Theta, \Phi) = \frac{3}{4\pi} \sin^2\Theta \sin^2\Phi \qquad \text{F.27}$$

where (Θ, Φ) are the decay angles of the rho.

For the spin flip case:

$$\rho \text{ spin flip} = \begin{pmatrix} \frac{1}{2} & 0 & \frac{x}{2} \\ 0 & 0 & 0 \\ \frac{x}{2} & 0 & \frac{1}{2} \end{pmatrix} \qquad \text{F.28}$$

where $x = \dfrac{\cos^2\beta - 1}{\cos^2\beta + 1}$

which gives the decay distribution:

$$W_F(\Theta, \Phi) = \frac{3}{4\pi} \sin^2\Theta \left(\frac{1-x}{2} + x \sin^2\Phi \right) \qquad \text{F.29}$$

Treiman Yang angle of ρ in $K^- p \rightarrow \Lambda p$

Curves are dashed — pseudo scalar exchange prediction

dotted — spin flip vector " "

line — spin non flip vector " "

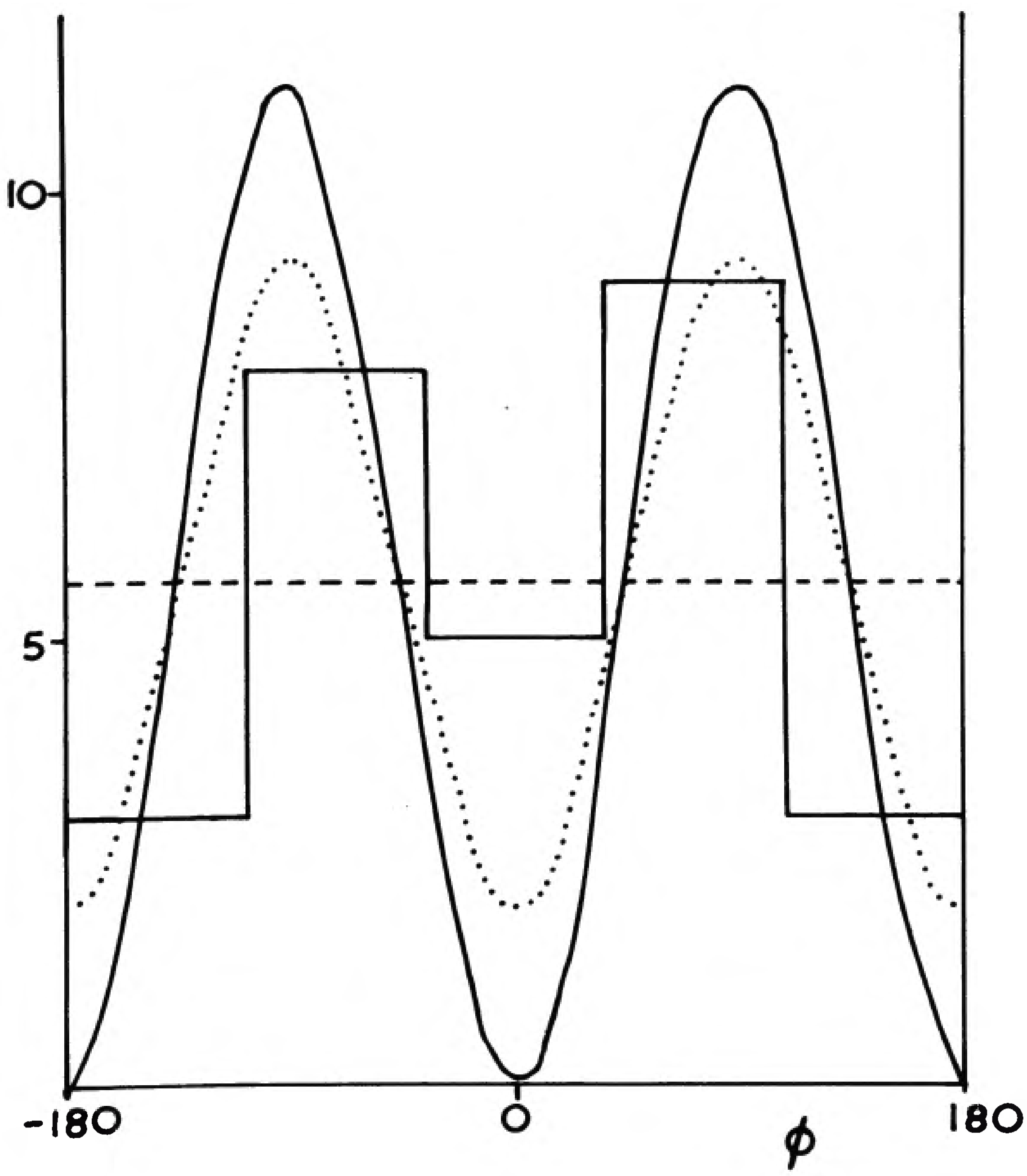

Fig. F1.

x is tabulated below as a function of t - the calculation is made by substituting in the expression for cos β in F.11.

t	-.1	-.25	-.5
x	0.60	0.73	0.71

Above t = -0.1 x falls rapidly as the value cos β = -1 is approached at the edge of the physical region. x decreases slowly for large negative values of t. Reference to Fig.5.5 shows that nearly all events lie in the region $-.1 > t > -.5$ in which x is reasonably constant. If we take x = 0.65 we get

$$W_F(\Theta,\Phi) = \frac{3}{4\pi}\sin^2\Theta\,(0.175 + 0.65\sin^2\Phi)$$

In Fig.F.1 the Treiman Yang distribution of Fig.5.6 is reproduced. The three curves represent pseudoscalar exchange (isotropy), spin non flip (strong $\sin^2$ modulation) and spin flip (weaker $\sin^2$ modulation). The spin non flip is in disagreement with experiment over the content of the central bin. The results are:

	χ^2 on Φ	P%	χ^2 on Θ	P%
Pseudo scalar	4.9	50%	>100	~ 0
Spin flip	3.0	50%	1.28	>50%
Spin non flip	9.0	8%		

The pseudoscalar exchange is ruled out by the Θ dependence (Fig.5.3). The data support the spin flip rather than the spin non flip.

<u>Note</u>. In the above calculation (as well as in those of chapter 6) it is assumed that the effects of absorption can be represented by a spin independent form factor. If this is so, the only effect of absorption on the decay distributions is to modify the coefficients appearing in the matrix element - in this case the variable x. This is taken into account by substituting <u>experimental</u> values for these variables. Since absorption is not completely spin independent in practice, the procedure is limited - it does however seem to be the best way of doing calculations with the single particle exchange model and is very easily extended to double peripheral processes (chapter 6).

REFERENCES TO APPENDIX F

(1) E. Ferrari and F. Selleri: Phys. Rev. Letters 7, 387 (1961).

(2) L. Stodolsky and J.J. Sakurai: Phys. Rev. Letters 11, 90 (1963).

(3) For instance: B. Kehoe: Phys. Rev. Letters 11, 93 (1963); J.M. Field: D.Phil. thesis (Oxford) (1964).

(4) J.D. Jackson et al: Phys. Rev. 139, B428 (1965).

(5) R.J.N. Phillips and W. Rarita: Phys. Rev. 139, B1336 (1965).

(6) Yuan Li and Michel B. Martin: Phys. Rev. 135, B561 (1964).

(7) The small number of events in the $K^-p \to \Lambda\rho^0$ reaction in this experiment prevented a meaningful analysis of the Λ asymmetry.

APPENDIX G

Angular distribution predictions for double peripheral processes

We consider the angular correlations induced by the exchange of nonets of pseudoscalar (P) and vector mesons (V) in double peripheral graphs of the types:

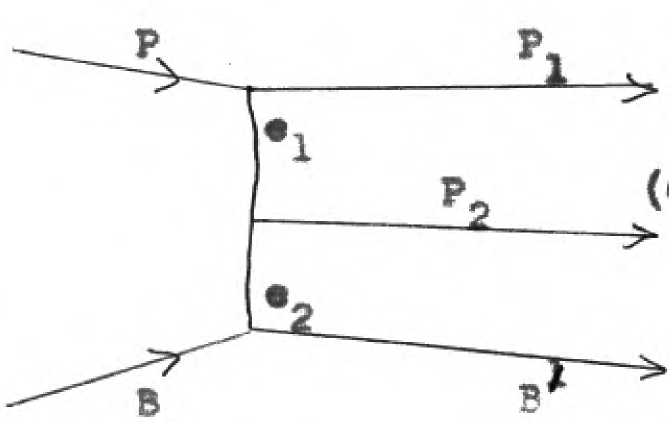

(G.1)

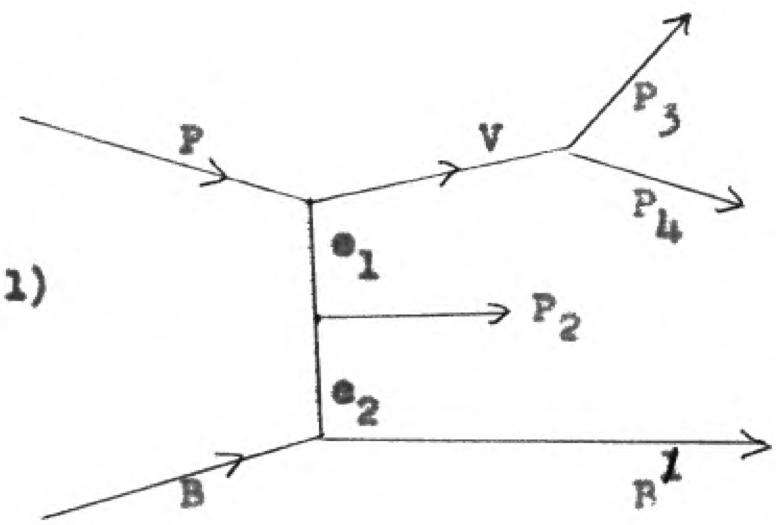

(G.2)

In reaction G.1 we deduce that e_1 is not pseudoscalar by spin parity conservation at the top vertex. Similarly in G.2, if e_1 is pseudoscalar then e_2 is not and vice versa.

We define the variables:

ϕ The angle between the planes $\underline{P} \times \underline{P}_1$ (or $\underline{V}$) and $\underline{B} \times \underline{B}^1$ in the rest frame of P_2

Θ The angle between $\underline{P}$ and $\underline{P}_3$ in the rest frame of V

Φ The angle between the planes $\underline{P} \times \underline{P}_2$ and $\underline{P} \times \underline{\;}_3$ in the rest frame of V.

We use the helicity state representation of spin angular momentum to derive the dependence of the matrix elements for G.1 and G.2 on these variables. We also define:

cos β_1 as the cosine of the scattering angle of the crossed reaction $e_2 + P_2 \rightarrow P + V$ (or P_1) in the rest frame of e_1.

cos β_2 similarly for $e_1 + P_2 \rightarrow B + B^1$ in the rest frame of e_2.

Defining a, b, c, d, e as the masses squared of P, B, P_1, P_2 and B^1 respectively we have by the methods of appendix F:

$$\cos \beta_1 = - \frac{(c-a)(t_2-d) + t_1(a+c+d+t_2) - t_1^2 - 2s_1t_1}{\left[(t_1-a-c)^2 - 4ac\right]^{\frac{1}{2}} \left[(t_1-t_2-d)^2 - 4t_2d\right]^{\frac{1}{2}}} \qquad \text{G.3}$$

$$\cos \beta_2 = - \frac{(d-t_1)(b-e) + t_2(b+d+e+t_1) - t_2^2 - 2s_2t_2}{\left[(t_2-t_1-d)^2 - 4t_1d\right]^{\frac{1}{2}} \left[(t_2-b-e)^2 - 4be\right]^{\frac{1}{2}}} \qquad \text{G.4}$$

where $s_1 = M^2(P_1P_2)$ and $s_2 = M^2(P_2B^1)$. t_1 and t_2 are the four momentum transfers of the e_1 and e_2 exchanges respectively.

Predictions for reaction G.1

For reaction G.1 we consider the angular momenta at the top vertex in the rest frame of V. With e_1 having spin parity 1^- an L = 1 coupling is required. Then e_1 has helicity zero by axial symmetry. A Lorentz transformation to the rest frame of e_1 leaves this helicity invariant. rotation through the angle β_1 brings the momentum vector of P_2 and the quantisation axis together. Such a rotation for the $j = 1$ system gives helicity amplitudes, a_λ :

$$(a_1, a_0, a_{-1}) = (\sin \beta_1/\sqrt{2}, \cos \beta_1, - \sin \beta_1/\sqrt{2}) \qquad G.5$$

The Lorentz transformation to the P_2 rest frame leaves the amplitudes invariant. Thus the helicity amplitudes of the exchanged vector meson in the rest frame of P_2 with respect to the plane $\underline{P} \times \underline{P}_1$ as zero of azimuth are given by G.5.

If e_2 is pseudoscalar then conservation of angular momenta in the rest frame of P_2 implies that the square of the matrix element is independent of $\emptyset$.

If e_2 is vector and couples to the baryons without spin flip a similar argument shows that the helicity amplitudes, b_λ, of e_2 in the P_2 rest frame with respect to the plane $\underline{P} \times \underline{P}'$ as zero of azimuth are:

$$(b_1, b_0, b_{-1}) = \frac{\sin \beta_2}{\sqrt{2}}, \cos \beta_2, - \frac{\sin \beta_2}{\sqrt{2}} \qquad G.6$$

Before coupling the helicities of e_1 and e_2 together we must refer them to the same axes (e.g. those of e_2). This involves the change of azimuth ϕ (each amplitude a_λ is multiplied by $e^{i\lambda\phi}$) and a rotation of 180° to reverse the z-axis of quantisation (which transposes the amplitudes a_1 and a_{-1} without change of sign). We get:

$$(a'_1, a'_0, a'_{-1}) = \left(\frac{-\sin\beta_1}{\sqrt{2}} e^{-i\phi}, \cos\beta, \frac{\sin\beta_1}{\sqrt{2}} e^{i\phi} \right) \qquad G.7$$

for the magnetic substate amplitudes, a'_m, of e_1. The amplitudes a'_{-m} and b_m are coupled with the Clebsch Gordon coefficient $\langle 1 \; m \; 1 \; -m \,|\, 10 \rangle$ to give the orbital motion ($L = 1$ $m = 0$) at this vertex. Since the coefficient $\langle 10 \quad 10 \,|\, 10 \rangle$ vanishes we collect only the terms:

$$-\frac{\sin\beta_1 \sin\beta_2}{2} \left(e^{i\phi} - e^{-i\phi}\right) \qquad G.8$$

in the matrix element.

Hence the prediction of this assignment is:

$$\left| \text{matrix element} \right|^2 \sim \sin^2\phi \qquad G.9$$

Similarly if <u>e_2 is vector and couples to the baryons with spin flip</u> the same kind of reasoning predicts a ϕ dependence:

$$\frac{1-x}{2} + x \sin^2\phi \text{ where } x = \frac{\cos^2\beta_1 - 1}{\cos^2\beta_1 + 1} \qquad G.10$$

As pointed out in the text these results may be derived more easily by applying crossing symmetry to the matrix element for production of the vector meson e_1 in a two body process:

$$\overline{P}_2 + B \rightarrow e_1 + B' ; \qquad e_1 \rightarrow \overline{P} + P_1 \qquad G.11$$

Predictions for reaction G.2

e_2 is pseudoscalar

In the rest frame of e_2 the orbital angular momentum ($L = 1$) and the spin of e_1 have $m = 0$ w.r.t. the direction of motion of e_1. Therefore e_1 has helicity $\lambda = 0$ - this remains invariant under the Lorentz transformation to the rest frame of e_1. A rotation through angle β_1 and Lorentz transformation to the rest frame of V gives e_1 helicity amplitudes:

$$\frac{\sin\beta_1}{\sqrt{2}}, \ \cos\beta_1, \ -\frac{\sin\beta_1}{\sqrt{2}}$$

Each value of e_1 helicity, λ, now couples to the corresponding V angular momentum state and the orbital motion ($L = 1 \quad m = 0$):

$$\langle \psi_V(\lambda) \mid \psi_{e_1}(\lambda)\, \psi_0' \rangle \sim \langle 1\lambda \mid 1\lambda\, 1 0 \rangle \qquad G.12$$

Therefore the magnetic substate amplitudes of V with respect to the P direction as polar axis and P_2 direction as azimuth are:

$$\frac{\sin \beta_1}{2}, \quad 0, \quad \frac{\sin \beta_1}{2}$$

The rotation matrix $d^j(\theta)$ for a $(j = 1)$ state is:

$$d^1_{mm'}(\theta) = \begin{bmatrix} (1 + \cos\theta)/2 & -\sin\theta/\sqrt{2} & (1 - \cos\theta)/2 \\ \sin\theta/\sqrt{2} & \cos\theta & -\sin\theta/\sqrt{2} \\ (1 - \cos\theta)/2 & \sin\theta/\sqrt{2} & (1 + \cos\theta)/2 \end{bmatrix} \qquad G.13$$

Now the magnetic substate of the V with respect to 1 & decay direction is pure m = 0 since it couples to the orbital motion of two scalar particles. We therefore rotate the V state to these new axes and pick out the amplitude of the m = 0 part. First rotation Φ about the polar axis:

$$\frac{\sin \beta_1}{2}\left(e^{i\Phi}, 0, e^{-i\Phi} \right) \qquad G.14$$

Now Θ to collect the m = 0 part only:

$$\frac{\sin \Theta}{\sqrt{2}} \quad \frac{\sin \beta_1}{2} \left(e^{i\Phi} - e^{-i\Phi} \right)$$

$$= \frac{i \sin \beta_1}{\sqrt{2}} \sin \Theta \sin \Phi$$

so that $\left| \text{M.E.}\ (\beta_1\beta_2\Theta\Phi\phi) \right|^2 \sim \sin^2\Theta \sin^2\Phi$ 0.15

where M.E. is the matrix element.

<u>e_2 is vector with spin non flip coupling to baryons</u>

In the B rest frame the helicity of e_2 is zero for spin non flip. Therefore it is given by $\left(\frac{\sin\beta_2}{\sqrt{2}},\ \cos\beta_2,\ \frac{-\sin\beta_2}{\sqrt{2}}\right)$ in P_2 rest frame. The helicity amplitudes of e_1 in P_2 C of M are given by $\left(\frac{\sin\beta_2}{2},\ 0\ ,\ \frac{\sin\beta_2}{2}\right)$ by coupling with the orbital motion as before. These amplitudes are with respect to the B direction as zero of azimuth. We now go to axes with P as zero of azimuth - each amplitude transforms by $e^{i\lambda\phi}$

$$\left(\frac{\sin\beta_2}{2}\, e^{i\phi},\ 0,\ \frac{\sin\beta_2}{2}\, e^{-i\phi}\right) \qquad 0.16$$

After transformation to the e_1 rest frame, rotation through β_1 gives us:

$$\begin{bmatrix} \frac{\sin\beta_2}{4}(e^{i\phi} + e^{-i\phi}) + \frac{\sin\beta_2\cos\beta_1}{4}(e^{i\phi} - e^{-i\phi}) \\ \frac{\sin\beta_1\sin\beta_2}{2\sqrt{2}}(e^{i\phi} - e^{-i\phi}) \\ \frac{\sin\beta_2}{4}(e^{i\phi} + e^{-i\phi}) - \frac{\sin\beta_2\cos\beta_1}{4}(e^{i\phi} - e^{-i\phi}) \end{bmatrix} \qquad 0.17$$

in the rest frame of V. The analysis now runs parallel to the pseudoscalar case. The V helicity amplitudes are got by multiplying by the appropriate Clebsch Gordan coefficient.

$$\frac{\sin\beta_2}{2}\cos\phi + \frac{i\sin\beta_2\cos\beta_1}{2}\sin\phi$$

$$0 \qquad\qquad 3.18$$

$$-\frac{\sin\beta_2}{2}\cos\phi + \frac{i\sin\beta_2\cos\beta_1}{2}\sin\phi$$

Then azimuthal change

$$\left(\frac{\sin\beta_2}{2}\cos\phi + \frac{i\sin\beta_2\cos\beta_1}{2}\sin\phi\right)e^{i\Phi}$$

$$0 \qquad\qquad 3.19$$

$$-\left(\frac{\sin\beta_2}{2}\cos\phi - \frac{i\sin\beta_2\cos\beta_1}{2}\sin\phi\right)e^{-i\Phi}$$

Now Θ rotation and collect m = 0 term only:

$$\frac{\sin\Theta}{\sqrt{2}}\left[\sin\beta_2\cos\phi\cos\Phi - \sin\beta_2\cos\beta_1\sin\phi\sin\Phi\right]$$

3.20

Therefore $M.E.(\phi\,\Theta\,\Phi)^2 \sim \sin^2\Theta(\cos\phi\cos\Phi - \cos\beta_1\sin\phi\sin\Phi)^2$

3.21

<u>e_2 is vector with spin flip coupling</u>

Then the helicity of e_2 in B rest frame is +1 for B spin $+\frac{1}{2}$:

In p_2 frame: $a_\lambda(e_2) = \dfrac{1 + \cos\beta_2}{2},\ \dfrac{\sin\beta_2}{\sqrt{2}},\ \dfrac{1 - \cos\beta_2}{2}$ G.22

In P_2 frame: $a_\lambda(e_1) = \dfrac{1 + \cos\beta_2}{2},\ 0,\ \dfrac{-1 + \cos\beta_2}{2}$ G.23

~~As above but~~ (with respect to $\underline{P} \times \underline{V}$ as zero of azimuth instead of $\underline{B} \times \underline{B}^{x}$):

$$a_\lambda(e_1) = \frac{1 + \cos\beta_2}{2}\,e^{i\phi},\quad 0,\quad \frac{\cos\beta_2 - 1}{2}\,e^{-i\phi} \qquad \text{G.24}$$

After Lorentz transformation to e_1 rest frame, rotation through angle β_1 and Lorentz transformation to V centre of mass:

$$a_\lambda(e_1) = \left\{\begin{array}{l} \dfrac{(1 + \cos\beta_1)}{2}\dfrac{(1 + \cos\beta_2)}{2}\,e^{i\phi} + \dfrac{(\cos\beta_2 - 1)}{2}\dfrac{(1 - \cos\beta_1)}{2}\,e^{-i\phi} \\[2ex] \dfrac{\sin\beta_1}{\sqrt{2}}\left(\dfrac{1 + \cos\beta_2}{2}\,e^{i\phi} - \dfrac{\cos\beta_2 - 1}{2}\,e^{-i\phi}\right) \\[2ex] \dfrac{(1 - \cos\beta_1)}{2}\dfrac{(1 + \cos\beta_2)}{2}\,e^{i\phi} + \dfrac{(\cos\beta_2 - 1)}{2}\dfrac{(1 + \cos\beta_1)}{2}\,e^{-i\phi} \end{array}\right. \qquad \text{G.25}$$

Multiplying by the appropriate Clebsch Gordan coefficient to get the helicity amplitudes of V and rotation of Φ to get $\underline{P}_3 \times \underline{P}_4$ as zero of azimuth:

$$a_\lambda(V) = \begin{cases} \left[\tfrac{1}{2}i(1+\cos\beta_1\cos\beta_2)\sin\phi + \tfrac{1}{2}(\cos\beta_1 + \cos\beta_2)\cos\phi\right] e^{i\Phi} \\ 0 \\ \left[-\tfrac{1}{2}i(1-\cos\beta_1\cos\beta_2)\sin\phi - \tfrac{1}{2}(\cos\beta_2 - \cos\beta_1)\cos\phi\right] e^{-i\Phi} \end{cases} \qquad 0.26$$

Rotation through polar decay angle Θ and collect m = 0 term only:

$$a_0(V) = \frac{\sin\Theta}{\sqrt{2}}\left[(\tfrac{1}{2}i\ \sin\phi + \cos\beta_2\cos\phi\tfrac{1}{2})(e^{i\Phi} + e^{-i\Phi}) + (\tfrac{1}{2}i\ \cos\beta_1\cos\beta_2\sin\phi + \tfrac{1}{2}\cos\beta_1\cos\phi)(e^{i\Phi} - e^{-i\Phi})\right]$$

$$= \frac{\sin\Theta}{\sqrt{2}}\left[i\ \cos\Phi\sin\phi + \cos\beta_2\cos\phi\cos\Phi - \cos\beta_1\cos\beta_2 \times \sin\phi\sin\Phi + i\ \cos\beta_1\cos\phi\sin\Phi\right] \qquad 0.27$$

The matrix element for B spin $-\tfrac{1}{2}$ is the same as above with the sign of $\cos\beta_2$ changed. This has no effect on the square of the matrix element so that the following applies also to an unpolarised target B.

$$\left| \text{M.E.} (\phi \Theta \Phi) \right|^2 \sim$$

$$\frac{\sin^2 \Theta}{2} \Big[\cos^2\Phi \sin^2\phi + \cos^2\beta_1 \cos^2\phi \sin^2\Phi$$

$$+ 2 \cos\beta_1 \cos\phi \sin\phi \cos\Phi \sin\Phi$$

$$+ \cos^2\beta_2 \cos^2\phi \cos^2\Phi + \cos^2\beta_1 \cos^2\beta_2 \sin^2\phi \sin^2\Phi$$

$$- 2 \cos\beta_1 \cos^2\beta_2 \sin\phi \cos\phi \sin\Phi \cos\Phi \Big] \qquad \text{G.28}$$